PARTICLE SCALE DYNAMICS OF COARSE GRANULAR MATERIAL

by

Kyle Douglas Williams

A thesis submitted in partial fulfillment
of the requirements for the degree of

MASTER OF SCIENCE
GEOLOGICAL ENGINEERING

At the

UNIVERSITY OF WISCONSIN-MADISON

Fall 2016

PARTICLE SCALE DYNAMICS OF COARSE GRANULAR MATERIAL

Approved:

Approved 12/2/16

Signature Date

William J. Likos, Professor

Approved 12/2/16

Signature Date

Dan Negrut, Associate Professor

Approved 12/2/16

Signature Date

Tuncer B. Edil, Professor Emeritus

To my wonderful wife:

This is your fault

Abstract

Developing a new wheeled or tracked vehicle for military use typically involves physical prototyping of preliminary vehicle designs and field tests to evaluate their performance in a range of conditions. Computational simulations of vehicle performance, including physics-based simulation of vehicle-terrain interaction, is an effective alternative for reducing costs of physical prototyping. Activities described in this thesis have been conducted in coordination with the Simulation Based Engineering Laboratory (SBEL) at the University of Wisconsin-Madison, which is actively engaged in physics-based simulation of vehicle-terrain interaction for military and other vehicles. The primary tool used for simulation is the Discrete Element Model (DEM) Chrono::Engine and the Chrono::Granular toolkit (Mazhar, et al., 2013).

The primary objective of this research was to provide a robust physical data set to validate Chrono::Granular simulations of coarse-grained granular material behavior using relatively simple and common geotechnical tests. Tests selected included laboratory fall cone tests and direct shear tests using dry and moist preparations of 20-30 Ottawa sand and 3 mm spherical glass beads. A special direct shear device was designed, constructed, and calibrated to provide direct visual observation of particle displacements for a single plane of particles subject to shearing. Shear stress-displacement relationships measured during shearing and individual particle displacements tracked using particle image velocimetry (PIV) were made available for comparison with discrete particle displacements simulated by DEM and Chrono::Granular. Results from the fall cone testing series, including measurements of cone penetration depth as a function of time, cone apex angle, drop height, and initial particle density were also made available for direct comparison with computational simulations. The suite of fall cone and direct shear test results was analyzed to investigate relationships among the testing parameters. A case study review of similarly unconventional applications of fall cone and direct shear testing and of applications of PIV to granular material is provided.

Results from the fall cone penetration test series indicate that penetration into coarse granular media is most affected over small ranges of drop height by the cone geometry (apex angles of 30° and 60°). Results from the direct shear test series indicate that shear displacement rate affects individual particle motion, with lower shear rates allowing more rotation and localized particle displacements than higher shear rates. Introducing water into the shear zone changes bulk shear strength and the character of individual particle motions. Direct shear tests with glass beads indicated that capillary bridges between particles caused displacement of particles in zones that had not moved in dry tests. Direct shear tests with sands indicated that the inclusion of water near the shear zone caused shear failure to occur outside the wetted zone along a different shear surface. Shear band development was observed to depend on shear displacement rate, applied normal force, and the presence or absence of moisture in the shear surface. Direct comparisons between the physical test results reported here and analog Chrono::Granular simulations not included as part of this thesis.

Acknowledgements

I first would like to thank my advisor Dr. William Likos for his support and guidance through the course of this research, helping to point me toward the right direction, and pushing me to make sure I had an understanding and justification for the things I saw beyond what I expected. I also want to thank my committee members, Dr. Dan Negrut and Dr. Tuncer Edil for their review of this work.

I would like to thank Mr. Xiaodong Wang, affectionately known to the Geological Engineering (GLE) program as “Buff,” for his assistance in the fabrication and set up of several of the tests run over the course of the research. I also want to thank the University of Wisconsin-Madison (UW) instrument shop for their assistance fabricating the direct shear apparatus.

I would finally like to thank my friends and family. You made the process of moving across country for school much easier, and were the source of good times that kept my spirits high. Thank you all so very much.

This project was sponsored by US Army TARDEC under Rapid Innovation Fund (RIF) grant W56HZV-14-C-0254. The support of Dr. Jayakumar Paramsothy is gratefully acknowledged. Any opinions, findings, and conclusions or recommendations expressed in this material are those of the author and do not necessarily reflect the views of US Army TARDEC.

Table of Contents

List of Tables

List of Figures

1 Introduction

1.1 Statement of the Problem

When evaluating a new wheeled or tracked vehicle to be used in the military, the designs must be prototyped and subjected to a series of physical tests to evaluate the vehicle performance, including vehicle-terrain interaction for a wide range of terrain types. The physical prototyping and testing process is costly and requires an extensive amount of time to complete. Computational simulation of vehicle-terrain dynamics is an alternative to direct physical testing and allows parametric evaluation of the vehicle design parameters.

The open-source, computational simulation package Chrono::Engine has been developed by the Simulation Based Engineering Laboratory (http://sbel.wisc.edu/) at the University of Wisconsin-Madison. As described by SBEL and illustrated in Figure 1.1, the Chrono platform has five foundational components that provide support for equation formulation, equation solution, proximity computation, parallel computing, and post-processing. The software is organized so that it draws on parallel computing, GPU computing, multi-core parallel computing, and distributed-memory parallel computing. The rigid body dynamics, flexible body dynamics, and fluid-solid interaction solution is built on the aforementioned foundational components. User toolkits (such as Chrono::Vehicle, Chrono::Granular, etc.) are in place to ease the pre/post-processing burden associated with Chrono simulation.

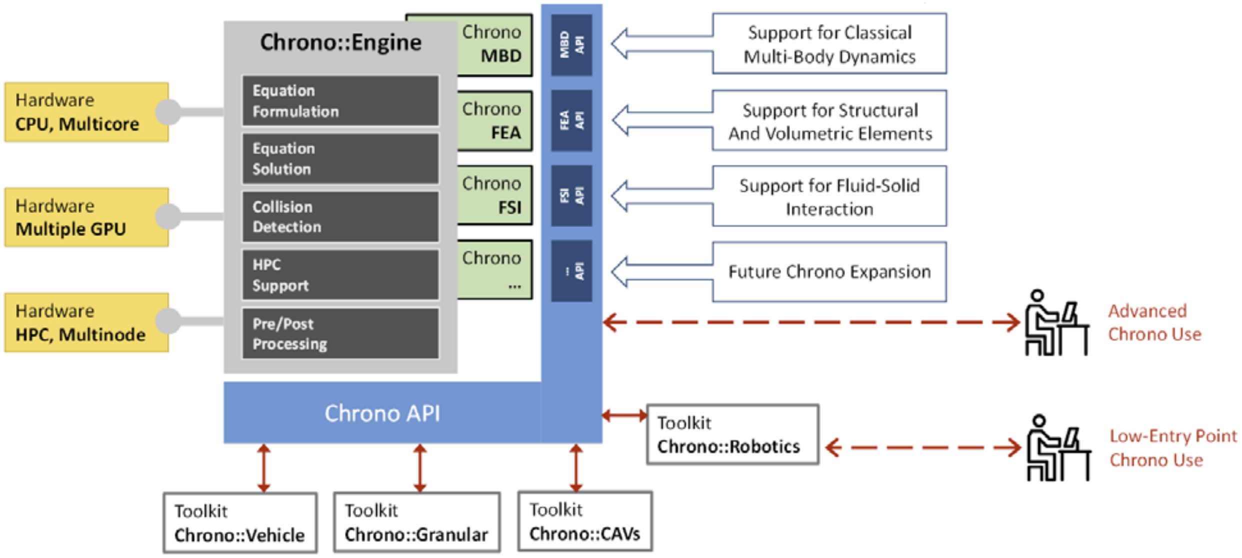

Figure 1.1 High-level organization of Chrono computational simulation engine (from http://api.chrono.projectchrono.org/faq_root.html)

1.2 Goals

Chrono::Granular is a toolkit within the suite of Chrono::Engine modules that employs discrete element modeling (DEM) for granular material such as soil. The purpose of this research consisted of two goals. The first goal was to provide a robust physical data set of bulk-scale and particle-scale behavior of coarse-grained granular material for comparison with and validation of analog simulations from Chrono::Granular. The second goal was to develop novel testing approaches for granular materials using unconventional applications of traditional geotechnical testing methods (fall cone and direct shear testing) and to utilize results from the tests to improve understanding of the behavior of dry and moist (unsaturated) granular media.

1.2.1 Objectives and Tasks

The accomplishment of the above-mentioned goals required several objectives. Each objective also required a series of tasks to complete them. The first objective was to perform fall cone penetration tests to supply static and dynamic penetration data for comparison with

Chrono::Granular simulations of analog tests. The tasks necessary to complete this objective are listed below:

- **Select the materials to be used**
- **Quantify the physical properties of the test materials**
- **Design and construct the test apparatus**
- **Select the testing program**
- **Complete the testing program**
- **Supply results for Chrono::Granular simulations**
- **Investigate possible relationships among testing program variables**

The second objective was to perform particle-scale direct shear tests incorporating particle image velocimetry (PIV) analysis to track individual particle displacements. A special direct shear device was designed, constructed, and calibrated to provide direct visual observation of particle displacements for a single plane of particles subject to shearing. Shear stress-displacement relationships were measured during shearing and individual particle displacements were tracked using PIV and made available for comparison with discrete particle displacements simulated by DEM and Chrono::Granular. The PIV analysis would allow for the individual particles (glass beads) or patches of particles (sands) to be tracked. The tasks necessary to complete this objective are listed below:

- **Select the materials to be used**
- **Quantify the physical properties of the test materials**
- **Design and construct the test apparatus**
- **Conduct bench line tests of the apparatus to establish consistency**
- **Select the testing program**
- **Complete the testing program**
- **Complete PIV analysis of direct shear tests**
- **Supply results for Chrono::Granular simulations**
- **Investigate the effects and possible relationships among testing program variables**

1.3 Organization of Thesis

This thesis is arranged into seven chapters including this introduction chapter and seven appendices. Chapter two consists of an investigation of the methods used over the course of the research and is broken into three sections. Each section introduces a common testing method used in the engineering community, i.e. penetration testing, direct shear testing, and PIV analysis. The testing methods' primary uses are discussed, and several instances where the tests are used in nontraditional ways are identified. Finally, a series of case studies are presented to show how these test methods were used to provide unique material properties and or characterize unique behaviors.

Chapter three consists of a discussion of the materials used in this research. Each section begins with a discussion of why the material was selected, and a brief description of the origin of the material. The subsequent subsection provides a description of material properties including grain size distribution, particle shape and morphology, moisture content, specific gravity, index density and void ratio, and bulk friction angle. Each subsection includes a description of the methods used to determine each respective property, as well as comparisons to literature and/or manufacturer reported values for those properties.

Chapter four consists of a description of the methods used to provide the physical results. The chapter is divided into two sections discussing the cone penetration and direct shear testing, respectively. Each section provides a discussion on the design and construction of the apparatus, an explanation of the experimental program used to provide the data set, and the procedures used for each test.

Chapter five provides a graphical summary of the data recorded. The chapter is divided into three sections, including cone penetration testing, dry direct shear testing, and wet direct shear testing.

Chapter six includes discussion and analysis of the results. The relationship between fall cone penetration values and drop height and material density is discussed. The influence of friction between the linear variable differential transformer (LVDT) rod and housing on measured impact velocity at the cone tip is discussed. The results for the direct shear testing are evaluated to identify the effect of shear displacement rate and water content in the shear zone on localized particle movements. The development of shear bands in both materials (sands and glass beads) are discussed. The behavior of water in the shear zone and potential ramifications are discussed.

Chapter seven summarizes the conclusions made from the physical data and qualitative observations. Recommendations based on the conclusions are also provided in this section. Chapter eight lists the references cited. Subsequent appendices contain the manufacturer data sheet for the glass beads, MATLAB image analysis script, a schematic of the direct shear apparatus, and detailed direct shear results. Direct comparisons between the physical test results reported here and analog Chrono::Granular simulations are not included as part of this thesis.

2 Background

2.1 Penetration Testing

2.1.1 Fall Cone Testing – Clays

Fall cone tests were first introduced in 1915 and were used to determine the Atterberg limits and undrained shear strength of fine-grained soils and clays (Lee & Freeman, 2007; Likos & Jaafar, 2014). Fall cone tests (i.e. British, Swedish) generally employ a metal cone with a specific apex angle (e.g., 30° or 60°) and mass (e.g., 80 g or 60 g). The cone is suspended with the tip of the cone touching a soil sample in a specified container. The cone is then released and allowed to penetrate vertically into the soil for a specified length of time. For liquid limit determination, the test is repeated several times at increasing water contents until the penetration (P) reaches a specified value corresponding to the liquid limit of the soil (e.g., P = 20 mm or 10 mm).

Because of the simple apparatus and test methods, the British and Swedish fall cone test methods were selected to provide static and dynamic loading data for validation of analog Chrono::Granular simulations. Tests were conducted using dry glass beads and sands, which is a significant deviation from conventional use of fall cone methods in geotechnical engineering practice. This would not be the first time that fall cone tests have been utilized in ways that were different for the intended use. For example, fall cone tests have been used to characterize the shear strength of organic sediments (Zentar, Abriak, & Dubois, 2009), to identify the time of setting for fly ash paste and fly ash-soil mixtures (Kang, Kang, & Ge, 2013), to determine the shear viscosity of soils with liquidity indices less than one (Cevikbilen & Budhu, 2011), to identify collapsible soils (Ayadat & Hanna, 2007), and as a method to identify capillary effects on stress states in unsaturated coarse grained soils (Likos & Jaafar, 2014). Three of these case studies are summarized below.

2.1.2 Case Study: Laboratory fall cone testing of unsaturated sand – William Likos and Rani Jaafar (2014)

Characterizing the behavior of unsaturated soils is a difficult process that requires complicated tests. Because of this difficulty, Likos and Jaafar (2014) identified that the traditional methods such as direct shear or triaxial testing are limited by practical constraints in practice, and proposed a simple method to identify the behavior of unsaturated coarse granular soils as a function of moisture content. Fall cone tests were proposed because of the simple nature of the test. Likos and Jaafar (2014) proceeded to investigate the suitability of fall cone tests to identify unsaturated soil behavior.

Four sands were selected for the investigation with average particle sizes of 0.19 mm (Ottawa sand), 0.31 mm (river sand), 0.57 mm (concrete sand), and 1.24 mm (Texas sand). Prior to fall cone testing, samples of the sands were subjected to water retention tests to construct the soil water retention curve (SWRC) for each sand. Once the SWRCs were constructed, the fall cone testing began. Likos and Jaafar (2014) used the equipment and methods specified in the British standard BS 1377-2 (British Standards Institution (BSI), 1990) with two specific changes: the cylindrical container (6.3 cm diameter and 6.0 cm deep) used was larger than specified in the standard (5.5 cm diameter and 4.0 cm deep) , and the cone fall time was extended from 5 s to 15 s to allow penetration to reach steady state. Samples of sand were prepared by compaction into the specimen container in several lifts to a range of void ratios and moisture contents, with the void ratios selected to match those used to determine the SWRC.

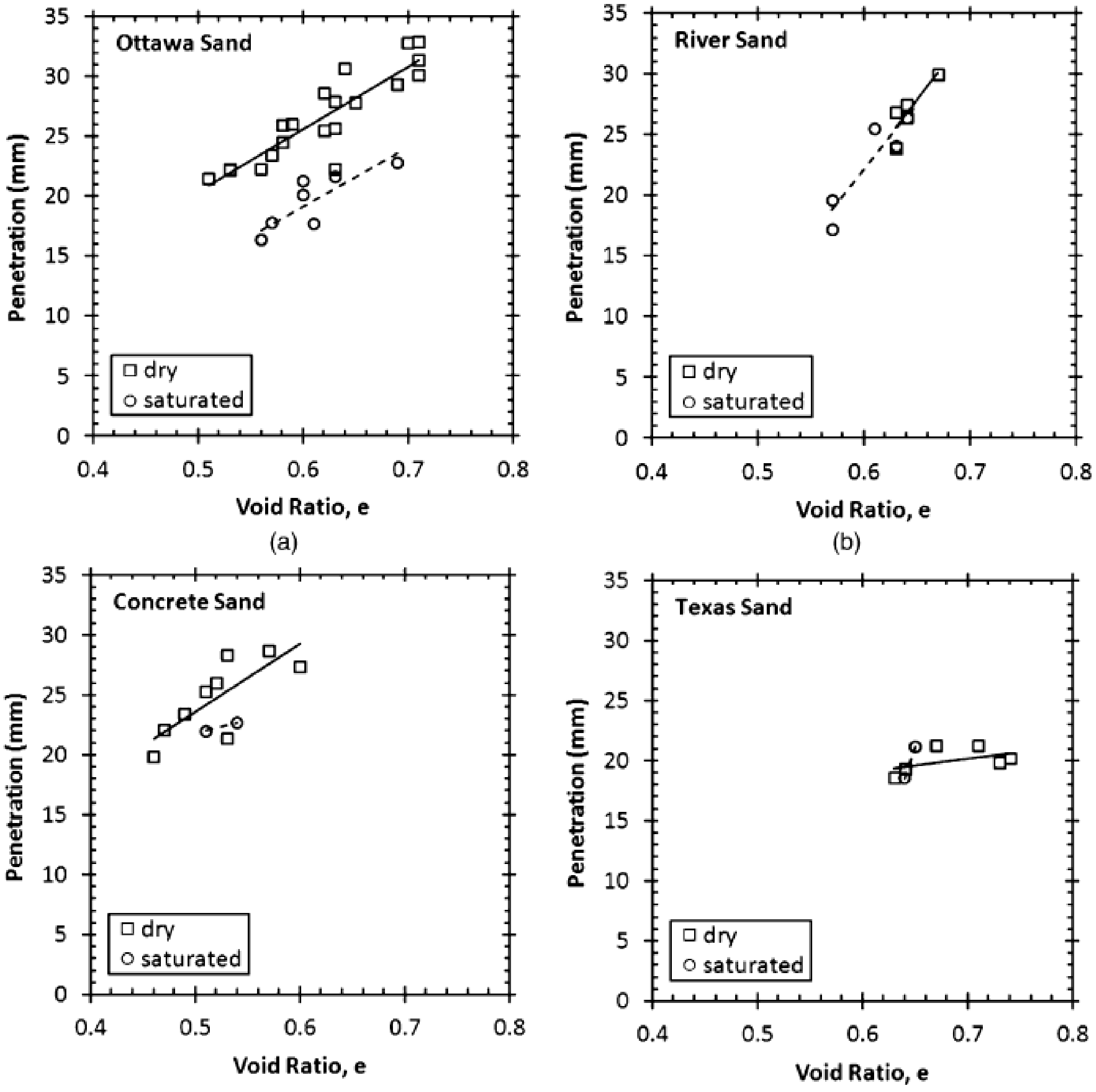

(a) (b) (c) (d)

Figure 2.1 Cone penetration as a function of void ratio for dry and saturated sands: (a) Ottawa sand; (b) river sand; (c) concrete sand; (d) Texas sand (Likos & Jaafar, 2014)

Likos and Jaafar (2014) first examined penetration results for saturated and dry sand samples. The results showed for both dry and saturated sands that as the void ratio decreased so did the penetration values. Likos and Jaafar (2014) found for smaller particle sizes the penetration values were more sensitive to void ratio changes than large particle sizes for both saturated and dry sands. The effects of void ratio on penetration are shown in Figure 2.1. The influence of saturation on penetration was most evident for the Ottawa sand. Likos and Jaafar (2014) observed that as the cone penetrated the sand, regardless of the moisture content, material heaved around the cone at the sand surface and appeared dry. This observation was attributed to flow of water into pores as the sand near the top surface dilated from the cone penetration.

Likos and Jaafar (2014) then evaluated the penetration results for unsaturated sands by plotting measured penetration against degree of saturation and separating the results by relative density of the sand. The results indicated in some cases that the lower relative density rests had higher penetration values, but the majority of the data was inconclusive.

Likos and Jaafar (2014) observed that the response of penetration to saturation exhibited behavior in a similar manner to other tests investigating material responses to saturation, thus linking the behavior to capillary stress and suction-stress interactions. The relationship between capillary stress and suction-stress is expressed using suction-stress characteristic curves, SSCC (Lu & Likos, 2006). Finally, Likos and Jaafar (2014) linked penetration to suction using the SWRC and SSCC (Figure 2.2), where it was noted:

> “penetration is largest for dry sands, decreasing sharply up to approximately residual saturation S_r, decreasing slightly and approximately linearly between residual saturation and a transition zone ranging from S [degree of saturation] of approximately 50-90% depending on the sand, and the increases more gradually to a penetration at full saturation.”

Furthermore, Likos and Jaafar (2014) presented a conceptual link between penetration and saturation as shown in Figure 2.3. At a saturation of zero, cone penetration is at its maximum. As saturation increases from zero to residual saturation, penetration begins to drop as

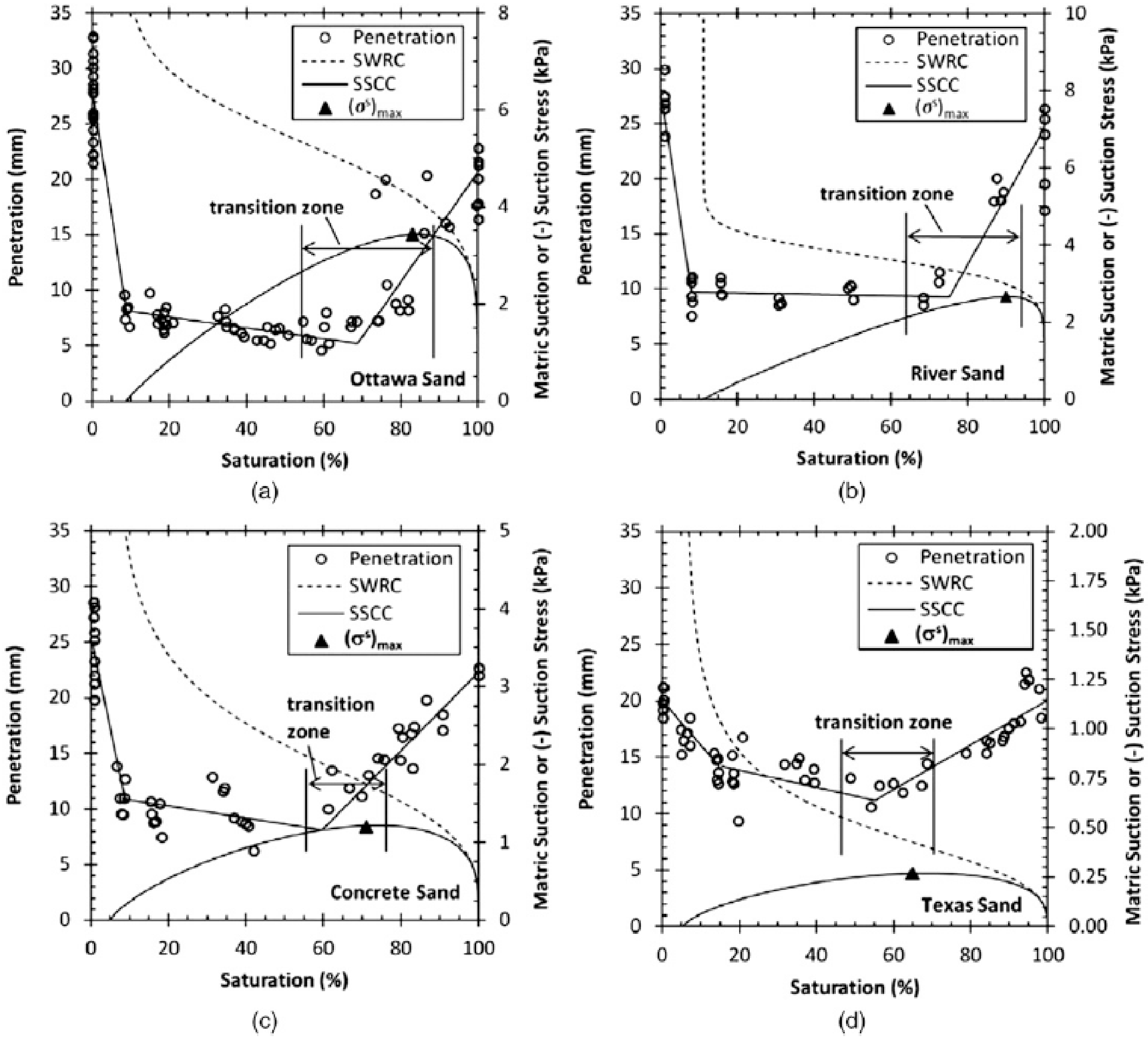

(a)

(b)

(c)

(d)

Figure 2.2 Penetration, matric suction, and suction stress as functions of void ratio for dry and saturated sands: (a) Ottawa sand; (b) river sand; (c) concrete sand; (d) Texas sand (Likos & Jaafar, 2014)

smaller pores in the soil matrix begin to fill and menisci begin to form, thus adding strength to the system. Penetration continues to decrease to a minimum value where suction stress reaches a maximum. Beyond the maximum suction stress point, penetration values increase up to full saturation, where the penetration value is still lower than the penetration of the dry material.

Using the relatively simple fall cone test, Likos and Jaafar (2014) were able to make observations between void ratio and cone penetration. Further observations of the material displacement under cone penetration indicated that the soil suction and effective stress state changed. The penetration trends with saturation were compared with the SWRC and SSCC, and were used to develop a conceptual model relating all three graphs. Likos and Jaafar (2014) concluded that fall cone tests have potential applicability as simple index test to examine the saturation-dependent response of unsaturated coarse granular soil.

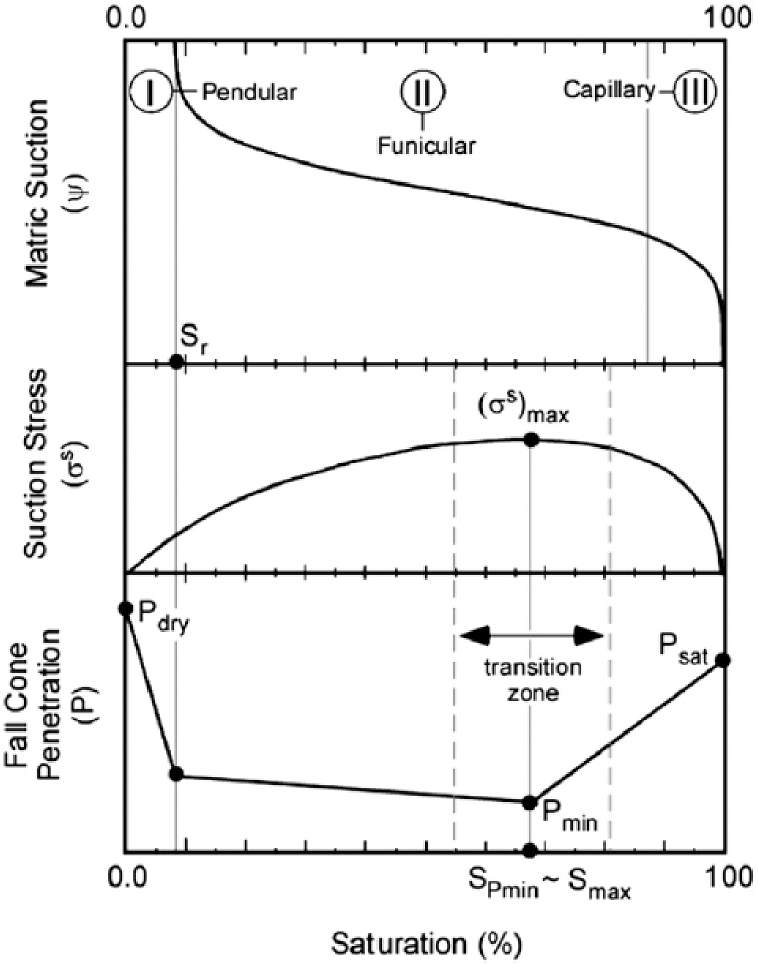

Figure 2.3 Conceptual model showing the three regimes: matric suction, suction stress, and cone penetration. (Likos & Jaafar, 2014)

2.1.3 Case Study: Identification of collapsible soil using the fall cone apparatus – Tahar Ayadat and Adel Hanna (2007)

Collapsible soils are those that experience a significant decrease in volume when subjected to wetting. Ayadat and Hanna (2007) describe these soils as being “wind-deposited silts and sands … alluvial flood plains, fans and mud flows, colluvial deposits, residual soils, volcanic buffs and man-made fill.” Ayadat and Hanna (2007) then discuss several established methods used to predict the collapse potential for coarse-grained soils but with limited applicability to fine-grained soils. Ayadat and Hanna (2007) then proceed to present a new method for determining the collapse potential for soils using the British fall cone. The method presented uses measured cone penetration and the minimum cone penetration (penetration limit) derived from a relationship between easily determined material properties to calculate the collapse potential for a series of samples.

Ayadat and Hanna (2007) used two series of mixed sans-clay samples having different weight ratios of sand and clay with varying initial moisture contents and compaction effort in their investigation. All of the samples were prepared in three layers, with each layer being compacted with a specified compaction effort. Each sample was subjected to fall cone penetration tests and oedometer tests. The first series of tests were used to investigate a possible relationship between the minimum cone penetration (cone penetration limit), the grain size uniformity coefficient, and the ratio of the dry unit weight to the saturated unit weight. Summaries of cone penetration results for the first series of tests are shown in Figure 2.4 and Figure 2.5. The initial results showed that there was a cone penetration limit that occurs at an optimum moisture content. When the optimum moisture content determined from the cone penetration tests was compared to the optimum moisture content determined from proctor compaction tests, Ayadat and Hanna (2007) found that the ratio of the two close to one for most

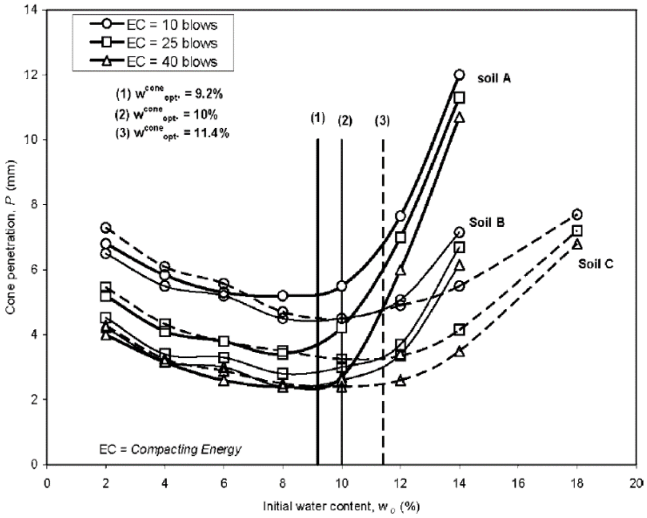

Figure 2.4 Cone penetration versus initial water content (Ayadat & Hanna, 2007)

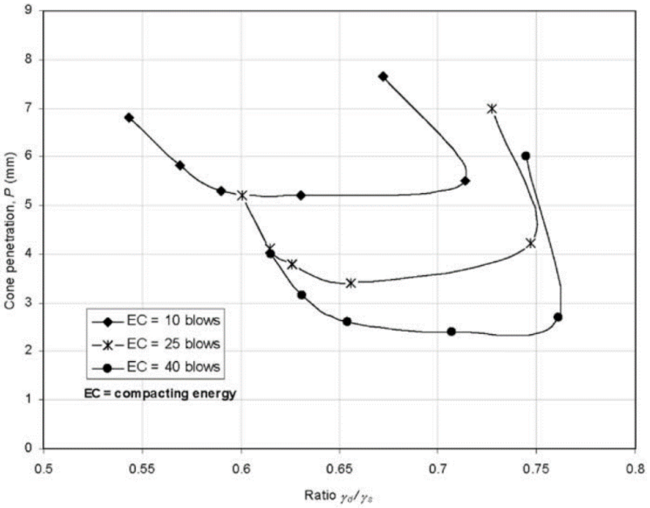

Figure 2.5 Cone penetration versus ratio γ_d/γ_s for Soil A (Ayadat & Hanna, 2007)

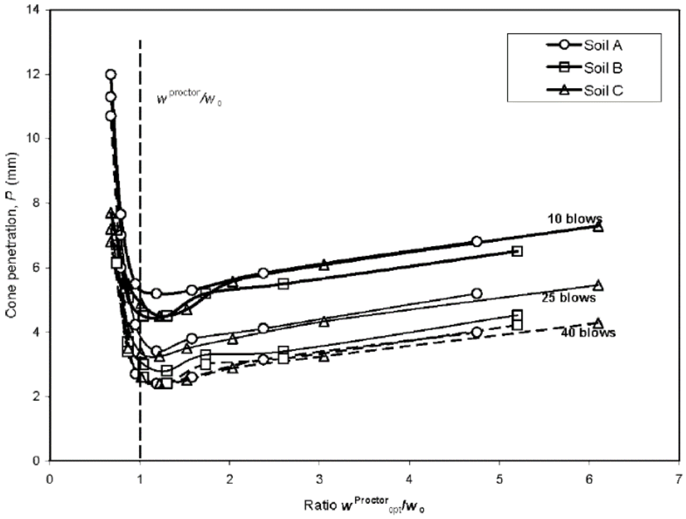

Figure 2.6 Cone penetration against ratio of optimum proctor moisture content and initial moisture content (Ayadat & Hanna, 2007)

of the tests and always higher than 0.95. This indicates that the moisture content at optimum proctor compaction could potentially be determined from cone penetration tests, but Ayadat and Hanna (2007) cautioned that “more data [is] needed before generalizing this conclusion”.

Ayadat and Hanna (2007) also showed (Figure 2.6) that the soils have a unique cone penetration limit identifying the transition point between collapsible and non-collapsible behavior.

Ayadat and Hanna (2007) then graphed cone penetration limit versus the ratio of dry unit weight to saturated unit weight and observed a linear relationship. The slope of the relationship was nearly the same in all the samples observed. The intercept parameter versus the uniformity coefficient was plotted and a linear relationship was also observed. Ayadat and Hanna (2007) presented Equation 2-1 that allows the cone penetration limit to be calculated. Ayadat and Hanna (2007) proceeded to plot the collapse potential versus the cone penetration values and observed a logarithmic relationship. Considering the boundary conditions, Ayadat and Hanna (2007) presented Equation 2-2 to predict the collapse potential for a given soil.

$$P_{lim} = -37\frac{\gamma_d}{\gamma_s} - 0.01C_u + 28 \qquad \textbf{2-1}$$

where:
P_{lim}= Cone penetration limit
$\frac{\gamma_d}{\gamma_s}$ = ratio of dry unit weight to saturated unit weight
C_u= uniformity coefficient

$$CP = a_2 * \ln\left(\frac{P}{P_{lim}}\right) + 1 \qquad \textbf{2-2}$$

where:
CP= Collapse potential
P_{lim}= Cone penetration limit
C_u= uniformity coefficient
a_2= fitting parameter given as

$$a_2 = \begin{bmatrix} \lambda = 0.04C_u + 6 & (P_{lim} \le 2.5) \\ \lambda + 7 & (2.5 < P_{lim} < 4.5) \\ -\frac{\lambda}{2} + 33 & (P_{lim} \ge 4.5) \end{bmatrix}$$

Ayadat and Hanna (2007) compared the collapse potential from the first series of tests with the values predicted by Equation 2-2. The measured results matched closely with those predicted (Figure 2.7). Ayadat and Hanna (2007) then compared the measured collapse potential from the second series of tests with the values predicted by Equation 2-2. The measured and predicted values were within 18% of each other on average (Figure 2.8.)

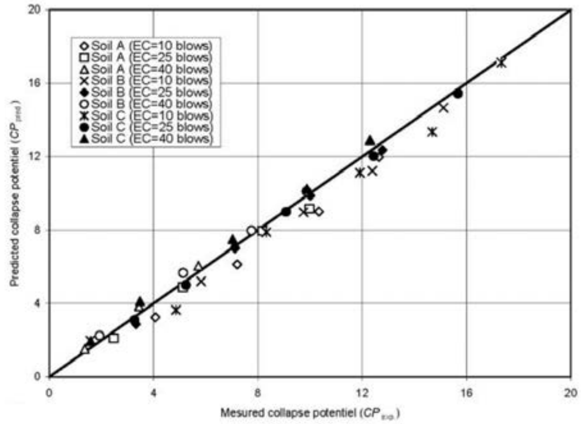

Figure 2.7 Comparison of experimental and theoretical results of collapse potential (CP) – Series I (Ayadat & Hanna, 2007)

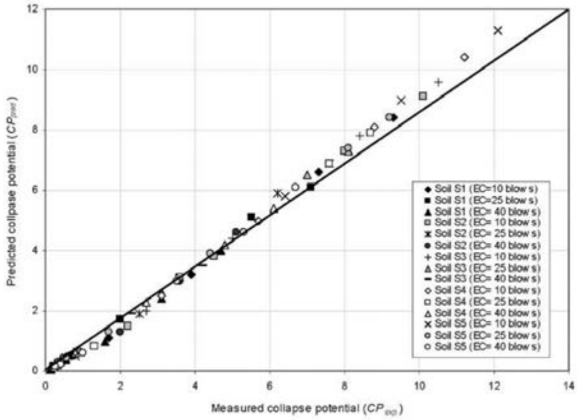

Figure 2.8 Comparison of experimental and theoretical results of collapse potential (CP) – Series II (Ayadat & Hanna, 2007)

Ayadat and Hanna (2007) were able to conclude that the fall cone test could be used to identify soil collapse, that optimum proctor moisture content could be related to optimum cone moisture content, that there is a limit on cone penetration that identifies the transition point between collapsing and non-collapsing behavior, that the collapse potential can be modeled based on soil parameters, and that the model is accurate for a specific range of soils with the parameters shown in Table 2-1. More research is needed to expand the model. However, the study illustrates that the fall cone test may provide an easier and quicker method to identify soil collapse and collapse potential.

Table 2-1 Allowable soil properties for model (Ayadat & Hanna, 2007)

Parameter	Minimum	Maximum
Uniformity Coefficient (Cu)	34	300
Ratio of dry unit weight to saturated unit weight $(\frac{\gamma_d}{\gamma_s})$	51.57	76.09
Optimum proctor moisture content (w_{opt})	8.5	12.0
Penetration range (mm)	1.8	12

2.1.4 Case Study: Modified Time of Setting Test for Fly Ash Paste and Fly Ash–Soil Mixtures - Xi Kang, Gi-Chun Kang, and Louis Ge (2013)

Fly ash is a residual produced from combustion of coal and is grouped into different classes. Class C fly ash has a chemical composition that leads to cementation when combined with water. The strength of the cementation is dependent on moisture content and time of setting. Kang et al. (2013) investigated the effectiveness of the method recommended in ASTM D-5239-04 for determining the time of setting for Class C fly ash and fly ash-soil mixtures, the effect of moisture content on time of setting for fly ash and fly ash-soil mixtures, and the effect that different fly ash to soil ratios in fly ash-soil mixtures has on strength and moisture content.

Kang et al. (2013) focused on five Class C fly ashes taken from five different power plants in Missouri: A) Rush Island, B) LaCygne, C) Nearman, D) Meramec, and E) Labadie, and a sample of Atchison, Missouri soil. It was shown that the ASTM D-5239-04 method was ineffective for determining the time of setting for several reasons. First, the required moisture content specified by ASTM created a fly ash paste that was too soft. The softness of the paste does not allow for the sample to be properly prepared in the Vicat container. Second, because of the fly ash paste softness, the Vicat needle (Figure 2.9) passed through the material with minimal resistance. Third, the setting time is calculated using linear interpolation of the Vicat penetration data, while the data trend is non-linear. Kang et al. (2013) proposed and tested a method centered on using the British fall cone to mitigate these issues. The procedure used by Kang et al. (2013) is detailed below as:

> “The fly ash/fly ash-soil mixture paste in the LL [liquid limit] state was prepared and placed in the Vicat cup with its surface leveled horizontally. The cup was then carefully transferred underneath the British fall cone and the cone tip was lowered until it touched the paste surface. The cone was immediately released and freely fell from the frame. The penetration value…was noted after approximately 10 s (until the cone stabilized in the paste). … The time intervals used were initial, 30 s, 1, 2, 4, 8, 15, and 30 min, and 1, 2, 4, and 8 h.”

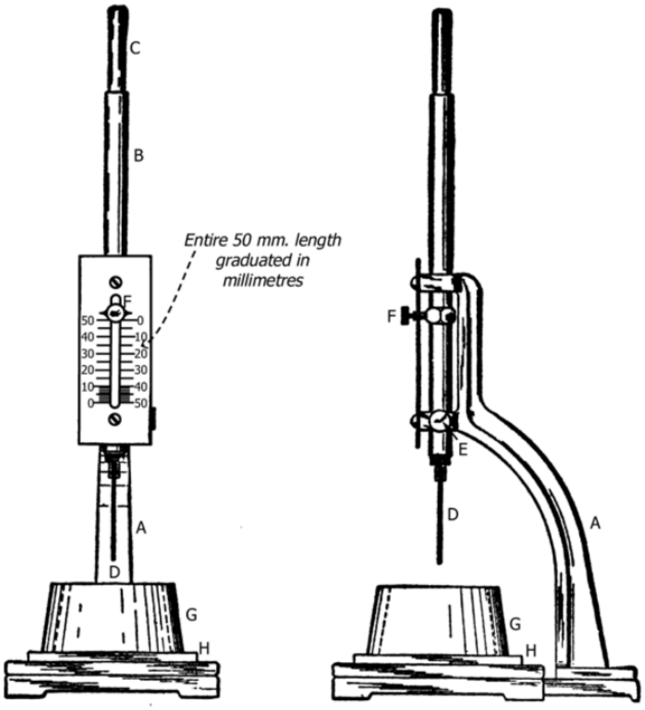

Figure 2.9 Vicat Apparatus (ASTM International, 2013)

Kang et al. (2013) first examined pure fly ash pastes and found that from the initial reading to the 3 min mark, four of the five fly ash paste samples exhibited a relatively flat section in the penetration vs. time trends before the trend decreased. Kang et al (2013) identified this point as the initial setting point, where the fly ash pastes began to solidify. Kang et al. (2013) identified a second point where the penetration vs. time trend became horizontal again, indicating a final setting point, where the fly ash pastes began to act as a solid. Figure 2.10 shows the penetration reading vs. time for the five different fly ash pastes. Kang et al. (2013) also repeated the tests at varying moisture content levels. Figure 2.11 shows the setting time results for fly ash A (Rush Island) at varying moisture contents.

Kang et al. (2013) also examined three different cases for fly ash-soil mixtures and found that adding fly ash to soil increased the time of setting of the fly ash, but removed the well-

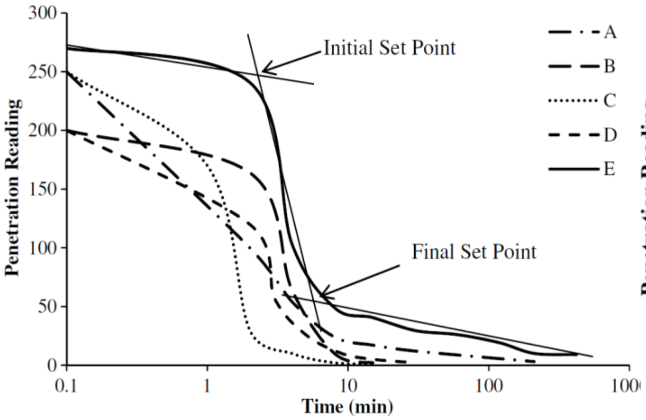

Figure 2.10 Time setting curves of different fly ashes. (Kang, et al., 2013)

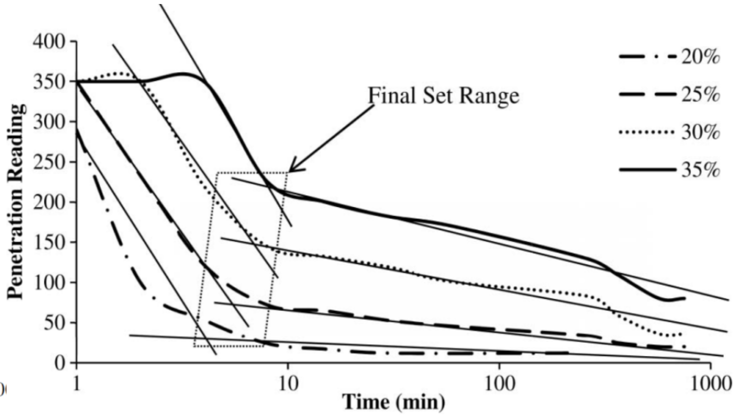

Figure 2.11 Time setting curve of Fly Ash A at different water contents (Kang, et al., 2013)

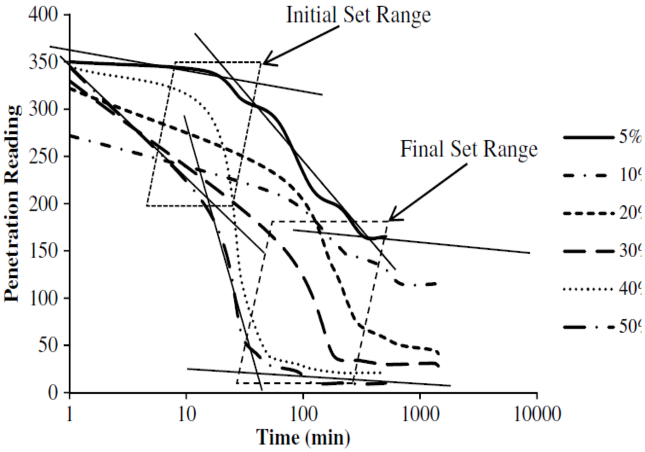

Figure 2.12 Time of setting of Fly Ash-Soil Mixture C. (Kang, et al., 2013)

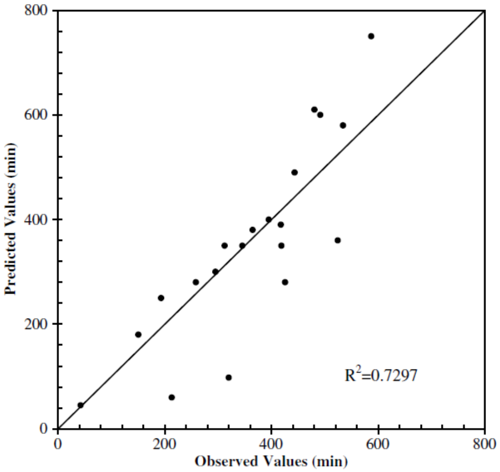

Figure 2.13 Observed versus predicted times of setting of Missouri fly ash. (Kang, et al., 2013)

defined initial and final setting points in Figure 2.10 In addition, Kang et al. (2013) found that when the fly ash and soils were mixed at the liquid limit (LL), the mixtures exhibited different behavior in the time of setting curve for mixtures containing different fly ash amounts. Figure 2.12 shows the transitional behavior of fly ash-soil mixture C.

Based on the results of the tests, Kang et al. (2013) showed that the British Fall Cone could be effectively used to determine the time of setting of Class C fly ash. The tests also showed that the LL is a critical point in the fly ash physical behavior. Kang et al. (2013)

suggested a regression based on the observed data as shown in Equation 2-3 (Kang, et al., 2013) . The actual setting time was plotted against the regression predicted setting time and is shown in Figure 2.13.

$$T(\text{min}) = \text{U} + \text{A}\omega \ - 5.6(\text{ash}/\text{soil}) - 1343.32(\text{CaO}/\text{SiO}_2) \qquad \textbf{2-3}$$

where:
T= Final time of setting
ω = water content of the mixture (%)
ash/soil = ash to soil weight ratio (%)
CaO/SiO_2 = CaO to SiO_2 weight ratio
U=regression parameter of 1014.8
A = regression parameter of 15.6

In conclusion, the British fall cone method provided a better method than the Vicat needle method when determining the time of setting for fly ash pastes and mixtures. The fall cone method indicated that the fly ash pastes and fly ash-soil mixtures had a point where setting began and where a majority of setting had been completed. In addition, a regression was performed on the data that provided a reasonable prediction of the final setting time. However, Kang et al. (2013) cautioned “it should be used cautiously, because in field conditions are much more variable than those in the laboratory.”

2.2 Direct Shear Testing

2.2.1 Primary Use

In the early 19th century, Arthur Langtry Bell investigated Rankine's theory of earth pressure and found that clays did not behave as Rankine's shear resistance assumption predicted. Bell proposed and used a direct shear device that investigated the divergence from Rankine's shear resistance assumption. Clays were placed in a cylinder that had a section that moved horizontally and a force was applied to it to shear the clay on two surfaces. The apparatus and results were used to determine the shear strength of clays including the cohesion term (Skempton, 1958). Modern direct shear tests operate in a similar manner, however most focus on shearing the soil on a single plane with a constant deformation rate instead of a stepped deformation by increasing the horizontal force at displacement steps.

Modern direct shear tests have been used to identify material responses beyond the shear strength of soils. Direct shear tests have been used, for example, to identify the increase in soil strength from the presence of live root structures (Jotisankasa & Taworn, 2016), to measure the flowability of food powders (Stasiak & Molenda, 2004), to identify the effect of drying and wetting on shear strength (Gallage & Uchimura, 2016), to investigate elastic waves in shear bands (Zhang, Li, Hou, Jiang, & Liu, 2012), to identify the mechanisms of the fluctuations in shear strength (Li & Aydin, 2010), and to quantify the scale dependency of shear strength (Fu & Dai, 2015). The investigations of Zhang et al. (2012), Fu & Dai (2015), and Li & Aydin (2010) are discussed here to show there is a precedent to use direct shear tests to investigate behaviors other than a soil's shear strength.

2.2.2 Case Study: Elastic waves in the presence of a granular shear band formed by direct shear – Qi Zhang, Yinchang Li, Meiying Hou, Yimin Jiang, and Mario Liu (2012)

Soils exhibit two different responses during direct shear testing. The first response a soil exhibits when being sheared is an elastic response. When subjected to direct shear testing with a specified normal load, the stress in the shear area increases at a linear rate until the soil yields. Soils with a low void ratio (dense) generally experience a peak in this stress before it decreases to the same value experienced by the same soil with a high void ratio (loose), which is referred to the residual or critical state. When the soil reaches this state, an increase in strain does not cause an increase in stress. At the critical state, the soil exhibits a plastic response. Zhang et al. (2012) proposed the question of how do these two behaviors, elastic and plastic, interact with each other and to what extent shear bands affect elastic wave propagation.

Zhang et al. (2012) investigated the material response in a conceptual manner before testing. At the microscopic level, particle contacts are critical for wave propagation. Zhang et al. (2012) state that if shearing occurs at a slow rate, where the time for one oscillation to occur produces a horizontal displacement less than one particle diameter, or if the ratio of the sound wave angular frequency to the shear rate is much smaller than one, then the sound wave propagation should be unaffected. At the macroscopic level, once a soil reaches critical state, the soil behaves plastically. Zhang et al (2012) conclude “propagation of waves depends critically on the system being elastic … so we must conclude that elastic waves do not exist.”

Zhang et al. (2012) used a direct shear apparatus that was 70 x 70 x 49 mm. Glass beads with a diameter ranging from 1.7-2.0 mm were utilized. The samples were prepared to a volume fraction (percentage of the shear box volume occupied by glass beads) of 0.648 ± 0.002 and

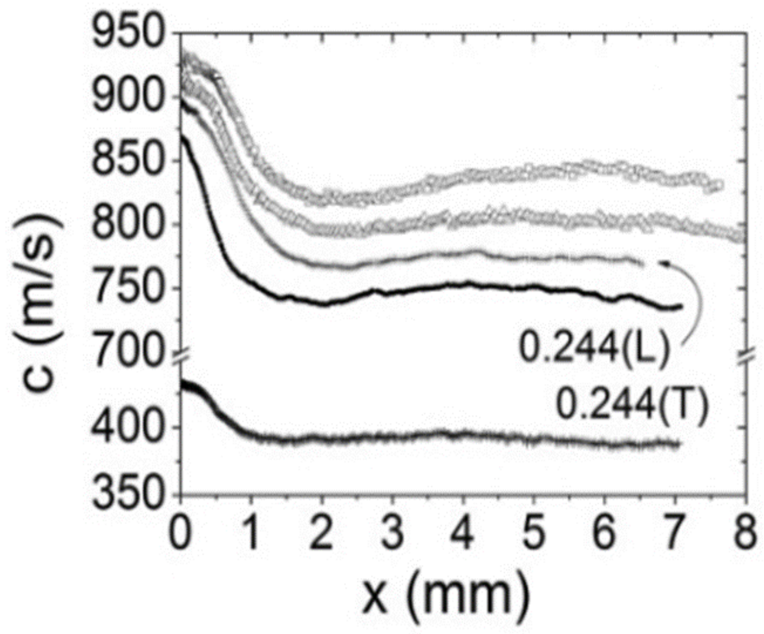

Figure 2.14 Evolution of sound velocity for the shear box experiment (Zhang, et al., 2012)

were subjected to several normal stresses. The normal stresses ranged from 183-366 kPa. The glass beads were sheared under a constant displacement velocity of 13.3 μm/s and the shear force was recorded. A receiver was placed in the direct shear box prior to the sample being formed. A transducer was placed on top of the sample before the normal load was applied. The transducer produced a 50 kHz sinusoidal wave every 0.02 seconds. Zhang et al. (2012) measured the sound velocities for four different normal loads while shearing. The results are shown in Figure 2.14.

Measured wave velocities were then compared with results predicted by elastic theory produced using granular solid hydrodynamics. A comparison of results is shown in Figure 2.15. Zhang et al. (2012) also attempted to determine the effect that shear bands had on the elastic results. Within the shear bands, the glass beads move around and interact with each other. Zhang et al. (2012) refers to this behavior as “granular temperature,” which “softens the contacts,

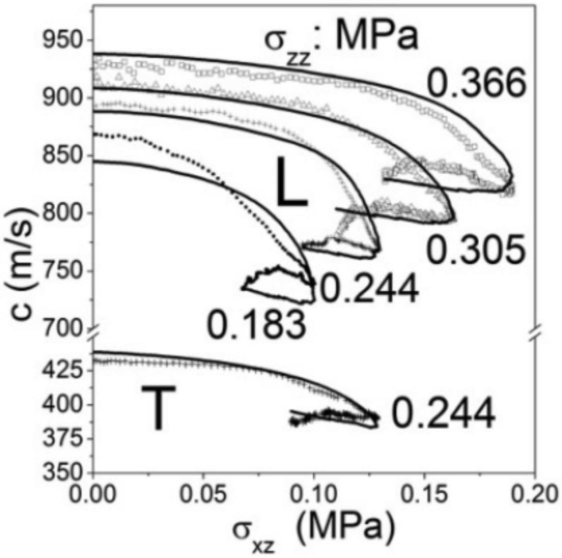

Figure 2.15 Variation of wave velocities with shear stress (Zhang, et al., 2012)

relaxes the stress, and restricts wave propagation" (Zhang, et al., 2012). Using granular solid hydrodynamics, an equation for wave propagation and decay length caused by the granular temperature was determined. However, Zhang et al. (2012) did not observe an effect in wave velocity and were unable to isolate the decay length from the measured results.

Zhang et al. (2012) found that elastic wave propagation was affected by the applied stress, the material density, or the granular temperature. The methods used were effective at identifying the effects of stress state and material density on wave propagation, but failed to identify the effects of granular temperature. Zhang et al. (2012) also found that prior to the glass beads losing contact from the shear force, granular temperature caused the elastic waves to stop. The granular solid hydrodynamics indicates that granular temperature affects the wave velocity and provides a dampening effect of elastic wave propagation. Zhang et al. (2012) chose to neglect the granular temperature effects for a narrow shear band, and found that direct shear testing was an accurate method for determining granular solid hydrodynamics parameters.

2.2.3 Case Study: Behavior of rounded granular materials in direct shear: mechanisms and quantification of fluctuations – Y.R. Li and A. Aydin (2010)

Li and Aydin (2010) point out that for as long as shear behavior of soils has been investigated, a model has not been created that can predict the soil response to strain. Li and Aydin (2010) present several studies where fluctuations in the vertical displacement and shear stresses were observed as the shear displacement increased. Li and Aydin (2010) specifically mention that "Shimizu (1997) indicated that the amplitude of fluctuation is so large, especially for dense sand, that it may cause the shear stress tom momentarily drop down to zero." Li and Ayden focused on determining the causes of the vertical and shear stress fluctuation, measuring the fluctuations, and determining any relationships between the fluctuations and material properties.

Li and Aydin (2010) utilized two materials in their investigation, glass sand (used in the production of glass) with a mean particle size of 0.32 mm and glass beads with a mean particle size of 3.2 mm. Three different configurations of samples were prepared, 100% glass beads, 100% glass sand, and a 50-50 mixture. The samples were subjected to direct shear tests using a shear box meeting ASTM D-3080 requirements. The samples were prepared in the shear box prior to being saturated and consolidated. Three different shear rates and four vertical stresses were used in the shear testing. The samples exhibited shear stress versus horizontal displacement trends typical of those for dense sands. Li and Aydin (2010) divided the shear stress response into four zones as shown in Figure 2.16. First, Li and Aydin (2010) identified that once the samples reach the point of peak stress, fluctuation in shear stress and vertical displacement began to appear. In zone three, the fluctuations increase in amplitude until the sample reaches the

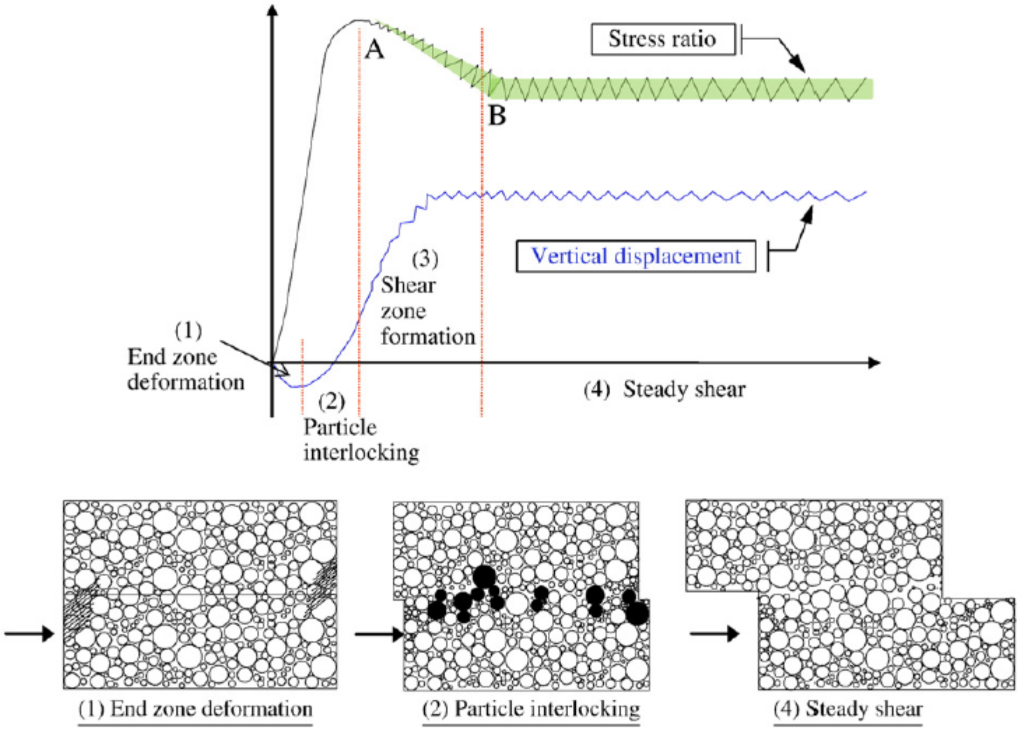

Figure 2.16 A four-stage shearing model for granular materials (Li & Aydin, 2010)

residual stress point. The behavior in the fluctuations was attributed to formation of the shear zone. Upon reaching the residual stress (zone 4) the fluctuations appeared to reach a steady state where the amplitude was no longer changing.

Second, Li and Aydin (2010) focused on the behavior or the stress ratio and vertical displacement fluctuations. Using the vertical displacement for a particle in a wave and Taylor (1948)'s expression of stress ratio, Li and Aydin (2010) related the amplitude and wavelength of the fluctuations to the dilation of the materials. The Discrete Fourier Transformation (DFT) was then used on the expression and three frequency ranges were identified that had significant peaks in amplitude. Li and Aydin (2010) explored how the frequency ranges observed from the stress ratio fluctuations DFT were influenced by different material properties, focusing on the first frequency range specifically and then all three frequency ranges together.

Li and Aydin (2010) found that the wavelength and amplitude corresponding to the first frequency range from the DFT analysis is an indication of the most predominant features of the shear surface. The wavelength and amplitude were found to be affected by the particle size distribution, the normal stress, and the shear rate. The wavelength is represented as the distance between the largest particles, and as the uniformity coefficient increases, the distance between the largest particles increases. The increase in the uniformity coefficient also increases the amplitude of the wave, by increasing the vertical distance a particle moves to overcome interlocking. Li and Aydin (2010) found that as the normal stress increases, the wavelength and amplitude of the fluctuations also increase. This behavior was attributed to a higher normal force densifying the sample, causing larger particles to interlock. Li and Aydin (2010) observed a decreasing trend for both wavelength and amplitude with regard to shear rate. This behavior was attributed to slow shear rates that allowed particles to densify and provide higher contact forces, whereas a higher shear rate does not readily allow for particles to densify. The wavelength and amplitude trends with regard to particle size distribution, normal stress, and shear rate are shown in Figure 2.17 through Figure 2.19. Li and Ayden found with regard to all three frequency bands, an increase in normal stress increases the wavelength, while shear rate appeared to have no effect. The increase is caused by smaller particles contributing to the roughness of the shear surface. Li and Ayden further concluded that the contribution from smaller particles to the surface roughness was the primary factor for this behavior.

Using direct shear testing, Li and Aydin (2010) showed that the fluctuations observed in stress ratio and the vertical displacements depended on particle distribution, applied normal stress, and shear rate. Li and Aydin (2010) concluded that the friction coefficient could be determined from the fluctuations as well as valuable information regarding soil properties.

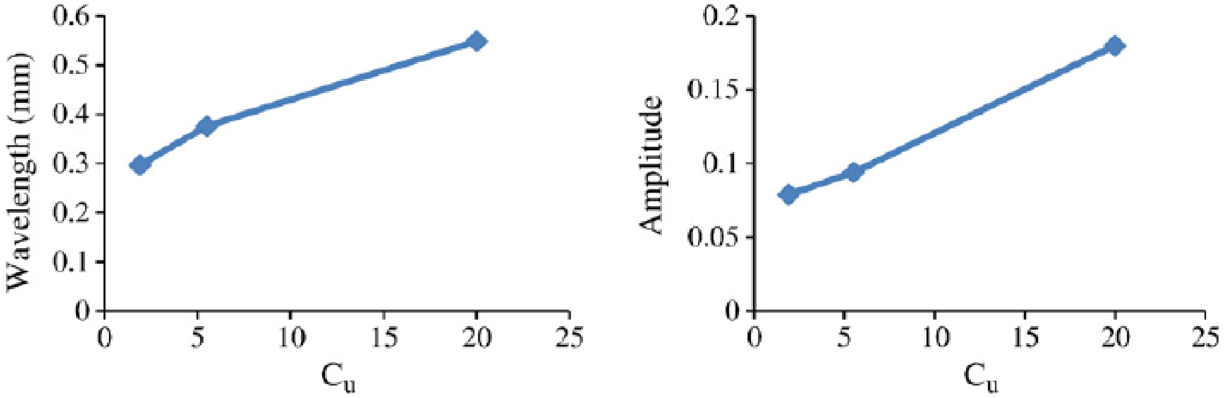

Figure 2.17 The characteristics of fluctuations at residual state as a function of coefficient of uniformity (C_u) (Li & Aydin, 2010)

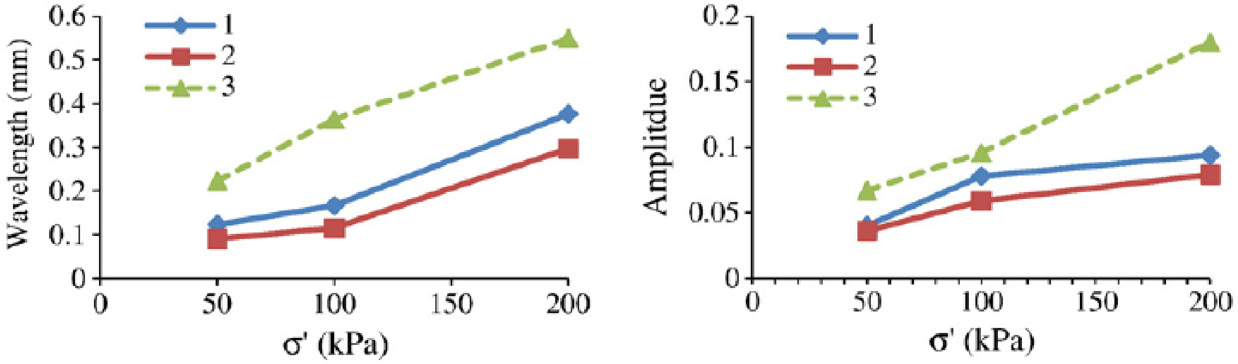

Figure 2.18 The characteristics of fluctuations at residual state as a function of effective normal stress for specimens tested at shearing rate of 0.06 mm/min (Li & Aydin, 2010)

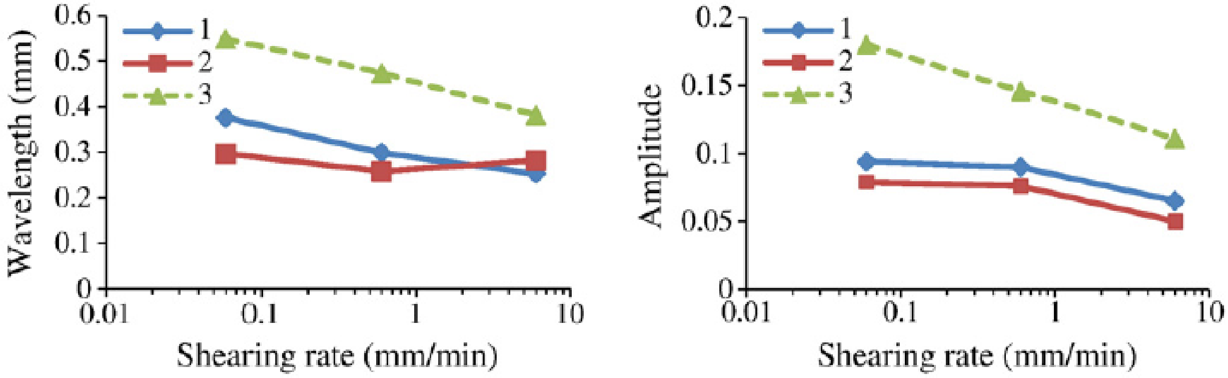

Figure 2.19 The characteristics of fluctuations at residual state as a function of shearing rates for specimens tested at 200 kPa normal stress (Li & Aydin, 2010)

2.2.4 Case Study: Scale dependence of shear strength for a coarse granular soil using superimposition-nest type of direct shear apparatus – Wen-Xi Fu and Feng Dai (2015)

Fu and Dai (2015) proposed a new type of direct shear apparatus and used it to investigate the effects of sample height, sample diameter, and shear box gap thickness on the shear strength of a material and the subsequent determination of the friction angle. The direct shear device operated much like a traditional direct shear apparatus, where the top portion is attached to a device to measure the shear force and where the normal force is applied to the sample, and the bottom portion is displaced to create the shear force. The new device consisted of a steel plate that was milled in such a way where a series of rings could be placed inside to progressively reduce the diameter of sample area inside the plate. The diameter-reducing rings allowed the samples to have diameters ranging from 6.2 cm up to 20 cm. Several of these plates were stacked to adjust the height of the sample. The plates were used for both the top portion and the bottom portion of the shear box. The plates allowed for the sample to be varied in height from 50 mm, with one plate for top and bottom, to 200 mm, four plates for the top and bottom of the shear box. Figure 2.20 shows the various configurations of the plates with the diameter-reducing rings.

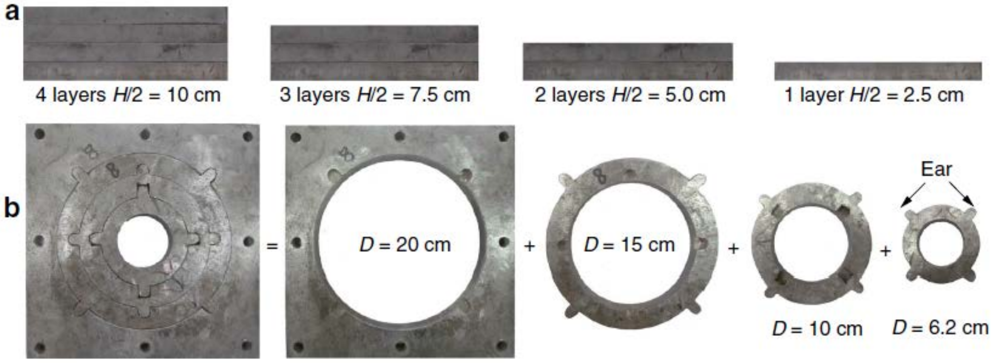

Figure 2.20 Front view (a) for the vertical superimposition of the DSB [direct shear box] half and top view (b) for the inner nest of steel plates. (Fu & Dai, 2015)

The modular shear box was placed between two large plates separated by vertical rods that provided the base plate and top plate. Rollers were located on the bottom plate to allow the bottom portion of the shear box to displace. The top plate provided a fixed surface allowing a jack to apply vertical stress to the sample. The distance between the top and bottom plate was variable, thus allowing different specimen heights and different gap thicknesses between the shear box halves to be examined.

Fu and Dai (2015) focused on testing a glacial-fluvial soil at the density and moisture content found in the field where the soil samples were obtained. For each test series, three vertical stresses were examined and the samples were consolidated prior to shearing. In addition, each soil sample had a strip of foam placed around the perimeter of the sample to reduce the amount of soil extruded through the gap between the shear box halves. Fu and Dai (2015) first examined the repeatability and reliability of the apparatus using five tests at each of the three vertical stresses without varying the sample diameter, sample height, or gap thickness. These tests produced results for each respective vertical stress that were in good agreement.

Fu and Dai (2015) proceeded to examine the effects of varying the gap thickness on the shear behavior of the samples. The height of the gap was varied from 0.9 mm to 15.1 mm. Fu and Dai (2015) found that small gap sizes restricted the movement and rotation of the soil particles, leading to particles crushing and fracturing. This behavior caused the shear forces at failure to be higher than the shear strength of the soil. When the gap was too large, material flowed out of the gap. The flow of the material out of gap caused the shear forces at failure to be lower than the shear strength of the soil. The results are showing in Figure 2.21. Fu and Dai (2015) subsequently recommended the gap size to be between 0.315 and 0.575 times the maximum particle size.

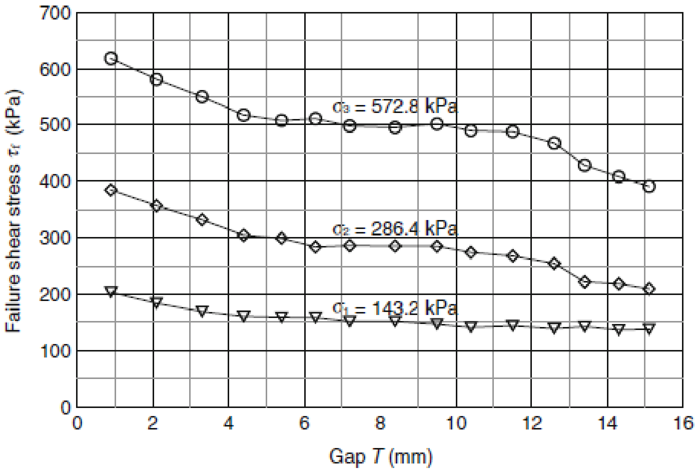

Figure 2.21 Variation of the failure shear stress τ_f with gap thickness. (Fu & Dai, 2015)

Fu and Dai (2015) used the results from the gap thickness to further investigate the effects of sample diameter for a constant gap thickness and sample height. The gap thickness was chosen between the range previously recommended. The samples were prepared using diameters of 61.8, 100, 150, and 200 mm. Fu and Dai (2015) found that similar to small gap sizes, small diameters restricted the movements of the particles, and increased the crushing and fracturing of the particles. This caused the measured shear strength of the soil to be higher than the actual shear strength of the soil. Fu and Dai (2015) found that to remove the effects from sample diameter, the ratio of the sample diameter to the maximum particle diameter should be larger than 7.5. When the ratio is larger than 7.5 the shear strength decreased to a constant value. These results are shown in Figure 2.22 (a).

Finally, Fu and Dai (2015) investigated the effects of sample height on measured shear strength. Using the results from the previous investigations, sample diameter and gap thickness were selected to remove those effects from the tests. The samples were prepared using heights of 50, 100, 150, and 200 mm. Fu and Dai (2015) found that similar to the sample diameter, small sample heights restricted the movements of the particles, and increased the crushing and

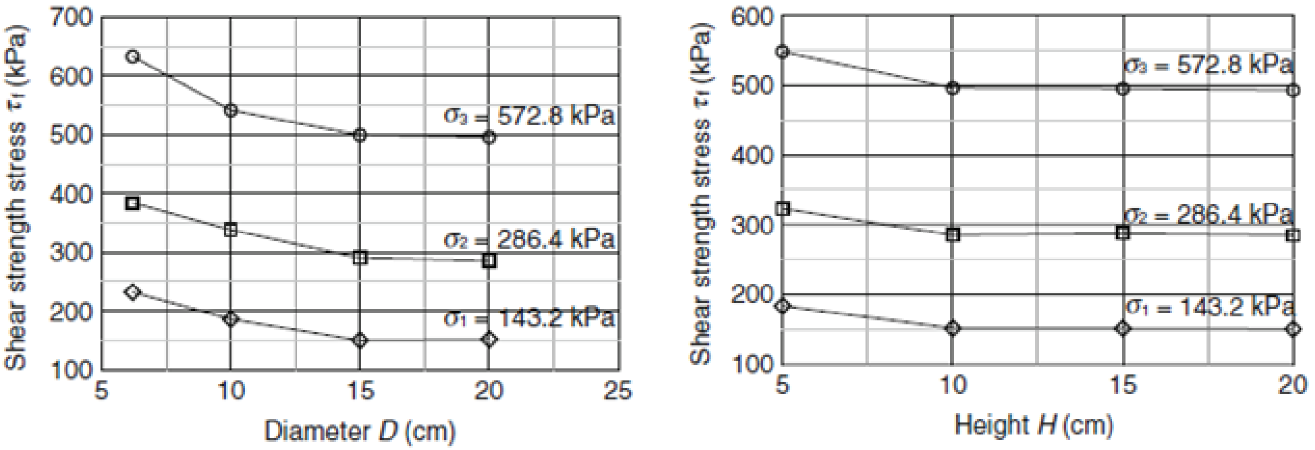

(a) (b)

Figure 2.22 Variation of the failure shear stress τ_f with sample diameter (a) and sample height (b) (Fu & Dai, 2015)

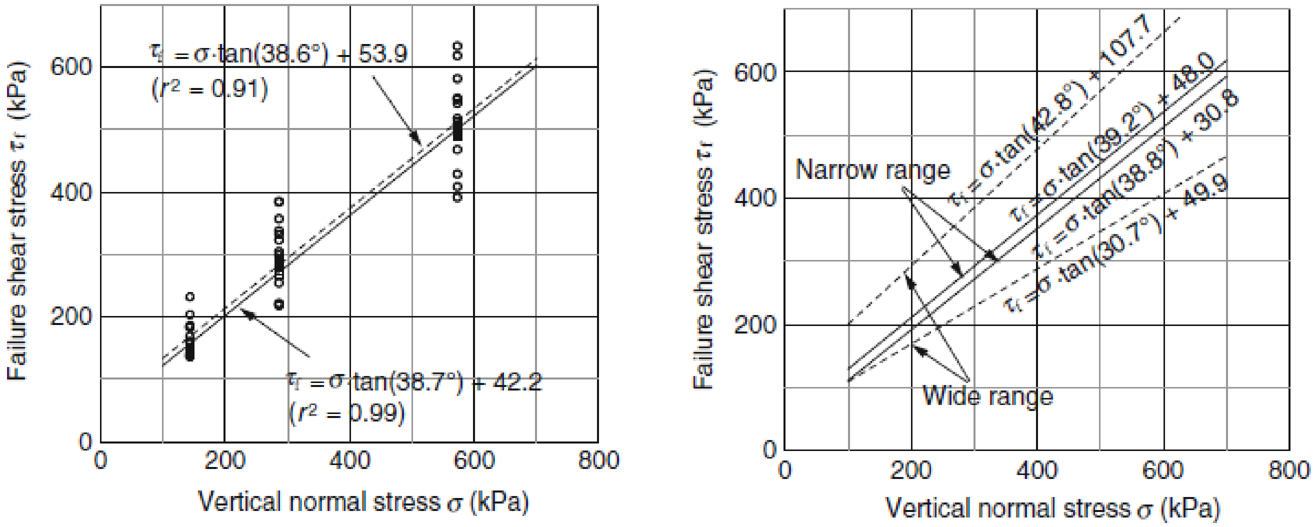

(a) (b)

Figure 2.23 Scatter point distribution (a) and MC [Mohr-Coulomb] shear strength envelope (b) (Fu & Dai, 2015)

fracturing of the particles. This caused the measured shear strength of the soil to be higher than the actual shear strength of the soil. Fu and Dai (2015) found that to remove the effects from sample height, the ratio of the sample height to the maximum particle diameter should be larger than 5. When the ratio is larger than 5, the shear strength decreased to a constant value. These results are shown in Figure 2.22 (b).

Fu and Dai (2015) used the results from each of the investigations to produce the Mohr-Coulomb failure envelopes (Figure 2.23). Considering only the tests where the effects of sample height, sample diameter, and gap thickness effects were removed, the friction angles were measured over a much narrower range of values, as indicated in Figure 2.23(b). Fu and Dai (2015) concluded that removing the effects of sample height, sample diameter, and gap thickness is critical to produce a more accurate shear strength envelope for a soil.

2.3 Particle Image Velocimetry

2.3.1 Development

Particle image velocimetry (PIV) is a technique originally used in fluid mechanics to characterize the behavior of fluid flows. Artificial markers are introduced into the fluid and as the markers pass by a camera they are illuminated with a laser. The camera then takes a rapid series of photos over a known time interval. The images are analyzed with a series of algorithms that determine the displacement vector, and subsequently velocity vectors of the markers, over the discrete photo intervals (White, et al., 2003 and Riethmuller, David, & Lecordier, 2013)

White et al. (2003) proposed and evaluated a new method of PIV analysis termed GeoPIV that uses the natural variation in grain size and color of soils to track deformations in geotechnical testing applications. GeoPIV has proven to be a valuable tool in the geotechnical community. GeoPIV has been used to identify displacements in slopes subjected to weathering (Voulgari, 2015), to identify the deformation patterns and differential settlement caused by staged construction of a levee (Jin, et al., 2014), to identify the failure mechanisms in helical piles (Beales Ferguson & Standing, 2012), to identify the failure mechanisms in geosynthetic-reinforced walls under earthquakes (Jackson, et al., 2012), and to relate the particle size behavior to the macro size behaviors in landslides (Bryant, et al., 2014), among other applications. The investigations of Beales Ferguson & Standing (2012), Jackson et al. (2012), and Bryant et al. (2014) are discussed here to illustrate the capabilities of GeoPIV in a wide range of applications.

2.3.2 Case Study: A 2-D model experimental study of helical piles in sand using geopiv software – T.A. Beales Ferguson and J. Standing (2012)

Beales Ferguson and Standing (2012) state that helical pile foundations were first introduced in 1830, but since that time national codes and standards have not presented a clear design requirement. Because of this, different companies have developed their own requirements and methods for helical pile design. The designs were based around shaft failure and bearing capacity failures of the piles. Beales Ferguson and Standing (2012) present a small-scale model to investigate the development of the failure mechanisms and what changes in failure mechanisms occur as displacement increases.

Prior research recommended selecting helix sizes based on the average soil particle size, and subsequently recommended a soil width based on helix size to remove boundary effects. Based on this recommendation, Beales Ferguson and Standing (2012) constructed a model that was 430 mm x 464 mm x 25 mm and had a transparent cover of 20 mm perspex over the 430 mm x 464 mm area. The transparent cover allowed images of the soil surface to be captured (photographed) under deformation. The pile used in the investigation was created in segments allowing multiple helix sizes, helix spacing, and shaft diameters to be tested. The assembled piles were pulled through the material at steps of 0.5 mm. After each 0.5 mm displacement, a photo was taken. The images were analyzed using GeoPIV to track the displacements of the soil particles and pile.

As the GeoPIV analysis began, Beales Ferguson and Standing (2012) encountered several issues. The first issue revolved around the number of files needed to execute the analysis, and the second was due to the imprecision when measuring the displacement of the pile. Beales

Ferguson and Standing (2012) wrote two separate MATLAB scripts to address these issues. The first script compiled the steps necessary to create files for the analysis and reduced user input. As a result of the methods used to measure the amount of displacement applied to the pile, the actual pile displacements did not correspond to the same image in all of the tests. The misalignment of displacement and images would not allow for direct comparison of the different tests. The second MATLAB script was written to interpolate the GeoPIV results and fill in the gaps in the results. The interpolation allowed for the results to be compared at the same intervals.

Beales Ferguson and Standing (2012) used the GeoPIV quiver plot function to compare the displacements of each test and contour plots to compare the strains. An example of the results is shown in Figure 2.24 and Figure 2.25. Focusing on the how the values compare in each test, Beales Ferguson and Standing (2012) found that bearing failures were the first to develop, followed by shaft failure. The results shown in Figure 2.24 and Figure 2.25 were used as a base line to compare tests with different helix spacings, helix orientations, and shaft diameters. Additional tests were conducted using four different helix spacings, three different helix rotations, and four shaft diameters. Beales Ferguson and Standing (2012) found that as the helix spacing increased, shaft failure occurred at higher displacements, as shown in Figure 2.26

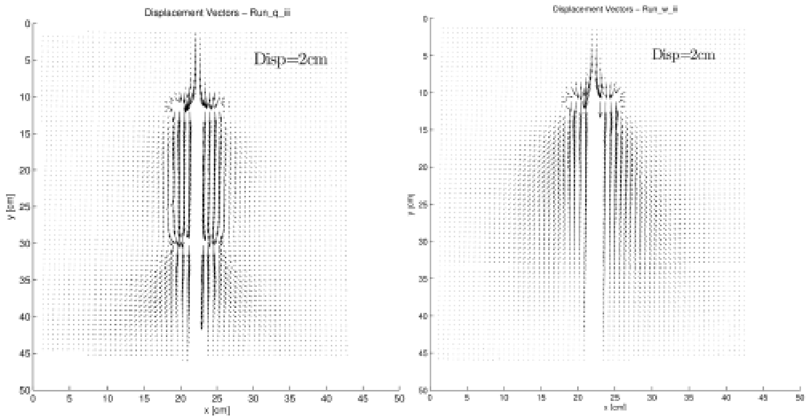

Figure 2.24 Vector plots of displacement: Left, shaft failure; right, bearing failure (Beales Ferguson & Standing, 2012)

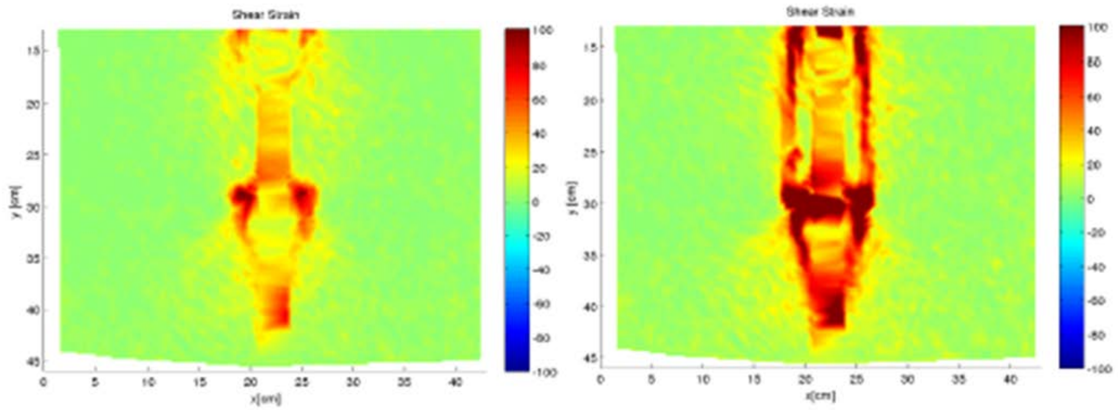

Figure 2.25 Shear strains [%]: Left, bearing mechanism at low displacement; right, shaft failure at high displacement (Beales Ferguson & Standing, 2012)

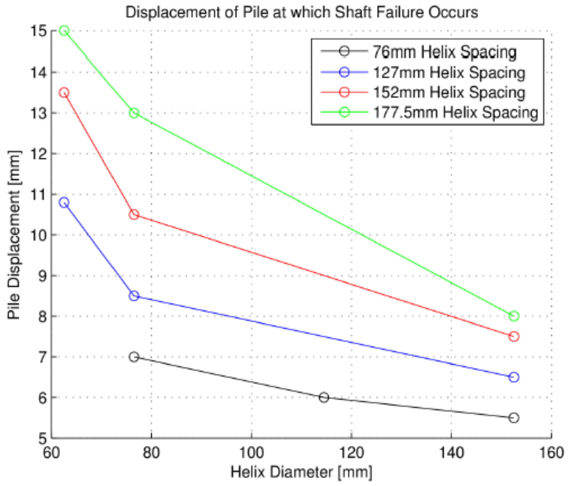

Figure 2.26 Graph showing the point of transition between failure modes (Beales Ferguson & Standing, 2012)

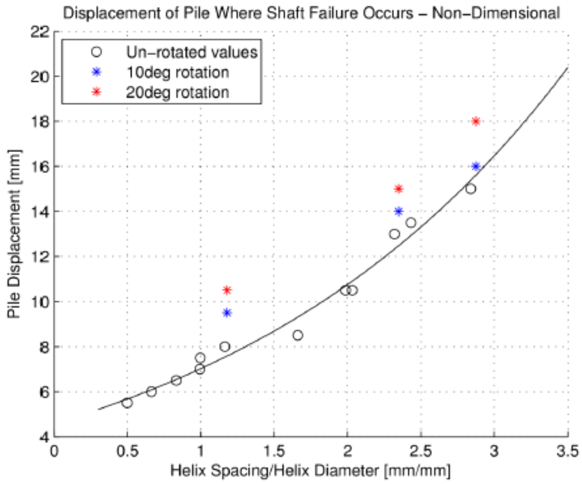

Figure 2.27 Non-Dimensional graph showing the point of transition between failure modes. (Beales Ferguson & Standing, 2012)

Beales Ferguson and Standing (2012) further concluded that for each helix spacing there is a lower bound on helix diameter (below which shaft failure will not occur) and a minimum amount of displacement to cause shaft failure. The pile displacement results were plotted versus the ratio of helix spacing to helix diameter (Figure 2.27). Beales Ferguson and Standing (2012) concluded that below a helix spacing to helix diameter of 0.5, shear failure would occur below the 4 – 5 mm predicted value. At a helix spacing to helix diameter above 5.0, shaft failure is unlikely to occur.

Using GeoPIV, Beales Ferguson and Standing (2012) produced displacement and shear plots of sand and helical piles under loading. The plots allowed the failure mechanisms at varying pile displacements to be identified. Once the failure mechanisms were identified, several relationships between the ratio of helix spacing to helix diameter were observed and quantified.

2.3.3 Case study: Seismic testing of model-scale geosynthetic-reinforced soil walls – Perry Jackson, Elisabeth T. Bowman, and Misko Cubrinovski (2012)

Prior to 1998, the design of geosynthetic reinforced soil (GRS) walls in New Zealand was not governed by a specific agency or design guideline. Because of this, several international standards and geosynthetic reinforcement manufacturer's design methods were used. Jackson et al. (2012) reference Murashev (2003), who proposed guidelines for GRS walls for the New Zealand Transportation Agency, which considered New Zealand's seismic conditions. At the time of writing the article, Jackson et al. (2012) indicated there had not been any construction of GRS walls with full-height ridged facing in New Zealand. Previous case histories stated that in seismic regions, GRS walls with full-height ridged facing performed better under seismic conditions than other GRS wall types, but the failure mechanisms were not fully understood. Jackson et al. (2012) present an experimental model using PIV that investigates the failure mechanisms and performance of GRS walls with full-height ridged facing.

Jackson et al. (2012) constructed a strong-box for testing on a 1g shake table using guidance from previous GRS shake table experiments. The box constructed was 1100 mm x 800 mm x 3000 mm long. The box accommodated the scaled down version of a 4.5 m tall wall. One of the sides of the strong box consisted of a 20 mm perspex sheet. The perspex sheet allowed for images of the backfill soil to be captured during testing. The images would be subjected to analysis using GeoPIV.

The model was prepared by first installing the facing panel and then placing Albany sand in 75 mm layers before compacting the layers using the shake table vibrations. Five layers of reinforcement spaced at 150 mm were placed as the model was filled with sand in layers. The model also had accelerometers placed in the backfill region, and displacement transducers were attached to the facing panel. Several model configurations were tested. Variations included three ratios of reinforcement length to wall height (0.6, 0.75, and 0.9) and wall inclinations of 90° and 70°. All of the models were subjected to shaking using a sinusoidal wave with a frequency of 5 Hz for 10 seconds with a base acceleration of 0.1 g. If the model did not fail, the test was repeated by increasing the base acceleration in an increment of 0.1 g until the model failed.

Jackson et al. (2012) examined the results of four of the tests where the length of reinforcement to wall height ratio and facing inclination was varied. The results indicated that failure occurs between 0.5 g and 0.7 g base accelerations. Jackson et al. (2012) presented one of the test results to discuss the typical response of the model. Figure 2.28 shows the model of the sample test prior to and after failing. The primary mode of failure was overturning, while sliding also contributed. Jackson et al. (2012) also found that as the base accelerations increased, the failure surface moved deeper and deeper into the model (Figure 2.29). Figure 2.29 does not show the failure surfaces below a base acceleration of 0.3 g as the change in the marker lines were not

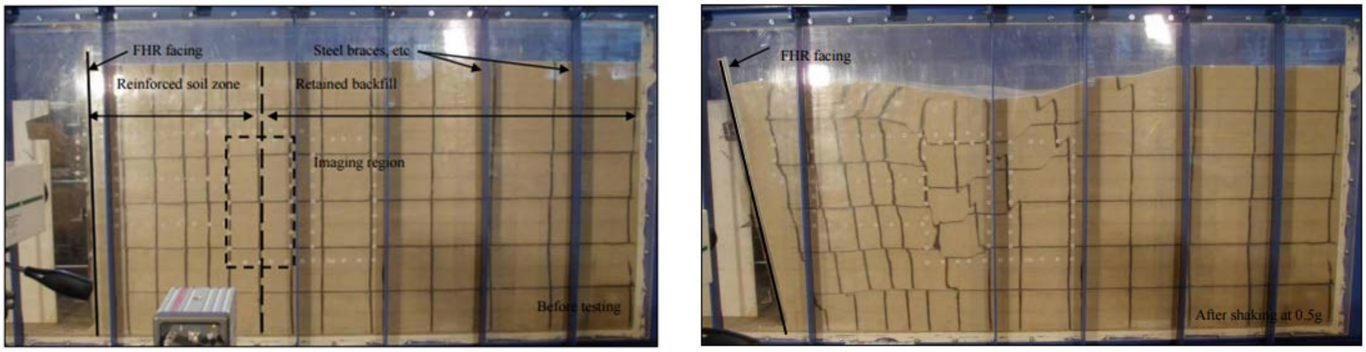

(a) (b)

Figure 2.28 Test 6 (a) before shaking and (b) after shaking at 0.5g, during which failure occurred. (Jackson, et al., 2012)

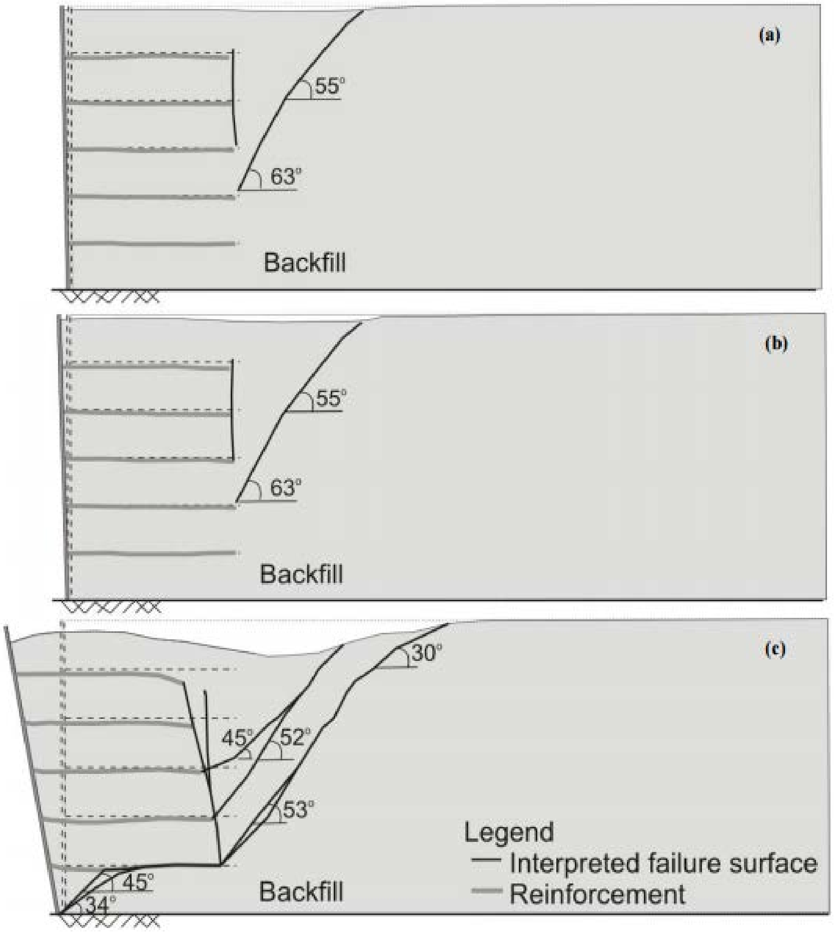

Figure 2.29 Interpretation of failure surfaces within the reinforced and retained backfill after the completion of (a) 0.3g, (b) 0.4g and (c) 0.5g shaking steps. (Jackson, et al., 2012)

observable. Examining the displacement at the top of the wall versus applied base acceleration, Jackson et al. (2012) found that increasing the reinforcement length to wall height, and/or increasing the wall face inclination angle led to an increase in resistance to base acceleration.

Jackson et al. (2012) then analyzed the images taken during the tests with GeoPIV. The GeoPIV analysis indicated that the failure surfaces began to develop sooner than what was visible from the naked eye. Jackson et al. (2012) found that as early as 0.2 g of base acceleration, 20% shear strain was present on a surface connected to the end of the second reinforcement layer, where the bottom most layers is the first. The increase in shear strain as the base acceleration increased is shown in Figure 2.30.

Using GeoPIV, Jackson et al. (2012) identified the non-visible responses of the model to low values of base acceleration and identified how the failure surfaces propagates. Identifying these features allowed Jackson et al. (2012) to conclude that the two-wedge model used in Japanese designs of GRS walls with full-height ridged facing is accurate.

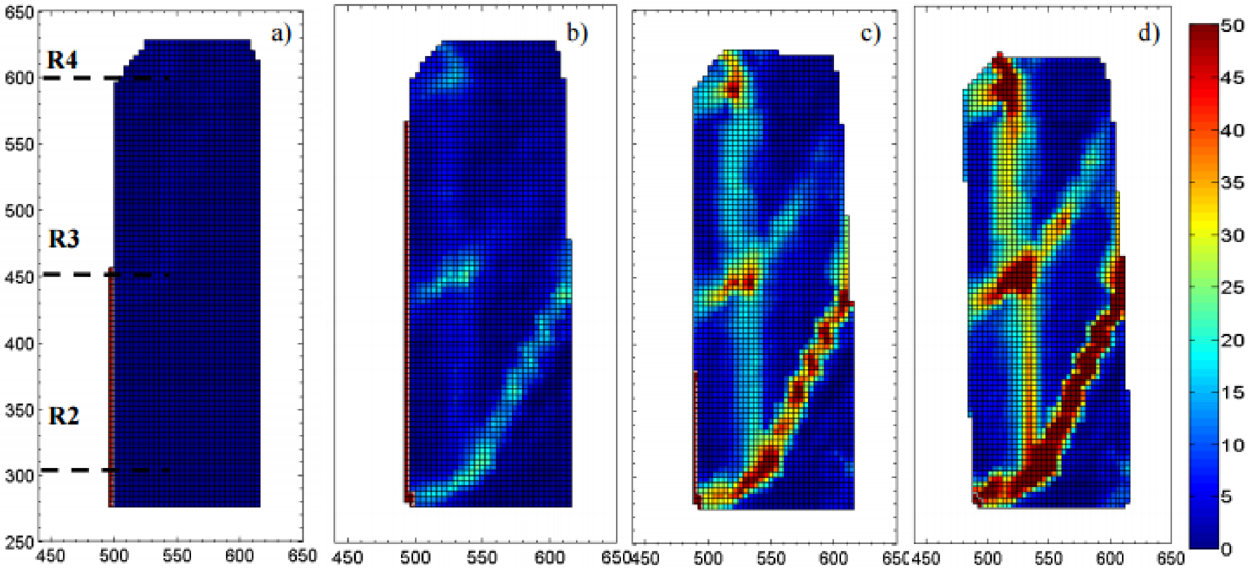

Figure 2.30 Residual shear strain of the imaging region of Test-6 reinforced with L/H = 0.6 and accumulated by the completion of: (a) 0.1g, (b) 0.2g, (c) 0.3g, and (d) 0.4 g shaking steps.
(Jackson, et al., 2012)

2.3.4 Case study: Observations of grain-scale interactions and simulation of dry granular flows in a large scale flume – Sarah K. Bryant, W. Andy Take, and Elisabeth T. Bowman (2014)

Bryant et al. (2014) suggest that investigating and attempting to predict how granular materials behave while flowing is a focal point for several different disciplines. The investigations are usually split into two different areas, large-scale response and particle-scale response. Large-scale response investigations focus on behaviors like landslide spreading, while particle-scale investigations focus on individual particle or particle group behaviors occurring within the flowing body. Previous investigations primarily focused on creating models that accurately represent particle behavior during different flow types or on models that accurately represent the behavior of horizontal dam break experiments. Several experiments have included large flume analysis of landslides, but these have been limited by difficulties with regard to the boundary conditions and an inability to investigate the interflow particle behaviors. Bryant et al. (2014) present a method using a landslide flume with transparent sides to investigate flow behaviors. Using GeoPIV and depth averaging numerical models, Bryant et al. (2014) sought to provide a connection between the particle scale behavior and the macro scale behavior in landslides.

The experiments consisted of releasing three volumes of ceramic beads (0.06, 0.17, and 0.34 m^3) down a landslide flume with transparent sides. The flume slope was inclined at 30° for a length of 8.23 m. A horizontal section of 36 m was located at the bottom of the slope to allow the material to come to a rest. The entire width of the flume was 2.09 m. The tests were conducted with the surface of the flume in two states, a smooth state and a rough state. At five places along the length of the flume slope, five cameras were placed to capture images of the ceramic bead flow as it progressed through the flume (Figure 2.31).

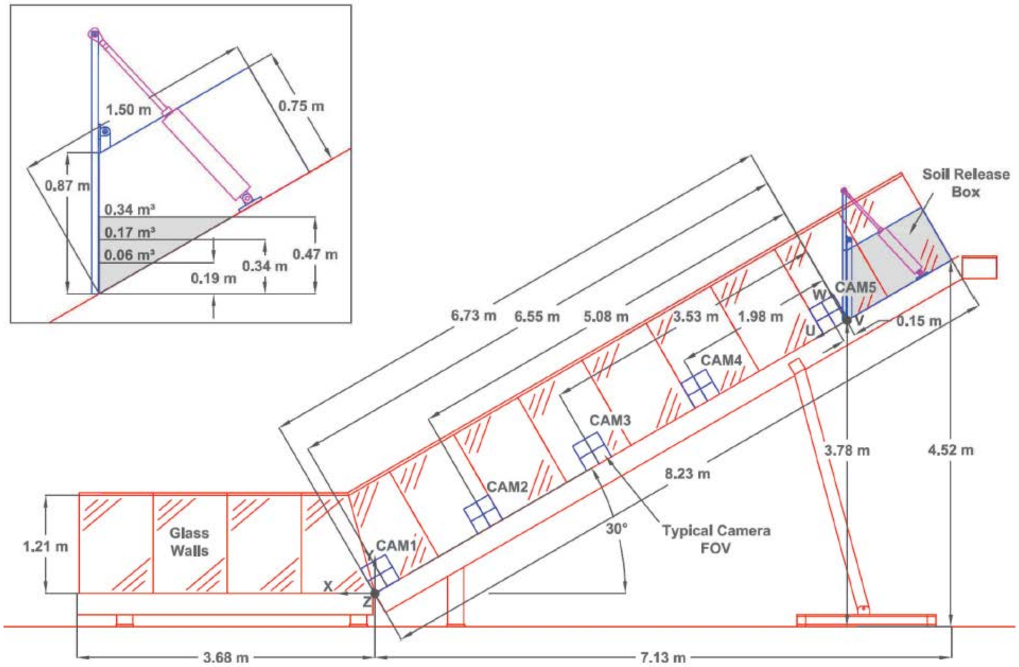

Figure 2.31 Diagram of the Queen's University landslide flume. (Bryant, et al., 2014)

Each of the tests was repeated five times to allow a high speed camera to capture images from above the center of the flume at each of the five horizontal locations. The images were then analyzed using GeoPIV to measure ceramic bead displacements during flow and to generate velocity profiles. Once the flow came to rest, the depth of the slide mass was recorded at regular spacing at the bottom of the slope.

Bryant et al. (2014) first discussed a series of observations regarding the behavior at the particle level. Using the velocity profiles generated by GeoPIV, the slide was found to exhibit several behaviors. In the first part of the slide, the particles were spread out from each other and jumped from location to location, the main body of the slide densified and began to slow, and the rear of the slide became loose again with the particles jumping from position to position. This behavior was observed at all camera locations except for the bottom camera due to its proximity to the slope transition. The overhead camera was used to investigate

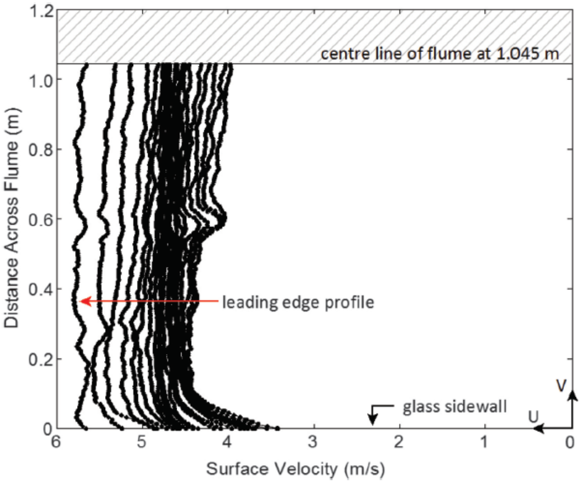

Figure 2.32 Surface velocity profiles for 0.34 m^3 volume tests on smooth surface. Time step between velocity profiles is 0.1 s (Bryant, et al., 2014)

the boundary effects on the slide velocity. Bryant et al. (2014) found that the boundaries reduced the flow by 0.5 m/s; however, the effect decreased to zero 50 mm from the edge (Figure 2.32.)

Bryant et al. (2014) qualitatively examined the results. The paths of several particles were tracked using several superimposed images at small time steps. Bryant et al. (2014) used these paths to identify the flow regimes occurring. In the front and rear of the slide, the particles were loosely arranged and jumping point to point, fitting the definition of the gas flow regime. In the main body of slide, the particles densified and presented more consistent features, fitting the description of the liquid flow regime. Liquid flow regimes were present in all of the tests except for the 0.06 m^3 slide volume, which remained in the gas flow regime. It was further observed that the height of the flows depended on the flow regime, and that gas regime flows had the highest flow height.

Bryant et al. (2014) quantitatively examined the results starting with the velocity-depth data. The data was used to calculate the shear strain rate and subsequently the inertial number. For regions

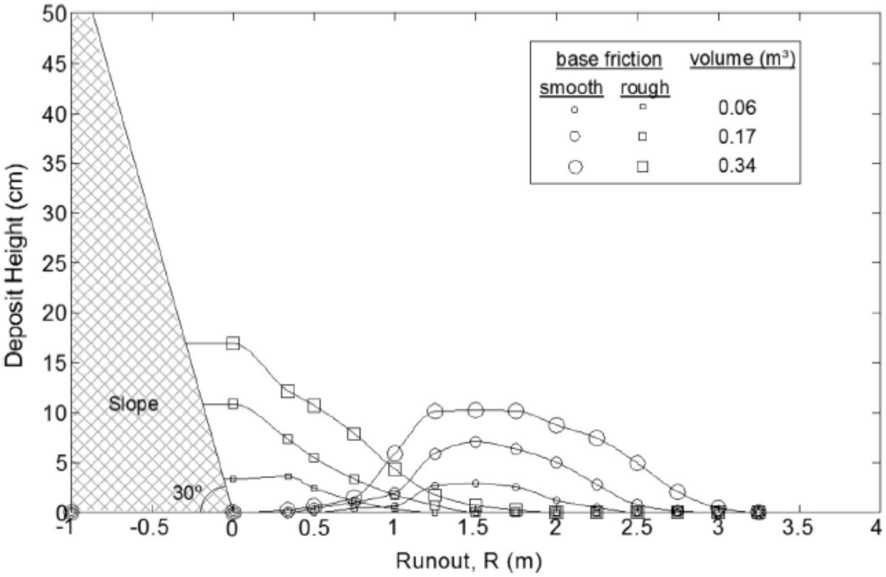

Figure 2.33 Final deposit profiles for all test configurations. (0,0) is the point where slope meets horizontal base. A typical result is shown for each test configuration. (Bryant, et al., 2014)

of gas regime flow, the shear strain rate and inertial number were lower than the values for liquid regime flows. Examining plots of the shear strain rate and inertial numbers for the different volumes for the smooth surface tests, Bryant et al. (2014) found that as the volume decreased so did the shear strain rate and inertial numbers in the gas regime regions.

Finally, Bryant et al. (2014) examined the behavior of the slide at the macro level. The primary focus was to determine the distance the material extended and the shape the material took once it left the slope of the flume and crossed onto the horizontal section. Bryant et al. (2014) found that the material extended further when the surface of the slide was smooth. For a rough surface, the material presented a higher mound when it came to rest. Both behaviors are shown in Figure 2.33. The physical experiment data was used to calibrate a depth-averaged numerical model (DAN). When the initial gas flow regime section was ignored, the model was found to be in good agreement. However, the basal friction angle determined for the rough and smooth surfaces using the numerical values

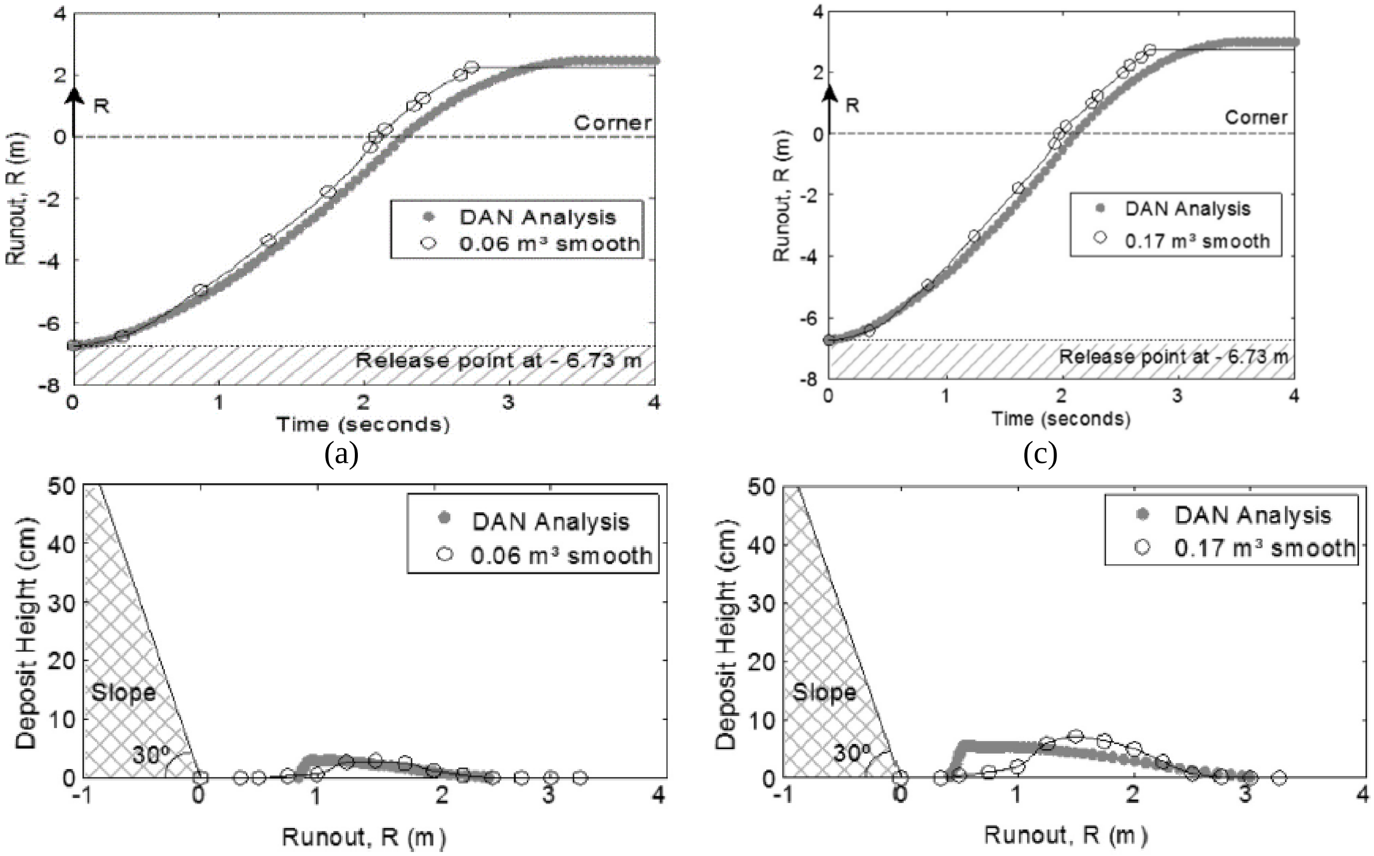

(a) (c)

(b) (d)

Figure 2.34 (a) Runout over time and (b) final deposit profiles of 0.06 m^3 test and DAN performance on smooth surface. (c) Runout over time and (d) final deposit profiles of 0.17 m^3 test and DAN performance on smooth surface. (Bryant, et al., 2014)

were lower than those determined in laboratory test. Bryant et al. (2014) found the lower values to be reasonable due to the different states the material during the investigation.

Using GeoPIV, Bryant et al. (2014) were able to examine the behavior of particles in the body of a simulated landslide. The behavior was then quantified to provide flow parameters. The flow parameters were then used in the back calculation to fit the depth-average numerical model. The calibrated model showed a reasonable match with the observed particle behaviors, thus completing the link from microscale to macro scale behavior.

3 Material Properties

This chapter provides a discussion of methodology in the selection of the materials used for this research. A discussion of the material properties, including grain size distribution, particle shape and morphology, moisture content, specific gravity, index density, void ratio, and friction angle is included. The methods used to determine these properties are briefly discussed.

3.1 Glass Beads

Mono-sized spherical glass beads were selected as the first material to support the validation of Chrono::Granular. The glass beads provided an ideal representation for Chrono::Granular simulations. Jaygo Inc. Dragonite® Soda Lime Glass Beads Type-M Article 5005 were selected. The glass bead data sheet can be found in Appendix A.

3.1.1 Grain Size Distribution

The grain size distribution of the glass beads was originally going to be determined using ASTM D6913-04 but the sieves available did not have enough variance around the manufacturer specified diameter range to accurately capture the variation of the particle sizes. A different approach was thus selected. Using MATLAB’S image processing suite, an image of 589 particles was processed to determine the average particle diameter and standard deviation in particle diameter. Pre- and post-analysis images are shown in Figure 3.1 and Figure 3.2, respectively. The image contained stacked particles in the bottom right corner, which were detected during the analysis. A scale was included as a reference point to convert the results from image space (dimensions in pixels) to real space (dimensions in mm). The results of the analysis and a comparison of a normal distribution of the received glass beads diameter to the manufacturer specifications are shown in Figure 3.3. The analysis indicates that the material

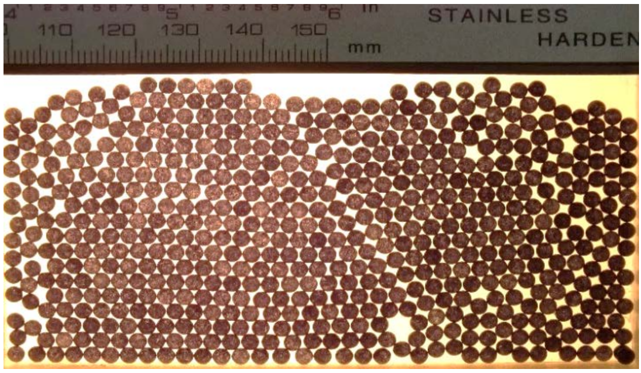

Figure 3.1 Glass bead image before analysis

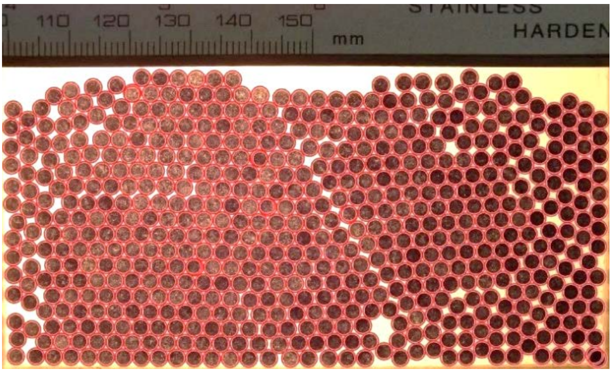

Figure 3.2 Glass bead image after analysis

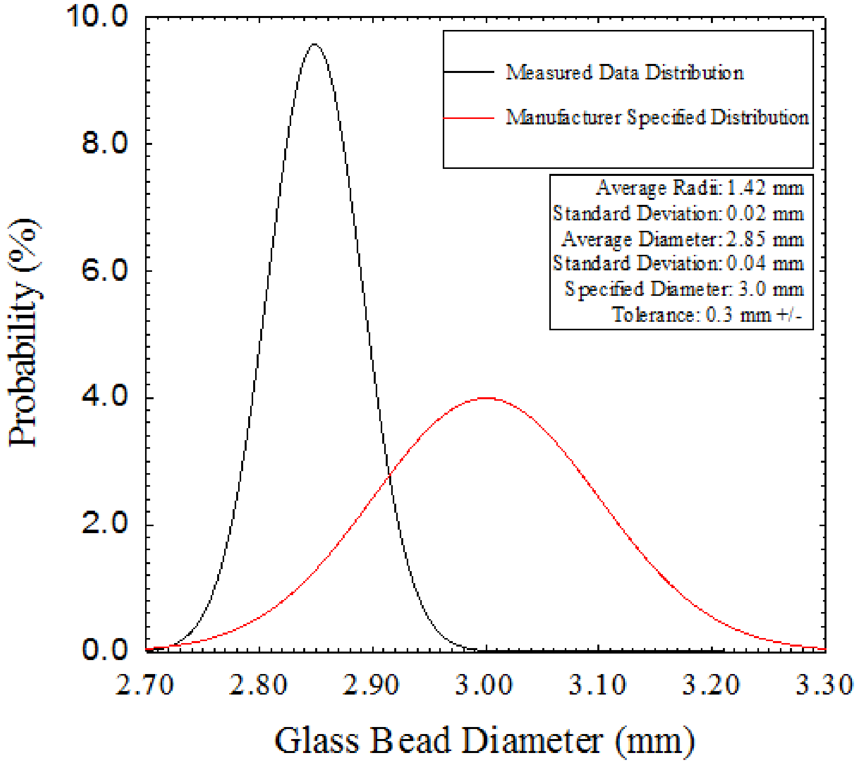

Figure 3.3 Glass bead particle size distributions

received has a smaller average and less variable particle diameter (2.85 mm ± 0.12 mm) than what the manufacturer specified (3.0 mm ± 0.3 mm). The MATLAB code used to analyze the image can be found in Appendix B.

3.1.2 Particle Shape and Morphology

One hundred four glass beads were visually examined under a stationary digital camera. The images of the glass beads were captured using a FUJIFILM FinePix S9400W digital camera, which has an image resolution of 4608 x 3546 pixels. The macro setting was enabled to allow for close up images. The glass bead images were imported into AutoCAD with a scale of 1 pixel equal to 1 unit. The perimeter of each glass bead was traced and the perimeter length recorded. The maximum particle diameter was determined by using the 2-point circle command, where the user selects the beginning and end points of the circle diameters, to create a circle that encompassed the entire glass bead. The center point of the circle was then used to determine the minimum diameter.

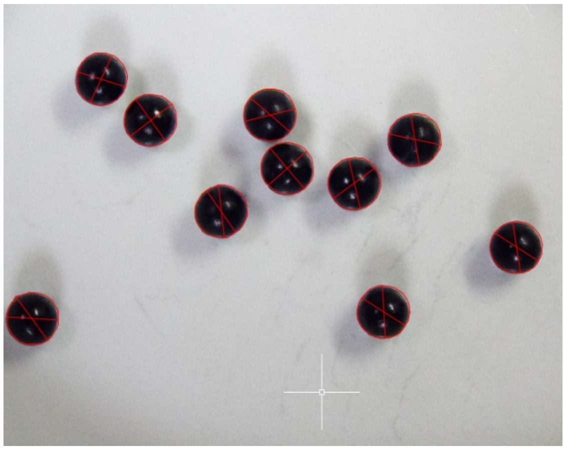

Figure 3.4 Image of glass beads in AutoCAD

The particle perimeter, maximum diameter, and minimum diameter were used to quantify the roundness and sphericity of the particles. The sphericity and roundness of each particle was classified using indices presented by Alshibli and Alsaleh (2004) as defined by Equation 3-1 and

Equation 3-2. Figure 3.5 provides a visual representation of the sphericity and roundness indices as well as a comparison with the Powers classification (Powers, 1982).

$$I_{sph} = \frac{1}{N}\sum_{i=1}^{N}\left|\frac{D_{equ(i)}}{d_{s(i)}} - \frac{D_{equ(i)}}{d_{L(i)}}\right| \qquad \textbf{3-1}$$

where:
I_{sph} = sphericity index
N= number of particles
$D_{equ(i)}$= equivalent particle diameter (perimeter/π)
$d_{s(i)}$ = shortest particle dimension
$d_{L(i)}$= largest particle dimension

$$I_R = \frac{1}{N}\sum_{i=1}^{N}\frac{P_{act(i)}}{\pi\left[\left(d_{s(i)} + d_{L(i)}\right)/2\right]} \qquad \textbf{3-2}$$

where:
I_R = sphericity index
N= number of particles
$P_{act(i)}$= actual particle perimeter
$d_{s(i)}$ = shortest particle dimension
$d_{L(i)}$= largest particle dimension

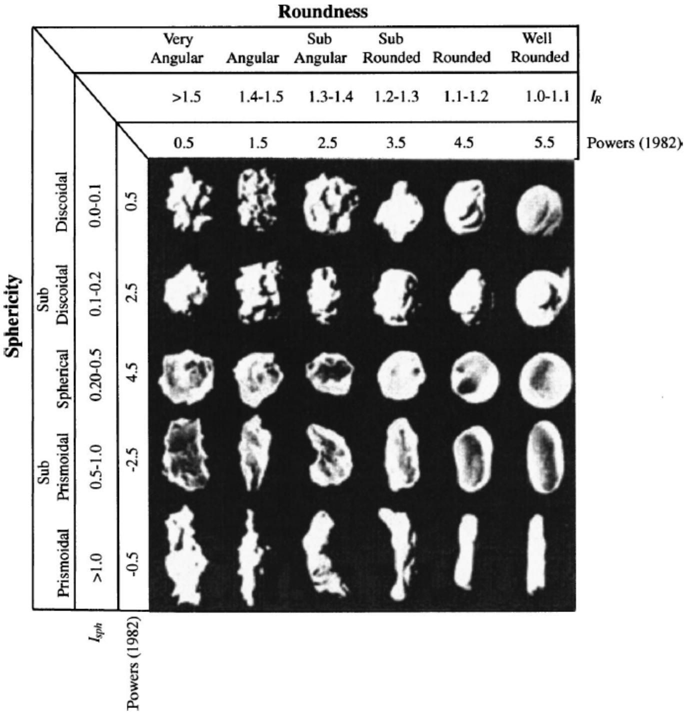

Figure 3.5 Comparison between Powers classification, I_{sph}, and I_r values (Alshibli & Alsaleh, 2004)

The glass beads sampled were all found to be well-rounded discoidal particles (table 3-1.) The glass beads were expected to be well-rounded and the variation in the diameter indicates that the particles are not perfectly spherical.

Table 3-1 Glass beads sphericity and roundness summary

Index	Sphericity	Roundness
Average	0.033	1.003
Median	0.030	1.003
Root Mean Square	0.036	1.00
Standard Deviation	0.014	0.0052

3.1.3 Moisture Content

The glass beads arrived in a clear plastic bag, and appeared to contain minimal moisture. A moisture content analysis was performed to determine if the glass beads would need to be oven dried to remove any additional moisture. The glass beads were analyzed using the procedure specified in ASTM D-2216. Five samples were placed into moisture cans and allowed to dry to a constant mass in an oven at 110°C. A summary of the results can be found in

table 3-2. The average moisture content was calculated to be 0.1%; however, this value is not indicative of the moisture present in the glass beads. After oven drying the samples, the color of the coating on the glass bead changed. This observation was interpreted to indicate that the mass loss was not from water in the sample, but was mass lost from the glass bead coating. The composition of this coating was not determined.

Table 3-2 Results of glass bead moisture content analysis

Moisture Can	**1B**	**2B**	**3B**	**4B**	**5B**
Can Mass (g)	30.63	25.26	19.78	19.85	25.13
Can + Moist Soil Mass (g)	118.28	113.41	82.34	82.71	78.23
Can + Dry Soil Mass (g)	118.24	113.38	82.27	82.65	78.19
Mass of Dry Soil (g)	87.61	88.12	62.49	62.80	53.06
Mass of Moisture (g)	0.04	0.03	0.07	0.06	0.04
Water Content (%)	0.0	0.0	0.1	0.1	0.1
Average Water Content (%)					0.1

3.1.4 Average Mass

The average mass for the glass beads was determined for later use during the direct shear test. One hundred glass beads were allowed to dry to a constant mass in an oven at 110°C. The glass beads were allowed to cool to room temperature before measuring their mass. A Denver Instrument M-120 scale with precision to 0.0001 g was used to determine the mass of each glass bead. The average mass was calculated as 0.0355g with a standard deviation of 0.0006 g.

3.1.5 Specific Gravity

A glass bead sample was selected to determine the specific gravity of the batch. The manufacturer specified that the glass bead specific gravity is 2.50. The glass bead sample was subjected to a vacuum pycnometry analysis specified by ASTM D854-14 to confirm the specific gravity. The specific gravity of the glass beads was calculated to be 2.51 at 25 °C. When the temperature correction factor was applied, the average specific gravity was determined to be 2.50, conforming with the manufacturer specified value.

3.1.6 Index Density and Void Ratio

The maximum and minimum bulk density of the glass beads were determined using the procedures specified in ASTM D4253-16 and ASTM D4254-16 respectively. ASTM D4253-16 allows for the minimum density to first be determined and the process continued to determine the maximum density. A standard 152.40 cm^3 (0.100 ft^3) mold was first weighed. The mold was filled loosely with glass beads using a funnel as specified in ASTM D4254-16. The surface of the glass beads was carefully leveled with the top of the mold and the mass was recorded. The sample was then placed on a vibratory table and allowed to densify. The distance from the surface of the glass beads and the mold was measured. This was repeated three times to determine an average minimum and average maximum density. The average minimum bulk density was calculated as 1503.97 kg/m^3 (1.50 g/cm^3) and the average maximum bulk density was calculated as 1631.96 kg/m^3 (1.63 g/cm^3).

The specific gravity determined from the vacuum pycnometry analysis and the maximum and minimum densities were used to determine the minimum and maximum void ratio of the glass beads. Using Equation 3-3 the minimum void ratios were calculated as 0.53 and the maximum void ratio was calculated as 0.66.

$$e = \frac{GS * \ \rho_w}{\rho_{dry}} \qquad \textbf{3-3}$$

where:
e = void ratio
GS= specific gravity
ρ_w= density of water
ρ_{dry} = dry maximum or minimum density

3.1.7 Friction Angle

The glass beads were subjected to a traditional direct shear test to determine the peak and residual (critical) friction angles using the procedure specified in ASTM D3080-11. The glass beads were analyzed using two different shear rates (0.5 mm/min and 1.0 mm/min) and three different normal stresses (140 kPa, 344 kPa, and 552 kPa.) The glass beads samples were prepared at two relative densities (greater than 90% and less than 10%) using Equation 3-4.

$$D_r = \frac{\rho - \rho_{min}}{\rho_{max} - \rho_{min}} \tag{3-4}$$

where
D_r =relative density
ρ_{max}= maximum density
ρ_{min} = minimum density
ρ = design density

Shear test results can be found in Figure 3.6 and Figure 3.7. The peak and residual (critical) friction angles were then calculated. A linear regression was used to determine the friction angles. The regression was forced to start from the origin. The results can be found in Figure 3.8. The peak friction angle was calculated as 34.3° at a rate of 0.5 mm/min and 35.67° at a rate of 1.0 mm/min. The residual friction angle was calculated as 32.01° at a rate of 0.5 mm/min and 30.28° at a rate of 1.0 mm/min. The results indicate that the glass bead friction angles (both peak and residual) are systematically dependent on shear displacement rate. Previous investigation of strain rate effects on friction angle for dry sands found that friction angle is independent of strain rate, but an increase in strain rate caused an increase in dilation response Svoboda (2013). Dai et al. (2016) found the friction angle is affected by dilatancy angle and particle size. Using both studies, there is potential for shear rate to increase the dilatancy response of the glass beads, leading to an increase in the friction angle do to dilatancy, when the friction angle should remain constant over a shear rate range.

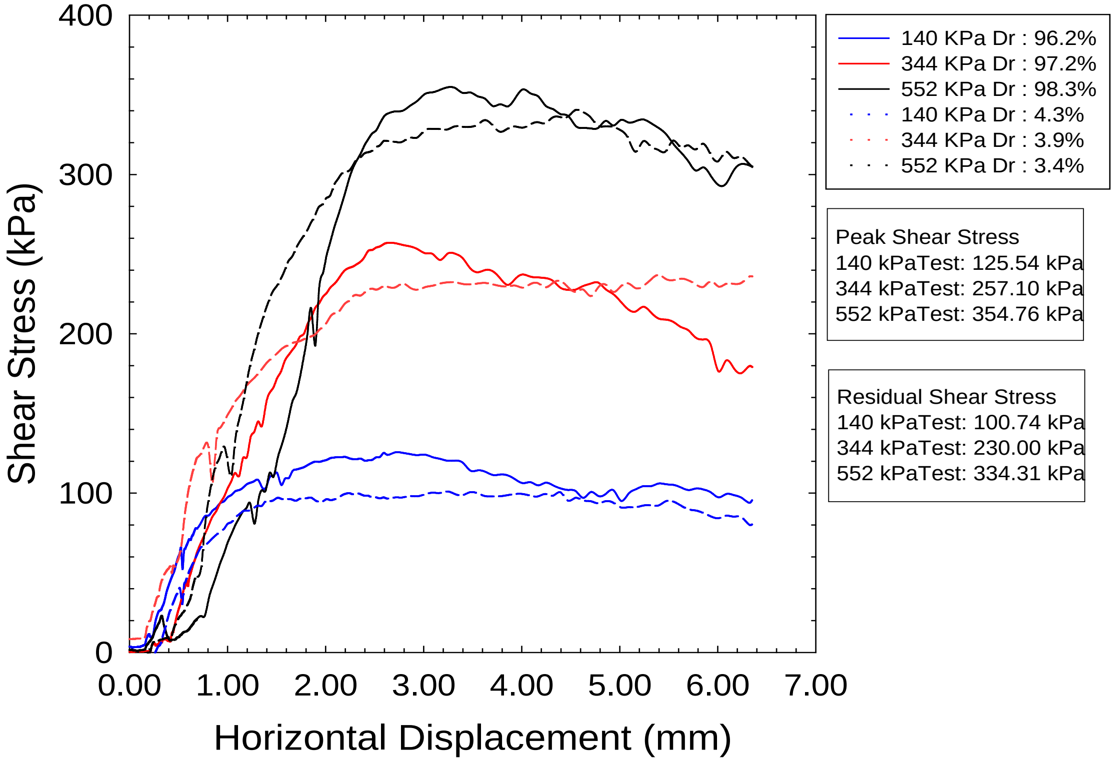

Figure 3.6 0.5 mm/min Glass Beads direct shear results

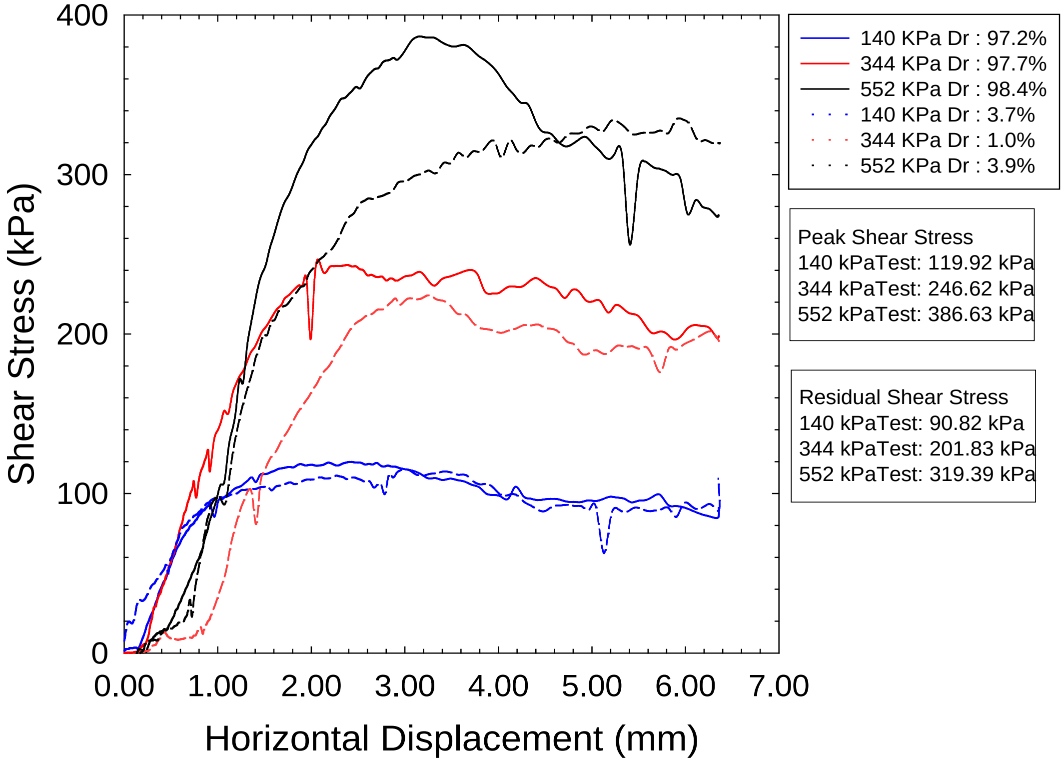

Figure 3.7 1.0 mm/min Glass Beads direct shear results

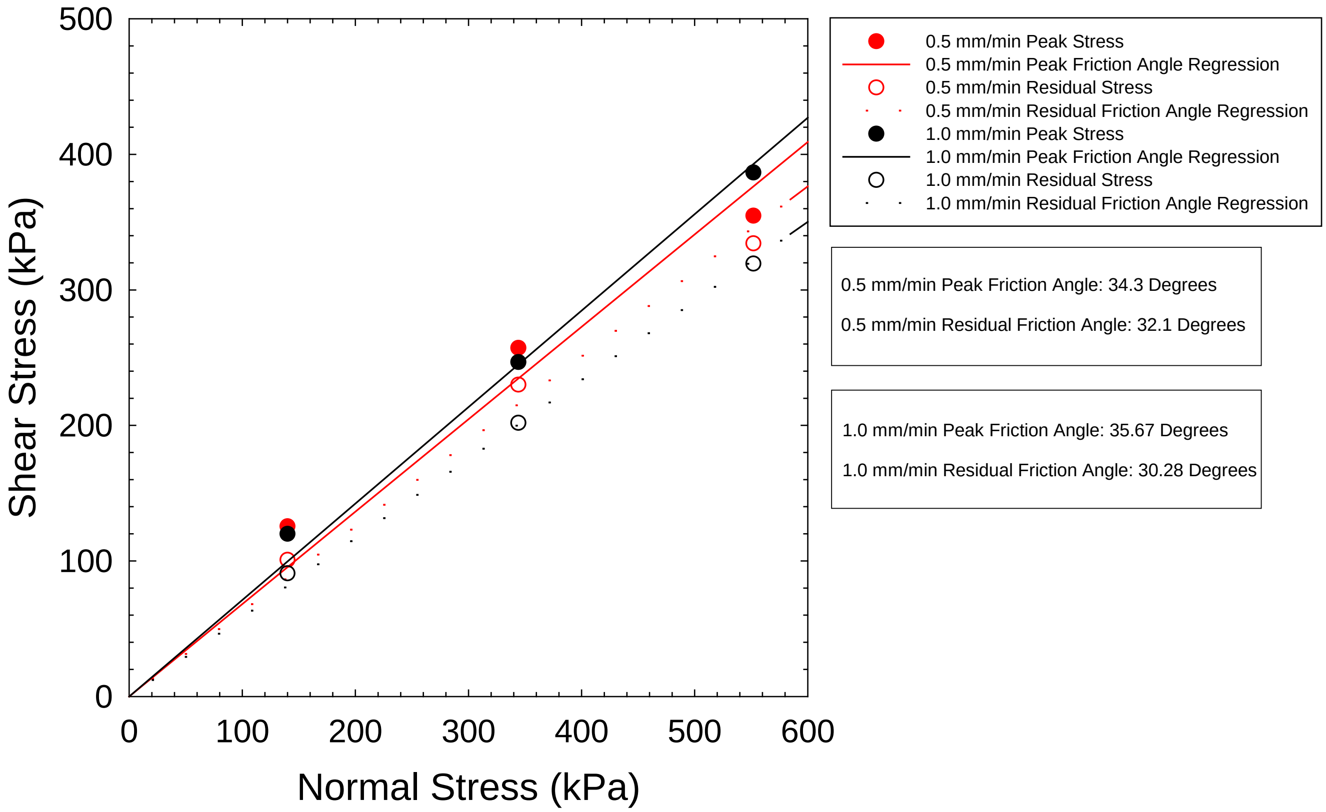

Figure 3.8 Glass bead friction angle results

3.2 Ottawa Sand

Spherical poorly-graded sand was selected as the second material to support the validation of Chrono::Granular and the investigation of the effects stress has on particle movements. The sand provided a more realistic scenario than the glass beads, but still provided an ideal analog (approximately spherical particles) for DEM simulations using Chrono::Granular. Test sand mined from Ottawa, IL and meeting the 20-30 ASTM gradation was selected to fill this role.

3.2.1 Grain Size Distribution

The sand was specifically selected because it was prepared to be uniform in size, with 85% to 100% of the sand specified to fall between the No. 20 sieve (0.841 mm openings) and the No. 30 sieve (0.595 mm openings). A sample of the sand was subject to a sieve analysis to verify conformance with ASTM C-778 as 20-30 Standard Sand. The No. 200 sieve was included in the analysis in addition to the sieves specified in ASTM C-778. A comparison between the ASTM 20-30 gradation (shaded area) and the measured sand sample's gradation can be found in Figure 3.9.

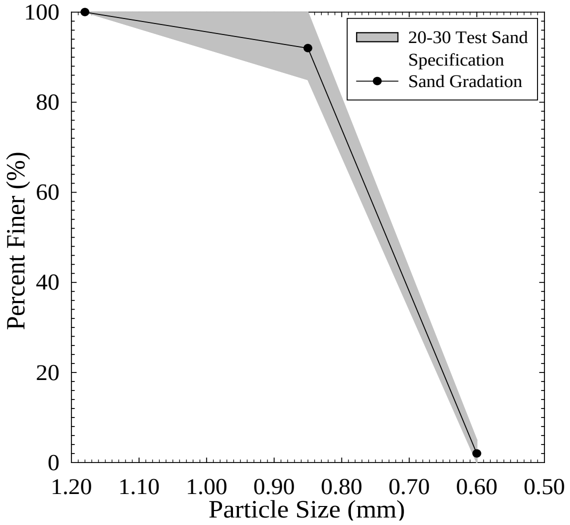

Figure 3.9 Sand sample gradation vs. 20-30 standard

3.2.2 Particle Shape and Morphology

One hundred and ten sand particles were examined under an optical microscope to determine particle shape and morphology. A Fisher Scientific StereoMaster microscope at 20x magnification was used to capture the images of the sand particles. The images of the sand particles were imported into AutoCAD with a scale of 1 pixel equal to 1 unit. Each particle’s perimeter was traced. The maximum particle diameter was determined by using the 2-point circle, where the user selects the beginning and end points of the circle diameters, command to create a circle that encompassed the entire particle. The center point of the circle was then used to determine the minimum diameter. Figure 3.10 shows the sand grains with the perimeter traced and the maximum and minimum diameters identified.

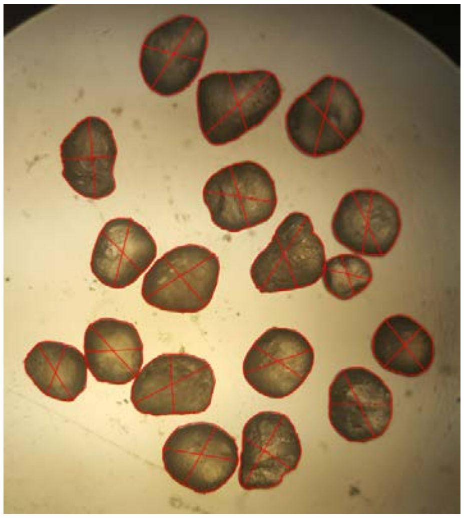

Figure 3.10 Image of sand grains in AutoCAD

The particle perimeter, maximum diameter, and minimum diameter were used to quantify the roundness and sphericity of the particles. The sphericity and roundness of each particle was classified using the sphericity and roundness indices presented by Alshibli and Alsaleh (2004) as defined by Equation 3-1 and Equation 3-2. Figure 3.5 provides a visual representation of the sphericity and roundness indices as well as a comparison with the Powers classification (Powers, 1982). The sand particles sampled were all found to be well rounded. A summary of the sphericity and roundness indices can be found in table 3-3. Figure 3.11 shows the percentage of each sphericity class represented in the sand sample. There were several particles that appeared to have notches where the sand grain had fractured.

Table 3-3 Sand particles sphericity and roundness summary

Index	Sphericity	Roundness
Average	0.297	1.039
Median	0.252	1.038
Root Mean Square	0.332	1.039
Standard Deviation	0.148	0.025

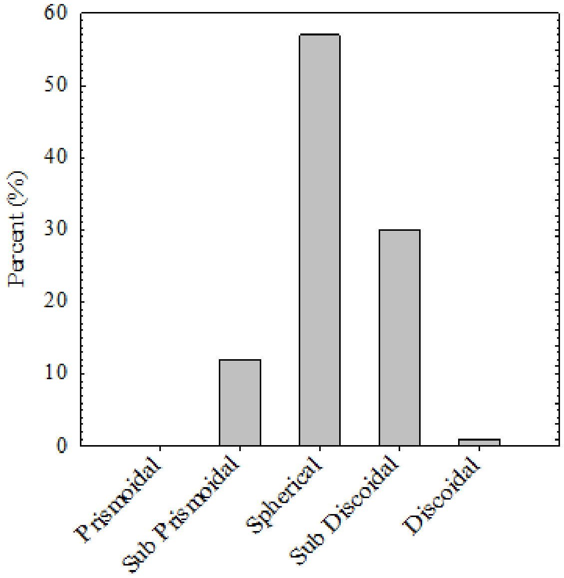

Figure 3.11 Sand grain sphericity distribution

3.2.3 Moisture Content

The sand arrived in a 50-lb bag and appeared to contain minimal moisture. A moisture content analysis was performed to determine if the sand would need to be oven dried to remove any additional moisture. The sand was analyzed using the procedure specified in ASTM D-2216. Five samples were placed into moisture cans and allowed to dry to a constant mass in an oven at

Table 3-4 Results of sand moisture content analysis

Moisture Can	JB6	A1	G22	A2	A3
Can Mass (g)	37.0	28.0	28.0	28.0	28.1
Can + Moist Soil Mass (g)	184.0	132.6	129.7	139.1	138.5
Can + Dry Soil Mass (g)	183.9	132.6	129.7	139.0	138.5
Mass of Dry Soil (g)	146.9	104.6	101.7	111.0	110.4
Mass of Moisture (g)	0.1	0.0	0.0	0.1	0.0
Water Content (%)	0.1	0.0	0.0	0.1	0.0
Average Water Content (%)			0.0		

110°C. A summary of the results can be found in table 3-4. The sand did not lose any mass when subjected to drying, indicating that the drying the bulk sand sample was unnecessary.

3.2.4 Specific Gravity

Two sand samples were selected to determine the specific gravity of the batch. The manufacturer specified that the sand specific gravity is 2.65. The sand samples were subjected to a vacuum pycnometry analysis specified by ASTM D854-14 to confirm the specific gravity. The specific gravity of the sand samples was calculated to be 2.660 and 2.646 at 25 °C. When the temperature correction factor was applied, the average specific gravity was determined to be 2.65. This value is consistent with 2.65 specified by the manufacture and 2.65 reported by Sundberg (1999) for 20-30 Ottawa sand.

3.2.5 Index Density and Void Ratio

The maximum and minimum density of the sand was determined using the procedures specified in ASTM D4253-16 and ASTM D4254-16 respectively. ASTM D4253-16 allows for the minimum density to first be determined and the process continued to determine the maximum density. A standard 152.40 cm^3 (0.100 ft^3) mold was first weighed. The mold was filled loosely with sand using a funnel as specified in ASTM D4254-16. The surface of the sand was carefully leveled with the top of the mold and the mass was recorded. The sample was then placed on a vibratory table and allowed to densify. The distance from the surface of the sand and the mold was measured. This was repeated three times to determine an average minimum and average maximum density. The average minimum density was calculated as 1521.27 kg/m^3 (1.52 g/cm^3) and the average maximum density was calculated as 1796.95 kg/m^3 (1.80 g/cm^3). These values are comparable to the maximum density of 1.79 g/cm^3 and minimum density of 1.52 g/cm^3 reported by Edil et al (2006) for 20-30 Ottawa sand.

The specific gravity determined from the vacuum pycnometry analysis and the maximum and minimum densities were used to determine the minimum and maximum void ratio of the glass beads. Using Equation 3-3 the minimum void ratios were calculated as 0.47 and the maximum void ratio was calculated as 0.74. These values are comparable to the minimum void ratio of 0.48 and maximum void ratio of 0.74 reported by Edil et al. (2006) for 20-30 Ottawa sand.

3.2.6 Friction angle

Samples of sand were subjected to a traditional direct shear test to determine the peak and residual (critical) friction angles using the procedure specified in ASTM D3080-11. The samples of sand were analyzed using two different shear rates (0.5 mm/min and 1.0 mm/min) three different normal stresses (140 kPa, 344 kPa, and 552 kPa) and two relative densities (greater than 90% and less than 10%) as defined by Equation 3-4. The results can be found in Figure 3.12 and Figure 3.13. The peak and residual (critical) friction angles were then calculated. A linear regression was used to determine the friction angles. The regression was forced to start from the origin. The results can be found in Figure 3.14. The peak friction angle was calculated as 35.9° at a rate of 0.5 mm/min and 38.9° at a rate of 1.0 mm/min. The residual friction angle was calculated as 33.0° at a rate of 0.5 mm/min and 33.4° at a rate of 1.0 mm/min. Sundburg (1999) found the peak and residual friction angles to be 35.5° and 30.9° degrees respectively. The 0.5 mm/min peak friction rate is comparable, while both the 0.5 mm/min and 1.0 mm/min rates have a residual friction angle that was 2° higher; however, the relative densities examined were higher and lower than Sundburg's.

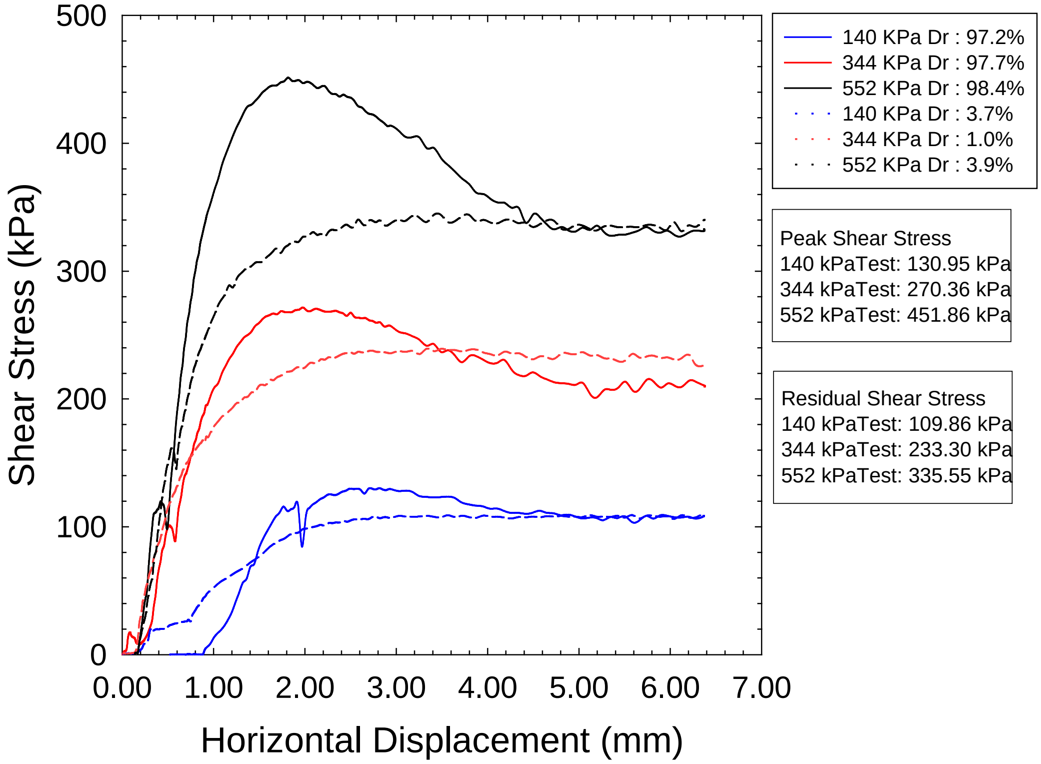

Figure 3.12 1.0 mm/min Sand direct shear results

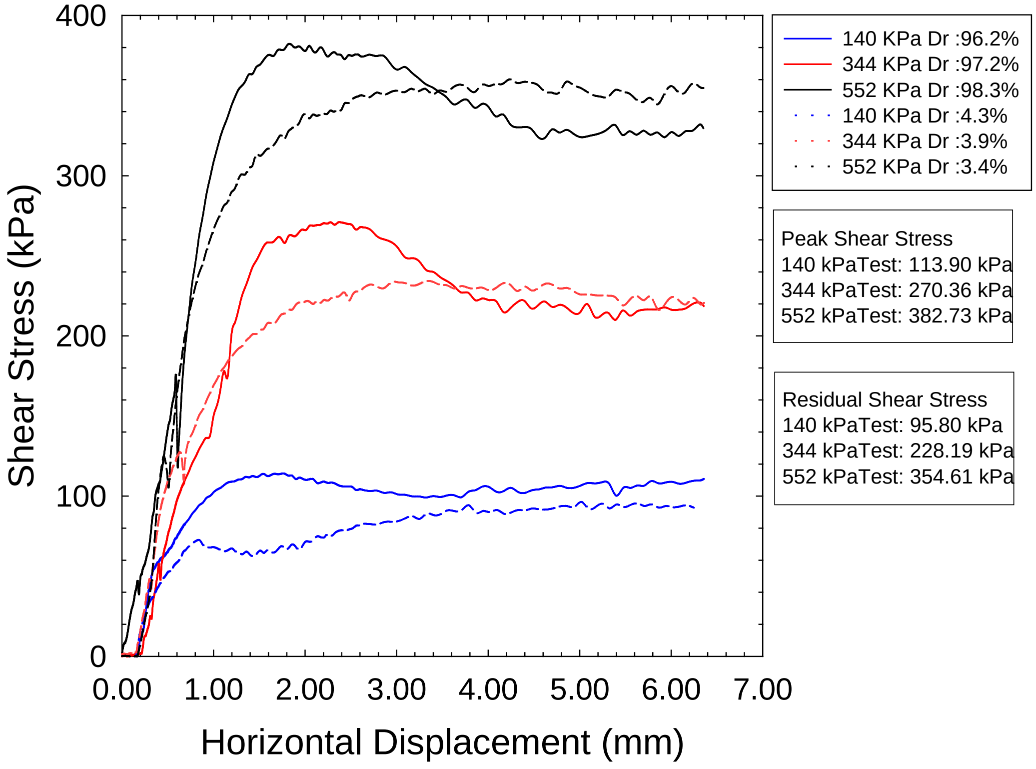

Figure 3.13 0.5 mm/min Sand direct shear results

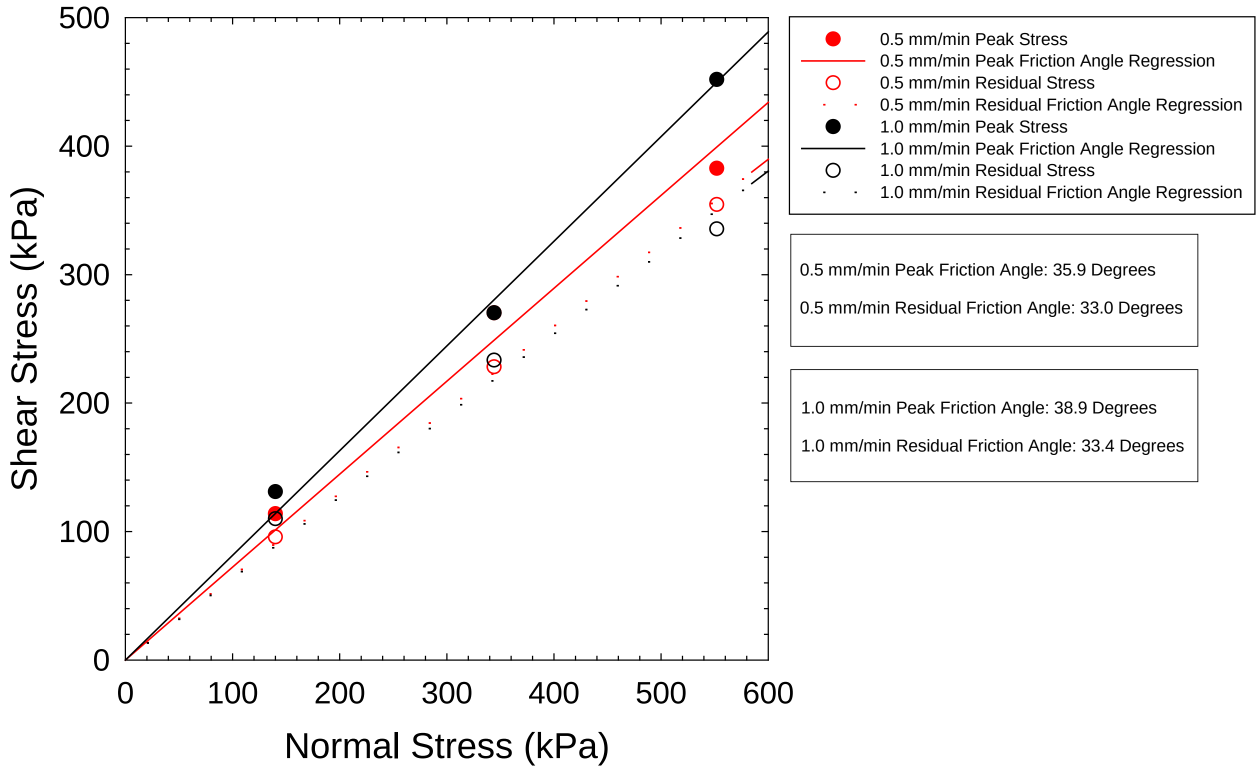

Figure 3.14 Sand friction angle results

4 Methods

4.1 Cone Penetration

4.1.1 Apparatus Description

The cone penetration testing was designed around the procedure and equipment specified in both the British (British Standards Institution (BSI), 1990) and Swedish (Swedish Geotechnical Society, 1992) standards as well as the procedure and methods presented by Likos and Jaafar (2014). The procedure and methods were modified to accommodate the experimental program specified in Section 4.1.2.

The cone penetration device was constructed using common geotechnical testing equipment and several select pieces of additional equipment. Specifically, 4” and 6” proctor compaction molds with the collar extensions, 4” and 6” extrusion plates, an Omega Model LD610 ± 100 mm stroke length linear variable differential transformer (LVDT), a 40 cm adjustable vertical stand with 0.1 mm fine adjustment, 30º and 60º apex angle fall cones with machined brass LDVT connectors, a balance sensitive to 0.01 g and a computer with National Institute’s Labview software to record the LVDT output.

The 30º and 60º apex angle fall cones were the British and Swedish standard fall cones respectively. The fall cones were removed from the plunger heads (Figure 4.1). The fall cones were then connected to brass adapters to facilitate connection to the LVDT rod (Figure 4.2). The LVDT was used to measure the displacement of the cone with time during penetration. First the zero point on the LVDT was determined and marked with a piece of tape, which prevented the rod from retreating further into the LVDT than the zero point. The LVDT was then attached to the adjustable vertical stand. The adjustable vertical stand allowed the LVDT to be raised and lowered based on the fall height for the test being conducted. The vertical stand had a range of

40 cm and was adjustable by 0.1 mm. The LVDT and stand were placed on an elevated platform that allowed full motion of the LVDT rod and for the fall cone to fall into the center of the 4” and 6” proctor molds.

The 4" and 6" proctor molds were those specified in ASTM D698. The extensions were left on the proctor molds for several reasons. The extensions facilitated the filling of the proctor molds and compaction for the high relative density cases, and allowed the material to move vertically when the cone penetrated without mass spilling out of the molds.

Figure 4.1 Fall cones without plungers

Figure 4.2 Fall cones with LVDT connectors

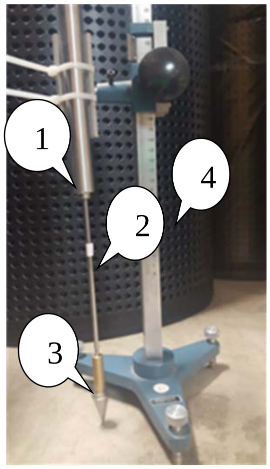

Figure 4.3 View of assembled apparatus 1. LVDT, 2. Zero Mark, 3. Fall cone and Adapter, 4. Adjustable Vertical Stand

Figure 4.4 Apparatus on elevated platform; sample prior to final lift of material

Table 4-1 Fall cone properties (Cone Height C_h and Width W defined in Figure 4.5)

Property	30 Degree Fall Cone	60 Degree Fall Cone
Cone Height, C_h (mm)	34.36	22.10
Width, W (mm)	9.21	19.86
Mass when attached to LVDT (g)	141.1	135.7
Young's Modulus (GPa)	193	193
Poisson's Ratio	0.3-0.31	0.3-0.31

4.1.2 Experimental Program

The experimental program for the fall cone penetration testing included both the glass beads and the sand prepared to two different relative densities using Equation 3-4. The density of the material was selected to achieve a relative density of 10% or less and 90% or greater using Equation 3-4. The samples were then subject to fall cone penetration testing using the 30° and 60° fall cones from varying heights normalized by the cone height. Figure 4.5 illustrates the relationship between cone height (C_h) and the drop height. For example, the 30° fall cone has a cone height, C_h, of 34.39 mm. The drop heights used are $0.0C_h$, $0.5C_h$, and $1.0C_h$, therefore, the drop heights for the 30° fall cone are 0.0 mm, 17.2 mm, and 34.4 mm respectively. Table 4-2 summarizes the complete fall cone penetration testing matrix.

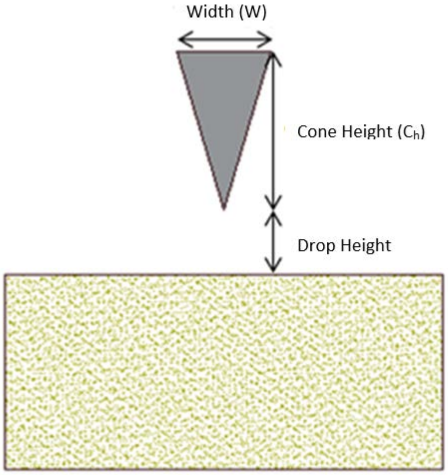

Figure 4.5 Relationship bewtween cone height and drop height

Table 4-2 Summary of cone penetration testing program

Material	Container	Cone Type	Relative Density	Fall Cone Drop Height
Glass Beads	4” Standard Proctor (944 ml)	30° Apex Angle	Relative Density < 10%	0.0 Cone Height 0.5 Cone Height 1.0 Cone Height
Ottawa Sand	6” Standard Proctor (2124 ml)	60º Apex Angle	Relative Density > 90%	

4.1.3 Procedure

The following procedure was used for each series of tests. The procedure was only modified slightly to achieve the desired change in the testing program (change in fall height, relative density, etc.). Prior to testing, bulk samples of the materials were allowed to air dry. Tests procedures were as follows:

1. Determine mass of sample needed to fill container at the target relative density.
2. Pour sample into container.
    a. For the low relative density case, the material is placed in accordance with ASTM D4254.
    b. For the high relative density case, the material is placed in lifts. After each lift, an extrusion plate is placed onto the material. The center of the extrusion plate is then hit with a standard proctor hammer ten times. This is repeated for a total of four lifts.
3. The cone is then lowered to the surface of the material to determine the zero elevation.
    a. For a fall height of 0.0 the LVDT stand is lowered to the zero mark on the LVDT rod without moving the cone.

   b. For a fall height of 0.5 the LVDT stand is lowered to the zero mark on the LVDT rod without moving the cone. The LVDT stand is then raised by the fall height. Then the cone is raised until the LVDT rod is at the zero mark.
   c. For a fall height of 1.0 the LVDT stand is lowered to the zero mark on the LVDT rod without moving the cone. The LVDT stand is then raised by the fall height. Then the cone is raised until the LVDT rod is at the zero mark
4. The recording software is activated.
5. The cone and LVDT rod is released allowing the cone to fall into the material until movement stops.

The following is a detailed description of the procedure above and how it was used when glass beads were placed in the 4" proctor, compacted to a high relative density, and subjected to penetration from the 30° fall cone from a drop height of 1.0.

1. Mass of glass beads needed to fill the 4" proctor is calculated using the maximum density.
2. Approximately 1/4 of the mass is poured into the proctor.
3. Material is covered with an extrusion plate and hit with a standard proctor hammer 10 times.
4. Steps 2 and 3 are repeated 3 times.
5. The cone and LVDT rod are then lowered to just touch the surface of the material.
6. The LVDT stand is lowered until the zero mark on the rod is reached.
7. The LVDT stand is raised by the drop height.
8. The cone and LVDT rod are then raised until the zero mark on the rod reaches the LVDT.
9. The recording software is then activated.

10. The cone and LVDT rod are released, allowing the cone to free fall into the material.
11. Steps 1-10 are repeated 2 more times.

4.2 Particle-Scale Direct Shear Testing

4.2.1 Apparatus Description

The direct shear apparatus was designed to perform in a similar manner as traditional direct shear apparatus, with a shear box divided into a moving and fixed portion, and a device to measure the shear force applied. The custom direct shear device used a shear box with reduced third dimension, allowing for a single plane of glass beads to be examined. However, the traditional design does not allow for the shear plane to be viewed as the sample was sheared. The side of the shear box was created clear acrylic viewing planes. The viewing planes were positioned at the manufacturer's maximum diameter tolerance for the glass beads used. The viewing planes could be removed for sample preparation, but could be fixed in place for testing. The viewing planes allowed for the entirety of the shear plane to be viewed during direct shearing of the glass beads. The viewing plane also allowed for the particles to be imaged and tracked using GeoPIV. GeoPIV was used to identify the particle-scale response during shearing. The shear device was not used in the vertical position, but at different horizontal inclinations. The material self-weight and additional acetal blocks were used to apply the normal force to the sample. The back surface of the shear box was constructed of transparent acrylic and the protective covering was left on the back. When a light was applied to the back to identify the glass beads, the protective covering dispersed the light removing a bright spot from the light. Figure 4.6 shows the constructed direct shear device prior to installation of the viewing plane, and Figure 4.7 presents a zoomed in image of the shear box with the viewing planes installed.

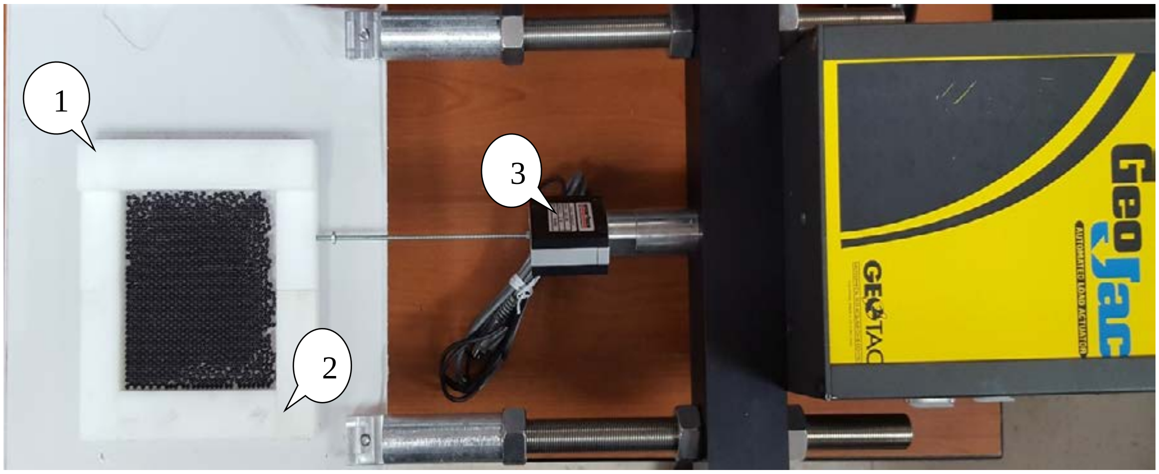

Figure 4.6 Assembled direct shear apparatus prior to viewing panel installation 1. Sliding portion of shear box, 2. Fixed portion of shear box, 3. Load cell

The direct shear device consisted of several parts that were individually constructed and then assembled with other common geotechnical testing equipment. The apparatus consisted of the fixed portion of the direct shear box, the sliding portion of the direct shear box, a load cell to measure the force necessary to move the sliding portion of the direct shear box, a stepper controlled motor frame to control the shear displacement rate, and the back plate to which the fixed portion of the shear box was mounted and provided the connection to the stepped control motor frame. Schematic drawings of the apparatus can be found in Appendix C.

The parts of the apparatus that were not constructed consisted of a stepper controlled motor frame and a load cell. The stepper controlled motor frame used was a GeoTAC GeoJac with the GeoTAC Sigma-1 loading software. The load cell used was an Interface ULC Ultra Low Capacity Load Cell model ULC-2N with a capacity of 2 N. A FUJIFILM FinePix HS25 EXR was used to capture the images of the materials undergoing shearing. The camera has a resolution of 16MP and a continuous shooting ability of 3 pictures per second initially with a steady rate of 1 picture per second. The camera was set up on a 57” pro series aluminum camera tripod for FUJIFILM cameras. The angle of the shear apparatus was controlled using a Silk Mini

II table-top tripod. The apparatus was placed onto the tripod and the height was adjusted until the desired level was reached. The angle was measured using a Husky 10” multi-function standard digital level accurate to 0.1°.

The first pieces assembled were the back plate and fixed portion of the shear box. The back plate was cut from a 0.220” thick sheet of abrasion resistant transparent acrylic and the protective covering was left on both sides. The protective covering was carefully removed from location of the shear box’s fixed portion. The fixed portions pieces were cut from 1” square acetal rod. The surface of the back plate and surface of the fixed portion were scored with a utility knife to create a better bond with the epoxy. The remaining protective covering was then removed from the top side. Two connectors were machined to connect the back plate to the GeoJac frame using the provided machine rods.

The sliding portion of the shear box was constructed using the 1” acetal rod. The surfaces where the rods were joined were first sanded and then carefully scored with a utility knife. The surfaces were then bonded together with the epoxy. A port was drilled into the side of the sliding portion of the shear box and tapped to allow a #4-40 rod to screw into it and connect to the load cell.

Initial testing showed that the material would jump out of plane. It was critical that the materials remained in plane. Two viewing planes were cut from the same material as the back plate. The shear box was machined to allow the viewing planes to rest within the shear box and provide a ceiling that was 3.30 mm from the surface of the back plate. The sliding portion of the shear box had two set screws installed to lock the viewing plane in place.

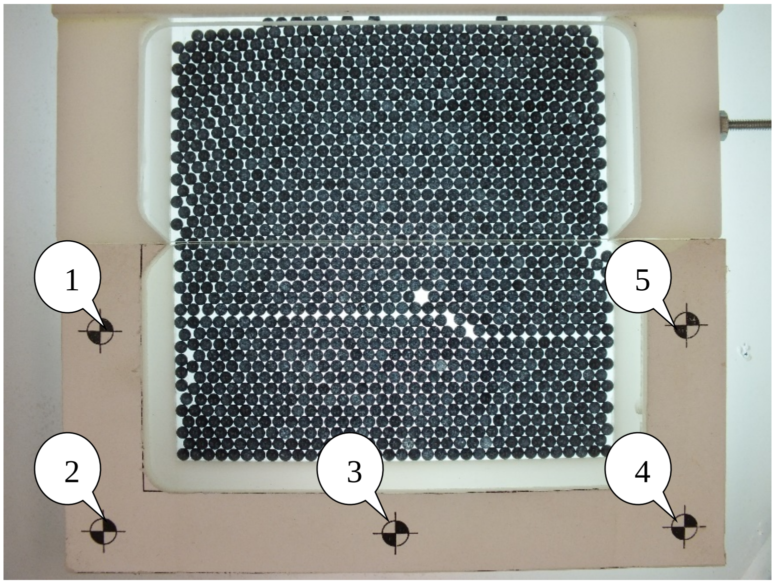

Figure 4.7 Control point locations

After the completion of the testing series, the movement of the particles would be determined using GeoPIV. The GeoPIV analysis would present the movement of the particle in image space (pixels). A subroutine in GeoPIV-RG would be used to convert the image space movements (pixels) to real space movements (mm). To do so, GeoPIV-RG relied on several control points with known real space (mm) locations known. Figure 4.7 shows the control point numbering, and Table 4-3 lists the control point locations in real space. The origin used in the testing was located at control point 2

Table 4-3 Control Point Real Space locations

Control Point Number	Horizontal Location (mm)	Vertical Location (mm)
1	0.0	53.37
2	0.0	0.0
3	66.68	0
4	133.49	0
5	133.49	47.07

4.2.2 Experimental Program

The experimental program for the fall cone penetration testing included both the glass beads and the sand prepared to two different density states. The sand density was determined based on reaching a relative density of 10% or less and 90% or greater using Equation 3-4. The glass bead density was determined based on reaching an area ratio of 0.72 or less and 0.79 or greater using Equation 4-1. The samples were then subjected to direct shear testing using 0.5 mm/min and 1.0 mm/min shear rates with varying normal forces. The normal forces were applied to the shear zone by inclining the direct shear apparatus and using the materials self-weight for the first inclination. For the subsequent inclinations, additional mass was applied to the top of the sample using sections cut from the 1" square acetal rods. Table 4-4 summarizes the complete direct shear testing matrix.

$$A_r = \frac{A_{sphere}}{A_{box}} \qquad \textbf{4-1}$$

where

A_r = Area Ratio

A_{sphere}= Area of spheres from image analysis

A_{box} = Area of shear box

Table 4-4 Summary of direct shear testing program

Material	Shear Rate	Shear Zone Moisture	Inclination	Density State	Additional Mass
Glass Beads	0.5 mm/min	Dry	18°	Relative Density < 10% Area Ratio < 0.72	No mass
					8.01 g
			24°		66.64 g (dry 0.5 mm/min)
Ottawa Sand	1.0 mm/min	600 µL		Relative Density > 90% Area Ratio > 0.80	53.64 (dry 1.0 mm/min)
			30°		67.19 g (wet)

4.2.3 Procedure

Prior to testing, a bulk sample of glass beads was washed with soap and water to remove any residue from previous handling and allowed to dry in an oven at 60 °C to a constant mass. A bulk sample of the sand was allowed to air dry prior to testing. These bulk samples provided the samples used in the testing program. Prior to performing the wet series of direct shear tests, 1 L of distilled water was dyed. The water was dyed using 400 μL of 20% rhodamine and water solution. The dyed water was to allow visual indication of the pore water during shearing. The following procedures were used for the glass beads and sand samples respectively. The procedures were only modified slightly to achieve the desired change in the testing program, i.e. a change in relative density, additional mass added, moisture added to the shear zone, etc.

Glass Bead Procedure

1. The direct shear device was lifted from horizontal to an incline where the rod connecting the back plate and the GeoJac could be placed in a recess on the back of the table top tripod camera support plate.
2. The tripod height was adjusted until the apparatus reached the desired inclination. The apparatus inclination was confirmed using the electronic level.
3. For wet tests, prior to the glass beads being added to the shear box, Rain-X ® was applied to the areas of the shear box where the glass beads to would come in contact with to create hydrophobic surfaces. The Rain-X ® was added to ensure the when the water was added to the shear tests, it would preferentially adsorb to the glass beads and not the shear box or viewing plane surfaces.
4. The glass beads were added to the shear box.
    a. For the low area ratio case, the glass beads were poured into the top shear box with the viewing planes in place until the glass beads were just below the edge of

    the top viewing plane. The open slot on the top of the shear box was covered and the bottom of the shear apparatus was lifted until the apparatus was horizontal. This allowed the glass beads to roll around and loosen. The apparatus was carefully lowered so as not to impart any more energy than that from the glass beads settling on their own into the system.

    b. For the high area ratio case, the glass beads were poured into the top of the shear box. The beads were agitated using a small wire to ensure the beads fell into a tight packing. This continued until the beads were even with the edge of the top viewing plane.

5. The inclination of the shear apparatus was checked again to ensure the apparatus was at the correct angle.
6. The required additional mass was added for the specific test being ran.
7. For tests with moisture, the moving portion of the shear box was carefully sild up along the back plate to create a gap large enough for a precision pipette to distribute 600 μL of dyed water along the shear zone. The moving portion was then carefully lowered back into place.
8. The motor control software was then configured for the test parameters and the initial position and load cell were zeroed.
9. The camera was then moved into place on a tripod in front of the apparatus, zooming in to capture the control points and the sample. The camera was set on rapid picture capture (capturing one image every second) and the focus was locked in position.
10. The motor control software was activated and the remote camera control was activated.

Sand Procedure

1. The direct shear device was lifted from horizontal to an incline where the rod connecting the back plate and the GeoJac could be placed in a recess on the back of the table top tripod camera support plate.
2. The tripod height was adjusted until the apparatus reached the desired inclination. The apparatus inclination was confirmed using the electronic level.
3. For wet tests, prior to the sand being added to the shear box, Rain-X ® was applied to the areas of the shear box that would contact the sand to create hydrophobic surfaces. The Rain-X ® was added to ensure the when the water was added to the shear tests, it would preferentially adsorb to the sand and not the shear box or viewing plane surfaces.
4. The sand was then added to the shear box.
    a. For the low relative density case, the shear apparatus was carefully lifted off the support tripod and lowered to the horizontal. The viewing planes were removed. The mass of sand calculated to meet the low relative density case was then added to the shear device using the method prescribed in ASTM D4254. The viewing planes were carefully added back to the shear apparatus. The apparatus was then carefully and slowly lifted back onto the support tripod so as not to impart any more energy than that from the sand settling on its own into the system.
    b. For the high relative density case, the mass of sand needed was poured into the top of the shear box. The shear apparatus was tapped on the edge to facilitate the sand densifying.
5. The inclination of the shear apparatus was checked again to ensure the apparatus was at the correct angle.

6. The required additional mass was added for the specific test being ran.
7. For tests with moisture, the shear device was carefully lifted off the support tripod and lowered to the horizontal position. The viewing panel was then carefully removed. A precision pipette was used to distribute 600 μL of dyed water along the shear zone. The viewing panels were carefully replaced. The direct shear apparatus was then carefully raised back up and lowered onto the support tripod.
8. The motor control software was then configured for the test parameters and the initial position and load cell were zeroed.
9. The camera was then moved into place on a tripod in front of the apparatus, zooming in to capture the control points and the sample. The camera was set on rapid picture capture (capturing one image every second) and the focus was locked in position.
10. The motor control software was activated and the remote camera control was activated.

5 Results

5.1 Cone Penetration Testing

The following sections present the results from the fall cone penetration testing series using dry glass beads and sands. The results are presented in graphical form showing displacement of the fall cone as a function of time since cone release. Each graph contains two to three boxes with information about the specific test results. The top-most box describes the parameters of the test, including the apex angle of the fall cone used (30° or 60°), the mass of the fall cone (141.4 g or 135.7 g), the height of the fall cone (C_h), the relative density (D_r) of the test material, and the drop height (D_h) of the cone. The second box specifies the maximum displacement (penetration) of the fall cone for each of up to three test trials. Some graphs include a third box below the legend. This box notes where the complete displacement trend was not recorded, but the ultimate displacement was recorded. The abbreviations used in each graph are as follows:

D_r = Relative Density

D_h =Drop Height

C_h = Cone Height

The results are separated into two sections. The first section presents the penetration trends for the glass beads, and the second section presents the penetration trends for the Ottawa sand. The sections are further divided to present the data for the 30 degree fall cone and 60 degree fall cone separately.

5.1.1 Glass Beads

30 Degree Fall Cone

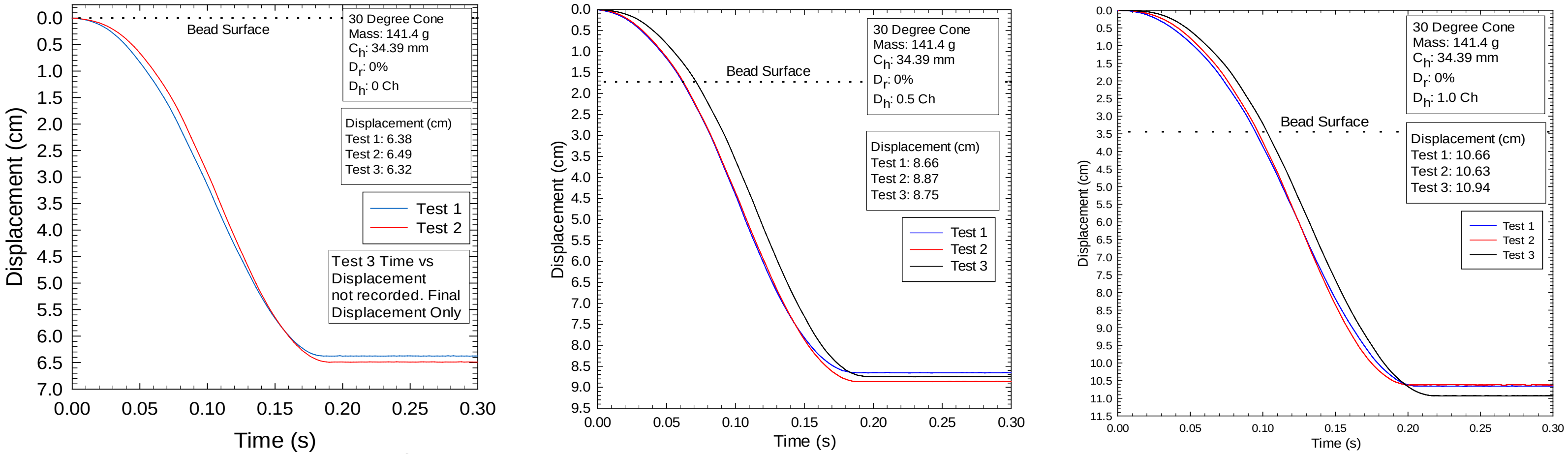
(a) (b) (c)

Figure 5.1 Cone penetration trends for low relative density in a 4" proctor: (a) 0.0 Drop height; (b) 0.5 Drop height; (c) 1.0 Drop height

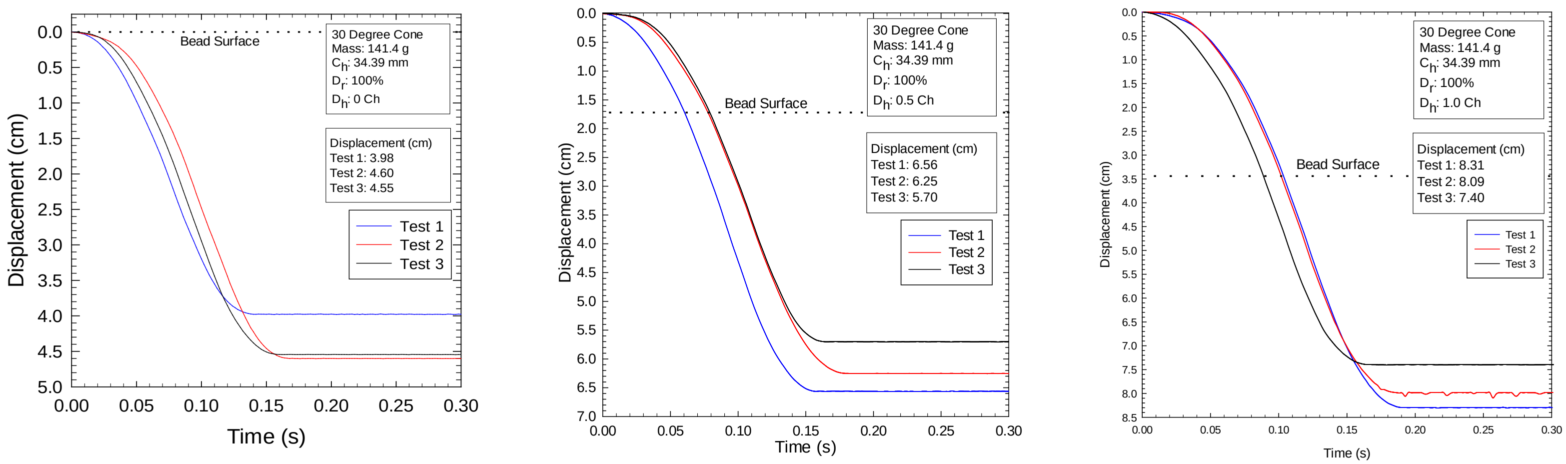
(a) (b) (c)

Figure 5.2 Cone penetration trends for high relative density in a 4" proctor: (a) 0.0 Drop height; (b) 0.5 Drop height; (c) 1.0 Drop height

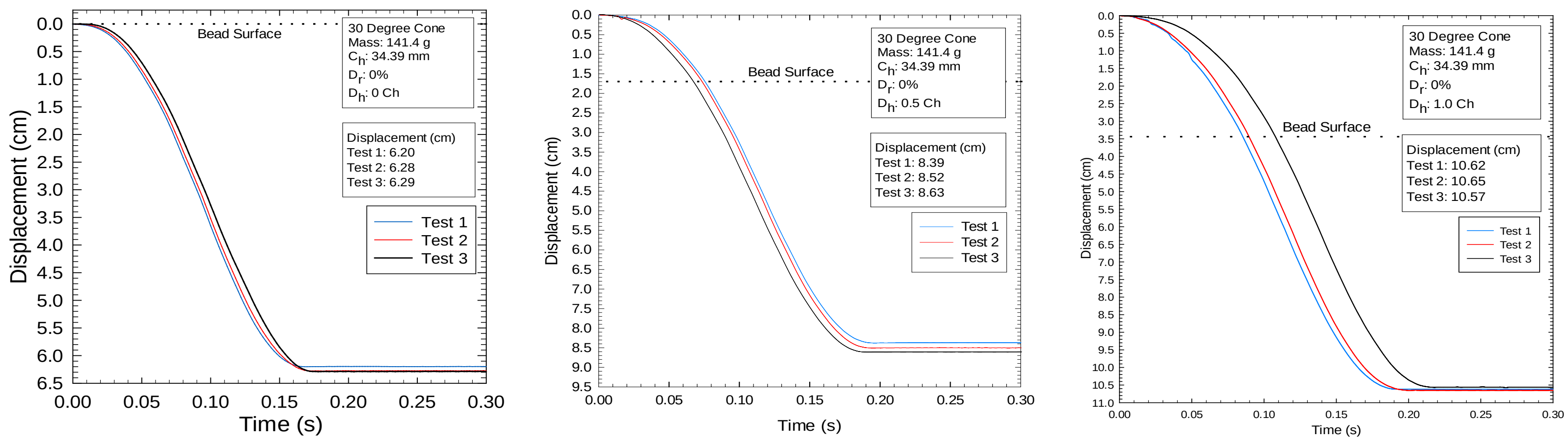
(a) (b) (c)

Figure 5.3 Cone penetration trends for low relative density in a 6" proctor: (a) 0.0 Drop height; (b) 0.5 Drop height; (c) 1.0 Drop height

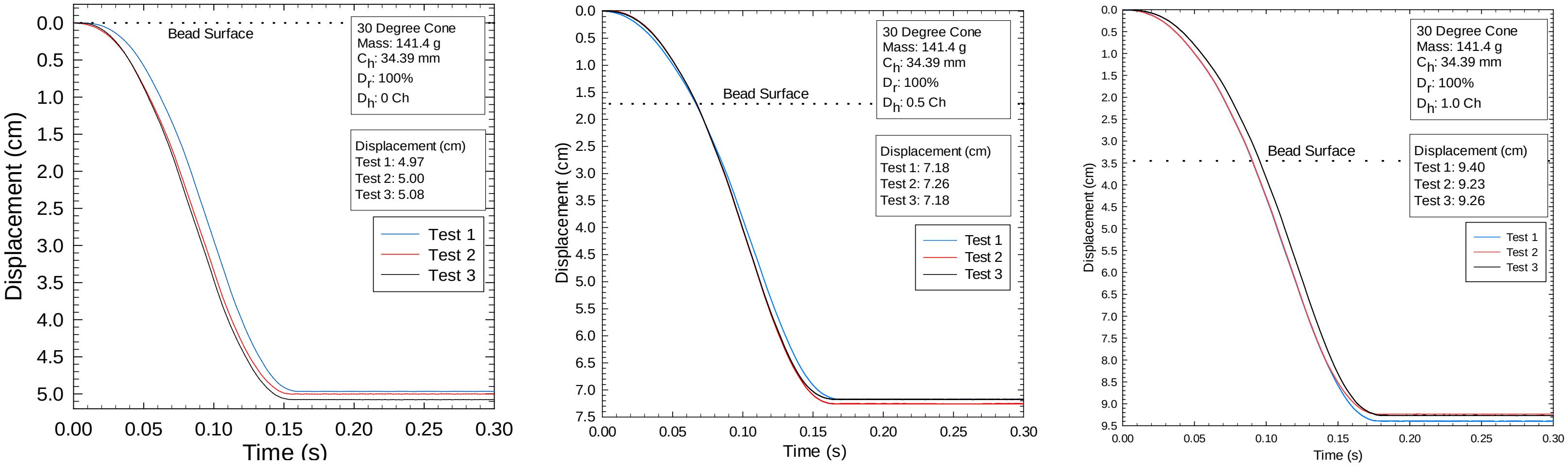
(a) (b) (c)

Figure 5.4 Cone penetration trends for high relative density in a 6" proctor: (a) 0.0 Drop height; (b) 0.5 Drop height; (c) 1.0 Drop height

60 Degree Fall Cone

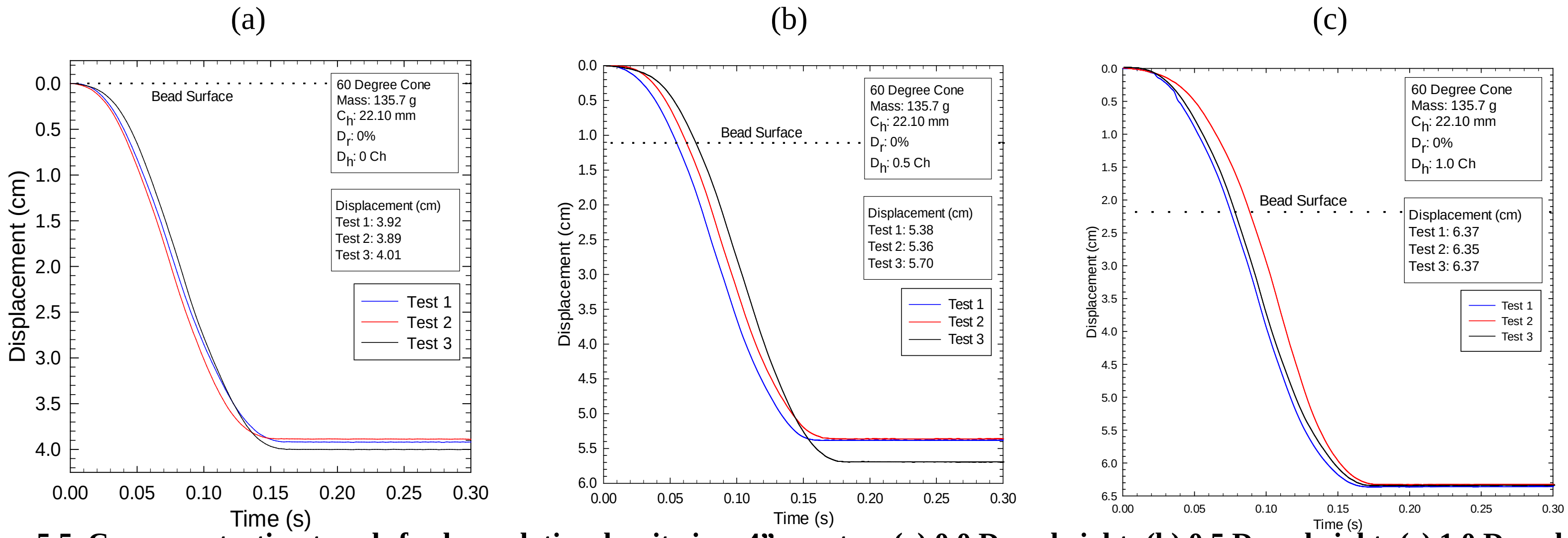
(a) (b) (c)

Figure 5.5 Cone penetration trends for low relative density in a 4” proctor: (a) 0.0 Drop height; (b) 0.5 Drop height; (c) 1.0 Drop height

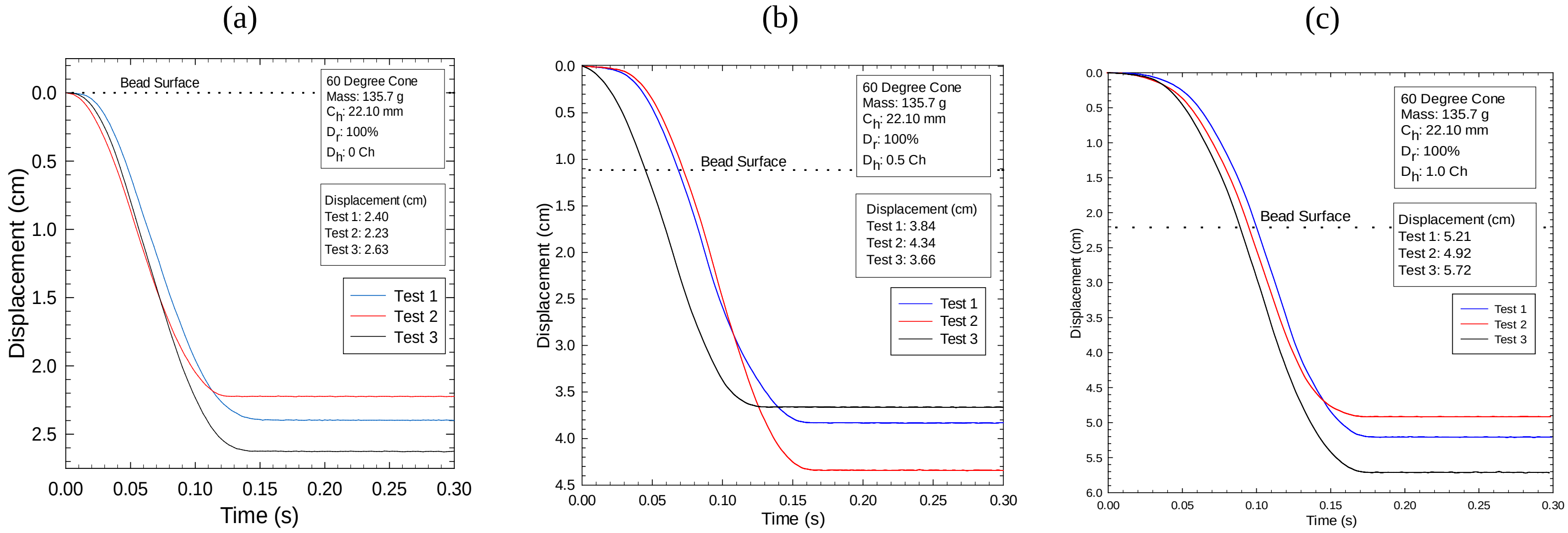
(a) (b) (c)

Figure 5.6 Cone penetration trends for high relative density in a 4” proctor: (a) 0.0 Drop height; (b) 0.5 Drop height; (c) 1.0 Drop height

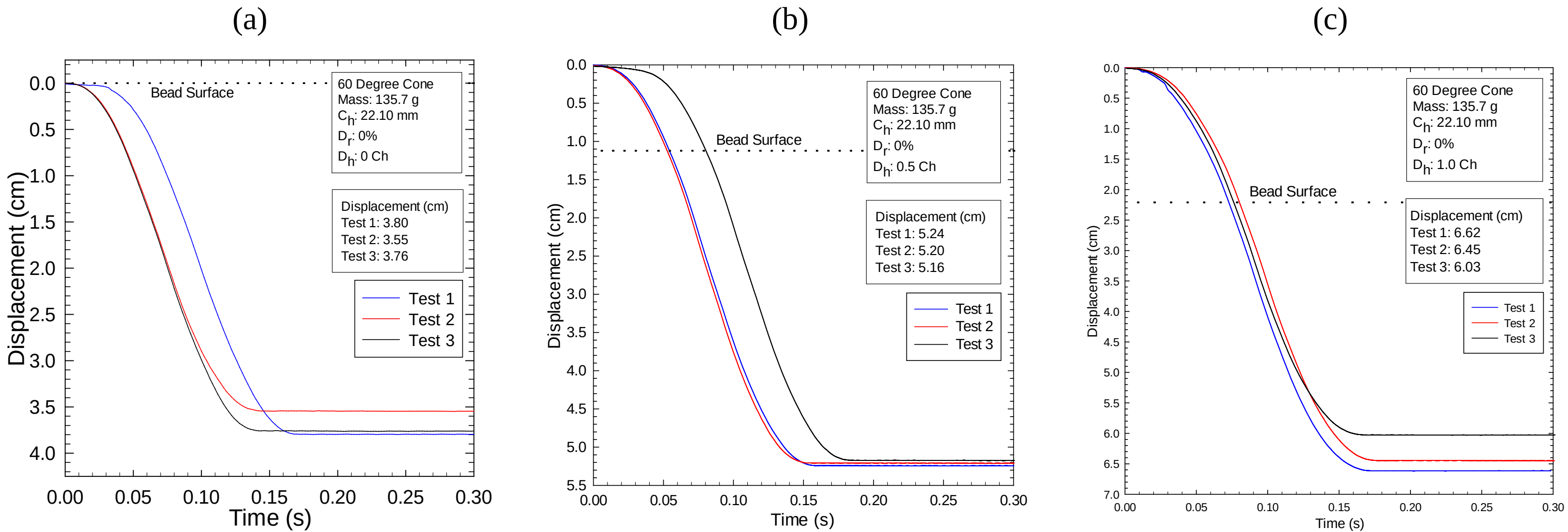

Figure 5.7 Cone penetration trends for low relative density in a 6" proctor: (a) 0.0 Drop height; (b) 0.5 Drop height; (c) 1.0 Drop height

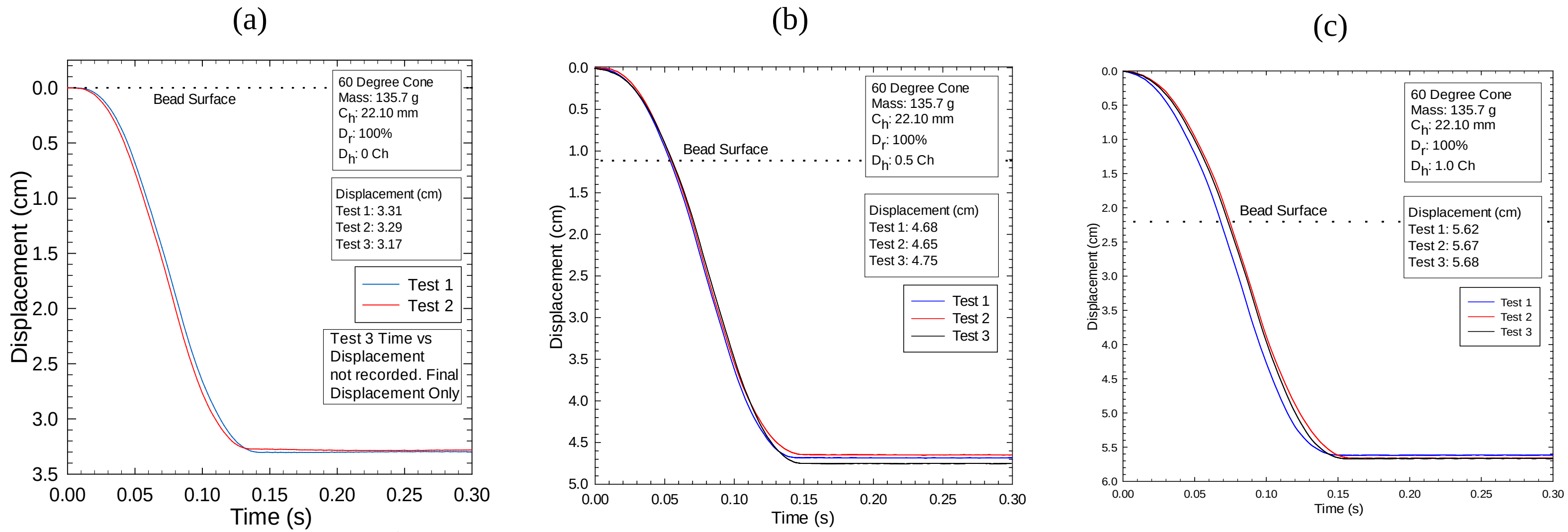

Figure 5.8 Cone penetration trends for high relative density in a 6" proctor: (a) 0.0 Drop height; (b) 0.5 Drop height; (c) 1.0 Drop height

5.1.2 Sand

30 Degree Fall Cone

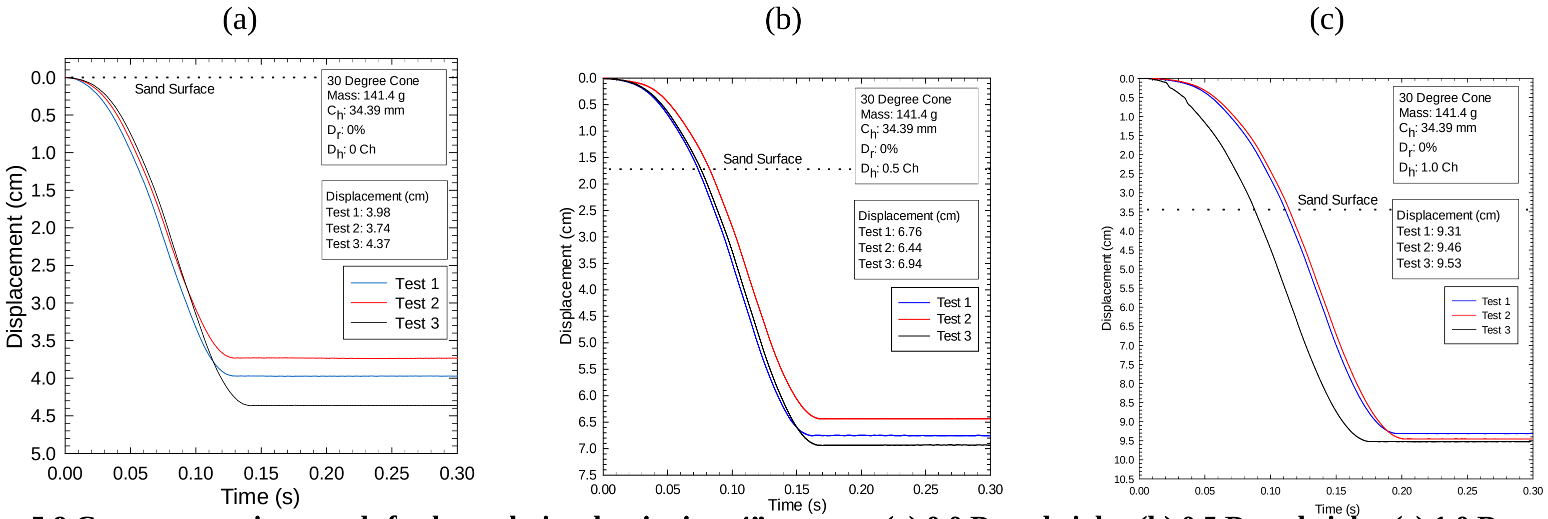

Figure 5.9 Cone penetration trends for low relative density in a 4” proctor: (a) 0.0 Drop height; (b) 0.5 Drop height; (c) 1.0 Drop height

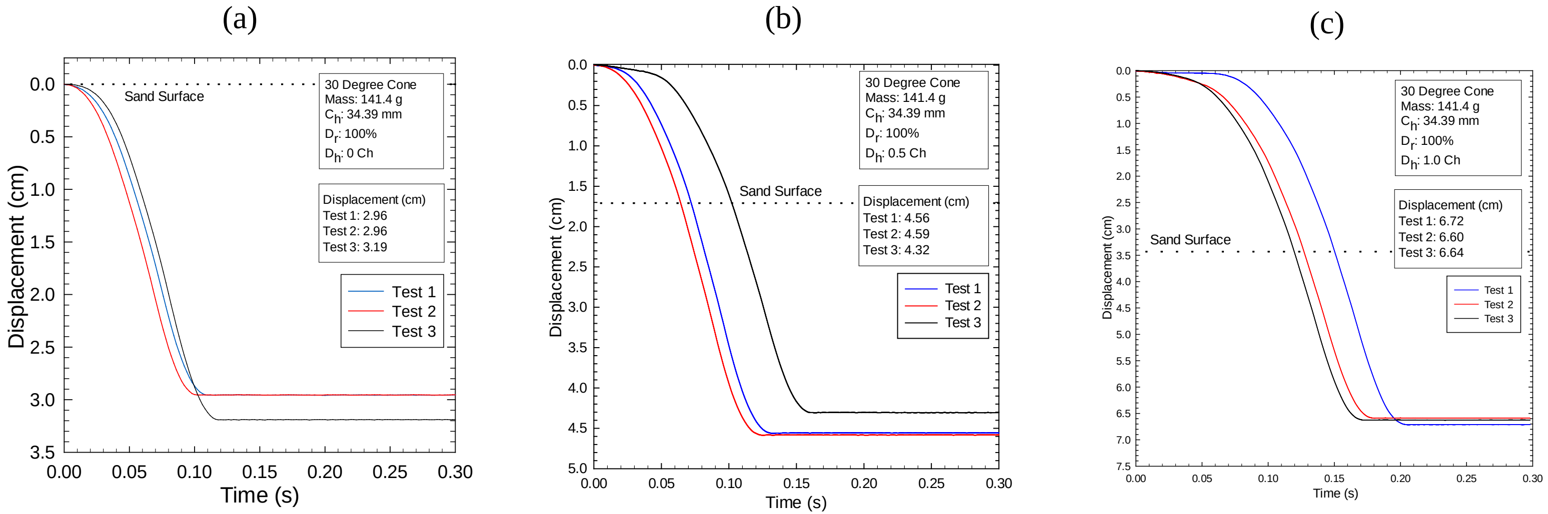

Figure 5.10 Cone penetration trends for high relative density in a 4” proctor: (a) 0.0 Drop height; (b) 0.5 Drop height; (c) 1.0 Drop height

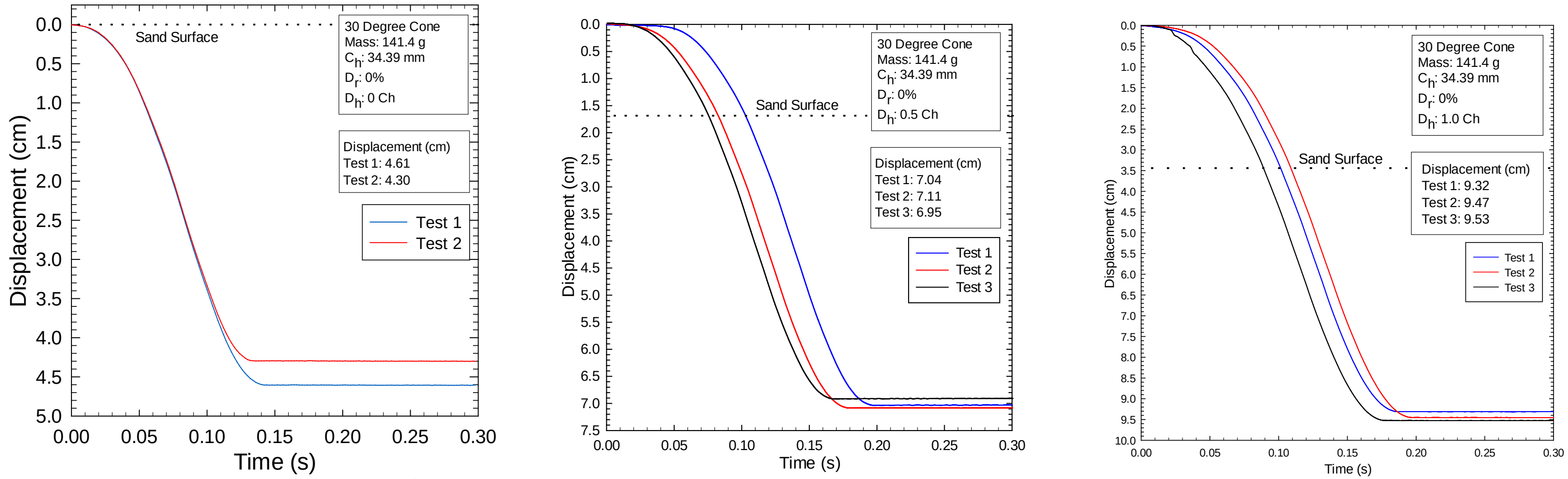

(a) (b) (c)

Figure 5.11 Cone penetration trends for low relative density in a 6" proctor: (a) 0.0 Drop height; (b) 0.5 Drop height; (c) 1.0 Drop height

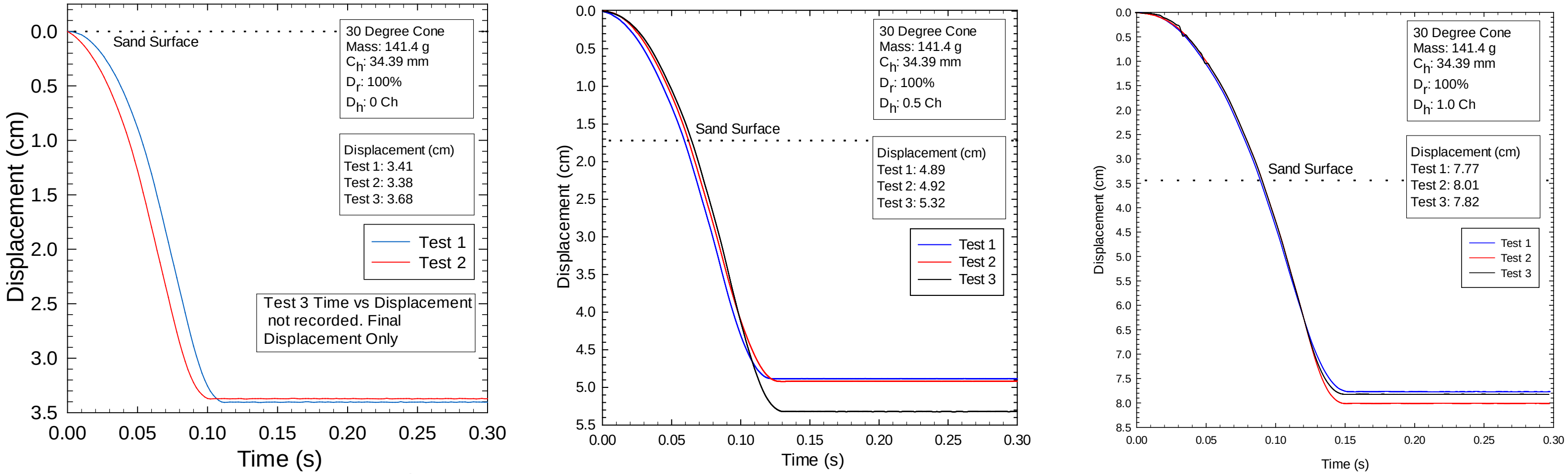

(a) (b) (c)

Figure 5.12 Cone penetration trends for high relative density in a 6" proctor: (a) 0.0 Drop height; (b) 0.5 Drop height; (c) 1.0 Drop height

60 Degree Fall Cone

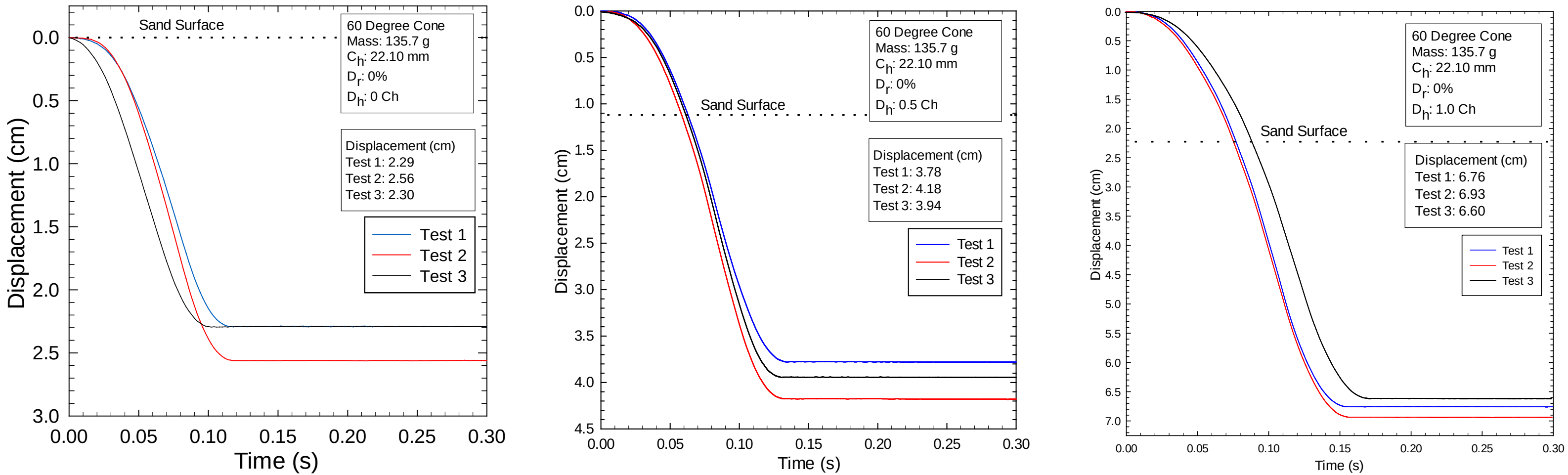

(a) (b) (c)

Figure 5.13 Cone penetration trends for low relative density in a 4" proctor: (a) 0.0 Drop height; (b) 0.5 Drop height; (c) 1.0 Drop height

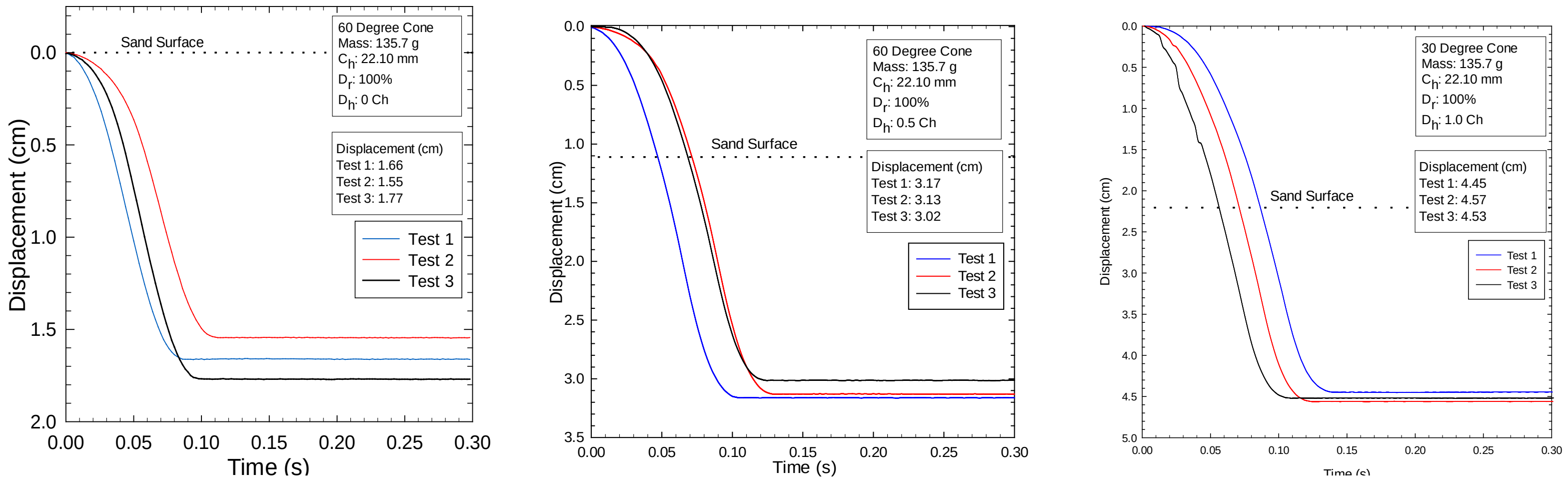

(a) (b) (c)

Figure 5.14 Cone penetration trends for high relative density in a 4" proctor: (a) 0.0 Drop height; (b) 0.5 Drop height; (c) 1.0 Drop height

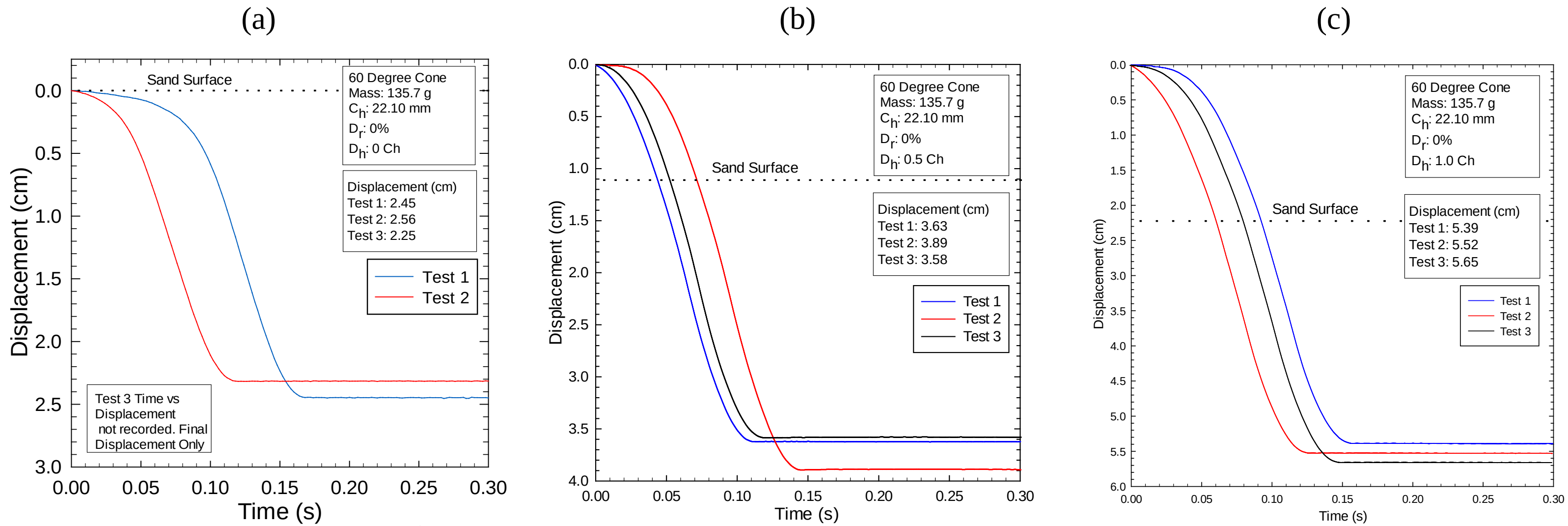
(a) (b) (c)

Figure 5.15 Cone penetration trends for low relative density in a 6” proctor: (a) 0.0 Drop height; (b) 0.5 Drop height; (c) 1.0 Drop height

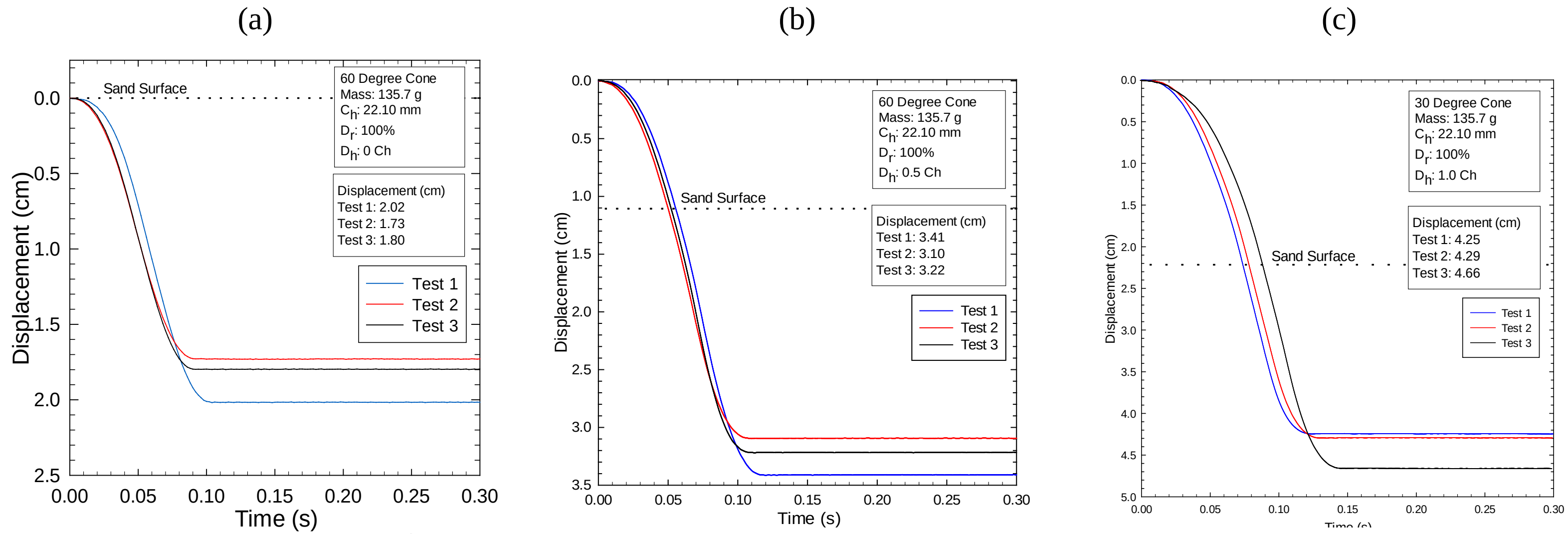
(a) (b) (c)

Figure 5.16 Cone penetration trends for high relative density in a 6” proctor: (a) 0.0 Drop height; (b) 0.5 Drop height; (c) 1.0 Drop height

5.2 Dry Direct Shear Testing

The following pages present select results from the dry direct shear testing series. The remainder of the results can be found in Appendix D and Appendix E. The results are presented in three graphs for each test. The graphs present the macroscopic shear response (shear force-displacement relationship), PIV results indicating tracking of particle- or particle patch displacements from the beginning of the shear test to the end of the shear test in image space (in terms of pixels) and in real space (vertical and horizontal location in mm). The plots of macroscopic shear response of the samples include a summary of the test parameters including: shear displacement rate (mm/min), particle packing density defined in terms of area ratio (A_r = total area of glass beads divided by the area of the shear box), the inclination angle of the shear device (degrees), the magnitude of any additional mass added to increase the normal force on the shear surface, and the total normal force acting on the shear surface. For results with glass beads, two additional descriptors include the total number of particles and the number of shear particles. The number of shear particles is the number of glass beads initially located above the split between the two portions of the direct shear box. Coordinates used to define real space are defined with respect to an origin (0,0) located at the bottom left control point (2) that is shown in the image space location image (see Figure 5.17a). The abbreviations used in each graph are as follows: D_r = Relative Density, and A_r =Area Ratio.

Results are presented in two subsequent sections. The first section presents a sample of the macroscopic and particle-scale response during direct shearing for one of the glass bead tests. The second section presents a sample of the macroscopic and particle-scale response during direct shearing for one of the sand tests. The GeoPIV analysis used to determine the particle-scale response of the materials is discussed in 6.2.1 below.

5.2.1 Glass Beads

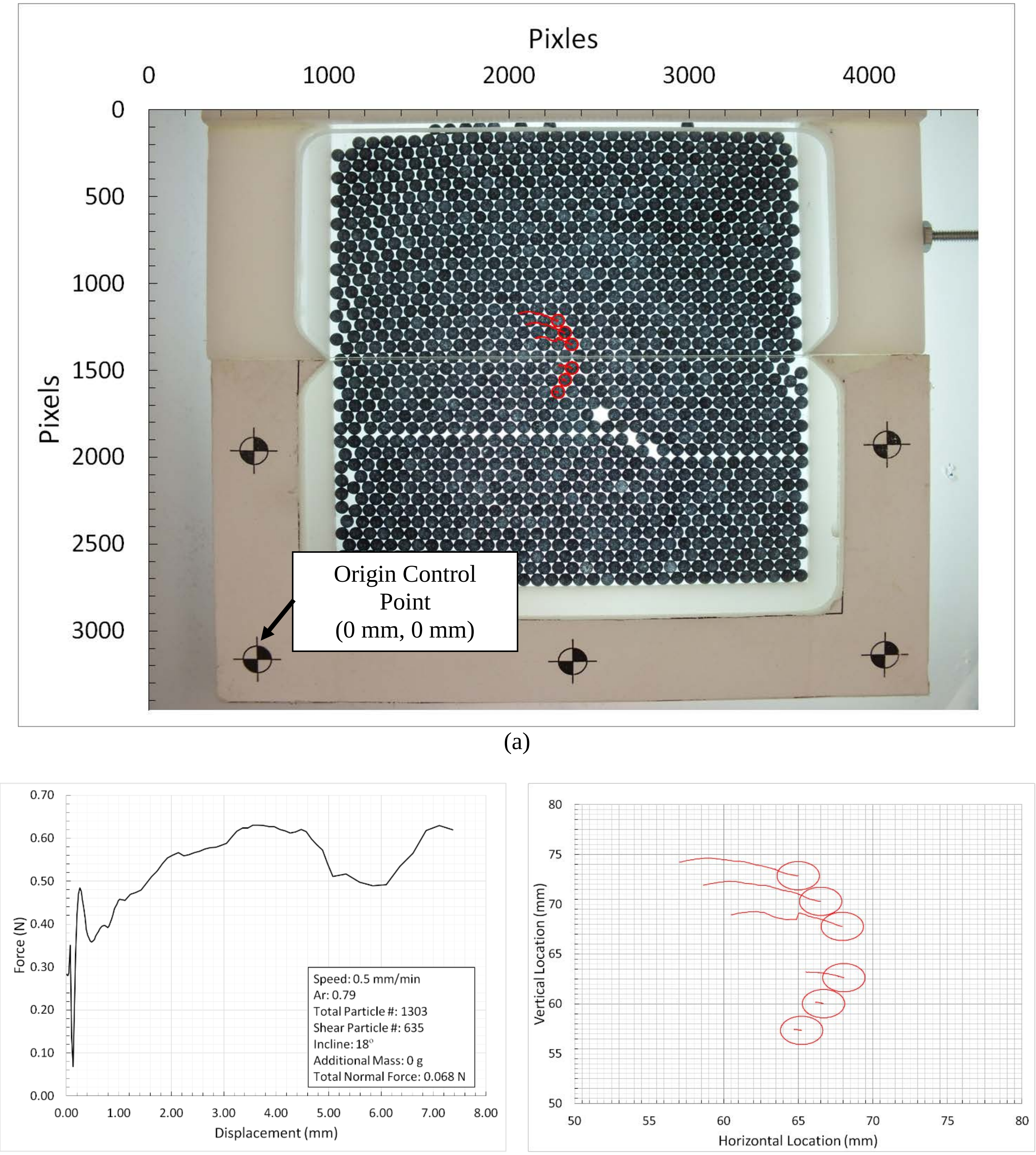

(a)

(b)

(c)

Figure 5.17 Glass bead results for 0.5 mm/min, dense state, 18° incline: (a) Image space movements, (b) Shear response, (c) Real space movements

5.2.2 Sand

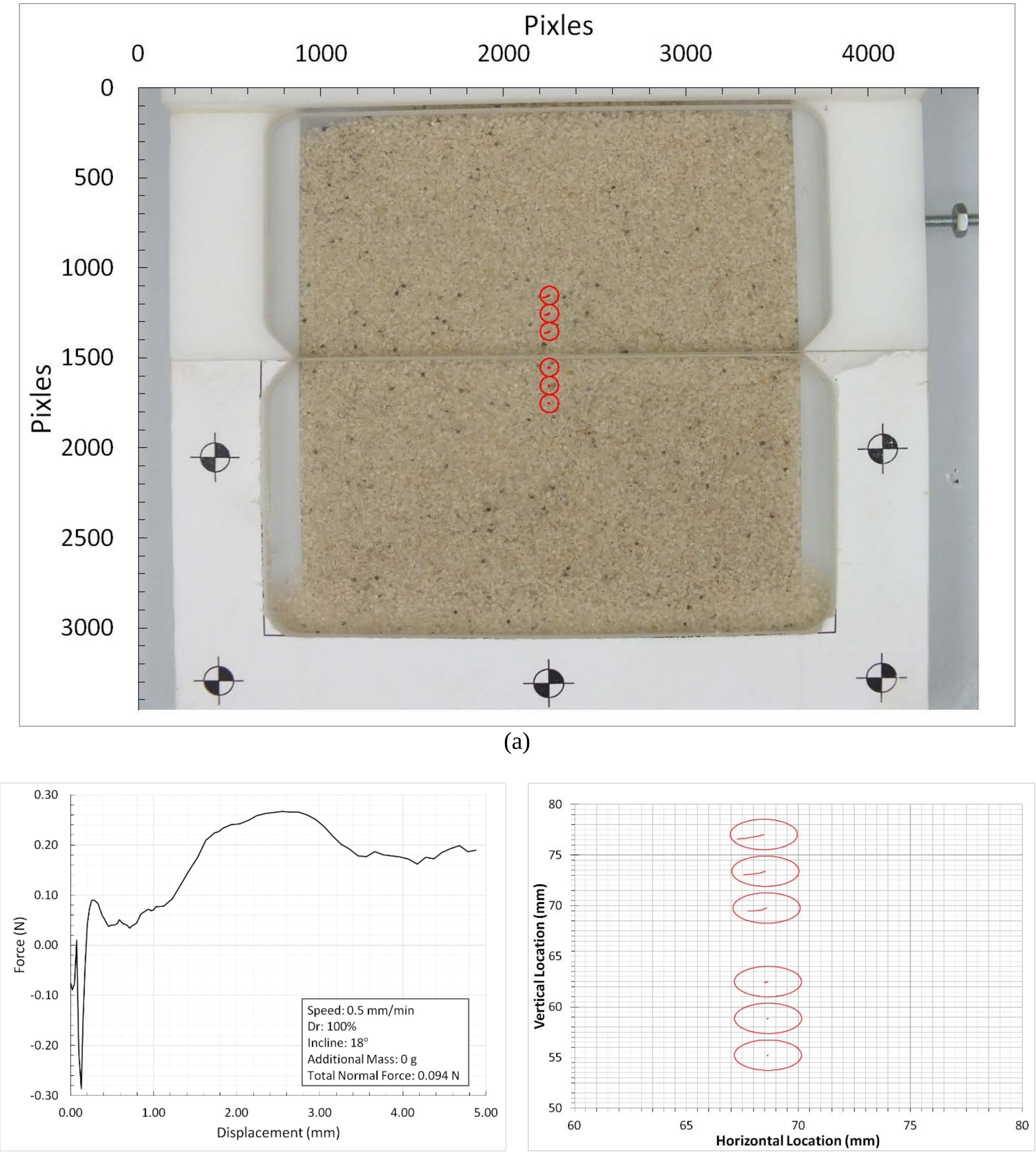

(a)

(b) (c)

Figure 5.18 Sand results for 0.5 mm/min, dense state, 18° incline:
(a) Image space movements, (b) Shear response, (c) Real space movements

5.3 Wet Direct Shear Testing

The following pages present select results from the wet direct shear testing series. The wet direct shear tests were performed with 600μL of dyed water injected into the shear zone, which can be seen as a purple/red color around the glass beads and sand particles The remainder of the results can be found in Appendix F and Appendix G. The results are presented in three graphs for each test. The graphs present the macroscopic shear response (shear force-displacement relationship), PIV results indicating tracking of particle- or particle patch displacements from the beginning of the shear test to the end of the shear test in image space (in terms of pixels) and in real space (vertical and horizontal location in mm). The plots of macroscopic shear response of the samples include a summary of the test parameters including: shear displacement rate (mm/min), particle packing density defined in terms of area ratio (A_r = total area of glass beads divided by the area of the shear box), the inclination angle of the shear device (degrees), the magnitude of any additional mass added to increase the normal force on the shear surface, and the total normal force acting on the shear surface. For results with glass beads, two additional descriptors include the total number of particles and the number of shear particles. The number of shear particles is the number of glass beads initially located above the split between the two portions of the direct shear box. The abbreviations used in each graph are as follows: D_r = Relative Density, and A_r =Area Ratio.

Results are presented in two subsequent sections. The first section presents a sample of the macroscopic and particle-scale response during direct shearing for one of the glass bead tests. The second section presents a sample of the macroscopic and particle-scale response during direct shearing for one of the sand tests. The GeoPIV analysis used to determine the particle-scale response of the materials is discussed in 6.2.1 below.

5.3.1 Glass Beads

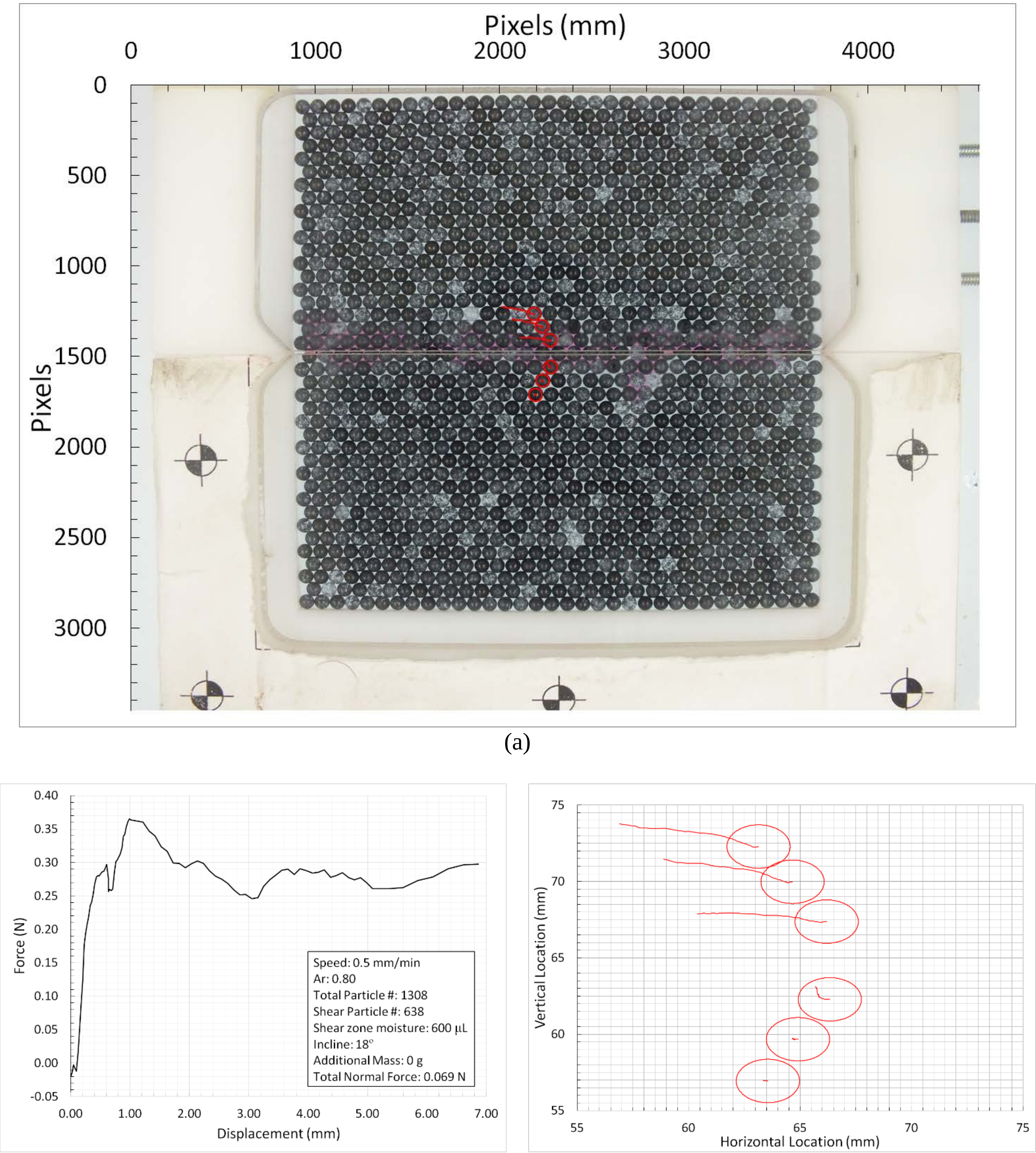

(a)

(b)

(c)

Figure 5.19 Glass beads results for 0.5 mm/min, dense state, 18° incline: (a) Image space movements, (b) Shear response, (c) Real space movements

5.3.2 Sand

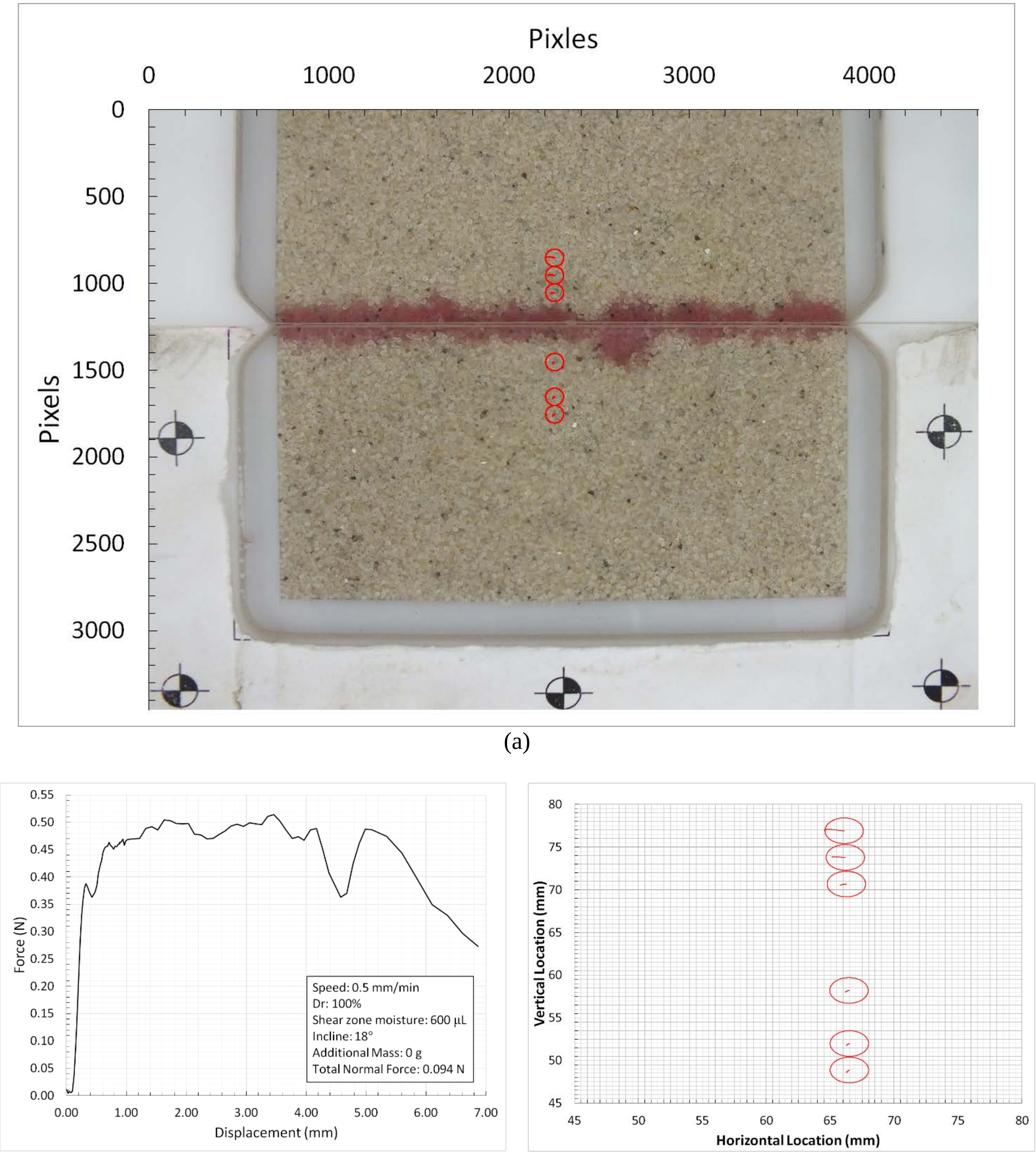

(a)

(b)

(c)

Figure 5.20 Sand results for 0.5 mm/min, dense state, 18° incline:
(a) Image space movements, (b) Shear response, (c) Real space movements

6 Discussion and Analysis

6.1 Fall Cone Testing

Generally speaking, the penetration of an object into a medium is controlled by three factors, the shape of the penetrating object, the impact velocity of the penetrating object, and the density and strength characteristics of the medium being penetrated. These three factors were examined by using two different fall cone geometries, three drop heights, and relative material densities of 0% and 100%. A comparative summary of the results can be found in Figure 6.1 through Figure 6.4. The penetration of the fall cone into each medium is presented as a function of the normalized drop height in each figure. Normalized drop height is defined as the ratio of the drop height to the cone height (D_h/C_h). Each of the following sections discusses each of the three factors and the observed behavior.

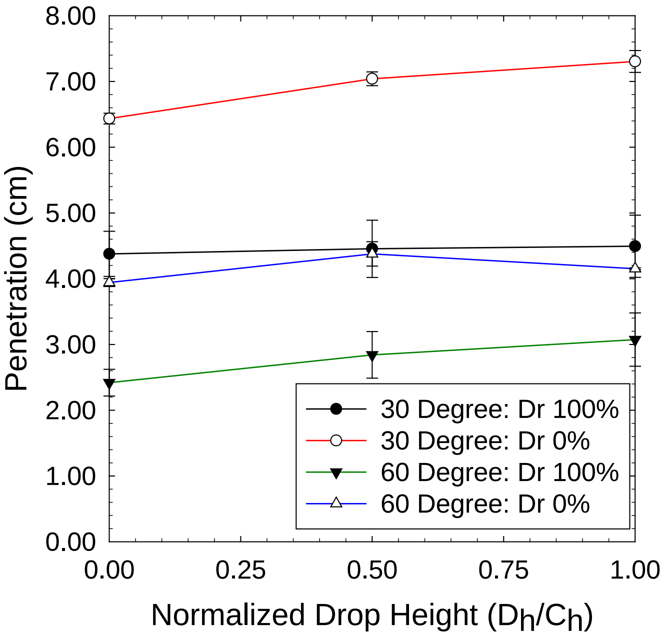

Figure 6.1 Glass bead penetration in 4” proctor

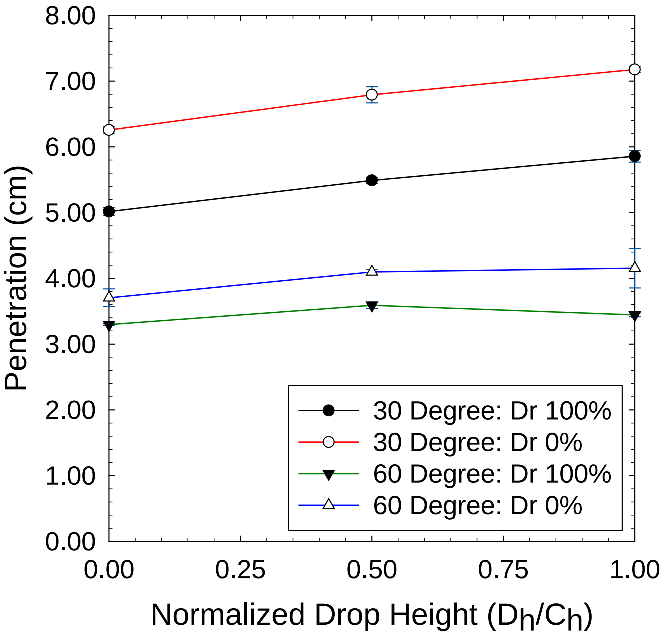

Figure 6.2 Glass bead penetration in 6” proctor

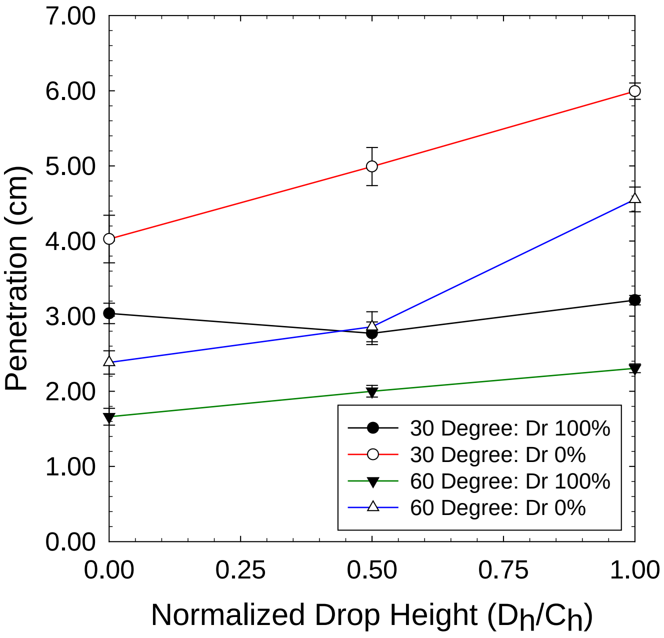

Figure 6.3 Sand penetration in 4” proctor

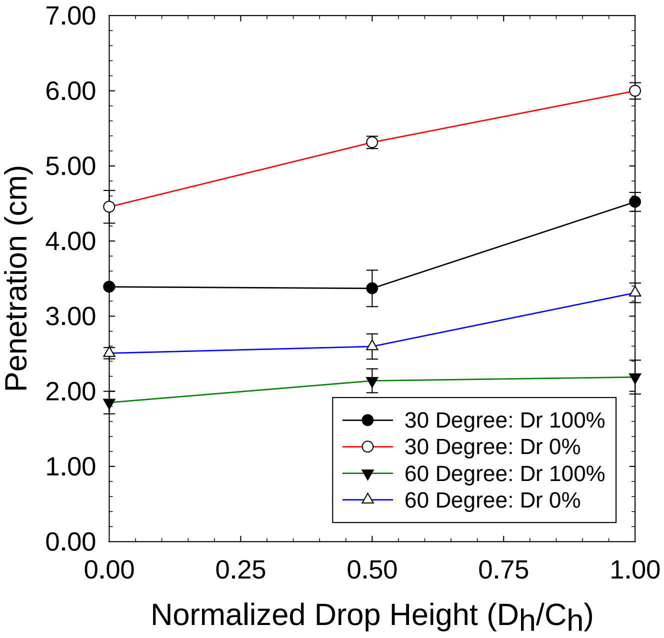

Figure 6.4 Sand penetration in 6” proctor

6.1.1 Penetration as a function of cone geometry

The effects of cone geometry were examined using the 30° British fall cone and the 60° Swedish fall cone. When examining all of the test results, an inverse correlation between projected cone area and penetration depth is apparent. As the projected area increases, the amount of penetration decreases. The 30° fall cone had a smaller projected area (67 mm^2) versus the 60° fall cone (310 mm^2). The materials were expected to exhibit a smaller penetration value with a larger projected area. The increase in the fall cone projected area results in a larger area of material providing resistance, and when the resistance increases, the amount of penetration is reduced.

The amount that the change in cone geometry influenced the penetration values was examined for each material. The glass bead tests showed the increase in apex angle from a 30° fall cone to a 60° fall cone resulted in a 32% to 45% reduction in penetration values. The average reduction in penetration was 39%. The sand tests showed that the increase in cone apex angle from a 30° fall cone to a 60° fall cone resulted in a 24% to 52% reduction in penetration values. The average reduction in penetration was 40%. Both the glass bead tests and the sand tests had an average reduction of ~40% in penetration values using the 60° cone.

This behavior has been previously observed in clayey soils with varying levels of moisture contents. Leroueil & Le Bihan (1996) conducted tests using clayey silts, silty clays, and lacustrine varved clay and found that the depth of 60° fall cone penetration compared to 30° fall cone penetrations was half as much, regardless of the soils plasticity index. While results from the current test series using sands and glass beads indicate an average reduction of 40%, this discrepancy suggests that that there are additional factors leading to a reduction in penetration using the 60° cone or an over penetration using the 30º cone. These factors are discussed in a subsequent subsection.

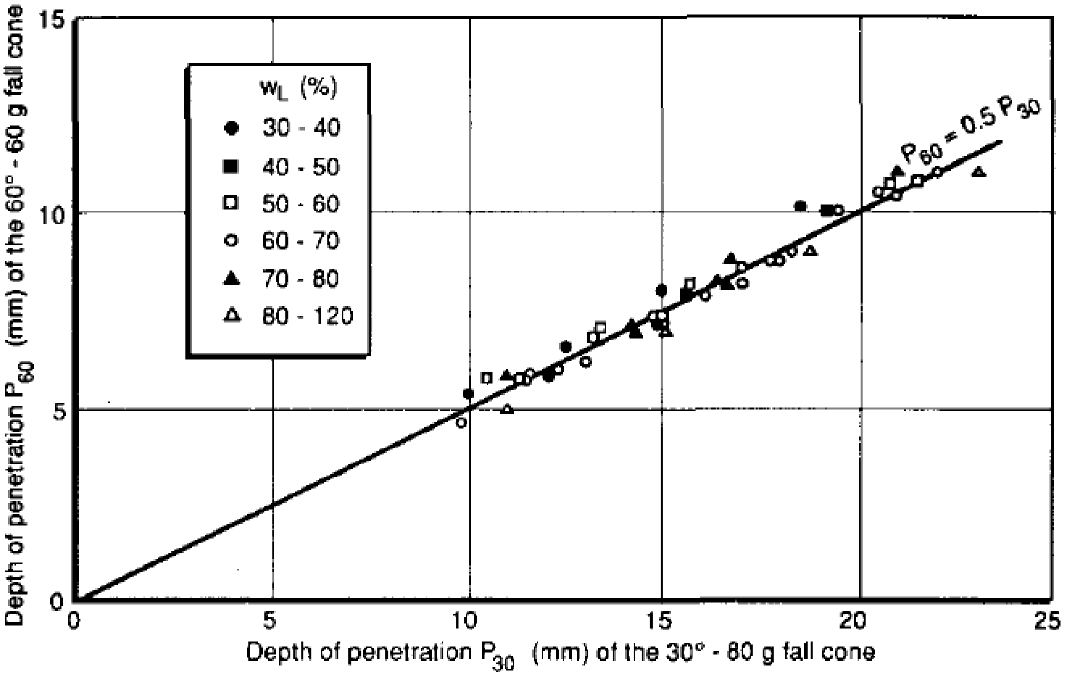

Figure 6.5 Relationship between the depths of penetration of the 60° - 60 g and 30° - 80 g fall cones for clayey silts, silty clays, and lacustrine caved clay (Leroueil & Le Bihan, 1996)

6.1.2 Penetration as a function of density

The effects of material density were examined by using two different relative densities for each material. The tests were conducted at relative densities of 0% and 100%. When examining all the test results, an inverse correlation between material density and penetration depth is apparent. As the relative density increases, the amount of penetration decreases. The materials were expected to exhibit a smaller penetration value for a higher material density. The increase in density results in a larger number of particles in the area where the cones would penetrate. Shearing resistance provided by the increase in particle numbers provides more resistance to the cone as it penetrates, thus arresting the movement of the cone at less penetration.

The amount that the change in relative density influenced the penetration values was examined for each material. The glass bead tests showed that the increase in relative density from 0% to a relative density of 100% had a 11% to 39% reduction in penetration values. The average reduction in penetration was 25%. The sand tests showed that the increase in relative density from 0% to a relative density of 100% had a 18% to 50% reduction in penetration values. The average reduction in penetration was 32%. Unlike the reduction in penetration resulting from cone geometry, the reduction in cone penetration from an increase in relative density was different for each material. The relative size between the fall cones and the test particles are believed to be the primary reason. The sand particles are significantly smaller than the fall cones, and densification reduced the void size and number. If the cone initially penetrated the surface at a void space, sand particles would be closer together to resist the penetration. However, the fall cone diameters were approximately 3 (30º cone) and 6 (60º cone) glass bead diameters. The densification of the glass beads still left proportionately larger void spaces. If the cone initially penetrated the surface at a void space, the cone could continue to penetrate to a larger depth before coming in contact with a glass bead. This lead to increased variability in the relationship between penetration and relative density. Essentially the cone could impact in a void space and show an additional 2.84 mm of penetration where as if the cone impacted the apex of a bead, it would begin to slow immediately.

6.1.3 Penetration as a function of drop height

The effects of cone drop height were examined by using three different drop heights. When examining all of the test results, a correlation between drop height and cone penetration was observed. Penetration increased with increasing drop height. This behavior was expected. With an increase in drop height, the velocity of the cone at contact with the materials surfaces increases. The increase in impact velocity corresponds to an increase in kinetic energy, which corresponds to an increase penetration. This behavior is observed in impact crater experiments. For example, Takita and Sumita (2013) show that crater depth varies linearly versus the log of kinetic energy,

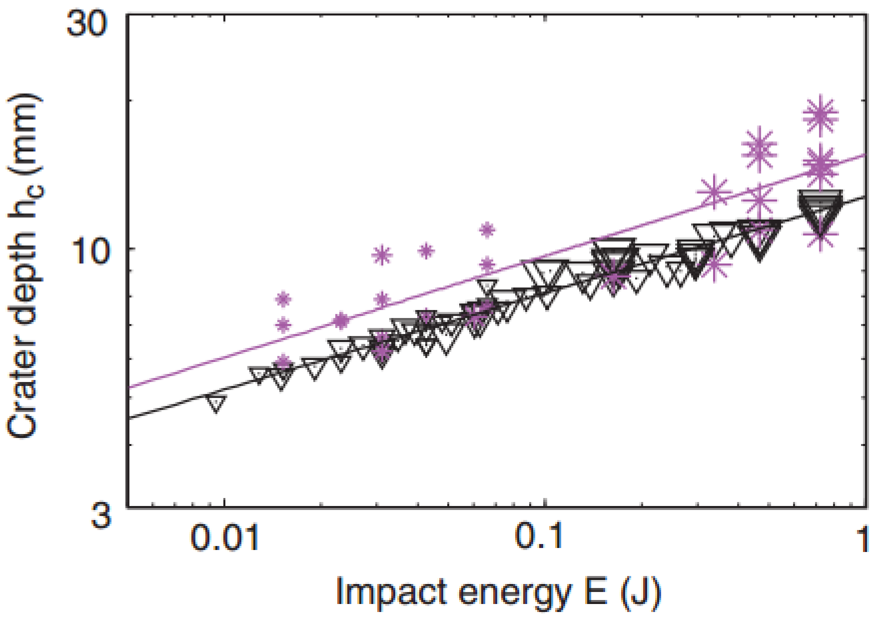

Figure 6.6 Crater depth hc (mm) as a function of impact energy E (J) at small S [degree of saturation] (S<0.04) (Takita & Sumita, 2013)

The amount that the change in cone drop height the penetration values was examined for each material. The glass bead tests showed the increase in drop height from 0.0 (cone tip flush with surface) to a 1.0 drop height (cone 1 full length above the surface) had a 6% to 92% increase in penetration values. The average increase in penetration was 38%. The contributing factor to the wide range for the increase in penetration depth with drop height for the glass beads was the glass bead arrangement. If the arrangement of glass beads were such that the cone fell into a void space, that is potentially 1.42 mm of extra fall distance and 1.42 mm of unresisted penetration below the surface. The sand tests showed the increase in drop height from 0.0 (cone tip flush with surface) to a 1.0 drop height (cone 1 full length above the surface) had a 3% to 27% increase in penetration values. The average increase in penetration was 12%.

In addition, the position plot for each of the fall cone above a 0.0 drop height was examined prior to the cone making contact with the surface of the materials. The data was used to create regressions equations for each of the position curves and solved for the time required to reach the material surface. The derivative of the position regression equation was evaluated at the time to reach the surface to determine the impact velocity. The impact velocities were compared with the respective penetration values (Figure 6.7). The 60° low relative density and 30° high relative density sand tests provided data with the best correlation between impact velocity and cone penetration. The remaining tests data had minimal correlation between impact velocity and cone penetration contrary the expected behavior. The results were expected to produce an upward linear trend, however several of the tests indicated almost horizontal trends. The horizontal trends indicate there are additional factors influencing the cone penetration into the material.

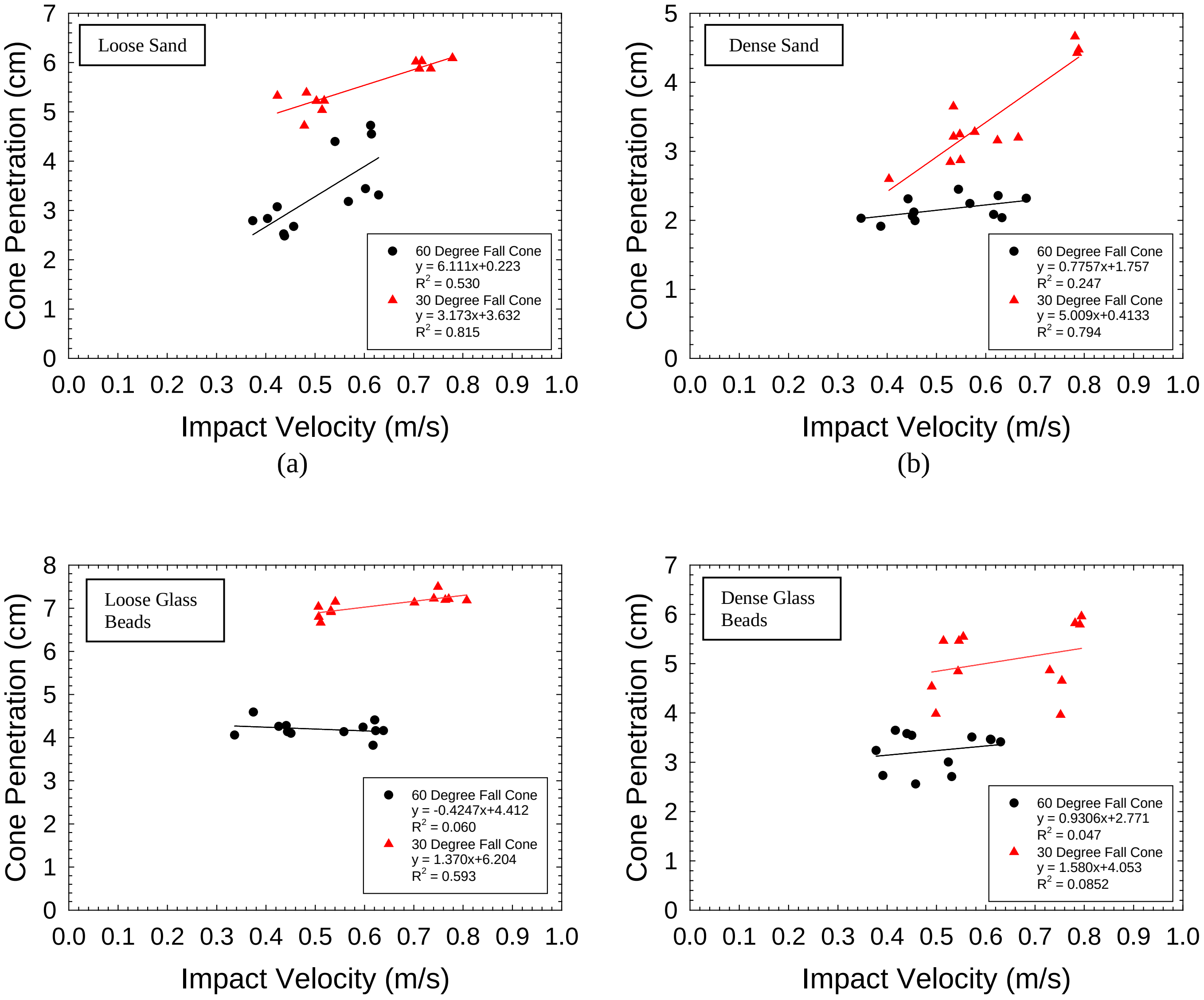

(a)

(b)

(c)

(d)

Figure 6.7 Penetration as a function of impact velocity for (a): Low D_r sand, (b) High D_r sand, (c) Low D_r Glass beads, (d) High D_r Glass Beads

6.1.4 Influence of friction between LVDT rod and rod housing on impact velocity

The data was analyzed from point of release to a distance of 0.5 Ch for both the 30° and 60° fall cones. Trend lines were generated from the lower and upper bounds of the data sets, neglecting extreme outliers. The trend lines were forced to have a displacement intercept of 0. This provided more conservative trend lines. The velocity ranges were calculated by solving for the time required to reach the material surfaces for the 0.5 and 1.0 D_h. This time was then used to determine the velocity at impact with the material. The accelerations were determined by taking the 2nd derivative of the trend line equations. The calculated acceleration was then compared with gravity to determine the friction forces. The data is presented in Table 6-1 through Table 6-4.

Table 6-1 30º Falling trends from glass results

Bounds	Trend Line Equation	R^2	Acceleration (m/s^2)	Friction (N)	0.5 D_h		1.0 D_h	
					Time (s)	Velocity (m/s)	Time (s)	Velocity (m/s)
Upper	$3.182t^2 - 0.0484t$	0.9984	6.36	0.488	0.0815	0.470	0.112	0.664
Lower	$4.313t^2 + 0.0265t$	0.9997	8.63	0.166	0.0602	0.546	0.0863	0.771

Table 6-2 30º Falling trends from sand results

Bounds	Trend Line Equation	R^2	Acceleration (m/s^2)	Friction (N)	0.5 D_h		1.0 D_h	
					Time (s)	Velocity (m/s)	Time (s)	Velocity (m/s)
Upper	$3.120t^2 - 0.0725t$	0.9943	6.24	0.505	0.0868	0.469	0.117	0.658
Lower	$4.313t^2 + 0.0474t$	0.9999	8.63	0.166	0.0579	0.547	0.084	0.772

Table 6-3 60º Falling trends from sand results

Bounds	Trend Line Equation	R^2	Acceleration (m/s^2)	Friction (N)	0.5 D_h		1.0 D_h	
					Time (s)	Velocity (m/s)	Time (s)	Velocity (m/s)
Upper	$3.240t^2 - 0.0652t$	0.9952	6.48	0.452	0.0695	0.385	0.0933	0.539
Lower	$4.427t^2 + 0.0975t$	0.9998	8.85	0.136	0.0403	0.454	0.0605	0.633

Table 6-4 60º Falling trends from glass results

Bounds	Trend Line Equation	R^2	Acceleration (m/s^2)	Friction (N)	0.5 D_h		1.0 D_h	
					Time (s)	Velocity (m/s)	Time (s)	Velocity (m/s)
Upper	$3.357t^2 - 0.0598t$	0.9936	6.71	0.421	0.0671	0.391	0.0905	0.548
Lower	$4.605t^2 + 0.0622t$	0.9999	9.21	0.081	0.0428	0.456	0.0629	0.642

In the initial selection and design of the testing apparatus it was assumed that frictional effects due to the LVDT rod would be negligible. To check this assumption, the accelerations were determined. The trend lines used to determine the impact velocity were also used to calculate the actual acceleration of the falling cone. The trend lines indicated a range of accelerations, also indicating a range of frictional forces exhibited.

This range of frictional variances could be attributed to the manner in which the LVDT rod was restrained. To maintain the zero mark on the rod before releasing, an additional lateral force could have been applied to the rod. This additional force could have caused the rod to move away from a vertical alignment. Once the rod was released this would cause additional friction as the rod moved to realign itself while falling. Several tests produced displacement trends with several data points indicating a large oscillation in the displacement. Visual observations did not present any indication of this. These data points were treated as noise and removed from the data sets; however, these points could be an indication of the additional friction forces generated from the realignment of the LVDT rod when falling.

However, it is worth noting that several of the tests produced a trend line that had an acceleration very close to that of gravity. This indicates that with proper setup and release, this testing apparatus can produce near frictionless results indicative of true free fall.

6.2 Direct Shear Testing

6.2.1 GeoPIV Analysis

The particle-scale response of the glass beads and sand was an important component to the validation data set for Chrono::Granular. GeoPIV-RG was utilized to identify and analyze the particle-scale movements. GeoPIV-RG is a particle image velocimetry (PIV) program developed for geotechnical engineering applications, GeoPIV, that uses new developments in image analysis algorithms and techniques (Stanier, Blaber, Take, & White, 2015), The process and parameters used to execute the analysis are presented below.

The first step in the analysis process was to address the naming convention if the images. The names assigned to the images by the camera were non-descriptive and the sequencing reset every time the camera changed image folders. The images for each test were renamed to uniquely identify the test the images represented, and a sequencing number was added to the end of the name.

The next step was to identify the parameters needed to successfully analyze the image sets. The parameters pertaining to image quality and mesh size were determined using Teng et al. (2015) as a guide. The sand tests' images were first evaluated to determine the ratio of average particle size to pixel ratio. The average size of the sand particles was 0.75 mm and corresponding to 20 to 25 pixels for PIV representation depending on the test. The mesh size for the analysis was then selected. Teng et al. (2015) found for their tests that a subset diameter of 70 pixels met recommended values for image texture (>10^5) and contrast (>15). The first subsets in the current analysis were thus generated using 70 pixels and increased until the generated subsets reach the recommended texture and contrast values. The initial subset diameter used in each test was 100 pixels. The sand was not seeded, no artificial or dyed particles added to the sand, and did not always reach the exact recommended value, but was always in proximity. The sand subsets however, met the texture recommendations. The subsets were arranged vertically in line with the center control point with three subsets on each side of the shear box division. The text files used to launch the GeoPIV-RG analysis were created with the analysis mod set as point to point with the recommended limits for max iterations (50), maximum norm of the shape function difference vector ($1\text{x}10^{-5}$), seed correlation coefficient tolerance (0.9), and full-field correlation tolerance

(0.75). If the analysis failed from failure to meet the tolerances, the subset diameter was increased to 125 pixels, the maximum iterations was increased to 100, the seed correlation coefficient tolerance was decreased to 0.8 and the full-field correlation tolerance was decreased to 0.65. At these values the tests completed and the results were calibrated using the control points to produce particle displacements in real space.

Initially, the same analysis approach was used for the glass bead tests, but with a small subset pixel diameter. A subset of diameter of 70 pixels was selected, creating a subset slightly larger than an individual glass beads; however, several issues arouse. The subset mesh generating script would not place the subsets centered on the glass beads. The subset location issue was resolved using a subset generating script from an older GeoPIV release (GeoPIV8). The older script prompts the user to select the center of the subset on the initial image. Using this method, three glass beads were selected above and below the shear box division in approximate vertical alignment with the center control point. The analysis was again run using the recommended parameter for GeoPIV-RG with the subsets generated from the GeoPIV8 script. The analysis results showed that the individual glass beads could be tracked, however one of the glass beads was tracked incorrectly. Another glass bead displaced into the previous location of the one being tracked, and GeoPIV-RG began tracking the replaced glass bead. GeoPIV-RG was abandoned because of this, and GeoPIV8 was used instead. GeoPIV8 uses a pixel search zone to find the new subset location, whereas GeoPIV-RG predicts the subset location based on neighboring subset deformation. Using GeoPIV8 with a subset diameter of 70 pixels centered on the glass beads and a search zone of 20 pixels, the remaining glass bead test images were analyzed. Finally, the results were calibrated using the control points to produce particle displacements in real space. At the completion of the GeoPIV-RG and GeoPIV8 analyses, the images were compiled into videos for each test. The videos were used to visually inspect the particle-scale response to shearing.

6.2.2 Influence of shear rate on particle movement

The dry direct shear tests were examined to investigate the influence, if any, of shear rate on discrete particle movements. The dry, densely packed glass bead tests were examined first. It was observed that the dense packing configuration does not allow for much individual particle movement while shearing. For each test, the glass beads dilated at the shear zone and moved in the direction of shearing. Figure 6.8 and Figure 6.9, for example, show the configuration of the glass beads after shearing. In each of the dense glass bead tests, the particles above the shear zone remained in the dense packing configuration. The particles in the shear zone dilated vertically to allow the shear surface to develop. Further discussion of the particle behavior in the shear zone is discussed in Section 6.2.5. Examination of videos from incremental images showed that the glass beads moved towards the viewing planes in addition to the vertical and horizontal movements. The third dimensional movement allowed for slight particle rearrangement and slightly reduced the extents of vertical dilation and horizontal movement. The 1.0 mm/min and 0.5 mm/min tests for 30° inclination were not compared due to different applied normal forces.

The loose glass bead tests were examined next. The random dispersion of the glass beads prohibited a direct particle to particle comparison. However, the general trends for particle motions were compared using the real space particle movements from the GeoPIV8 analysis. Increasing the shear rate from 0.5 mm/min to 1.0 mm/min resulted in more horizontal displacement. This behavior was observed in all the loose glass bead test cases. Videos of the loose glass tests were examined to identify this behavior. The videos for the 0.5 mm/min test indicated that as the displacement of the shear box increased, the glass beads rotated and moved

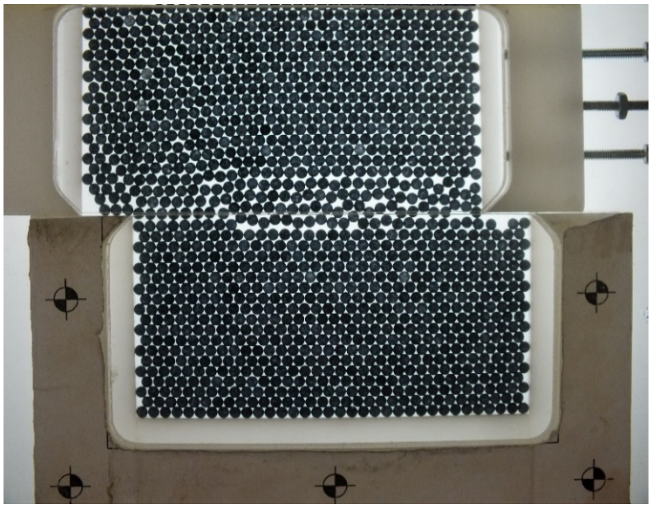

Figure 6.8 Dense glass beads at end of shearing for 0.5 mm/min at 24°

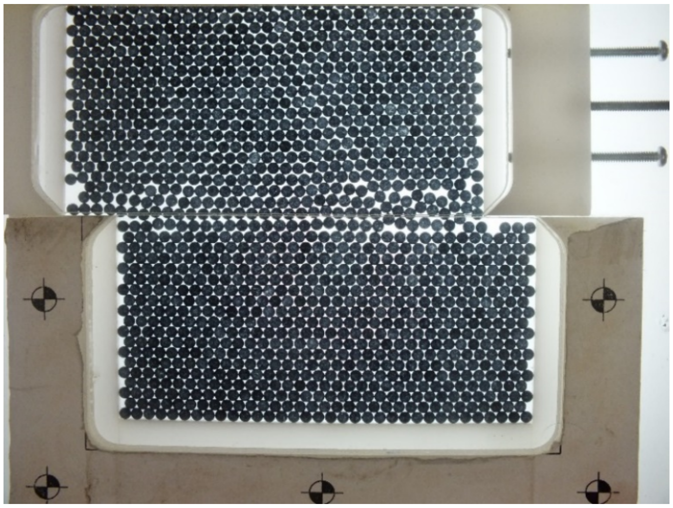

Figure 6.9 Dense glass beads at end of shearing for 1.0 mm/min at 24°

around each other. Li and Aydin (2010) observed a similar behavior, indicating that low shear rates facilitate shear-induced packing (contraction). The videos of the 1.0 mm/min tests indicated that as the horizontal displacement of the shear box increased, the glass beads had a rigid, skeletal response, i.e. as a solid body and not individual particles. The rigid response reduced the shear packing observed in the slower displacement rate tests, translating to a larger horizontal particle movements.

The direct shear results for the dense sands were examined next. Due to the significantly smaller size of sand particles, GeoPIV-RG was used to track the motion of several patches of particles rather than individual particles. Each patch contained approximately 64 particles of sand. Each of the dense sand test pairings (18°, 24°, and 30° inclinations) responded differently to the changes in shear rate. The 18° inclination tests exhibited dilative behavior at 1.0 mm/min and contractive behavior at 0.5 mm/min. The 24° inclination tests exhibited a slightly contractive response of similar magnitude for both the 0.5 mm/min and 1.0 mm/min shear rates. The 30° inclination tests exhibited a stronger contractive response for both the 0.5 mm/min and 1.0

mm/min tests. A contraction response is expected for loose sand being sheared, not dense sand. The macroscopic shear responses for each of the tests exhibited the profile for dense sands, with shear stress increasing to a peak point and declining to a residual value. This indicated that the response of the sand was as anticipated, but the movement was not. Previously the glass beads had been observed to move against the viewing plane, thus skewing the true horizontal and vertical movements. This is the suspected cause of the particle patch movements not matching the strength response of the sand.

Finally, the results for the loose sands were examined. Both 18° inclination tests experienced motion less than half a millimeter in any direction. This indicates that at low normal forces the displacement of the shear box was packing the sand sample instead of shearing it. Both 24° inclination tests exhibited a different response. The application of additional normal force compacted the sand. The compaction reduced the amount of shear packing from the shear force, and horizontal movement became apparent in the sand patches. The increase in shear rate from 0.5 mm/min to 1.0 mm/min increased the magnitude of compaction from the normal force and subsequent horizontal displacement of the sand patches. The 30° inclination tests did not exhibit as large a compaction from the additional normal force as the 24° incline tests. The reduced compaction resulted in less horizontal movement than both the 24° inclination tests. However, for both 30° inclination the additional normal force was greater and the sand patches exhibited primarily horizontal movement.

6.2.3 Influence of water content in shear zone on particle movement

Another area of interest centered on understanding the effect of introducing water into the shear zone on observed particle movements. The same test series was completed as the dry tests except that 600 μL of dyed water was added to the anticipated shear zone prior to shearing. As in the previous section, the images of the tests were compiled into videos. The videos were used in conjunction with the results from the GeoPIV analysis to qualitatively describe observations. The videos and real space particle movements were analyzed to identify the effects, if any, adding water to the shear zone had on particle movement.

Test with the glass beads were first examined due to the relatively large size of the particles. The large particle size allowed for the water bridges between the particles to be easily observed. The most ideal case (dense packing of glass beads) was focused on first. Each of the dry, densely packed glass bead tests exhibited peculiar behavior. Once the shear band developed, any additional horizontal displacement would cause portions of the shear band to collapse. The glass beads would fall irregularly back into the valleys created by two adjacent glass beads. This occurred once the glass bead passed the apex of the glass bead below it. Introducing water into the shear zone greatly reduced the irregularity of the glass bead movements in the shear band. When the wet glass beads were sheared, the glass beads dilated vertically as before. However, when the shear band fully opened, the relative motion between the layers was greatly reduced. In addition, when the glass beads displaced beyond the apex of the glass beads below, half of the shear band collapsed simultaneously. Figure 6.10 and Figure 6.11 illustrate this behavior for the 0.5 mm/min, 24° inclination test for dry and wet dense glass beads respectively. Another observation was made with regards to glass beads below the division in the shear box. Below the shear box division, the glass beads did not move unless interlocking occurred along the shear surface. Introducing water into the shear zone changed this behavior. During shearing, glass beads connected across the shear box division via water bridges acted together in their movements. The glass bead above the shear box division tended to pull the lower glass bead along with it. Figure 6.12 illustrates this behavior.

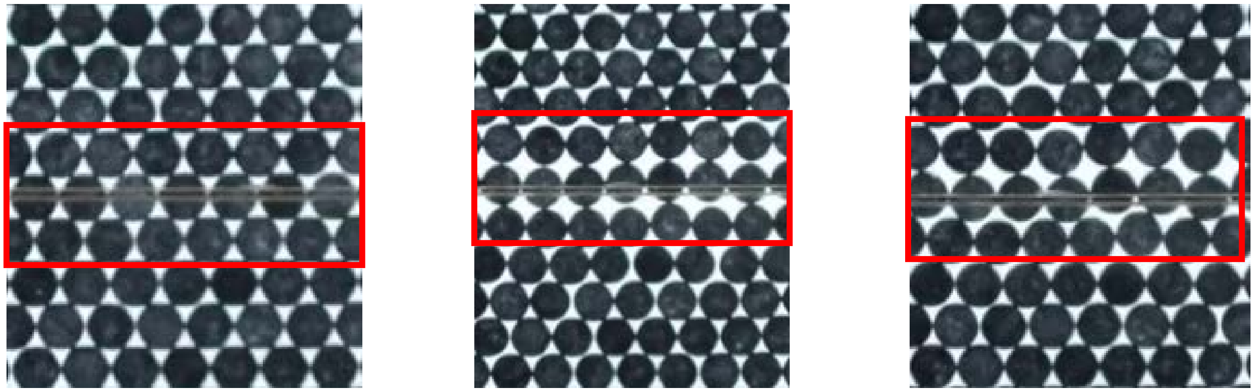

(a) (b) (c)

Figure 6.10 Zoomed in images of dry 0.5 mm/min Glass beads inclined at 24º (a) prior to shear zone opening, (b) with an open shear zone, and (c) with shear zone reduced

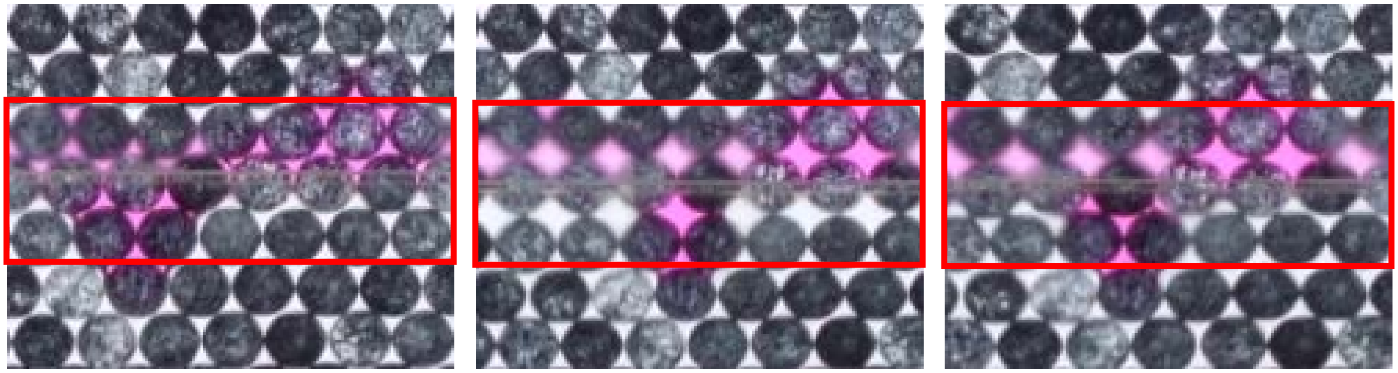

(a) (b) (c)

Figure 6.11 Zoomed in images of wet 0.5 mm/min Glass beads inclined at 24º (a) prior to shear zone opening, (b) with an open shear zone, and (c) with shear zone reduced

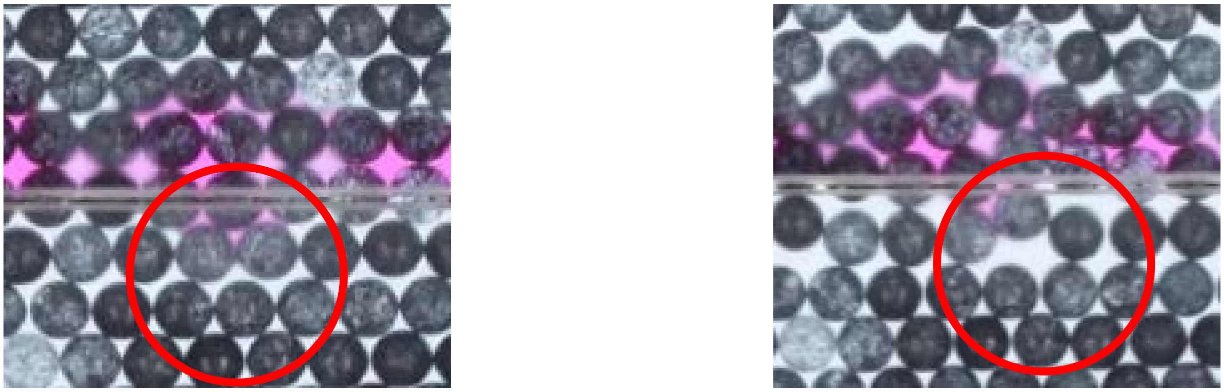

(a) (b)

Figure 6.12 Zoomed in images of wet 1.0 mm/min Glass beads inclined at 18º (a) prior to vertical movement in circled region and (b) after vertical movement in circle region

The next focus was on the behavior of the loose glass beads. As with the investigation of shear rate, the random particle arrangement off the loose glass beads prohibited a direct comparison between the wet and dry conditions. The GeoPIV analysis and test videos allowed for the general trends to be compared, and several observations were made. In each of the 0.5 mm/min, dry, loose glass bead tests, a compression front due to shear-induced packing was identified. The compression front was observed extending into the lower, fixed portion of the shear box. The introduction of water into the shear zone changed this behavior. In general, the water created a division in the behavioral response of the glass beads, with the glass beads responding differently in the upper and lower shear box regions. First, the introduction of water into the shear zone isolated the lower portion of the loose glass beads from the compression front. This resulted in the glass bead movement decreasing as the distance from the shear zone increased. Second, introducing water into the shear zone isolated the compression front in loose glass beads above the shear zone. This caused the glass beads above the shear zone to move more horizontally. The isolating effects of water in the shear zone decreased with increases in normal force and increases in shear rate. Figure 6.13 shows this behavior for the 0.5 mm/min,

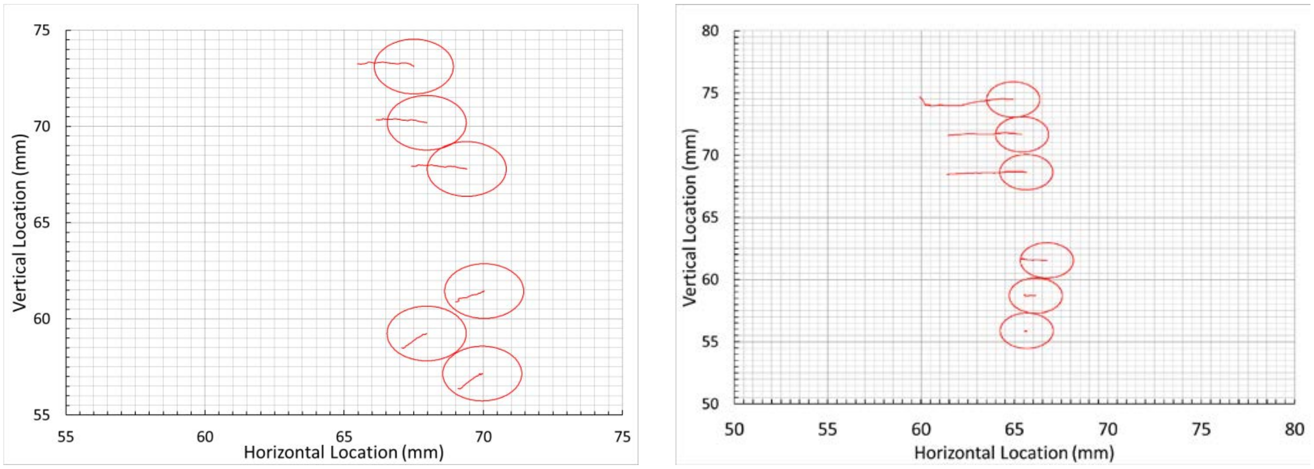

(a) (b)

Figure 6.13 0.5 mm/min loose glass beads inclined 24° (a) dry and (b) wet GeoPIV physical location results

24° inclination, dry and wet loose glass bead tests respectively. In Figure 6.13, the 65 mm mark on the vertical location axis is the approximate location of the shear box division. An interesting effect was observed when several glass beads were located closely together. Several instances were observed of bridged particles being created. The addition of water to the loose glass beads led to groups of glass beads being connected by several water bridges. When the glass beads were sheared, these groups of particles moved together as one large macro particle.

Finally, the effects of water in the shear zone were investigated for both the loose and dense sand tests cases. The patches of sand analyzed using GeoPIV-RG were located above and below the wetted region, and thus did not capture the behavior in the wetted zone. However, upon examination of the GeoPIV-RG results, the inclusion of water in the shear zone did not affect the behavior of sand particles outside the wetted regions. For instance, in the dry, loose sand tests, a compression front was observed as the shear box displaced into the sand. This behavior was observed in the dry regions of the wetted loose sand tests. The behavior of the sand particles in the wetted region was examined using the videos created from the test images. Examining the test videos led to several observations in both the loose and dense wet sand tests. First, the water acted as a quasi-cementation agent, with the water bridges connecting the sand particles contributing extra strength to the sand through capillary forces. In both the loose and dense sand tests, the movement of the sand particles was greatly reduced. Movement of the wetted sand particles only occurred adjacent to the right side of the shear box, where the shear force was applied. As the normal force and shear rate increased, the extent of the particle movement along the shear plan increased. In the wetted region when the sand particles moved, they moved as a group. This indicated that the shear force grew large enough to overcome the

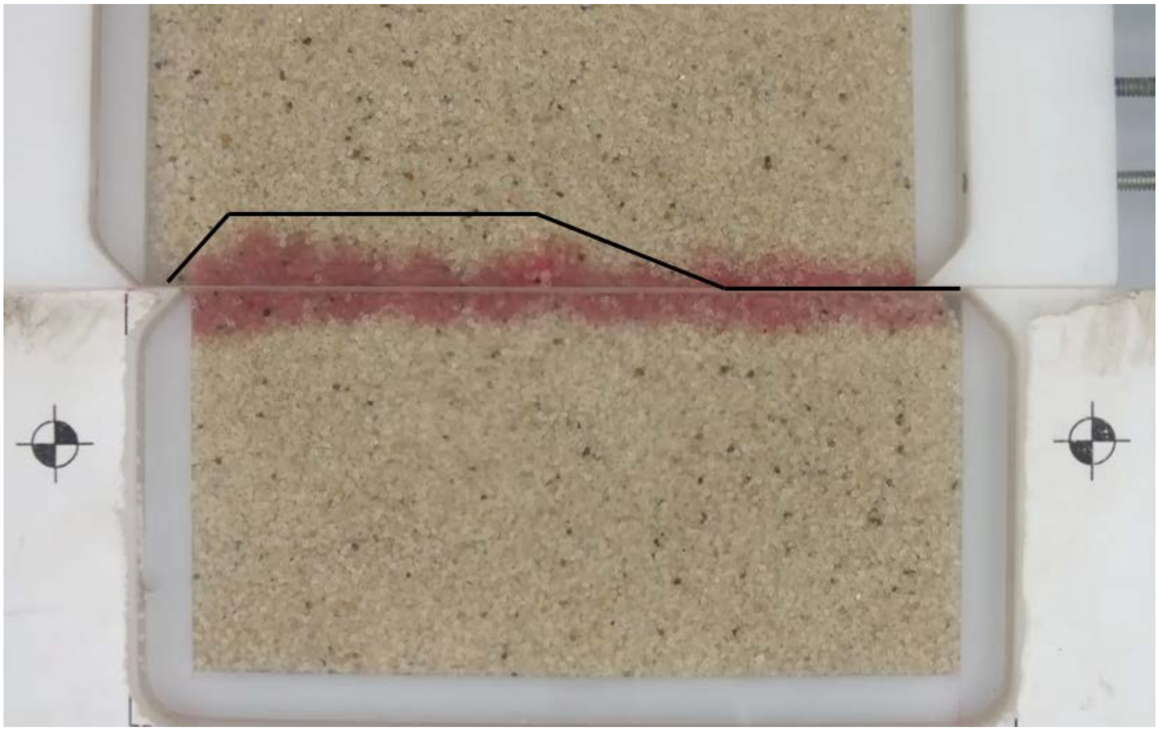

Figure 6.14 Approximate shear zone location for 0.5 mm/min dense sand at 24° test.

capillary forces to create a shear plane. The second observation pertains to the shear plane itself. The construction of the shear box creates a preferential shear plane at the division of the shear box halves. When water was added to this region, the actual shear plane that developed changed substantially. Not only did the shear plane change locations, the shear plane also changed shape. Figure 6.14 presents the location of the observed shear plane for the 0.5 mm/min, 24° inclination, dense sand with water added test. Fu and Dai (2015) indicated that the actual shear plane varies due to particle rotation, but remains primarily horizontal in the area of the preferential shear plane. The observed shear plane remained in the area of the preferential shear plane for a short distance before angling upward and extending out of the wetted region. Continuing for some distance, the shear plane angled back to horizontal. The shear plane continued parallel to the preferential shear plane for some distance. The shear plane then angled back down to meet the shear box division at the far end of the shear box. This behavior was observed in each of the moist sand tests. The slope and relative location of the incline exiting the wetted region was different for each normal force and shear rate application. It is speculated that the shear force needed to shear along the entire wetted preferential shear plane was much higher than the shear force necessary for the shear plane to turn and climb out of the wetted region.

6.2.4 Behavior of water in the shear zone

Investigating the effects that adding water to the shear zone had on particle movements allowed for observation of the water's behavior in the shear zone. Focusing on the behavior of the water in the shear zone led to several interesting observations. The first observation was most visible in the dense glass bead tests. Adding water to the shear zone filled the voids between the glass beads, indicating that the pores became saturated. As shearing began, the glass beads tended to move horizontally. For the horizontal movement to occur, the glass beads would have to climb over the neighboring glass bead (dilation). When dilation occurred, the pore size between neighboring glass beads increased. The increasing pore size caused the pore water pressure in the pore to become increasingly negative. As the distance between glass beads increased, the pore size ultimately became too large to support the negative pore pressure. As a result, the pore drained of water, and the water move elsewhere in the system. The interesting part of the behavior occurred when the glass beads came back together. In areas where water remained in the vicinity, as the pore spaces collapsed water refilled the pore spaces. Figure 6.15 shows the progression from the initial state (a), as shearing force was applied and pore sizes began to increase (b) to a point where the pore sizes were too large to support the negative pore water pressure (c), ending with the void space collapse and the voids refilled with water. This behavior was observed in both the loose and dense particle packing, and for both of the shear rates tested for glass beads.

A similar behavior was observed during the direct shear tests on moist loose sand. The low relative density of each tests created varying void sizes in the sample. When water was added, both the large and small pore spaces alike were saturated. As the shear force was applied, the loose sand particles were pushed together, densifying the sample. The densification of the sand sample caused the larger voids to be filled with sand particles reducing the void size. Subsequently the water was observed to leave the larger void spaces as the void size decreased. As the water left the large voids, the water expanded into the dry regions of the loose sand. Figure 6.16 shows the extent of the wetted area before and after shearing for the 1.0 mm/min,

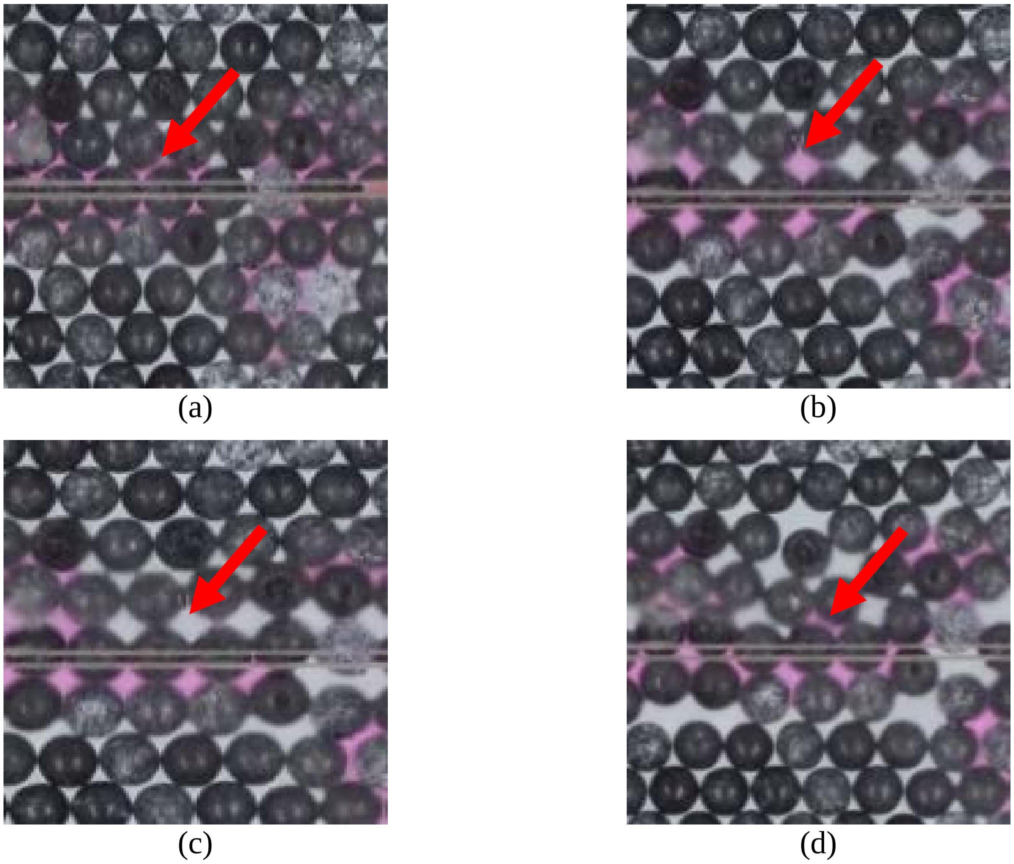
(a) (b) (c) (d)

Figure 6.15 Progression of glass bead pore water behavior (a) prior to shearing, (b) shearing begins and spacing increases, (c) negative pore pressure too great and pore empties, and (d) pore size reduces and refills with water

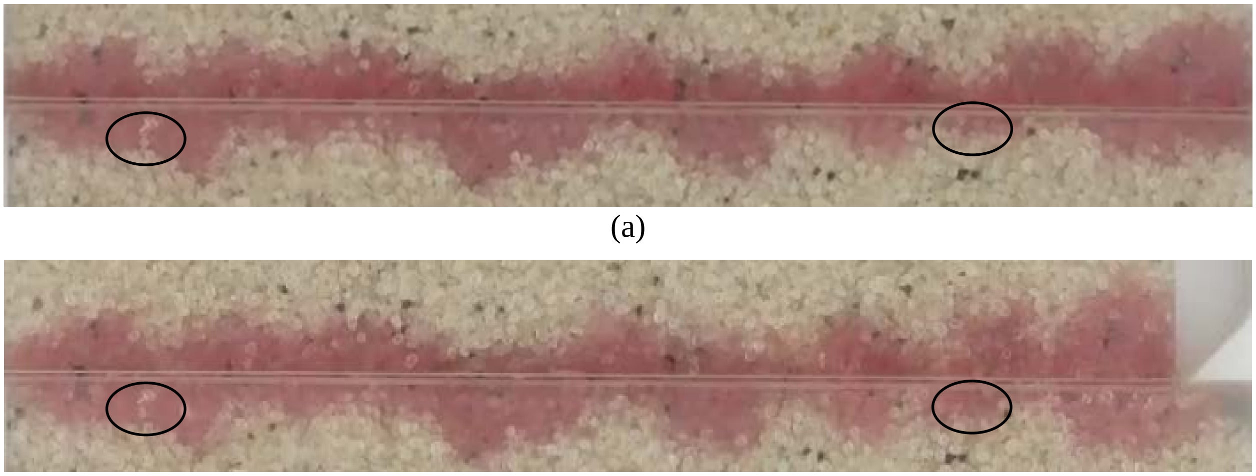

(a)

(b)

Figure 6.16 Extents of water for 1.0 mm/min loose sand inclined 18° (a) before shearing and (b) after shearing.

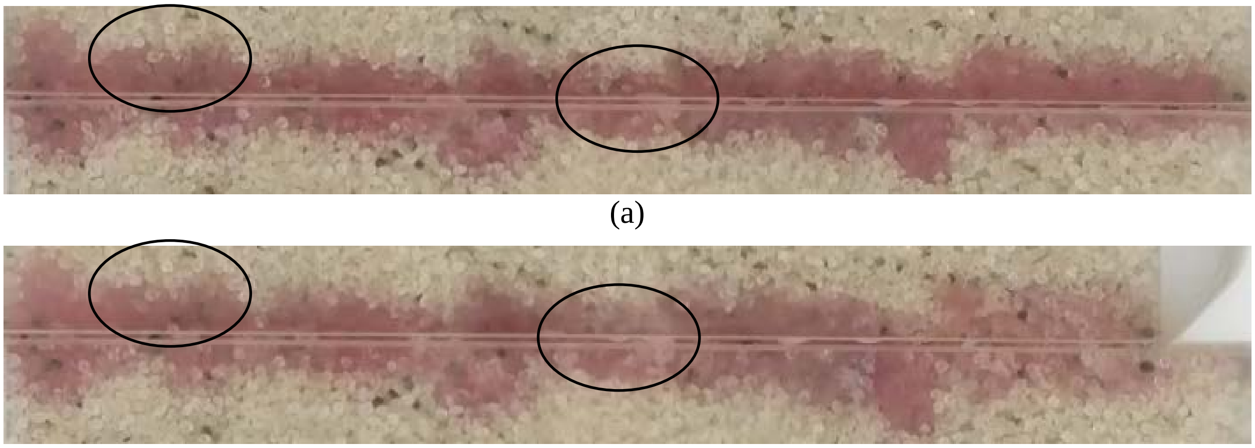

(a)

(b)

Figure 6.17 Extents of water for 1.0 mm/mm dense sand inclined 18° (a) before shearing and (b) after shearing.

18° inclination, wet, loose sand test. Figure 6.16 also has several areas circled were changes in the extent of the wetted area are most visible. This behavior increased with increased normal force and shear rate.

A combination of the behaviors observed during the glass bead tests and the loose sand tests was observed for the dense sand tests. Adding water to the shear zone filled the voids between the sand particles, indicating that the pores became saturated. As shearing began, the sand particles tended to move horizontally. For the horizontal movement to occur, the sand particles would have to climb over the neighboring sand particles (dilation). When dilation occurred, the pore size between neighboring sand particles increased. The increasing pore size caused the pore water pressure in the pore to become increasingly negative. As the distance between sand particles increased, the pore size ultimately became too large to support the negative pore pressure. As a result, the pore drained of water, and the water move elsewhere in the system. Unlike the glass bead tests where the water remained in the vicinity of its initial location, the water behaved as observed in the loose sand tests. The water left the larger pore spaces and expanded into the dry sand regions. Figure 6.17 shows the extent of the wetted area before and after shearing for the 1.0 mm/min, 18° inclination, wet, dense sand test. Figure 6.17 also has several areas circled were changes in the extent of the wetted area are most visible. This behavior increased with increased normal force and shear rate. In addition, water was observed leaving the un-sheared areas. The behavior in these areas was attributed to the water bonding with the viewing plane. Rain-X® was applied to the viewing area to prevent the water from bonding with the viewing plane. However, the method used to prepare the sample allowed the sand to rub against the viewing plane. The contact between the viewing plane and sand possible removed some of the Rain-X®, allowing the water to attach to the viewing plane. As the viewing plane moved horizontally with the shear plane, the water was dragged along with it.

6.2.5 Development of Shear Bands

The final focus of the analysis was investigating the development of shear bands during the direct shear tests. In direct shear tests, shear bands develop at and around the shear surface, where relative deformations are the highest. The videos created from the test images were used to identify and compare the shear band development of the various tests.

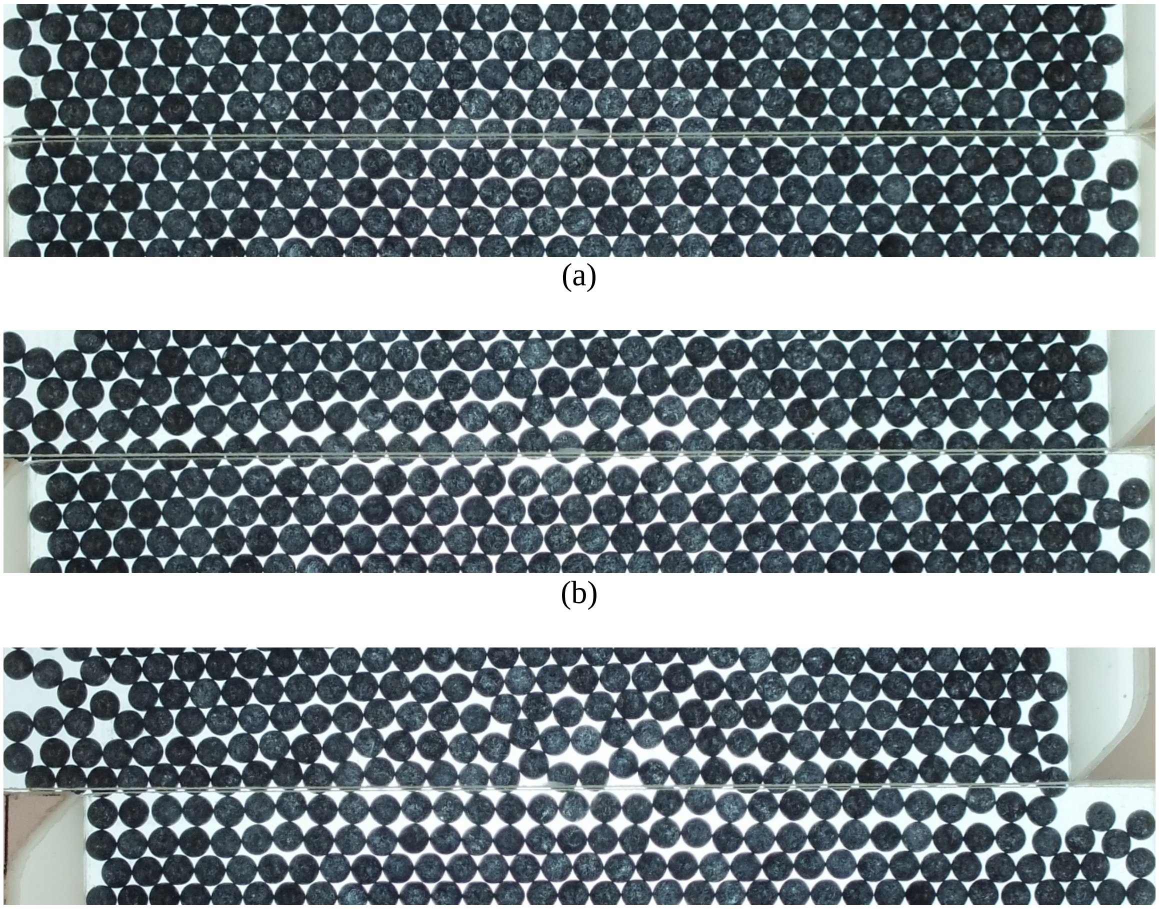

(a)

(b)

(c)

Figure 6.18 0.5 mm/min, 18°, dense dry glass bead shear band development(a) before shearing, (b) half particle width displacement , and (c) test completion

The videos of the dry, dense glass beads were examined first. Examining the 0.5 mm/min test, the shear bands were observed to initially be one particle in width. The shear band width was constant for horizontal displacements of less than half a particle width. When the horizontal displacement increased beyond half a particle width, the shear band became less consistent in width. Some portions of the shear zone would collapse. Other portions had more glass bead particles become engaged in shearing, widening the shear band. Figure 6.18 shows the progression from the initial state to horizontal displacements greater than half a particle width. As the normal force applied increase, the amount of particle engaged increase in the region where the shear force was applied. The 1.0 mm/min glass beads developed a similar shear band with two exceptions.

First, the shear bands were more stable. The shear bands maintained a constant width for horizontal displacements less than 1.5 particle widths, 3x larger than the 0.5 mm/min tests. The second difference observed occurred as the horizontal displacement increased beyond half a particle width. When glass beads in the shear band passed the first apex of the stationary glass bead (half a particle displacement) the shear band partially collapsed. As the horizontal displacement continued to increase, the shear band reopened to the previous width. Figure 6.19 illustrates how the shear band opens as horizontal displacement reaches half a particle width displacement, collapses as the horizontal displacement increase, and reopens after the horizontal displacement is greater than one and a half particle widths. A comparison of the final shear band appearance between the 24º inclination, dry, dense glass test with a shear rate of 0.5 mm/min and 1.0 mm/min is shown in Figure 6.20.

Next, the videos of the wet, dense glass beads were examined. The shear band in each of the wet, dense tests developed and behaved in a similar manner as the shear band in the dry, dense tests. The shear band in the 0.5 mm/min, wet, dense glass bead tests opened completely as the horizontal displacement reached half a particle width. The shear band also partially collapsed and reopened beyond the half particle horizontal displacement. Introducing water into the shear zone removed the more random movement as additional particles were engaged beyond the half particle displacement. However, as observed in the dry tests, at large horizontal displacements the shear band became less defined. A similar behavior was observed in the 1.0 mm/min, wet, dense glass bead tests. The shear band behaved in the same manner as the dry tests with the

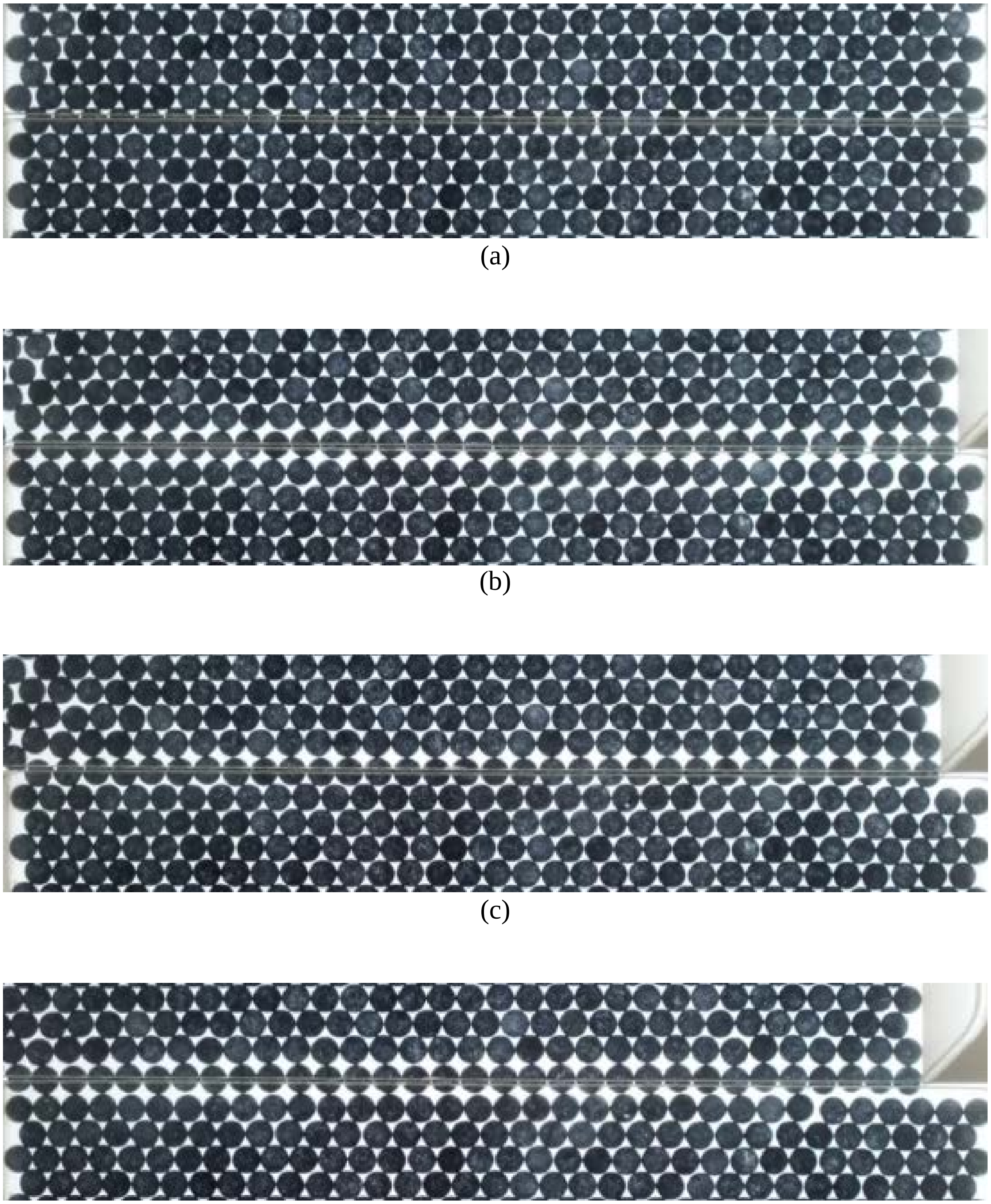

(a)

(b)

(c)

(d)

Figure 6.19 1.0 mm/min, 24°, dense dry glass bead shear band development (a) prior to shearing, (b) 0.5 particle width displacement, (c) as shear band partially closes, and (d) shear band reopening

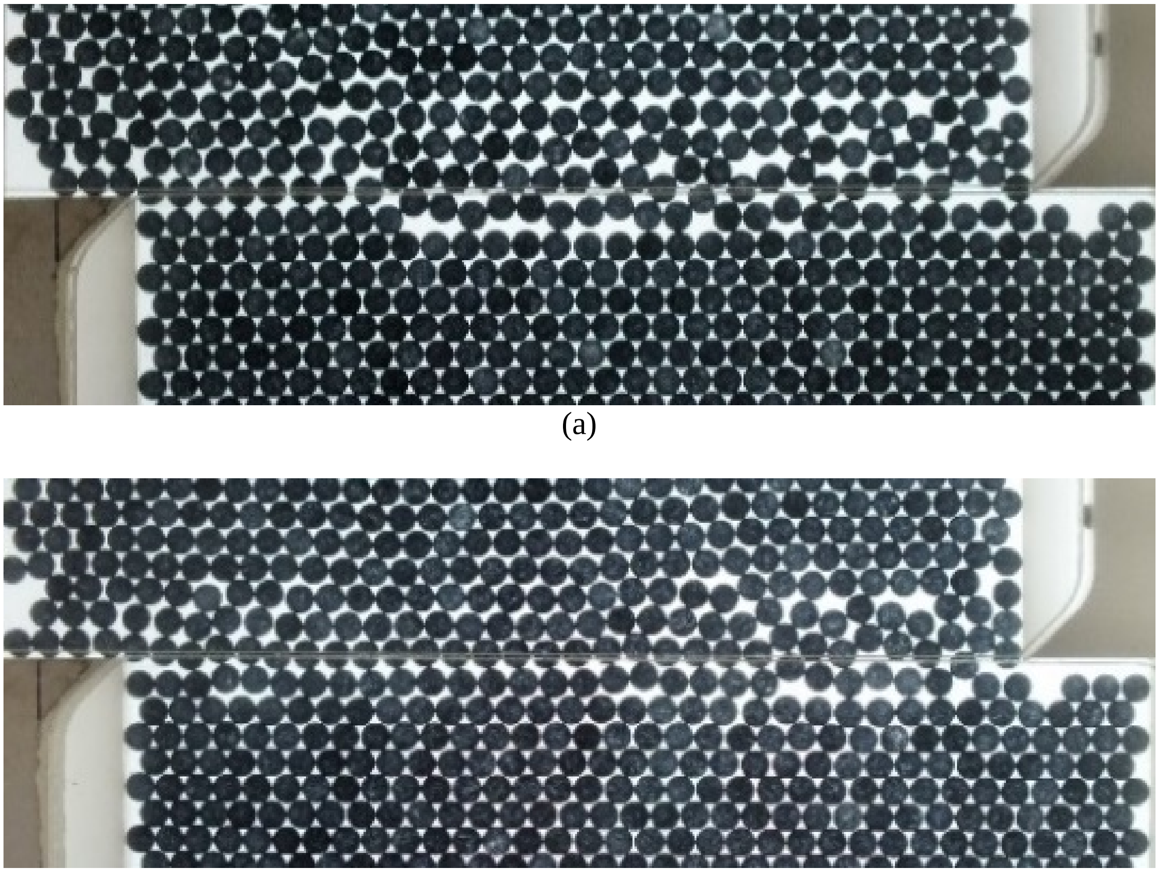

(a)

(b)

Figure 6.20 Comparison shear band for 24º inclination, dry, dense glass beads shear at (a) 0.5 mm/min and (b) 1.0 mm/min

exception horizontal displacements beyond 1.5 particle width. At that point, the inclusion of water reduced the more random movement as additional particles were engaged. Figure 6.21 and Figure 6.22 offer a comparison between the 0.5 mm/min, 24º inclination, dense glass beads dry and with water respectively. In Figure 6.21 (c), as the shear band collapsed, the geometry of the upper portion shear band changed. Figure 6.21 (b) shows a cubic packing before collapse and Figure 6.21 (c) shows as the top layer began to displace past the middle layer, the particle arrangement became less cubic and more irregular. When water was added, the cubic packing was maintained more ideally as the shear zone collapsed (Figure 6.22 (b) and Figure 6.22 (c)).

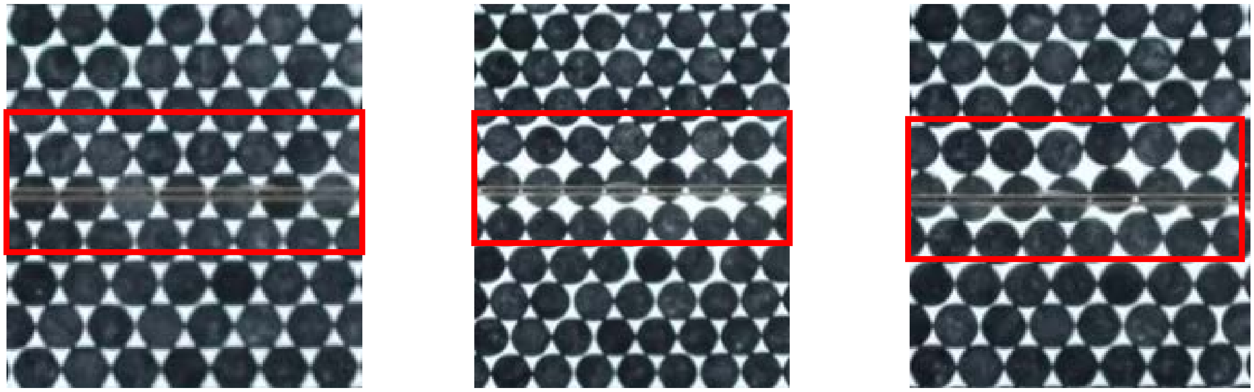
(a) (b) (c)

Figure 6.21 Zoomed shear band images for dry 0.5 mm/min dense glass beads inclined at 24º (a) prior to opening, (b) first opening, and (c) partially collapsed

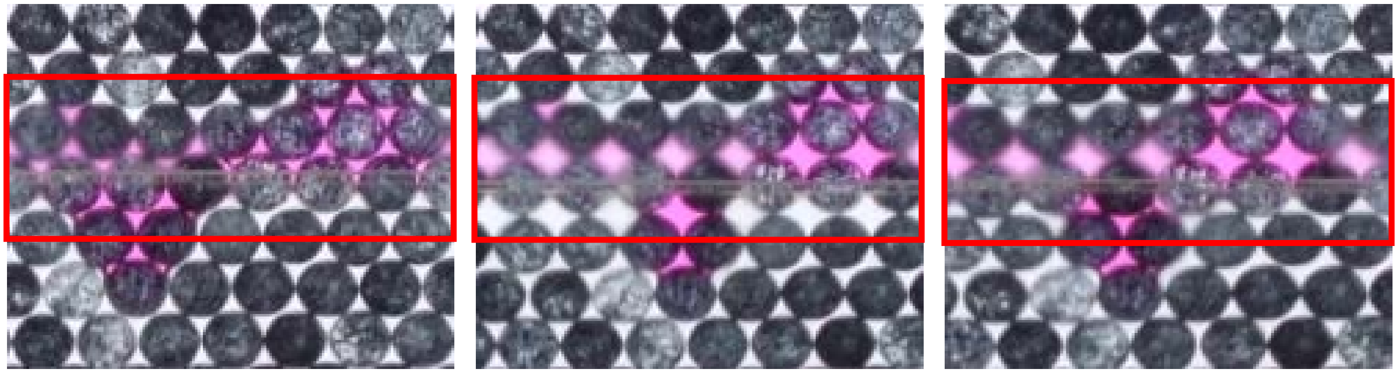
(a) (b) (c)

Figure 6.22 Zoomed shear band images for wet 0.5 mm/min dense glass beads inclined at 24º (a) prior to opening, (b) first opening, and (c) partially collapsed

The next step in the analysis was to examine the shear band development in the dry loose glass beads. Utilizing the videos of the test images to identify a shear band in the dry, loose glass beads was inconclusive. Regardless of the normal force, as the horizontal displacement of the shear box increased, the glass beads rotated and rearranged themselves. The rearrangement was inconsistent and did not present a systematic pattern. Some of the particles moved from the lower portion of the shear box into the upper portion. While other particles moved in the reverse direction. Some chains of particles moved in straight lines, while other chains moved in arcs. However, an interesting observation was made during the 1.0 mm/min dry, 24º inclination, loose glass bead test. The glass beads moved up and over in an arching pattern over a group of glass beads that remained stationary.

The wet, loose glass bead tests were examined following the analysis of the dry, loose glass beads. Adding water to the shear zone provided a stabilizing effect. The stabilizing effect produced a more defined shear movement. The effect became more evident as the normal force and shear rate increased. However, the effect was not large enough to stabilize the significant internal movements. The internal movements prevented the development of a clear shear band as was present in the dense glass bead tests.

The next series of tests examined were the dry, loose and dense sand tests. Previous investigations showed for the dense sand tested, the shear band with was similar in size to the D_{60} of the sand (Peerun, Ong, & Choo, 2015). Based on this observation, for the 20-30 Ottawa sand used, the shear band should be approximately 0.75 mm wide. The construction of the apparatus was a significant hindrance when trying to identify the shear bands in both the loose and dense dry sands. The tripod used to support the camera was not directly attached to the direct shear device. Because of this, the camera was not always centered above the shear box division, nor was the camera lenses parallel to the viewing planes. The misalignment of the camera caused the thickness of viewing plane to be visible. The shear band was anticipated to form along the division in the shear box. Because the viewing planes were significantly thicker (5.6 mm) than the anticipated shear zone (0.75 mm), the region where the shear band would form was obscured.

Finally, the development of the shear band was investigated for the loose and dense wet sand tests. An interesting behavior was previously observed in both the loose and dense, wet, sand test. The water was introduced at the horizontal boundary of the upper and lower shear box. As in the loose and dense dry tests, the camera misalignment prevented the shear band to be investigated at the boundary of the shear box halves. However, during shearing a portion of the shear zone and subsequent shear band moved out and above the wetted region of the sands. The videos of the wet sands were examined to identify the extent of the shear band. In both the loose and dense wet sand tests, the macroscopic motions were visible to the naked eye. The motions identifying the shear band would occurred in a region approximately 0.75 mm wide, corresponding to a region 20 pixels wide in each of the videos. Examining the videos, the motions were not visible to the naked eye and were subsequently unidentified.

7 Conclusions and Recommendations

7.1 Conclusions

Fall cone and direct shear tests were conducted to provide a robust physical data set for the validation of Chrono::Granular and to investigate the effects of material and test parameters on bulk particle behavior and particle-scale motions. Glass beads and Ottawa sand were examined at different relative densities, ranging from less than 10% to greater than 90%, and subjected to different fall cone drop heights, and direct shear testing using three normal forces, two shear rates, and two different moisture states. The conclusions obtained from this research are presented below:

1. Cone geometry greatly affected the penetration values for both the sand and glass bead tests. Changing from a 30º to a 60° fall cone reduced the cone penetration values 40%. This agreed with the observations and conclusions made by Leroueil and Le Bihan (1996). Cone penetration was found to be most sensitive to cone geometry.
2. Relative density had an inverse relationship to cone penetration. As the relative density increased, cone penetration decreased. Increasing the relative density from 0% to 100% resulted in an average cone penetration reduction pf 25% and 32 % for the glass beads and sand respectively.
3. The glass beads and sand responded differently to cone penetration with the variations in relative density. This was attributed to the differences in relative particle size. The fall cones were three and six (30º and 60º fall cones respectively) glass bead diameters wide. As the cone impacted the surface of the glass beads, regardless of density, the point of impact greatly influenced cone

penetration. If the cone pierced a void at the surface, penetration continued for a distance before being restrained, while impacting the apex of a glass bead resulted in the cone slowing immediately.

4. Over a limited range of cone drop heights tested, an increase in drop height corresponded to an increase in cone penetration. The average cone penetration for the glass beads increased 38% and increased 12% for the sand. As previously indicated, the glass bead penetration values depended on where the fall cone first pierced the surface, i.e. void space or glass bead apex.
5. Frictional forces created from the interaction of the LVDT rod and rod housing greatly influenced impact velocity. Variations in impact velocity created variation in the penetration values.
6. Shear rate affected how the loose sand and loose glass beads responded to shear force in direct shear tests. Low shear rates allowed for particle rearrangement, whereas high shear rates create a rigid, skeletal response.
7. Shear rate affected how dense and dense glass beads responded to the shear force. Low shear rates created more random particle motions at high displacements, whereas high shear rates reduced the random particle motions at high displacements.
8. Including water into the shear zone reduced particle motions due to capillary forces. The capillary forces also have the potential to engage and move particles that would not have been affected in the dry state.
9. The compression front observed in the loose sand a glass bead tests was isolated in the upper portion of the shear box by introducing water into the shear zone.

10. In direct shear tests using wet sand, the shear surface first developed in the wetted region before climbing out of the wetted region and returning to horizontal. This indicated that the force necessary for the shear surface to relocate was less than the force required to overcome the capillary forces.
11. When sheared, the water in the shear area for the sand left the larger pores (air entry) and the extent of the wetted soil increased.
12. Shear band development for glass beads was dependent on shear rate and normal force. Higher shear rates and normal forces resulted in a more stable shear band. The inclusion of water in the shear zone stabilized the shear band response to horizontal displacement.

7.2 Recommendations

7.2.1 Improvements to the Materials

With regards to the fall cone tests, both materials performed within reason. However, the sand proved to be an issue with the direct shear tests. The image analysis software requires a specific amount of contrast and texture in the images to be accurately analyzed. At the distance the photos were taken, adequate texture was achieved, but the similarity in grain colors did not provide enough contrast. The tests were able to be completed at lower tolerances than recommended. Therefore, it is recommended that if 20-30 Ottawa sand is used in any PIV analysis, the sand be seeded with either artificial markers or dyed to provide adequate contrast in the images.

7.2.2 Improvements to Fall Cone Penetration Apparatus

In general, the apparatus performed very well. There are only two areas where improvements are warranted. The first area is the release mechanism. In all of the tests, the rod of the LVDT was held in place between two fingers. Some of the tests had noise in the results that resembled an oscillation. The oscillation did not affect the final results, but was an indication that something was not functioning as designed. The second area is the position of the fall cone mechanism. Maintaining perfect vertical alignment with the type of stand used was difficult due to how the LVDT was attached to the vertical stand. When the stand was positioned over the specimen prior to release, any bump to the LDVT would change the alignment. Section 6.1.4 discusses the influence of friction between the LDVT rod and rod housing on the falling speed and impact velocity of the fall cone. Both of these areas were identified as possible causes that reduced impact velocity, and caused variation in cone penetration values. Addressing these areas with a more stable release mechanism and a more stable connection between the LDVT and the adjustable stand would improve these issues.

7.2.3 Improvements to Direct Shear Apparatus

The amount of changes that should be made to the direct shear device is substantially more than the fall cone apparatus and are presented below:

1. The fixed portion of the shear box and the base plate should be machined out of one block of material.
2. The moving portion of the shear box should also be machined from one block instead of assembled from three pieces.
3. The moving portion of the shear box needs to be heavier. When the materials were sheared they pushed up against the fixed viewing plane and lifted it off the base plate. This allowed sand to get under the moving portion and create spikes in the shear force results.

4. Alignment screws should be installed to fix the sliding portion to the base plate when filling the shear box with materials.
5. The viewing planes should be held in place with a method other than set screws, or the set screws should be placed in the side opposite the load frame for easy access.
6. The viewing plane edge at the shear zone should be formed in such a way that allows for water to be introduced into the shear zone without removing or adjusting the moving portion of the shear box.
7. The camera should be mounted to the shear apparatus in such a manner where the camera is perfectly perpendicular to the base plate centered on the shear zone.
8. A camera that takes photos at a higher frame rate and that does not have to be reactivated after a certain number of photos should be used.
9. A more robust mechanism should be created to control the incline of the shear apparatus.

8 References

Alshibli, K. A., & Alsaleh, M. I. (2004). Characterizing Surface Roughness and Shape of Sands Using Digital Microscopy. *Journal of Computing in Civil Engineering, 18*(1), 36-45.

ASTM International. (2004). Standard practice for characterizing fly ash for use in soil stabilization. *ASTM D5239-04*. West Conshohocken, PA.

ASTM International. (2010). Standard test methods for laboratory determination of water (moisture) content of soil and rock by mass. *ASTM D2216-10*. West Conshohocken, PA.

ASTM International. (2011). Standard test method for direct shear test of soils under consolidated drained conditions. *ASTM D3080-11*. West Conshohocken, PA.

ASTM International. (2013). Standard specification for standard sand. *ASTM C778-13*. West Conshohocken, PA.

ASTM International. (2013). Standard test methods for time of setting of hydraulic cement by vicat needle. *ASTM C191-13*. Pa, West Conshohocken.

ASTM International. (2014). Standard test methods for specific gravity of soil solids by water pycnometer. *ASTM D854-14*. West Conshohocken, PA.

ASTM International. (2016). Standard test methods for maximum index density and unit weight of soils using a vibratory table. *ASTM D4253-16*. West Conshohocken, PA.

ASTM International. (2016). Standard test methods for minimum index density and unit weight of soils and calculation of relative density. *ASTM D4254-16*. West Conshohocken, PA.

Ayadat, T., & Hanna, A. (2007). Identification of collapsible soil using the fall cone apparatus. *Geotechnical Testing Journal, 30*(4), 1-12.

Beales Ferguson, T. A., & Standing, J. (2012). A 2-D Model Experimental Study of Helical Piles in Sand Using GeoPIV Software. *Civil and Environmental Engineering Student Conference.* London, UK: Imperial College London.

British Standards Institution (BSI). (1990). British standard methods of tests for soils for civil engineering purposes. *BS 1377-2*. London.

Bryant, S. K., Take, W. A., & Bowman, E. T. (2014). Observations of Grain-scale Interactions and Simulation of Dry Granular Flows in a Large-scale Flume. *Canadian Geotechnical Journal, 52*(5), 638-655.

Cevikbilen, G., & Budhu, M. (2011). Shear viscosity of clays in the fall cone test. *Geotechnical Testing Journal, 34*(6), 1-6.

Dai, B. B., Yang, J., & Zhou, C. Y. (2016). Observed effects of interparticle friction and particle size on shear behavior of granular materials. *International Journal of Geomechanics, 16*(1).

Edil, T., Bosscher, P., & Sundberg, A. (2006). Soil-structure interface shear transfer behavior. *Geomechanics II* (pp. 528-543). American Society of Civil Engineers.

Fu, W.-X., & Dai, F. (2015). Scale Dependence of Shear Strength for a Coarse Granular Soil using a Superimposition-nest Type of Direct Shear Apparatus. *Arabian Journal of Geosciences, 8*(12), 10301-10312.

Gallage, C., & Uchimura, T. (2016). Direct shear testing on unsaturated silty soils to investigate the effects of drying and wetting on shear strength parameters at low suction. *Journal of Geotechnical and Geoenvironmental Engineering, 142*(3).

Jackson, P., Bowman, E. T., & Cubrinovski, M. (2012). Seismic Testing of Model-scale Geosynthetic-reinforced Soil Walls. *Bulletin of the New Zealand Society for Earthquake Engineering, 45*(4), 171-183.

Jin, S. W., Choo, Y. W., Kim, Y. M., & Kim, D. S. (2014). Centrifuge modeling of differential settlement and levee stability due to staged construction of enlarged embankment. *KSCE Journal of Civil Engineering, 18*(4), 1036-1046.

Jotisankasa, A., & Taworn, D. (2016). Direct shear testing of clayey sand reinforced with live stake. *Geotechnical Testing Journal, 39*(4), 608-623.

Kang, X., Kang, G.-C., & Ge, L. (2013). Modified Time of Setting Test for Fly Ash Paste and Fly Ash-Soil Mixtures. *Journal of Materials in Civil Engineering, 25*(2), 296-301.

Lee, L. T., & Freeman, R. B. (2007). An alternative test method for assessing consistency limits. *Geotechnical Testing Journal, 30*(4), 1-8.

Leroueil, S., & Le Bihan, J.-P. (1996). Liquid limits and fall cones. *Canadian Geotechnical Journal, 33*(5), 793-798.

Li, Y. R., & Aydin, A. (2010). Behavior of Rounded Granular Materials in Direct Shear; Mechanisms and Quantification of Fluctuations. *Engineering Geology, 115*(1-2), 96-104.

Likos, W., & Jaafar, R. (2014, August). Laboratory Fall Cone Testing of Unsaturated Sand. *Journal of Geotechnical and Geoenvironmental Engineering, 140*(8), 04014043, 1-10.

Lu, N., & Likos, W. J. (2006). Suction stress characteristic curve for unsaturated soil. *Journal of Geotechnical and Geoenvironmental Engineering, 132*(2), 131-142.

Mazhar, H., Heyn, T., Pazouki, A., Melanz, D., Seidl, A., Bartholomew, A., . . . Negrut, D. (2013). Chrono: a parallel multi-physics library for rigid-body, flexible-body, and fluid dynamics. *Mechanical Sciences, 4*(1), 49-64.

Murashev, A. (2003). *Guidelines for design and construction of geosynthetic-reinforced soil structures.* Transfund New Zealand.

Peerun, I., Ong, D., & Choo, S. (2015). Behavior of reconstituted sand-sized particles in direct shear tests using PIV technology. *5th Asian Regional Conference on Soil Mechanics and Geotechnical Engineering, ARC 2015: New Innovations and Sustainability*, (pp. 354-359).

Powers, M. C. (1982). Comparison charts for estimating roundness and sphericity. *AGI Data Sheets*. Alexandria, VA: American Geological Institute.

Riethmuller, M., David, L., & Lecordier, B. (2013). Particle Image Velocimetry. In *Laser Velocimetry in Fluid Mechanics* (pp. 159-281). Hoboken, NJ: John Wiley & Sons, Inc.

Shimizu, M. (1997). Strain fields in direct shear box tests on a metal-rods model of granular soils. *Deformation and Progressive Failure in Geomechanics,* 151-156.

Skempton, A. W. (1958). Arthur Langtry Bell (1874–1956) and His Contribution to Soil Mechanics. *Géotechnique, 8*(4), 143-157.

Stanier, S. A., Blaber, J., Take, W. A., & White, D. J. (2015). Improved image-based deformations for geotechnical applications. *Canadian Geotechnical Journal*, 727-739.

Stasiak, M., & Molenda, M. (2004). Direct shear testing of flowability of food powders. *Research in Agricultural Engineering, 1,* 6-10.

Sundberg, A. J. (1999). *Interface Behavior of Granular Media in Direct Shear*. Master's Thesis.

Svoboda, J. (2013). Impact of strain rate on the shear strength and pore water pressure generation of clays and sands. *(Master's Thesis)*. (Order No. 1558765). Available from ProQuest Dissertations & Theses Global. (1551196533). Retrieved from http://search.proquest.com.ezproxy.library.wisc.edu/docview/1551196533?accountid=465

Swedish Geotechnical Society. (1992, June 15). Recommended standard for cone penetration tests.

Takita, H., & Sumita, I. (2013, August 26). Low-velocity impact cratering experiments in a wet sand. *Physical Review E - Statistical, Nonlinear, and Soft Matter Physics, 88*(2).

Taylor, D. (1948). *Fundamentals of soil mechanics.* New York: John Wiley and Sons.

Teng, Y., Stanier, S. A., & Gourvenec, S. M. (2015). Synchronized multi-scale image analysis of soil deformations. *International Journal of Physical Modelling in Geotechnics*.

Voulgari, C. (2015). An experimental model for slopes subject to weathering. *IOP Conference Series: Earth and Environmental Science. 26.* International Symposium on Geohazards and Geomechanics.

White, D., Take, W., & Bolton, M. (2003). Soil deformation measurement using Particle Image Velocimetry (PIV) and photogrammetry. *Geotchnique, 53*(7), 619-631.

Zentar, R., Abriak, N.-E., & Dubois, V. (2009). Fall cone test to characterize shear strength of organic sediments. *Journal of Geotechnical and Geoenvironmental Engineering, 135*(1), 153-157.

Zhang, Q., Li, Y., Hou, M., Jiang, Y., & Liu, M. (2012). Elastic Waves in the Presence of a Granular Shear Band Formed by Direct Shear. *Physical Review. E, Statistical, Nonlinear, and Soft Matter Physics, 85*(3 Pt 1), 031306, 1-5.

Appendix A Jay go Inc. Dragonite ® Soda Lime Glass Beads Type-M Data Sheets

JAYGO
INCORPORATED

Dragonite® Soda Lime Glass Beads

Type M - Article 5000 Available sizes 1.5mm to 9.0mm

Article	Diameter	Tolerance	Resistance to compression	Bulk density	Pieces per lb.
5002	1.5 mm	+/- 0.2 mm	750 - 800 N	93.60 lbs/cu.ft.	102,886
5003	2.0 mm	+/- 0.2 mm	950 - 1050 N	93.60 lbs/cu.ft.	43,404
5004*	2.5 mm	+/- 0.2 mm	1350 - 1450 N	93.60 lbs/cu.ft.	22,222
5005	3.0 mm	+/- 0.3 mm	1500 - 1700 N	93.60 lbs/cu.ft.	12,859
5006*	3.5 mm	+/- 0.3 mm	2050 - 2250 N	93.60 lbs/cu.ft.	8,095
5009	4.0 mm	+/- 0.3 mm	2300 - 2500 N	93.60 lbs/cu.ft.	5,422
5010	4.5 mm	+/- 0.3 mm	2600 - 2800 N	93.60 lbs/cu.ft.	3,809
5011	5.0 mm	+/- 0.3 mm	3000 - 3300 N	93.60 lbs/cu.ft.	2,777
5012	6.0 mm	+/- 0.3 mm	3800 - 4200 N	92.35 lbs/cu.ft.	1,604
5013	7.0 mm	+/- 0.3 mm		92.35 lbs/cu.ft.	1,009
5014	8.0 mm	+/- 0.4 mm		92.35 lbs/cu.ft.	677
5015	9.0 mm	+/- 0.4 mm		90.48 lbs/cu.ft.	472

Resistance to compression: internal test with Compressive strength inspector No. 10004.1, Company Hegewald & Peschke
*special sizes available by request

Technical / Physical Data

Melting point	1404	°C	
Softening point (Littleton point)	721	°C	($10^{7,65}$ dPas)
Transformation temperature	550	°C	(10^{13} dPas)
Specific thermal Conductivity	1.129	W/Km	
Coefficient of expansion	9.36	10^{6} (1/K)	(20-400 °C)
Specific thermal capacity	1.335	kJ/kg K	(> 600 °C)
Refractive index	1.5225		
Youngs-Module	65	GPa	
Hardness according to Mohs	6		
Specific weight	2.50	kg/dm3	Test with Pyknometer according DIN ISO 787-10
Abrasion after 9 h grinding	19.25	weight%	Abrasion test dd. 28.10.2005; Test conditions: Laboratory mill PML H/V, Speed 13,4 m/s, Filling grade 70 Vol.% Milling suspension: 4 kg Water, 1 kg Titandioxide Beads: Art. 5002, 1,50 mm
Air bubbles inside bead (> 0,3 mm)	≤ 1.0	%	Visual test: internal control of 200 Glass beads by Microscope

Jaygo, Inc. manufacturers and supplies various types of equipment for the Chemical, Food and Pharmaceutical Industries:

- Continuous high speed grinding mills
- Heavy Duty low speed dispersers
- High speed dispersers
- Filters/Dryers
- Sigma Blade Mixers/Extruders
- Conical ScrewBlenders
- High speed turbulent mixers
- Reactors
- Liquid filters
- Vacuum Deaerators
- General fabrication

Modern test room facilities at our plant to test your product on any of the above equipment.

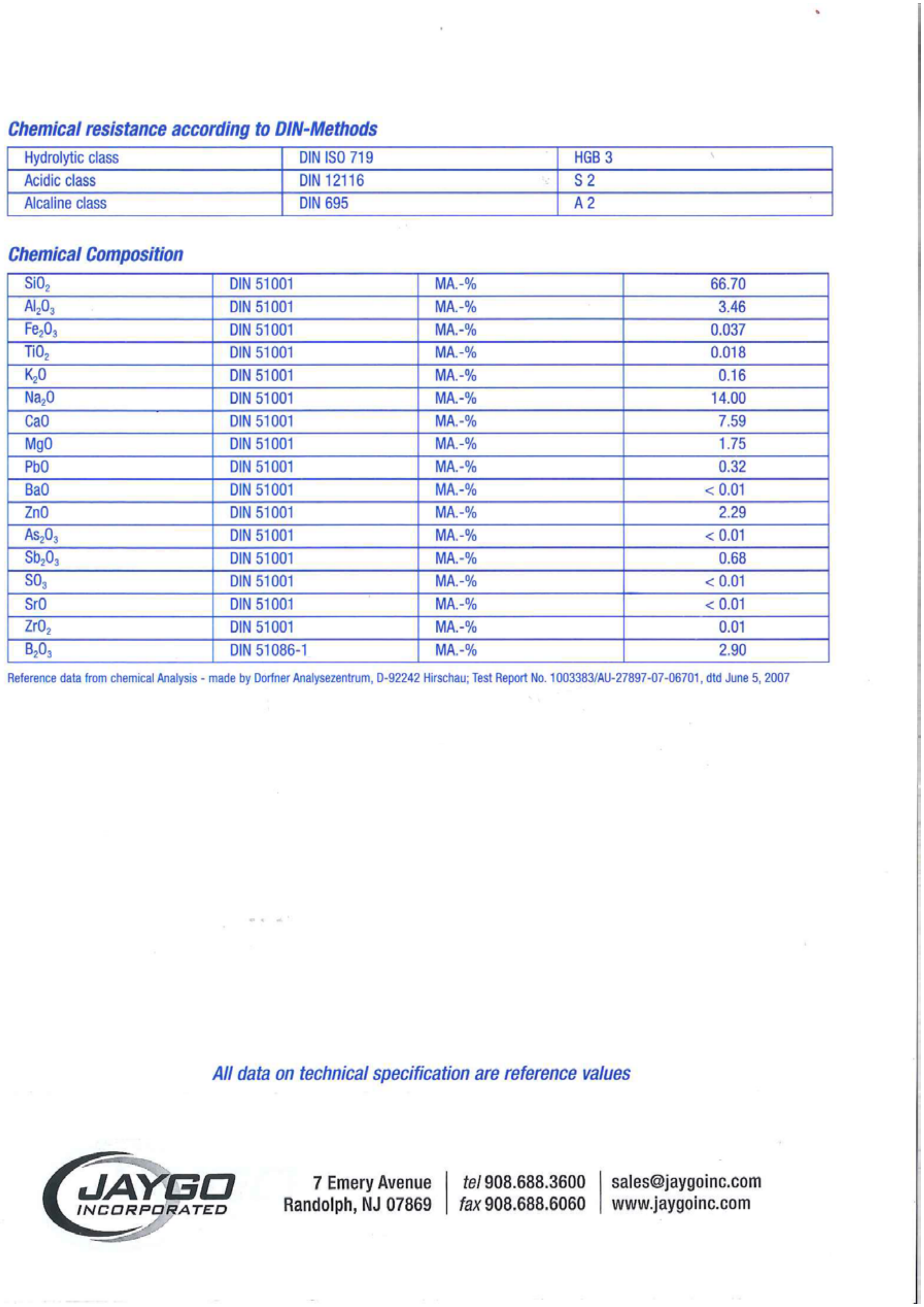

Chemical resistance according to DIN-Methods

Hydrolytic class	DIN ISO 719	HGB 3
Acidic class	DIN 12116	S 2
Alcaline class	DIN 695	A 2

Chemical Composition

SiO_2	DIN 51001	MA.-%	66.70
Al_2O_3	DIN 51001	MA.-%	3.46
Fe_2O_3	DIN 51001	MA.-%	0.037
TiO_2	DIN 51001	MA.-%	0.018
K_2O	DIN 51001	MA.-%	0.16
Na_2O	DIN 51001	MA.-%	14.00
CaO	DIN 51001	MA.-%	7.59
MgO	DIN 51001	MA.-%	1.75
PbO	DIN 51001	MA.-%	0.32
BaO	DIN 51001	MA.-%	< 0.01
ZnO	DIN 51001	MA.-%	2.29
As_2O_3	DIN 51001	MA.-%	< 0.01
Sb_2O_3	DIN 51001	MA.-%	0.68
SO_3	DIN 51001	MA.-%	< 0.01
SrO	DIN 51001	MA.-%	< 0.01
ZrO_2	DIN 51001	MA.-%	0.01
B_2O_3	DIN 51086-1	MA.-%	2.90

Reference data from chemical Analysis - made by Dorfner Analysezentrum, D-92242 Hirschau; Test Report No. 1003383/AU-27897-07-06701, dtd June 5, 2007

All data on technical specification are reference values

JAYGO INCORPORATED

7 Emery Avenue
Randolph, NJ 07869

tel 908.688.3600
fax 908.688.6060

sales@jaygoinc.com
www.jaygoinc.com

Appendix B Matlab Image Analysis Script

```
%% This script is used to detect circles and determine their radii using
imfindcircles
%
% Things you need to know prior to the use:
% Diameter range in pixels
% Limits of circle center locations in pixel coordinates. Again, use Paint.
clear


d = 120;
r1 = (d/2)-(d*0.05);
r2 = (d/2)+(d*0.05);




x1 = 140;  %Top Left
x2 = 4500;  %Bottom Right
y1 = 510;  %Top Left
y2 = 2650;  %Bottom Right

scale = 42.58; %1 mm = XX pixels





%% Step 1: Load the Image
%
% You need to know the exact file name of the image with the extension,
% case sensitive

color = imread('Sample5.jpg'); %color
gray = rgb2gray(color);        %Gray Scale
bw = im2bw(color,0.25);           %Binary - Change the # as necessary to get
right intensity

% Remove the following comments if you want to see the image when loaded

% subplot(4,1,1)
% imshow(color);
% subplot(4,1,2)
% imshow(gray);
% subplot(4,1,3)
% imshow(bw);


%% Step 2: Quick Check

% This step does a quick fit
[centers1, radii1] = imfindcircles(color,[r1 r2],'ObjectPolarity','dark');


%% Step 3: Refining
```

```
% this step is where the you refine the circles

[centers1, radii1] = imfindcircles(gray,[r1 r2],'ObjectPolarity','dark', ...
    'Sensitivity',0.9823);

%[centers2, radii2] = imfindcircles(color,[r1 r2], 'ObjectPolarity','dark',
...
          %'Sensitivity',0.98,'Method','twostage');

imshow(color);
h = viscircles(centers1, radii1,'EdgeColor','b');
%viscircles(centers2, radii2,'EdgeColor','r');


%% Step 4: Removes circles outside of box
%
% This step removes the noise outside of the box
 z = 1;
 centers = zeros(1,2);



 for n = 1:length(centers1);
     x = centers1(n,1);
     y = centers1(n,2);
     r = radii1(n,1);
     if ((x + r) <= x2) && ((x - r) >= x1) && ((y + r) <= y2) && ((y - r) >=
y1);
       centers(z,1) = x;
       centers(z,2) = y;
       radii(z,1) = r;
       diameter (z,1) = r*2;
       z = z + 1;
     end
 end
 delete (h)
 imshow(color)
 h = viscircles(centers, radii,'EdgeColor','r');

 %% Step 5 : Converting to realworld and statistics
 % Convert to real space


 cv = 1/scale;
 radii = radii .* cv;
 diameter = diameter .* cv;
 % Gets the average and stdev
 number = z
 ave_Radii = mean(radii)
 stdev_Radii = std(radii)
 ave_Dia = mean(diameter)
 stdev_Dia = std(diameter)
```

Appendix C Direct Shear Apparatus Schematics

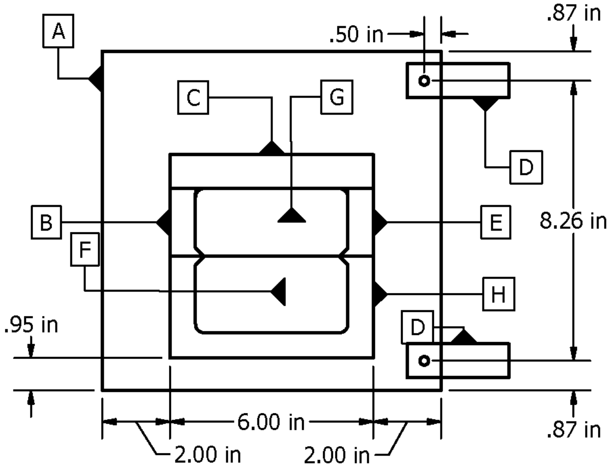

PARTS LIST			
ITEM	QTY	PART NUMBER	DESCRIPTION
Base	1	A	
Rolling Part Left	1	B	Left portion of the moving section of the shear box
Floating Part	1	C	Connects left and right portions of the shear box
Adapters	2	D	Adapters to connect load frame to shear device
Rolling Part Right	1	E	Right portion of the moving section of the shear box. Connects to load cell
Bottom Pane	1	F	Clear pane that restricts vertical material movement in fixed shear box portion
Top Pane	1	G	Clear pane that restricts vertical material movement in moving shear box portion
Fixed Portion	1	H	Fixed portion of the direct shear box

DRAWN Kyle Williams	11/3/2016	University of Wisconsin - Madison
TITLE Particle-Scale Direct Shear Device	Overview	SHEET 1 OF 12

NOTES:

1. CONSTRUCTED FROM 0.220" ABRASION RESISTANT ACRYLIC
2. 0.25" DIAMETER HOLES ARE TAPPED FOR 0.25" DIAMETER THREADED BOLT

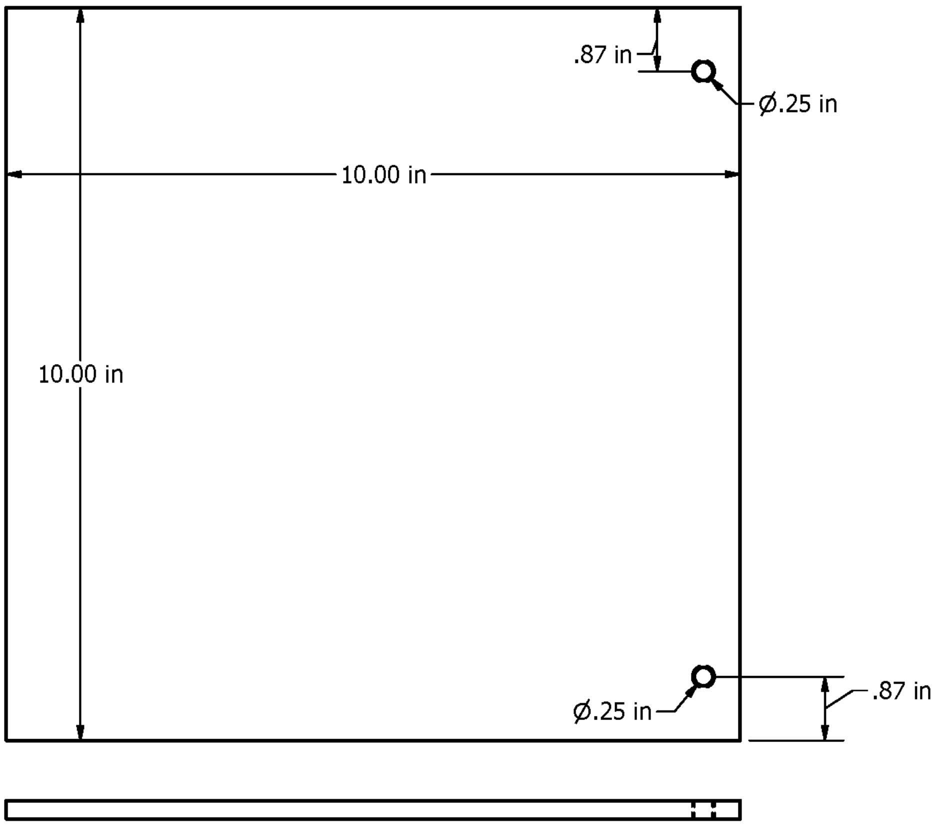

DRAWN Kyle Williams	11/3/2016	University of Wisconsin - Madison
TITLE Particle-Scale Direct Shear Device	Base	SHEET 2 OF 12

NOTES:

1. CONSTRUCTED FROM 0.220" ABRASION RESISTANT ACRYLIC

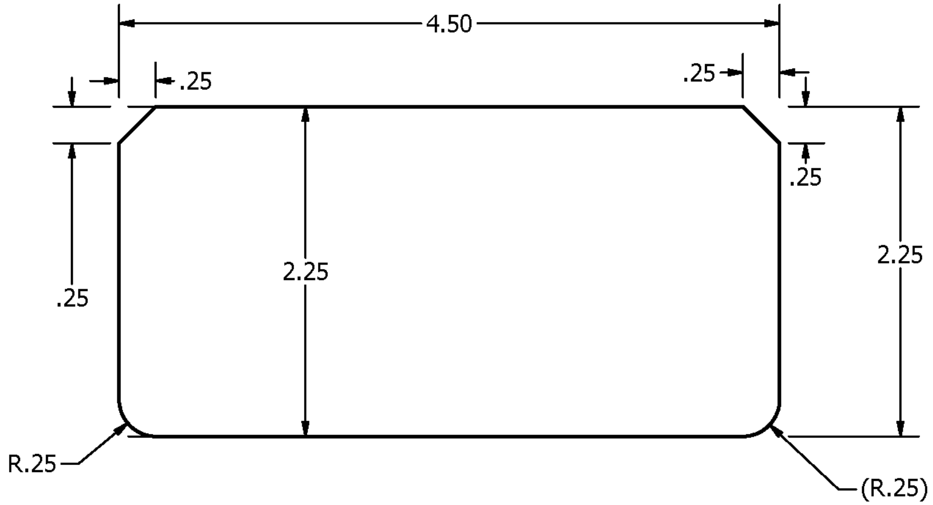

DRAWN Kyle Williams	11/3/2016	University of Wisconsin - Madison
TITLE Particle-Scale Direct Shear Device	BOTTOM VIEWING PANE	SHEET 3 OF 12

NOTES:

1. CONSTRUCTED FROM 1" DIAMETER ALUMINUM ROD
2. 3 SET SCREWS WERE INSTALLED ALONG BOTTOM OF CONNECTOR
3. 0.25" DIAMETER HOLE TAPPED FOR 0.25" DIAMETER THREADED BOLT

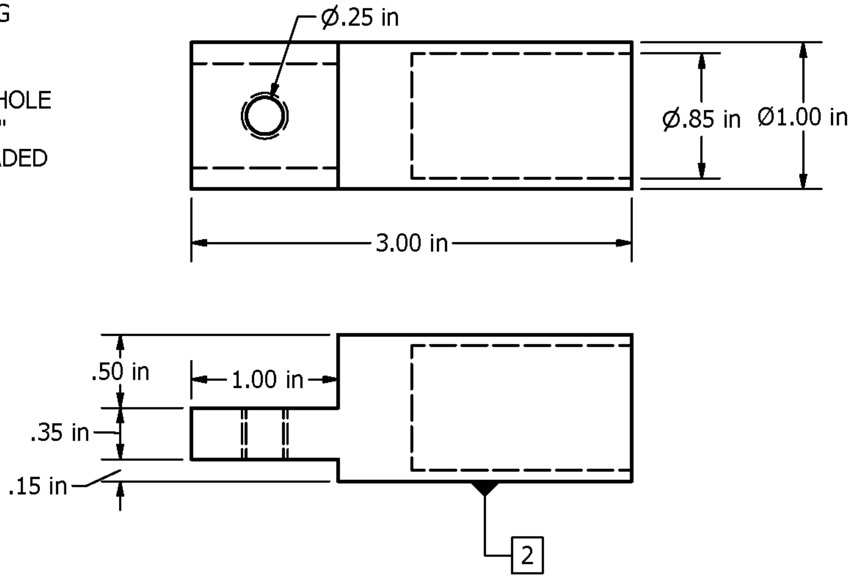

DRAWN Kyle Williams	11/3/2016	University of Wisconsin - Madison
TITLE Particle-Scale Direct Shear Device	CONNECTOR	SHEET 4 OF 12

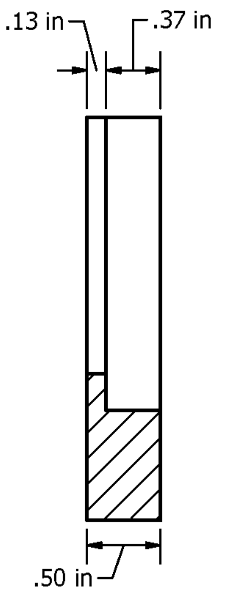

SECTION A-A
SCALE 1 : 1

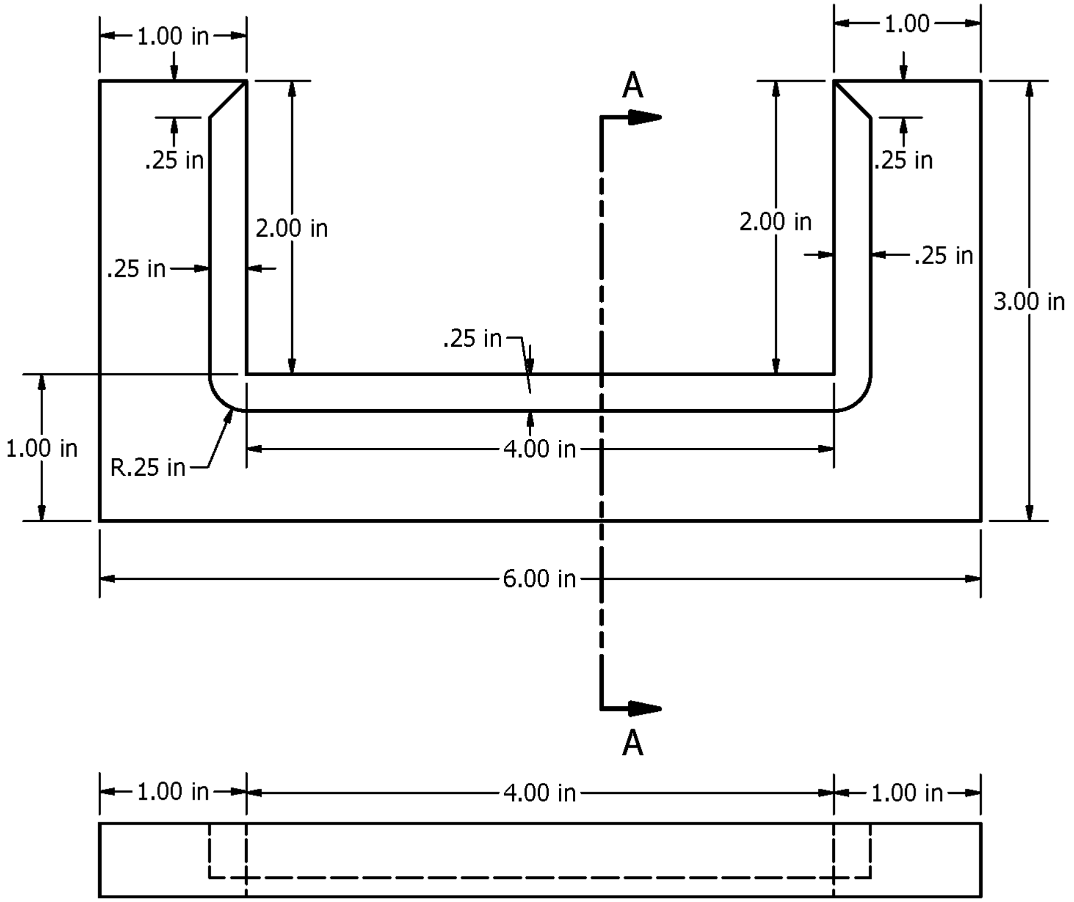

NOTES:

1. CONSTRUCTED FROM 1" SQUARE ACETAL ROD

DRAWN Kyle Williams	11/3/2016	University of Wisconsin - Madison
TITLE Particle-Scale Direct Shear Device	FIXED PORTION OF SHEAR BOX	SHEET 5 OF 12

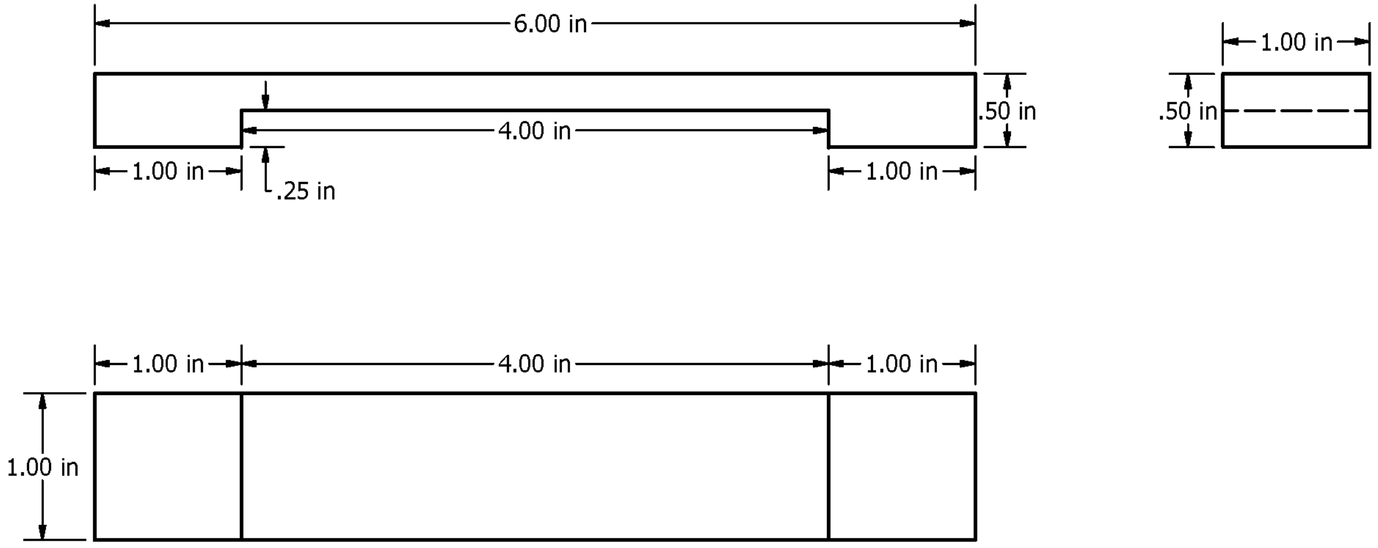

NOTES:

1. CONSTRUCTED FROM 1" SQUARE ACETAL ROD

DRAWN
Kyle Williams
11/3/2016
University of Wisconsin - Madison
TITLE
Particle-Scale Direct Shear Device
FLOATING PART
SHEET 6 OF 12

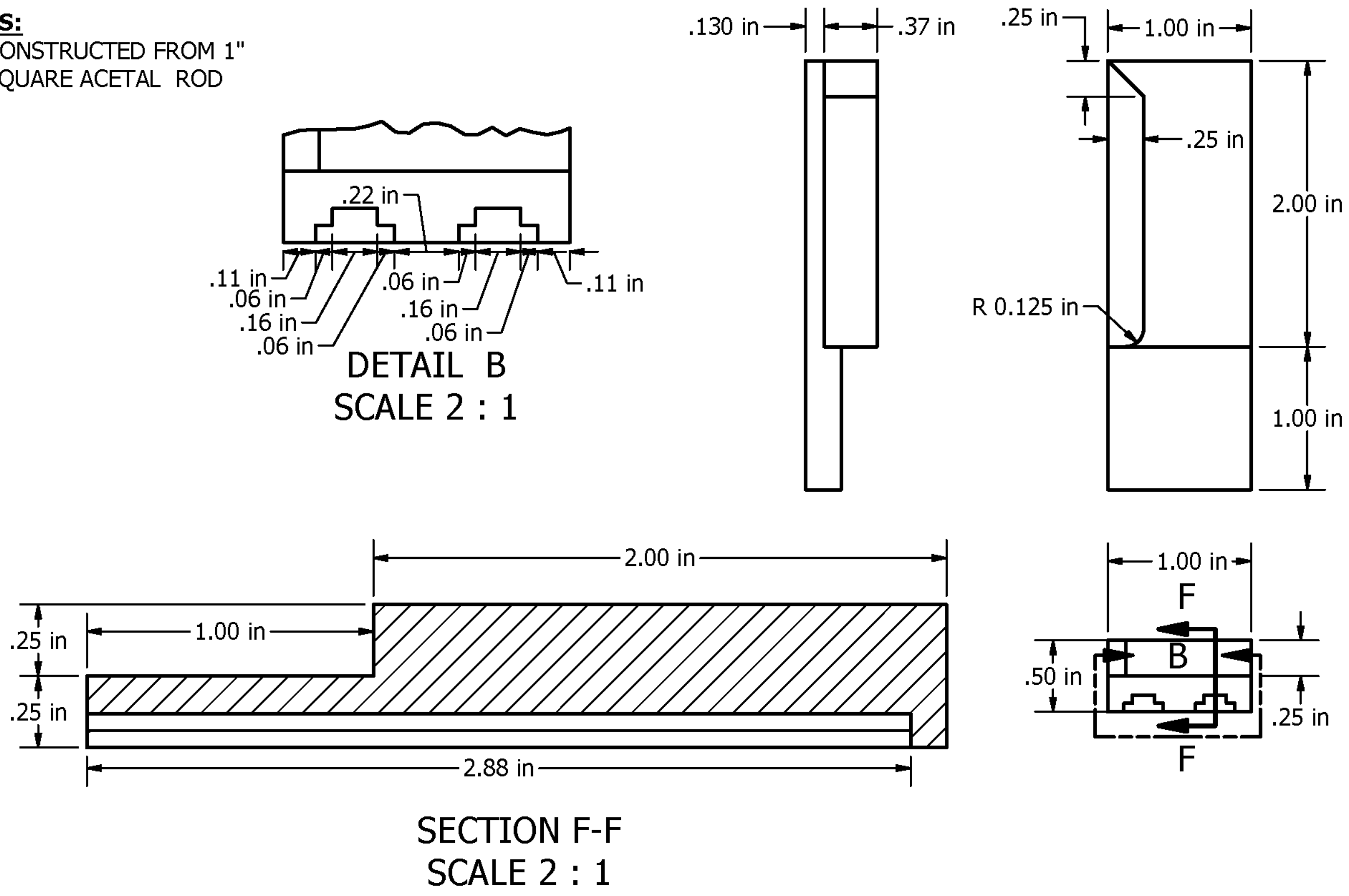

NOTES:

1. CONSTRUCTED FROM 1" SQUARE ACETAL ROD

DRAWN
Kyle Williams

11/3/2016

University of Wisconsin - Madison

TITLE
Particle-Scale Direct Shear Device

ROLLING PART LEFT

SHEET 7 OF 12

NOTES:

1. CONSTRUCTED FROM 1" SQUARE ACETAL ROD
2. ALL 0.09" DIAMETER HOLES TAPPED FOR 4-40 THREADED ROD

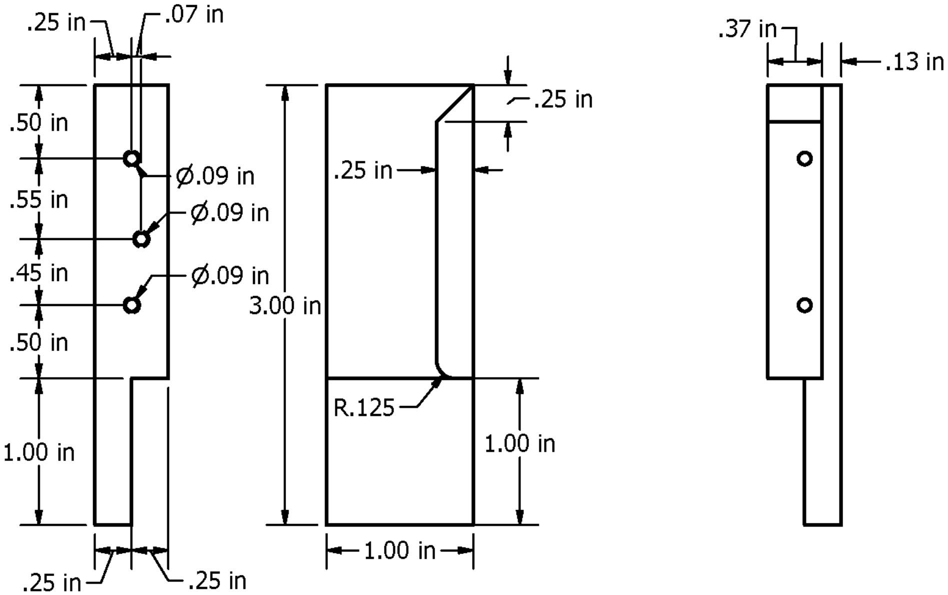

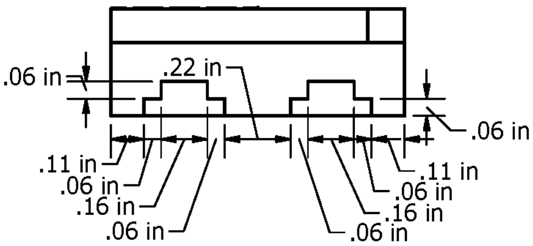

DETAIL G
SCALE 2 : 1

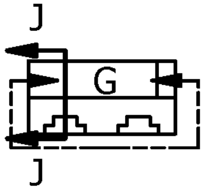

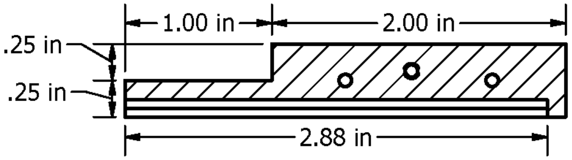

SECTION J-J
SCALE 1 : 1

DRAWN
Kyle Williams
11/3/2016
University of Wisconsin - Madison
TITLE
Particle-Scale Direct Shear Device
ROLLING PART RIGHT
SHEET 8 OF 12

NOTES:

1. CONSTRUCTED FROM 0.220" ABRASION RESISTANT ACRYLIC

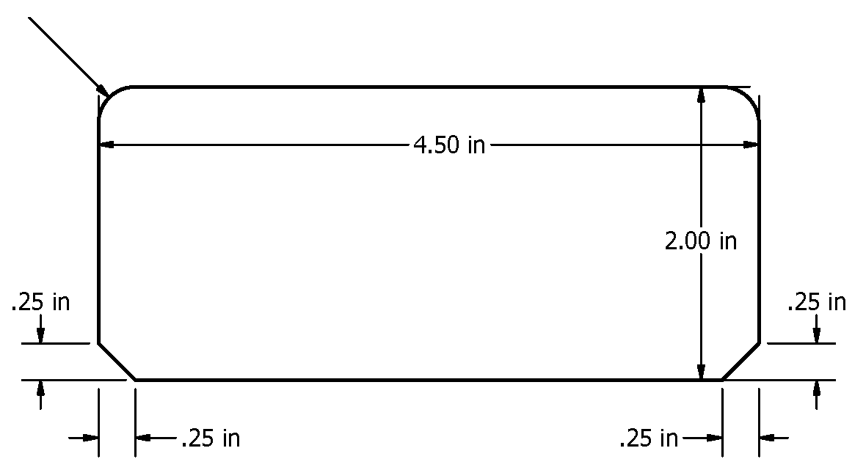

DRAWN
Kyle Williams

11/3/2016

University of Wisconsin - Madison

TITLE
Particle-Scale Direct Shear Device

TOP VIEWING PANE

SHEET 9 OF 12

NOTES:

1. CONSTRUCTED FROM 1" SQUARE ACETAL ROD

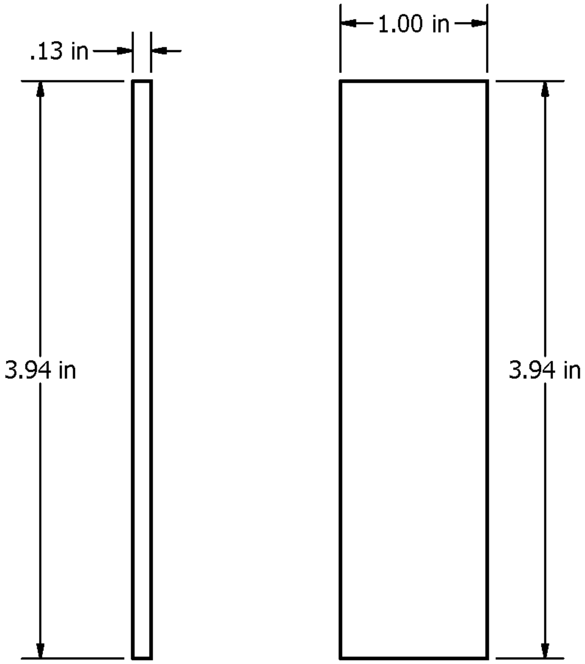

DRAWN Kyle Williams	11/3/2016	University of Wisconsin - Madison
TITLE Particle-Scale Direct Shear Device	8.01 g mass	SHEET 10 OF 12

NOTES:

1. CONSTRUCTED FROM 1" SQUARE ACETAL ROD
2. TOTAL MASS OF BOTH PARTS AND EPOXY = 53.64 g

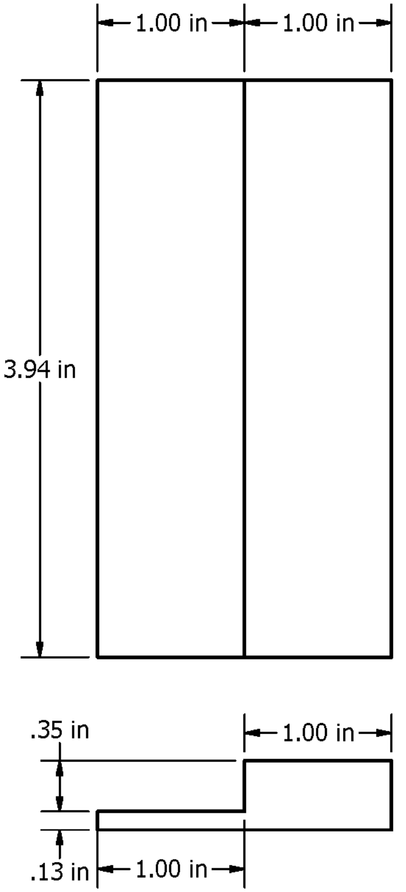

DRAWN Kyle Williams	11/3/2016	University of Wisconsin - Madison
TITLE Particle-Scale Direct Shear Device	53.64 g mass	SHEET 11 OF 12

NOTES:

1. CONSTRUCTED FROM 1" SQUARE ACETAL ROD
2. REPRESENTS BOTH 66.64 g AND 67.19 g ADDITIONAL MASS BLOCKS
3. DIFFERENCE BETWEEN TESTS DUE TO EPOXY WEIGHT

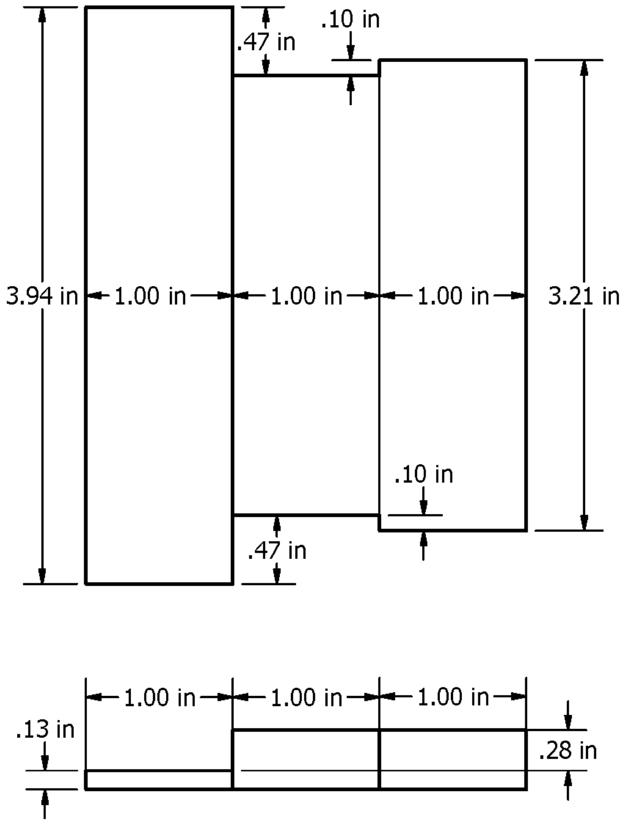

DRAWN Kyle Williams	11/3/2016	University of Wisconsin - Madison
TITLE Particle-Scale Direct Shear Device	66.64 g AND 67.19 g MASS	SHEET 12 OF 12

Appendix D Dry Glass Beads Direct Shear Results

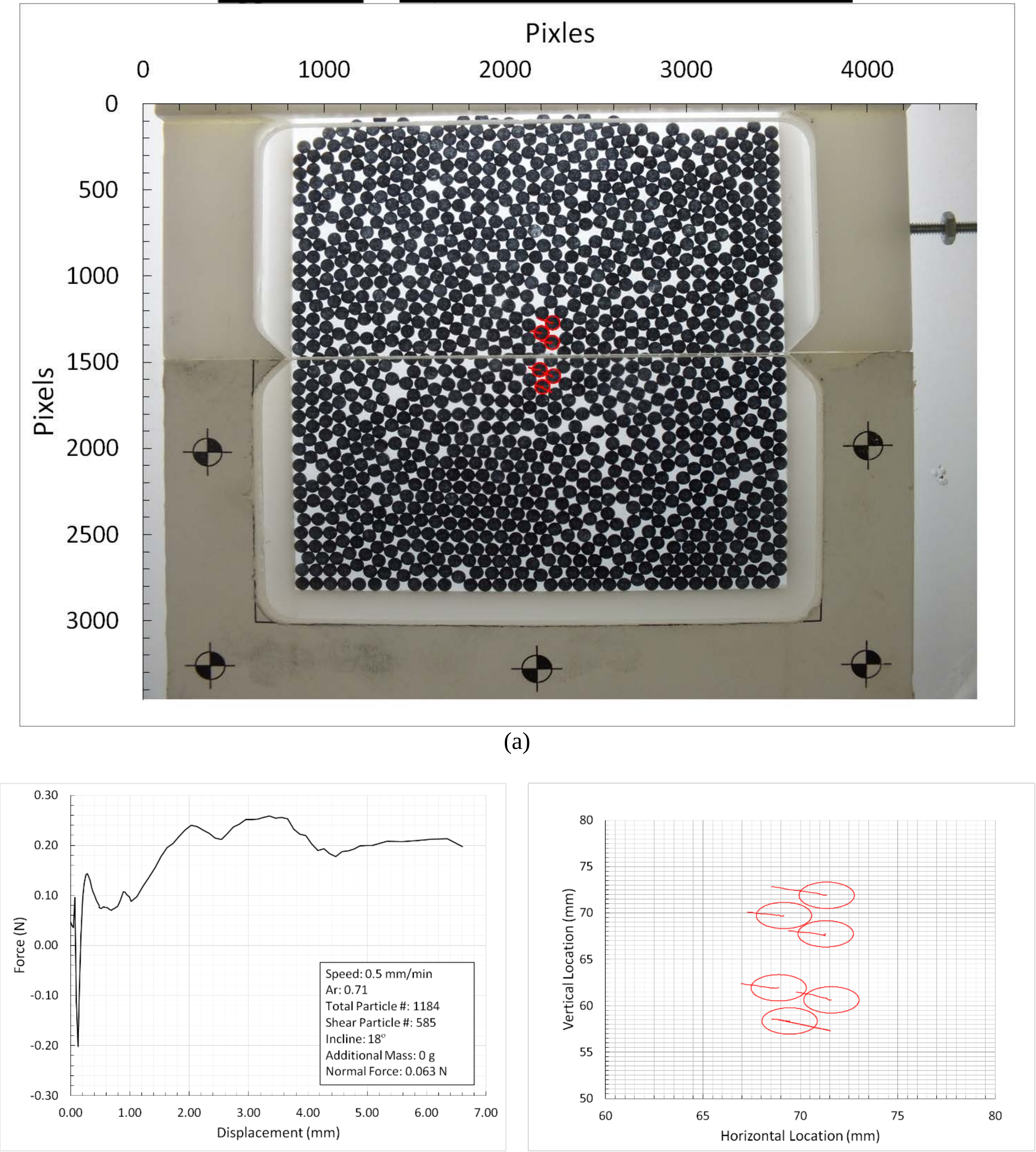

(a)

(b)

(c)

Figure: D.1 Glass bead results for 0.5 mm/min, loose state, 18° incline: (a) Image space movements, (b) Shear response, (c) Real space movements

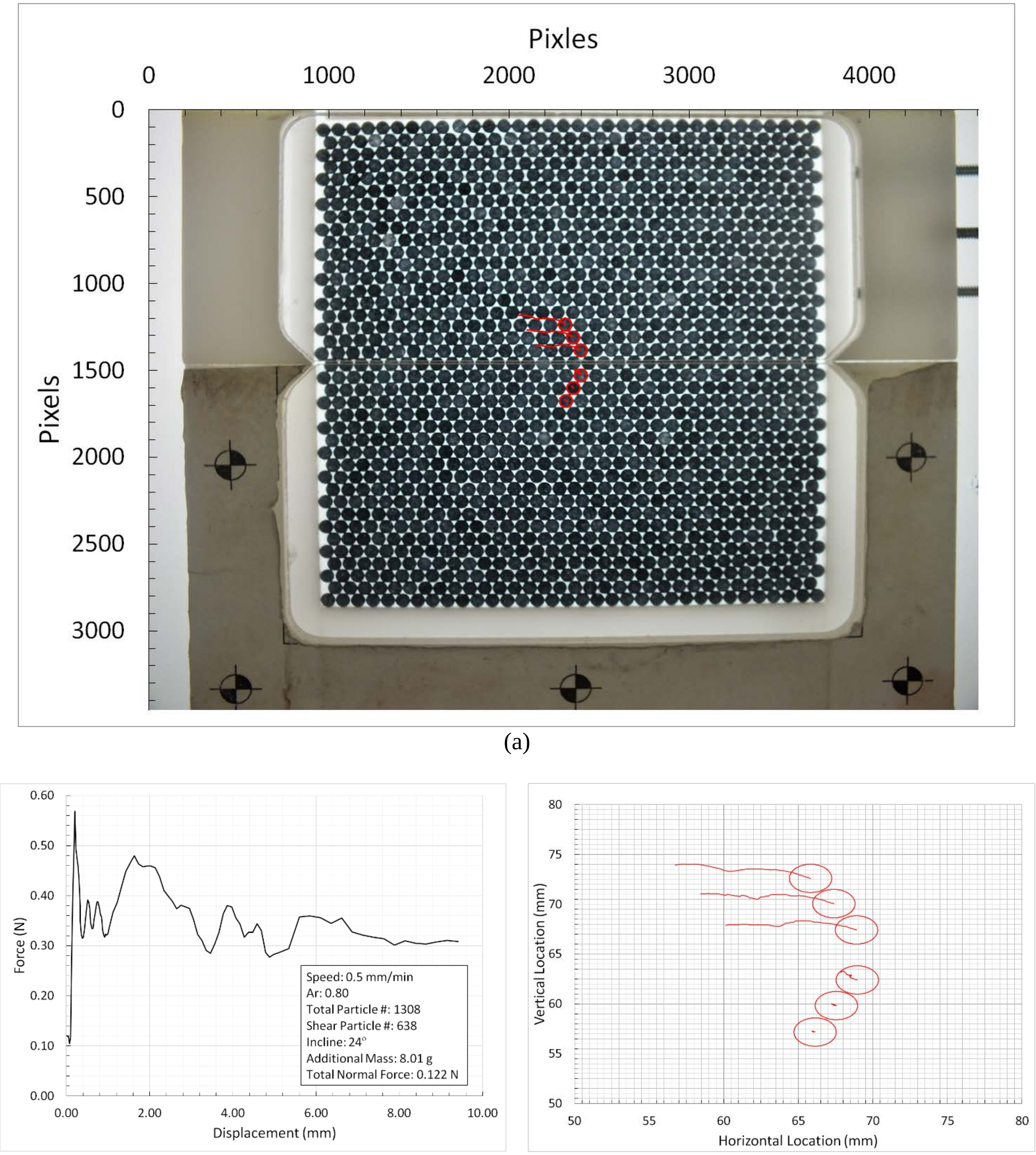

(a)

(b)

(c)

Figure: D.2 Glass bead results for 0.5 mm/min, dense state, 24° incline:
(a) Image space movements, (b) Shear response, (c) Real space movements

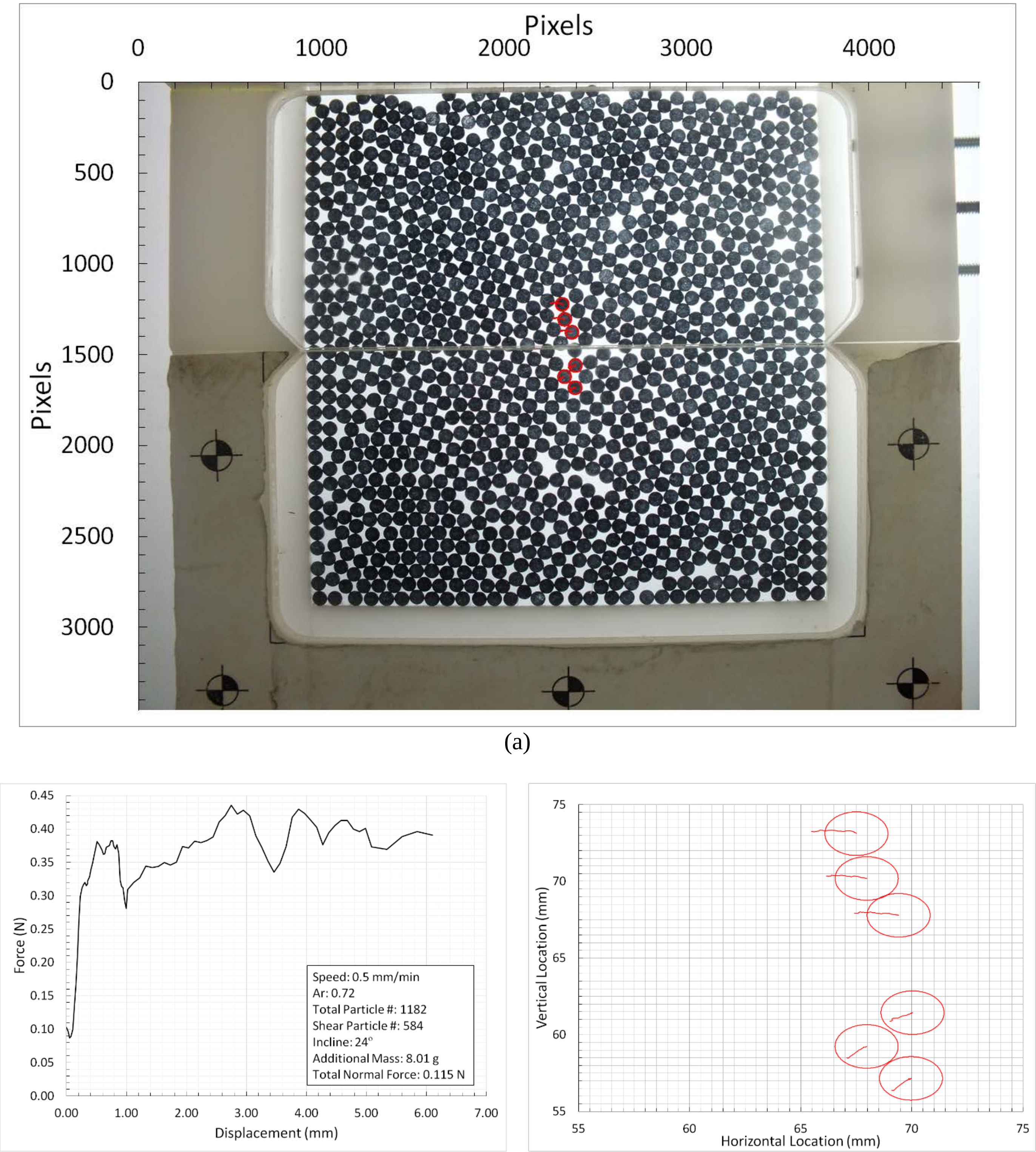

(a)

(b)

(c)

Figure: D.3 Glass bead results for 0.5 mm/min, loose state, 24° incline:
(a) Image space movements, (b) Shear response, (c) Real space movements

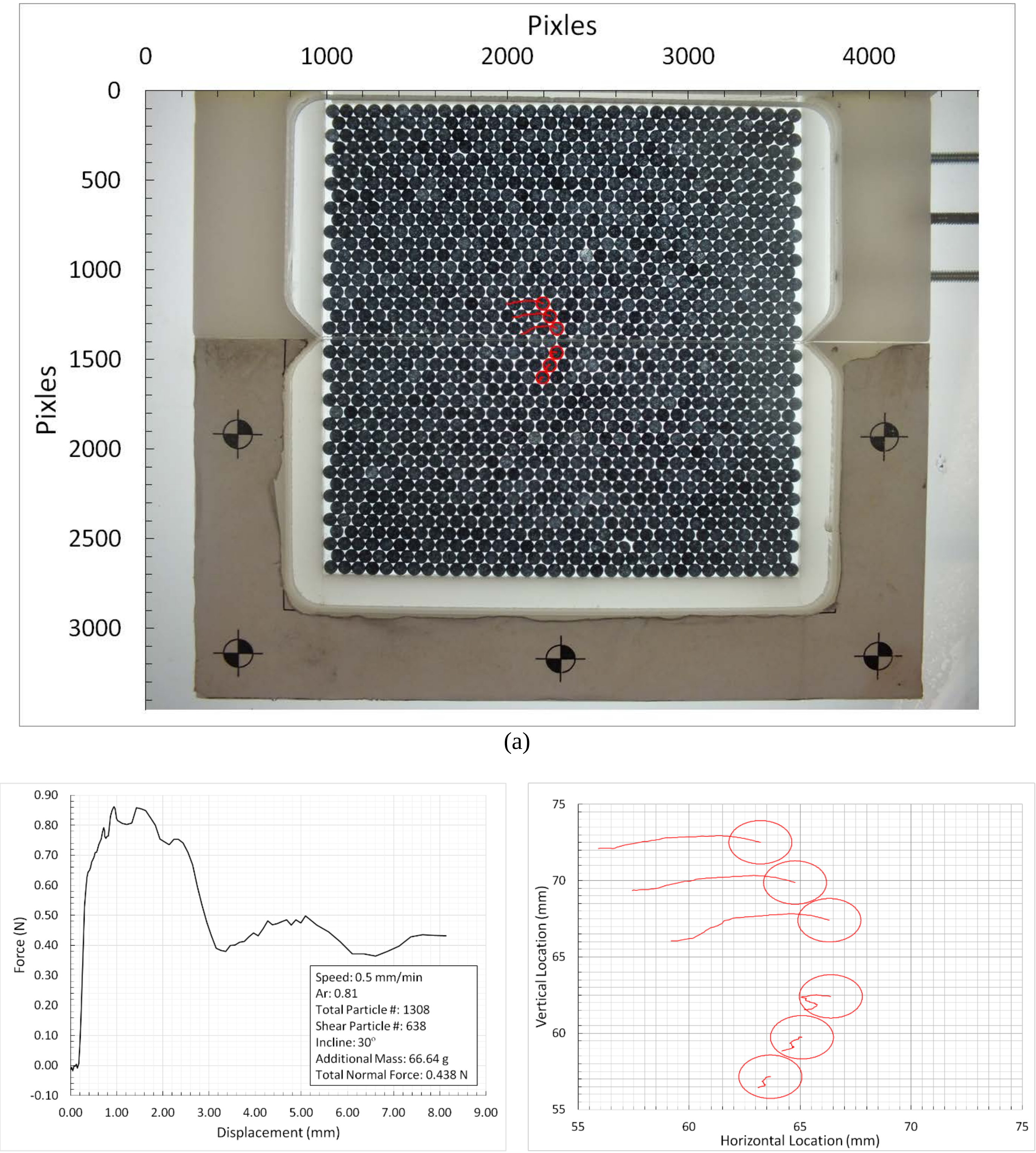

(a)

(b)

(c)

Figure: D.4 Glass bead results for 0.5 mm/min, dense state, 30° incline: (a) Image space movements, (b) Shear response, (c) Real space movements

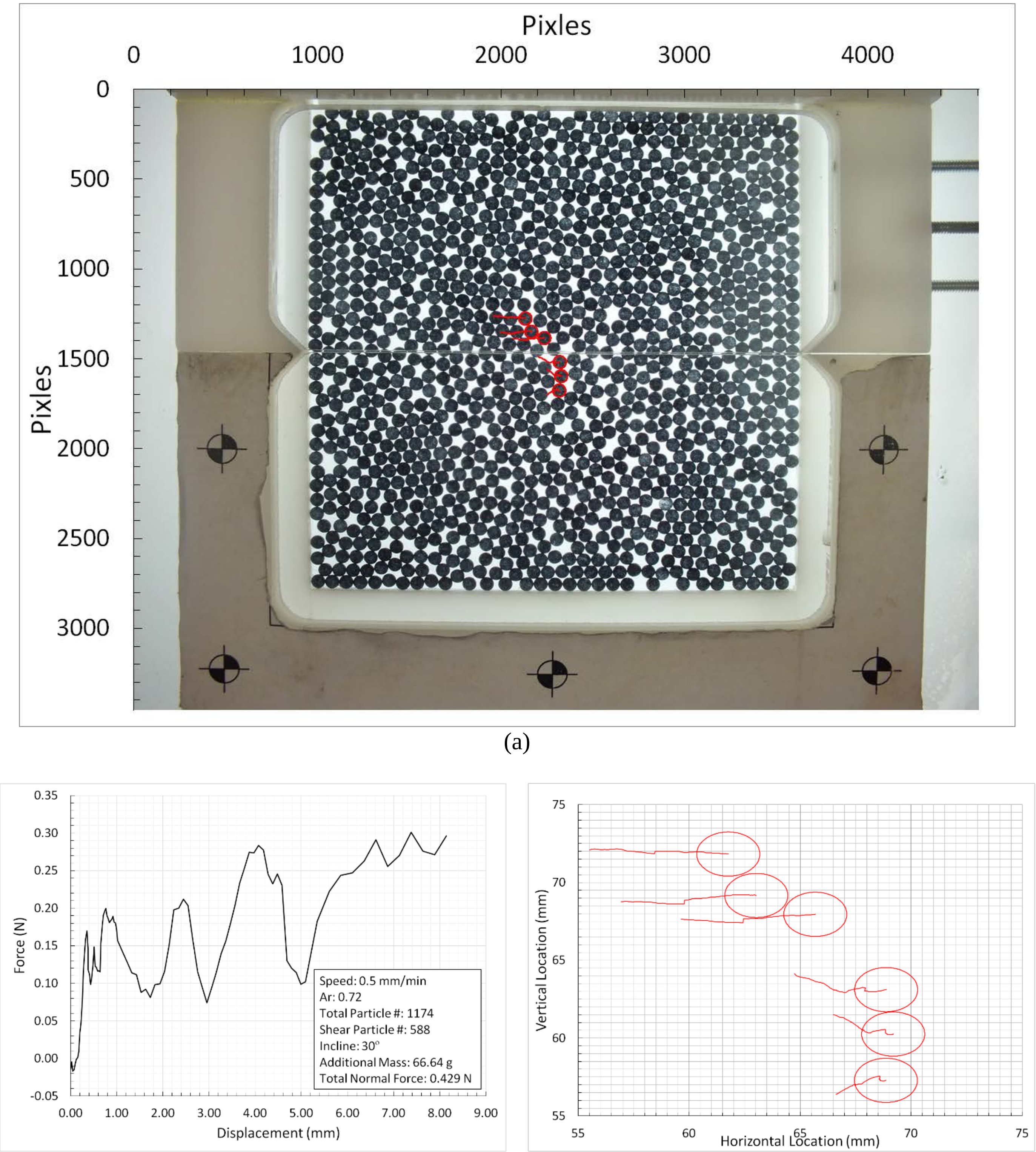

(a)

(b)

(c)

Figure: D.5 Glass bead results for 0.5 mm/min, loose state, 30° incline:
(a) Image space movements, (b) Shear response, (c) Real space movements

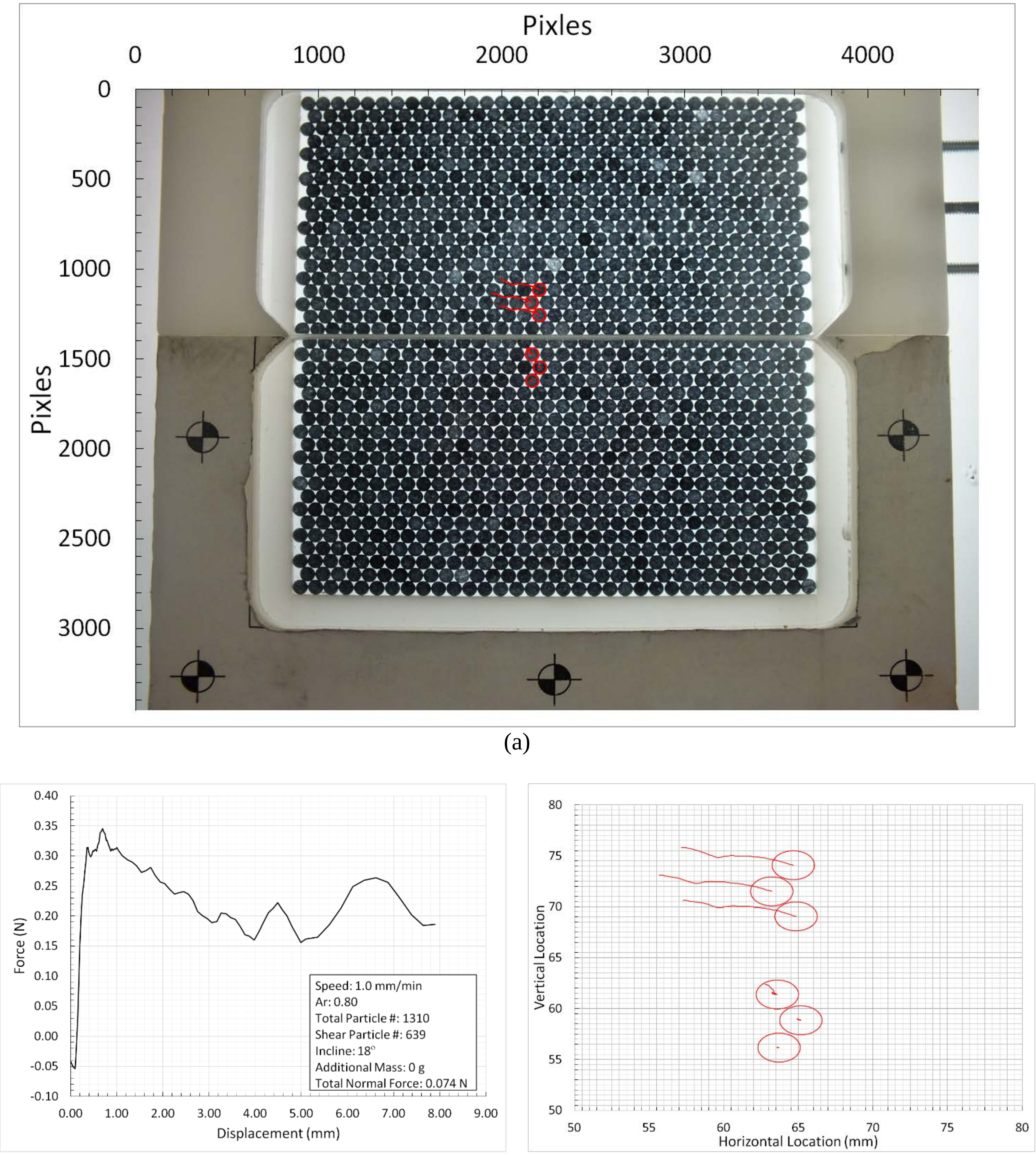

(a)

(b) (c)

Figure: D.6 Glass bead results for 1.0 mm/min, dense state, 18° incline:
(a) Image space movements, (b) Shear response, (c) Real space movements

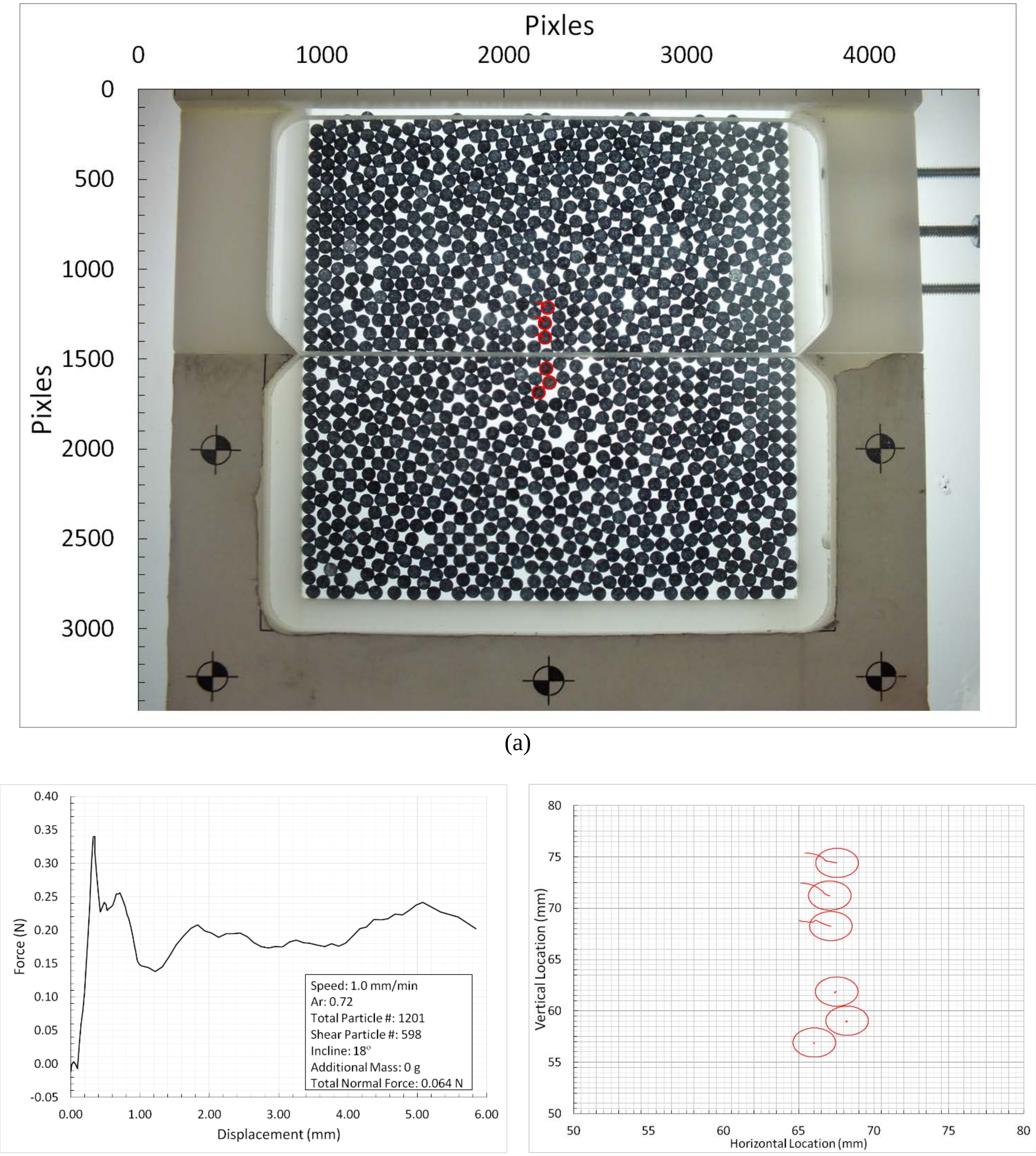

(a)

(b)

(c)

Figure: D.7 Glass bead results for 1.0 mm/min, loose state, 18° incline: (a) Image space movements, (b) Shear response, (c) Real space movements

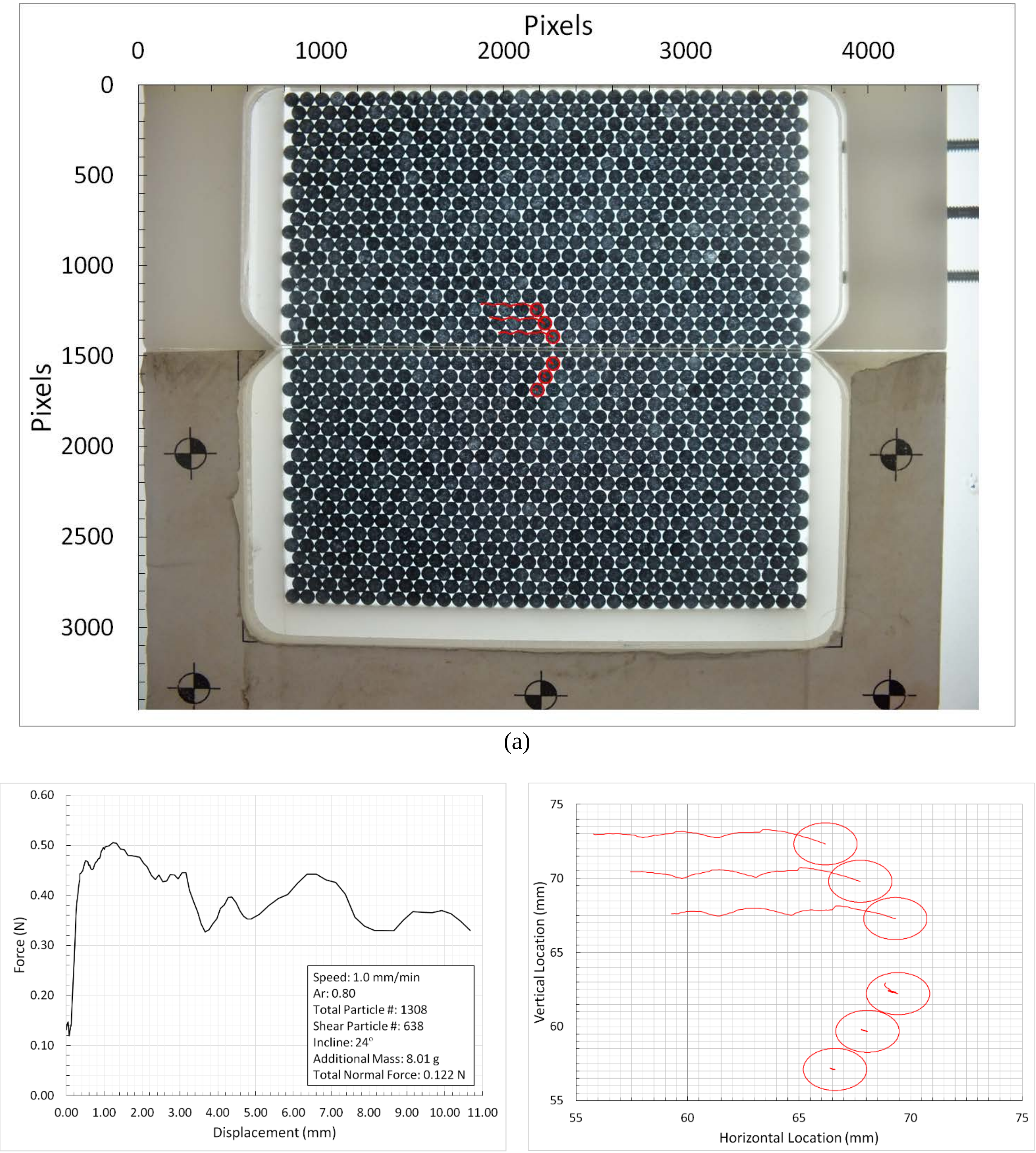

(a)

(b)

(c)

Figure: D.8 Glass bead results for 1.0 mm/min, dense state, 24° incline: (a) Image space movements, (b) Shear response, (c) Real space movements

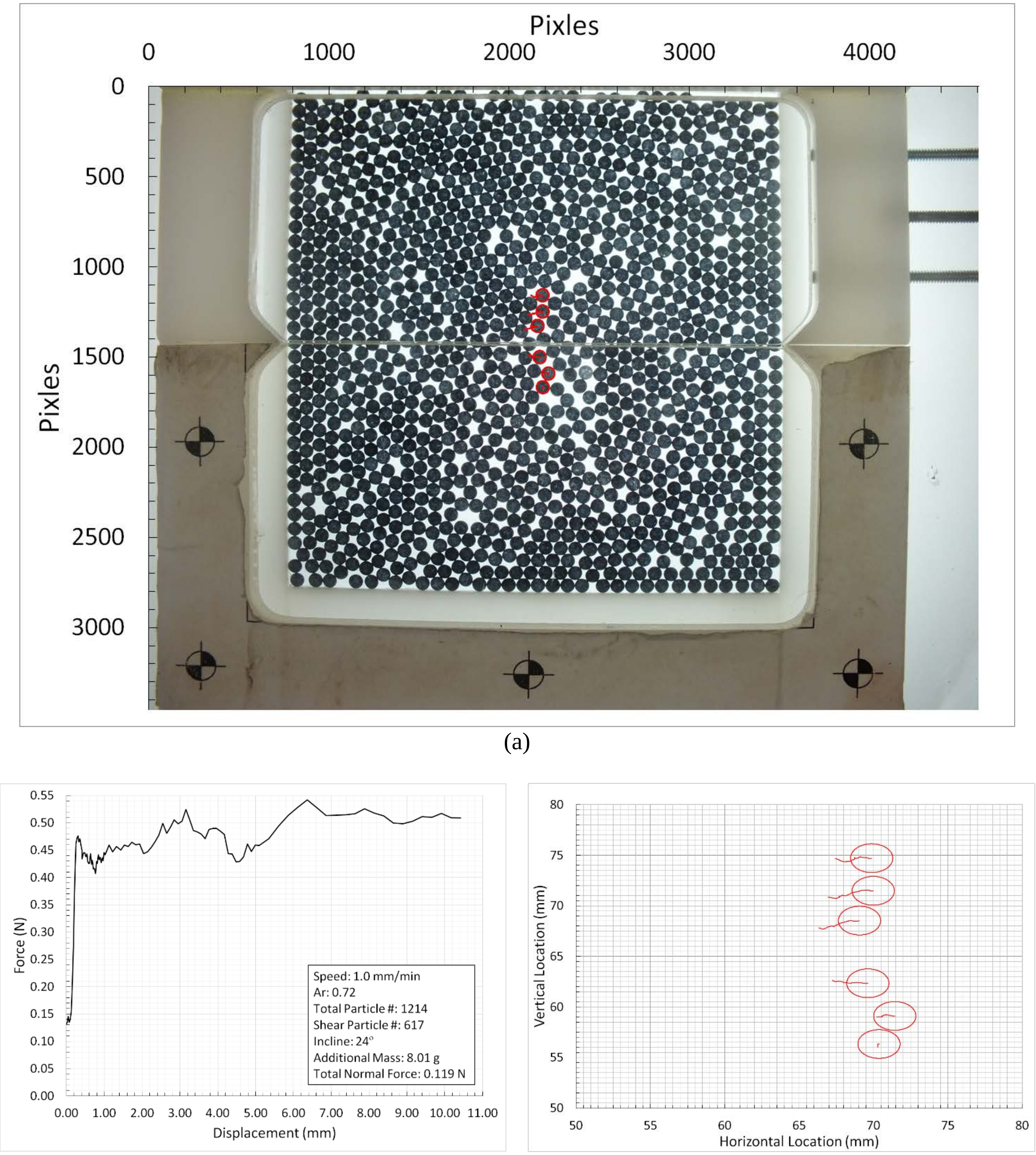

(a)

(b)

(c)

Figure: D.9 Glass bead results for 1.0 mm/min, loose state, 24° incline:
(a) Image space movements, (b) Shear response, (c) Real space movements

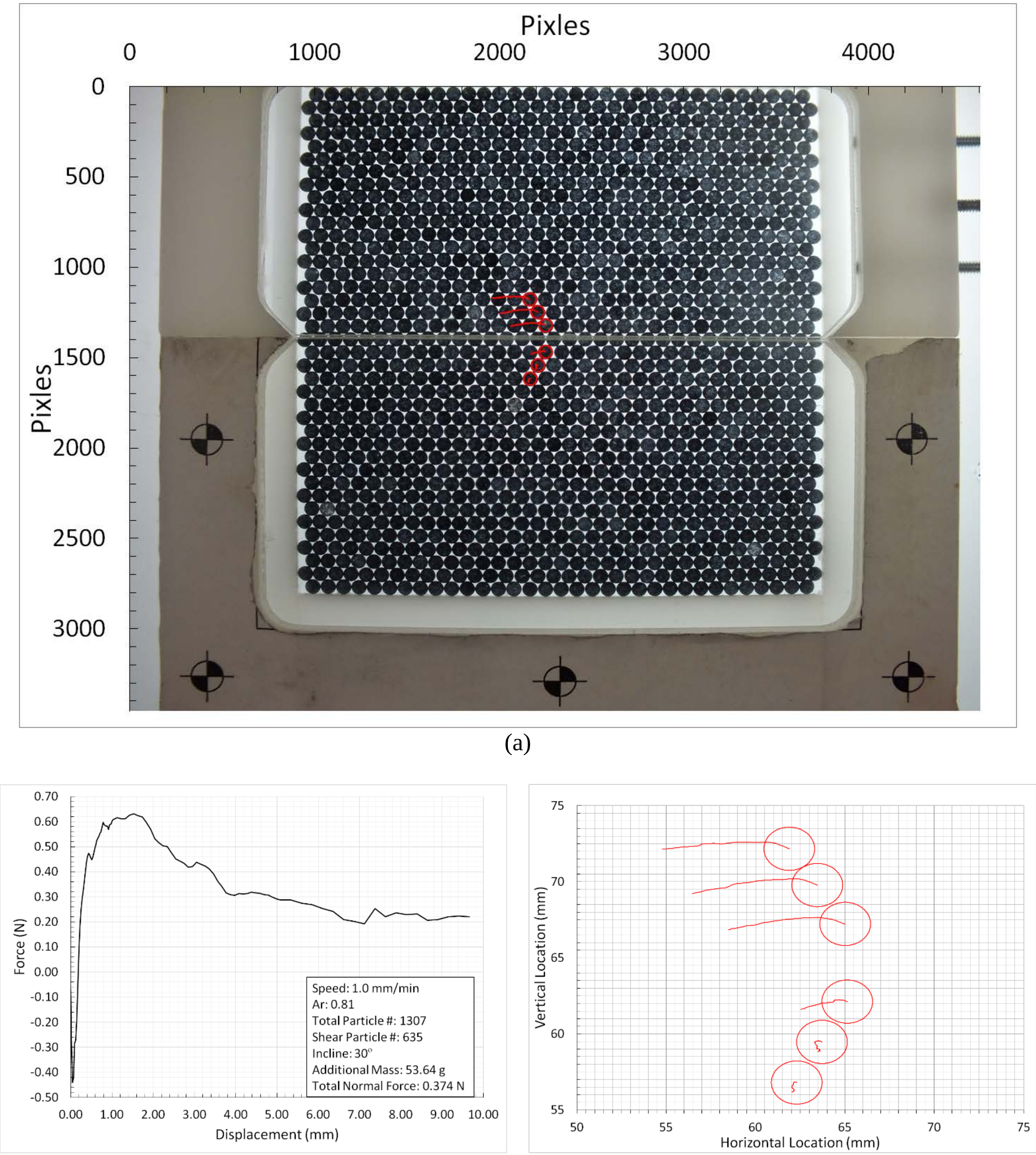

(a)

(b)

(c)

Figure: D.10 Glass bead results for 1.0 mm/min, dense state, 30° incline:
(a) Image space movements, (b) Shear response, (c) Real space movements

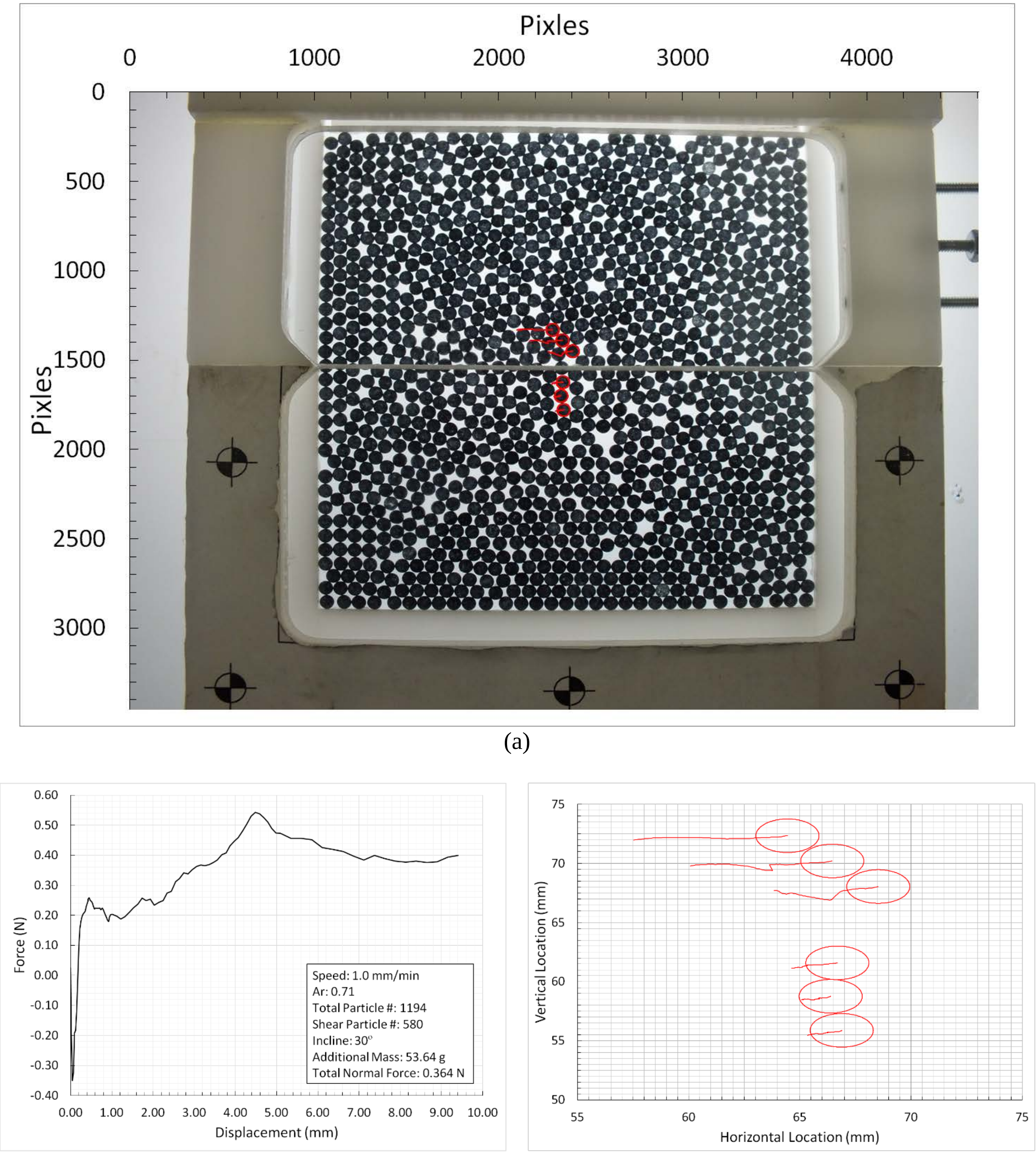

(a)

(b)

(c)

Figure: D.11 Glass bead results for 1.0 mm/min, loose state, 30° incline:
(a) Image space movements, (b) Shear response, (c) Real space movements

Appendix E **Dry Sand Direct Shear Results**

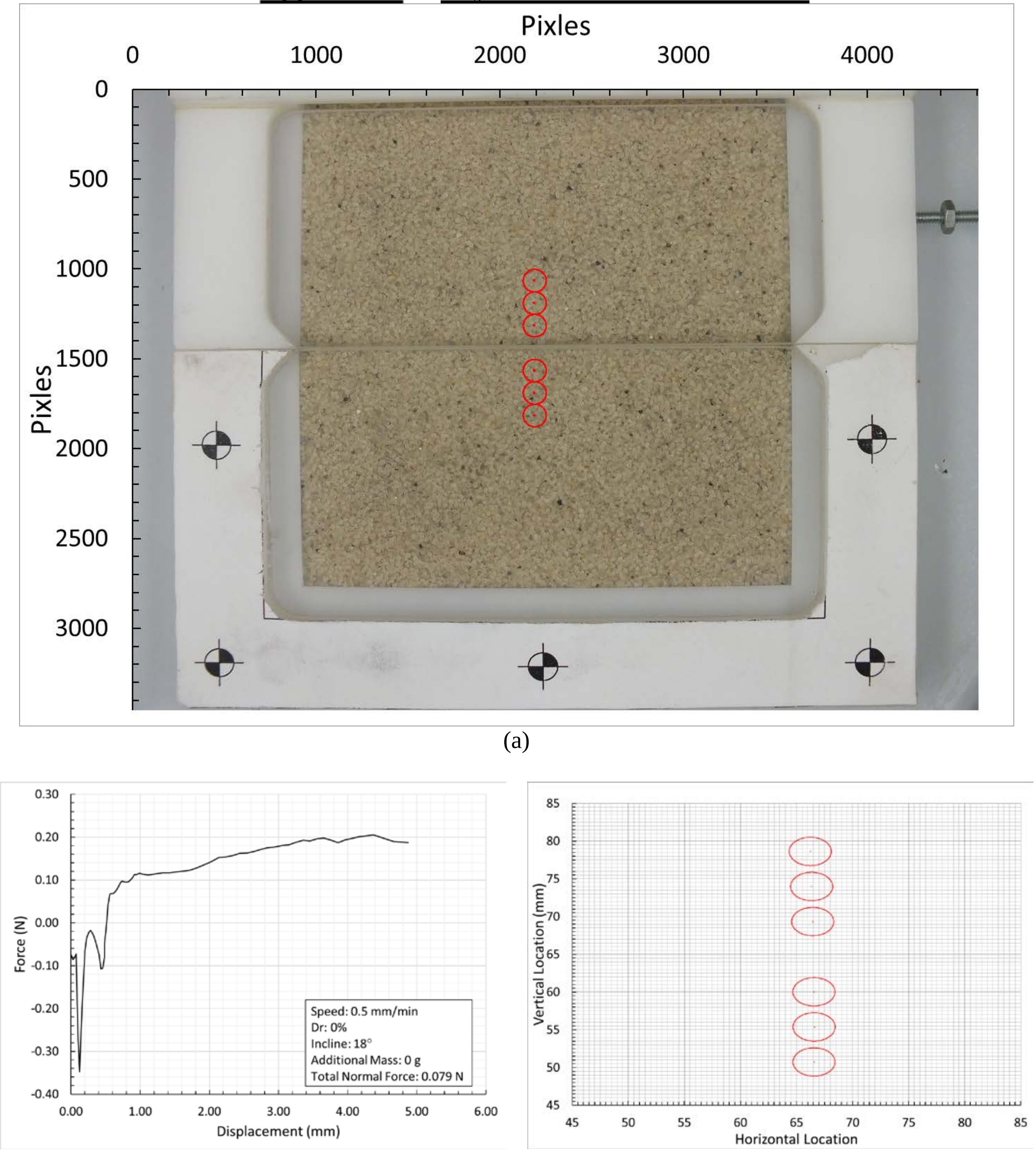

(a)

(b)

(c)

Figure: E.1 Sand results for 0.5 mm/min, loose state, 18° incline:
(a) Image space movements, (b) Shear response, (c) Real space movements

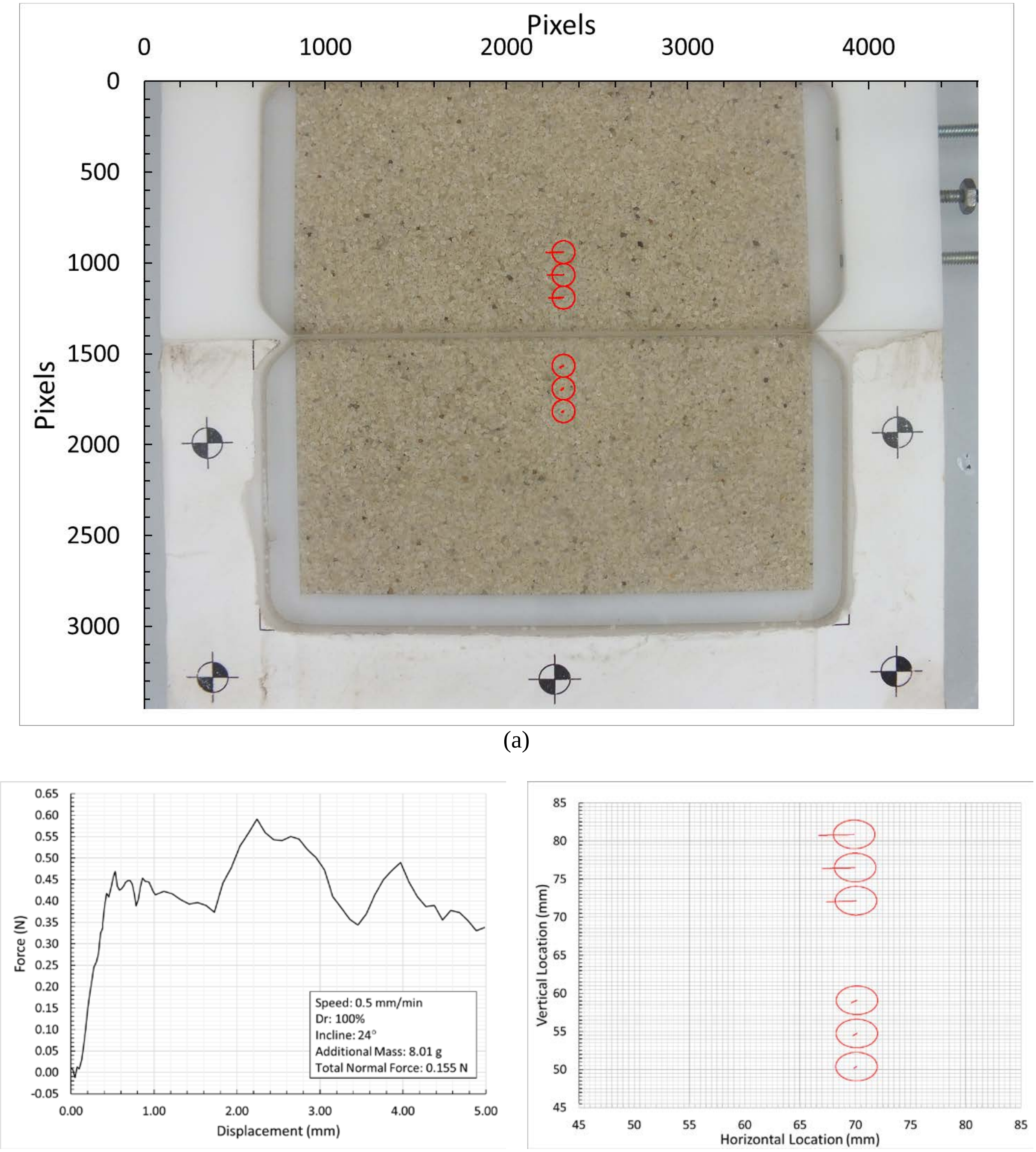

(a)

(b)

(c)

Figure: E.2 Sand results for 0.5 mm/min, dense state, 24° incline:
(a) Image space movements, (b) Shear response, (c) Real space movements

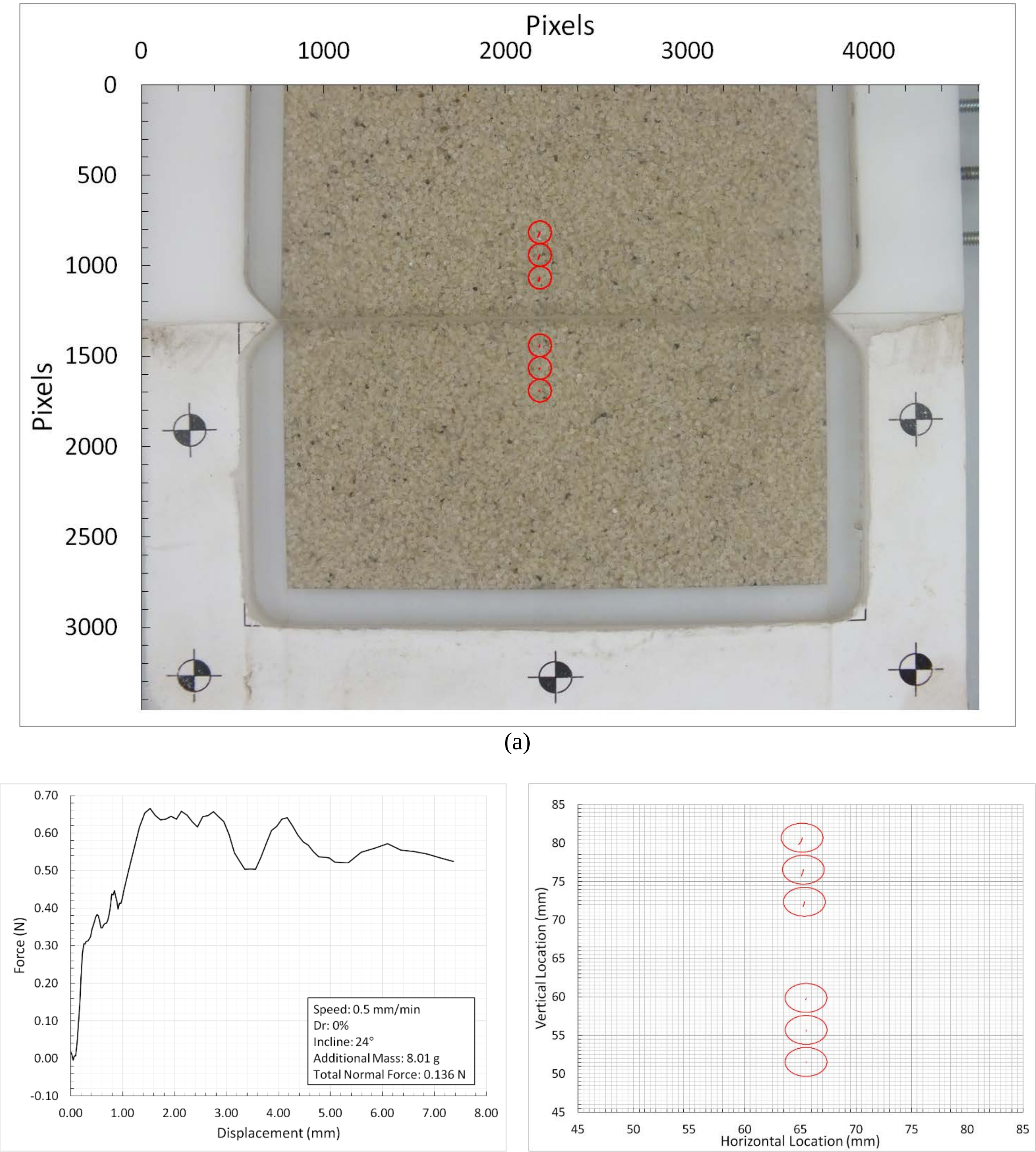

(a)

(b)

(c)

Figure: E.3 Sand results for 0.5 mm/min, loose state, 24° incline:
(a) Image space movements, (b) Shear response, (c) Real space movements

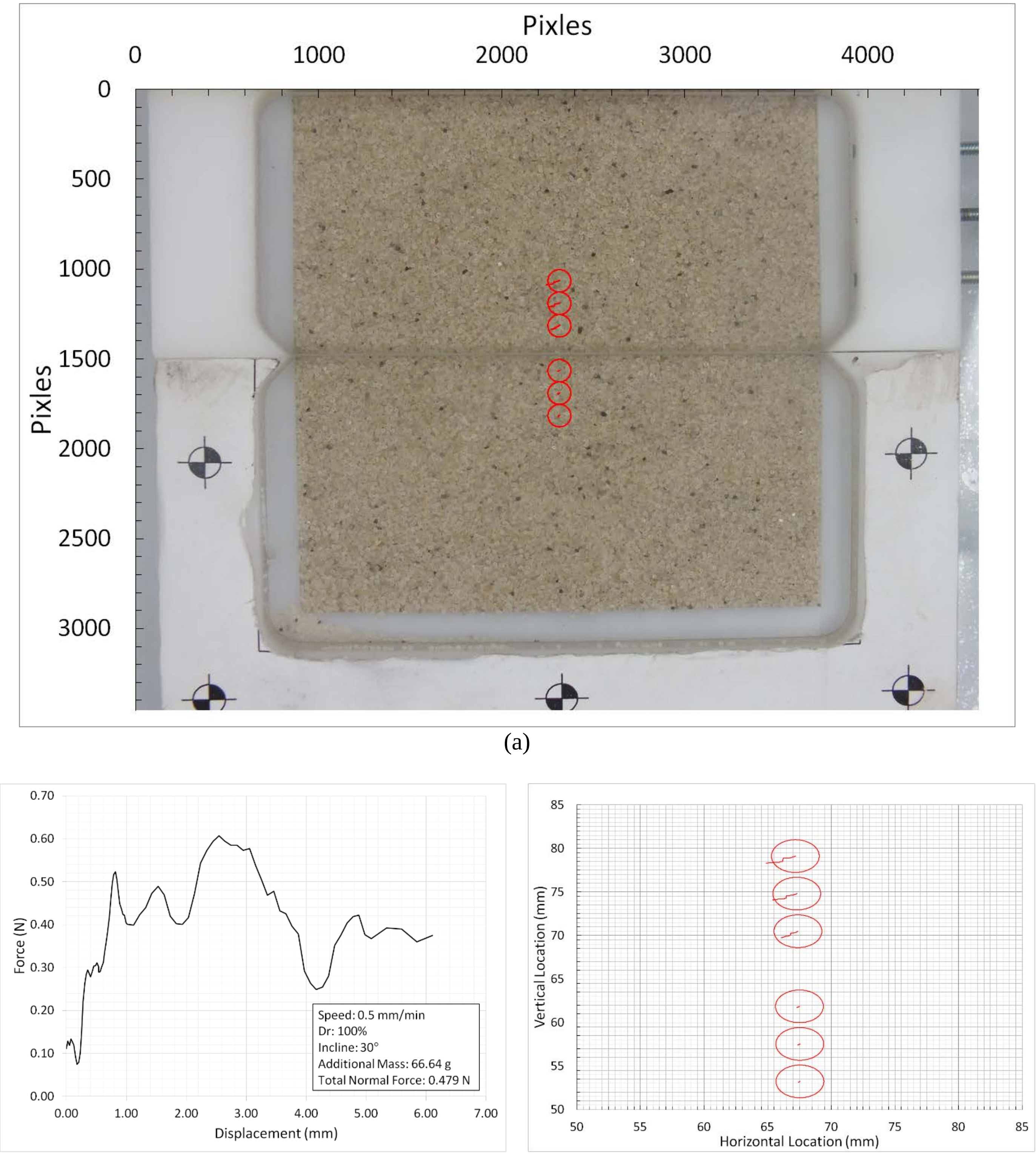

(a)

(b)

(c)

Figure: E.4 Sand results for 0.5 mm/min, dense state, 30° incline: (a) Image space movements, (b) Shear response, (c) Real space movements

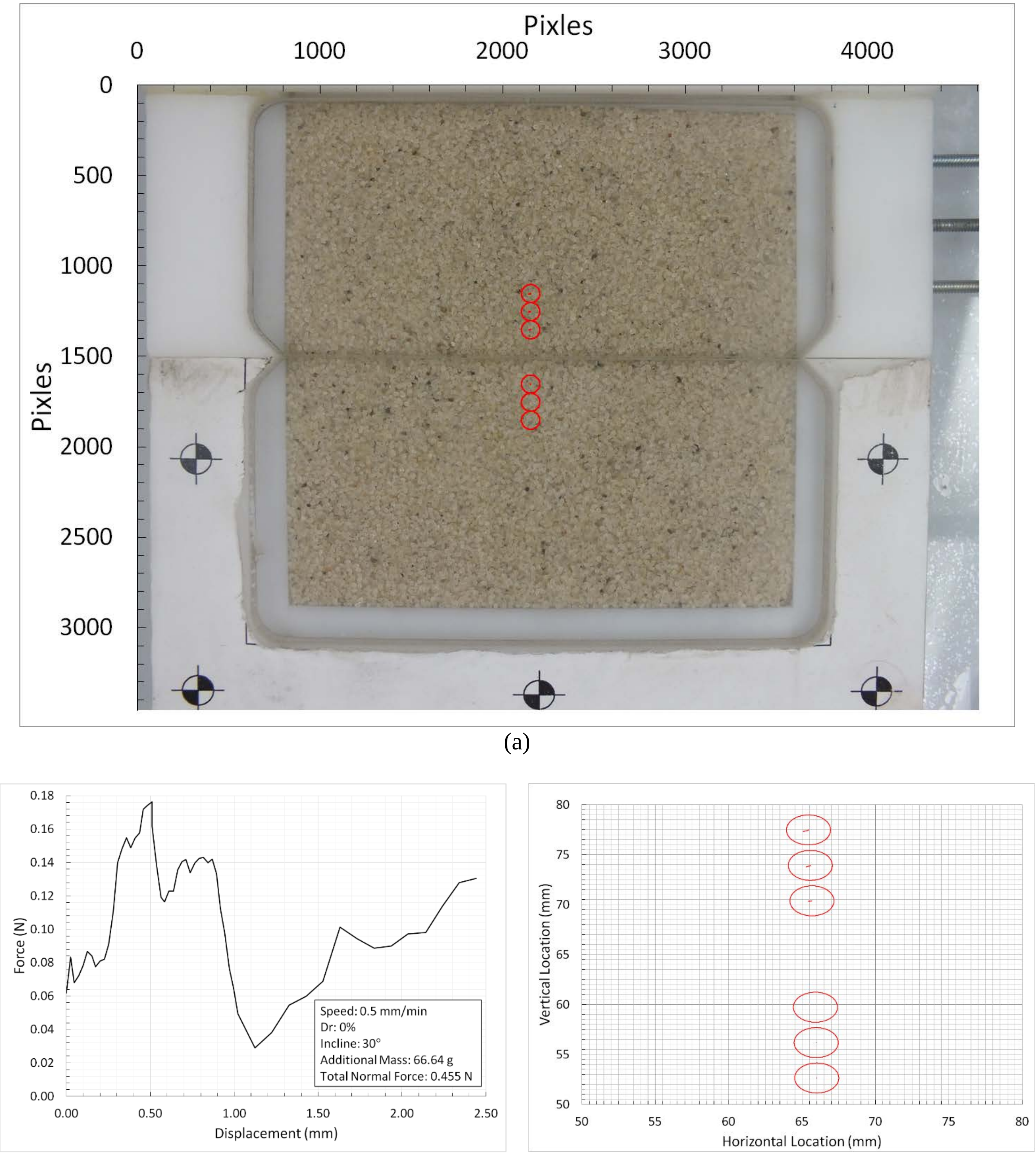

(a)

(b)

(c)

Figure: E.5 Sand results for 0.5 mm/min, loose state, 30° incline:
(a) Image space movements, (b) Shear response, (c) Real space movements

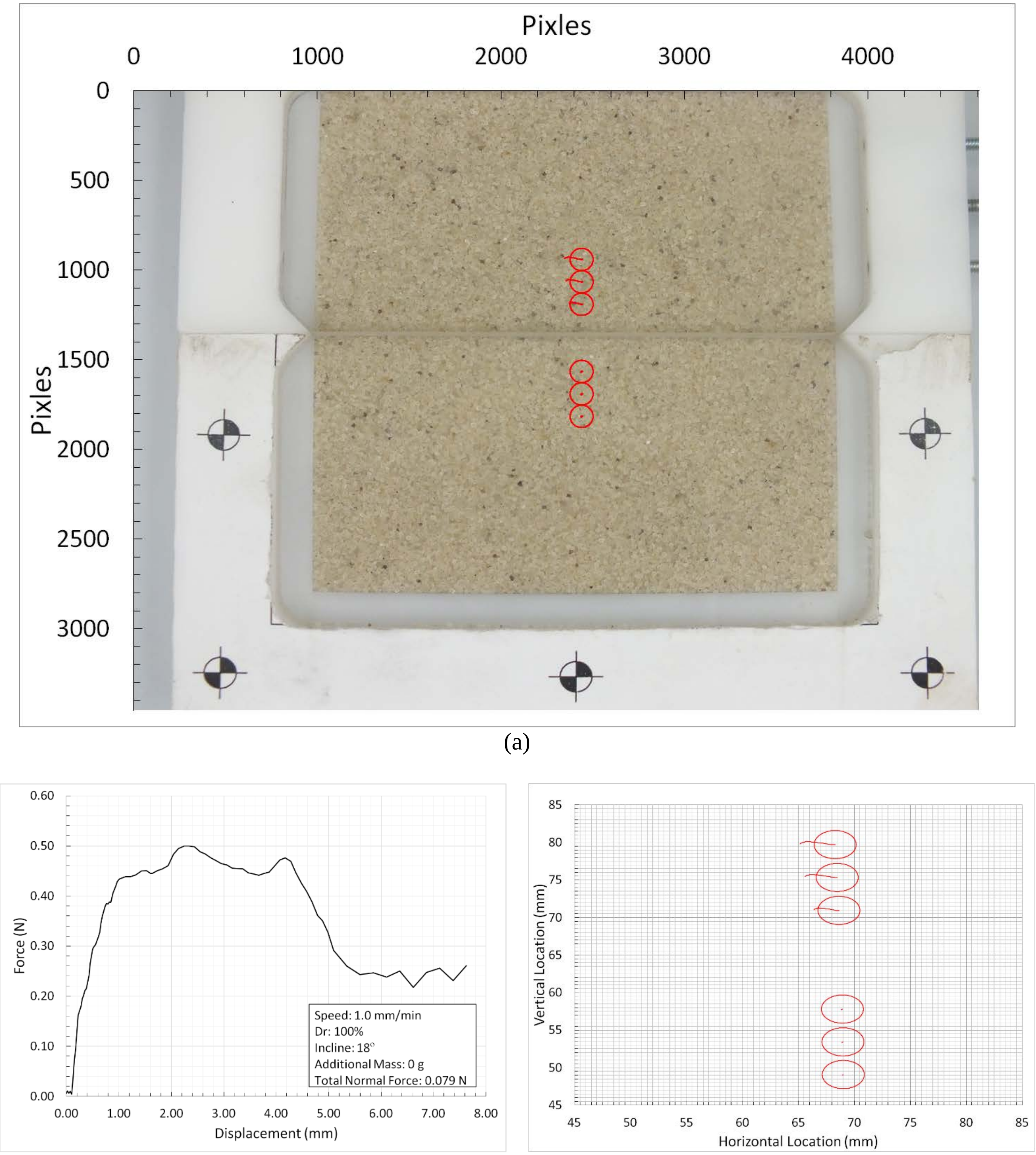

(a)

(b)

(c)

Figure: E.6 Sand results for 1.0 mm/min, dense state, 18° incline:
(a) Image space movements, (b) Shear response, (c) Real space movements

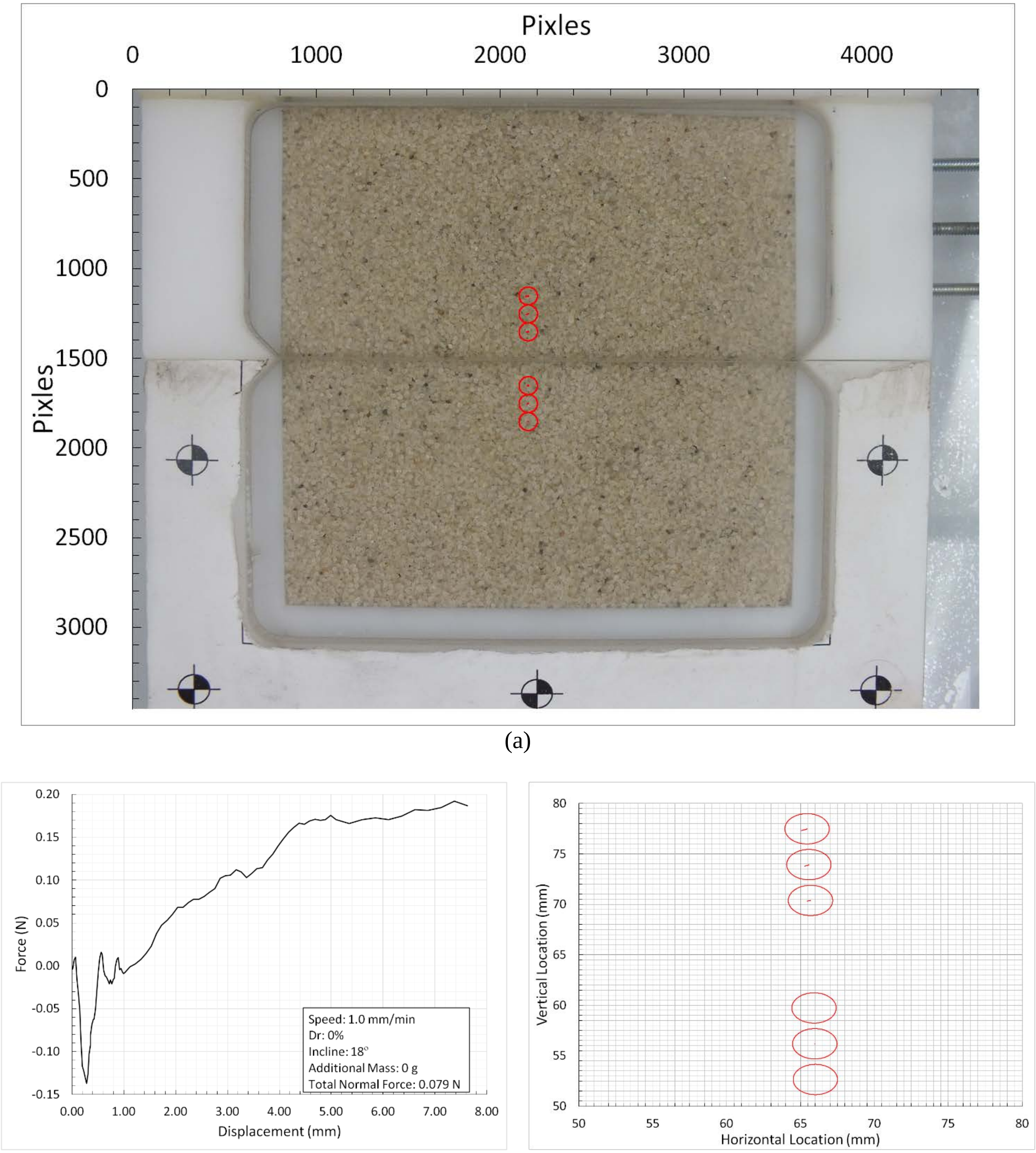

(a)

(b)

(c)

Figure: E.7 Sand results for 1.0 mm/min, loose state, 18° incline:
(a) Image space movements, (b) Shear response, (c) Real space movements

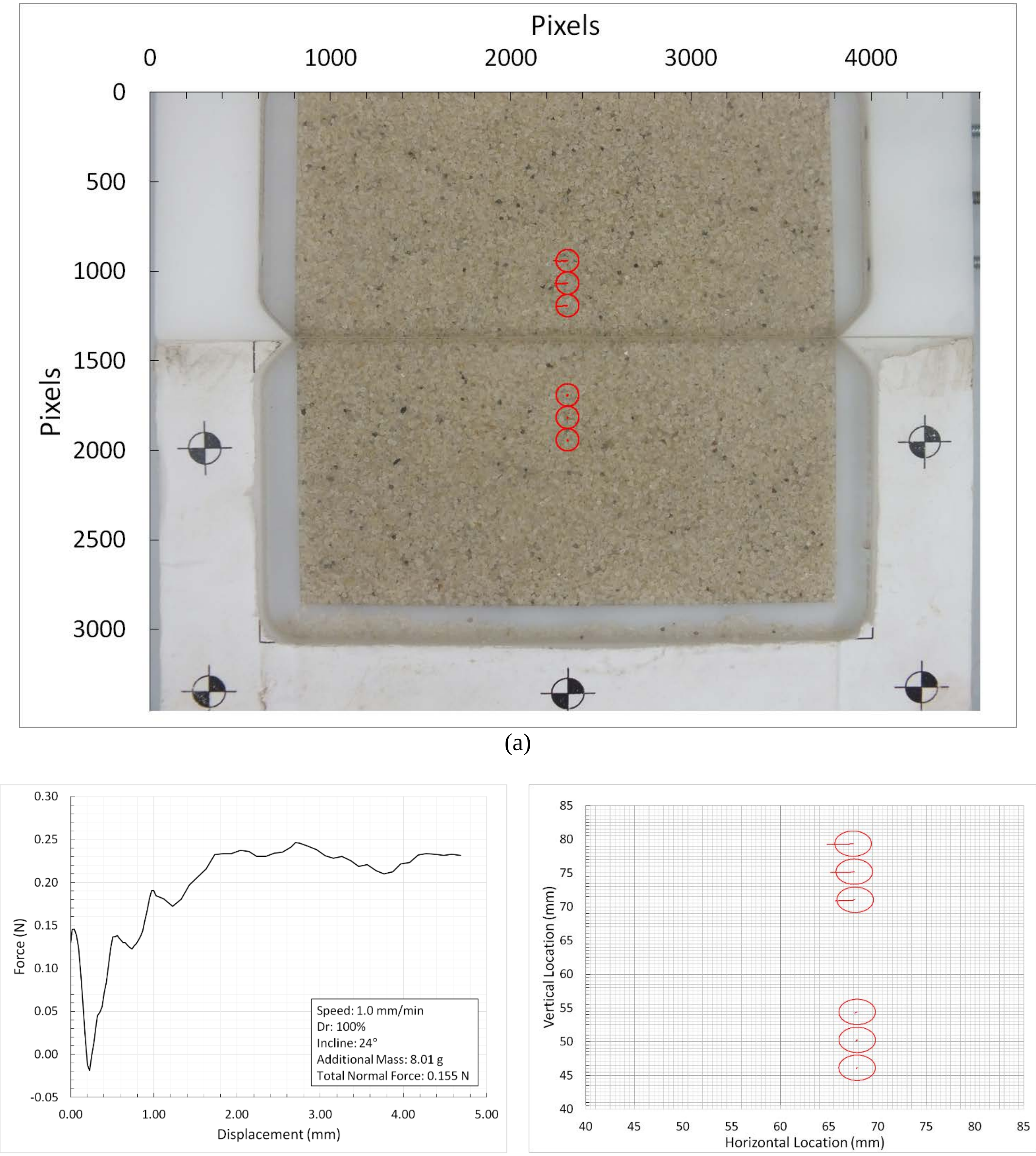

(a)

(b)

(c)

Figure: E.8 Sand results for 1.0 mm/min, dense state, 24° incline: (a) Image space movements, (b) Shear response, (c) Real space movements

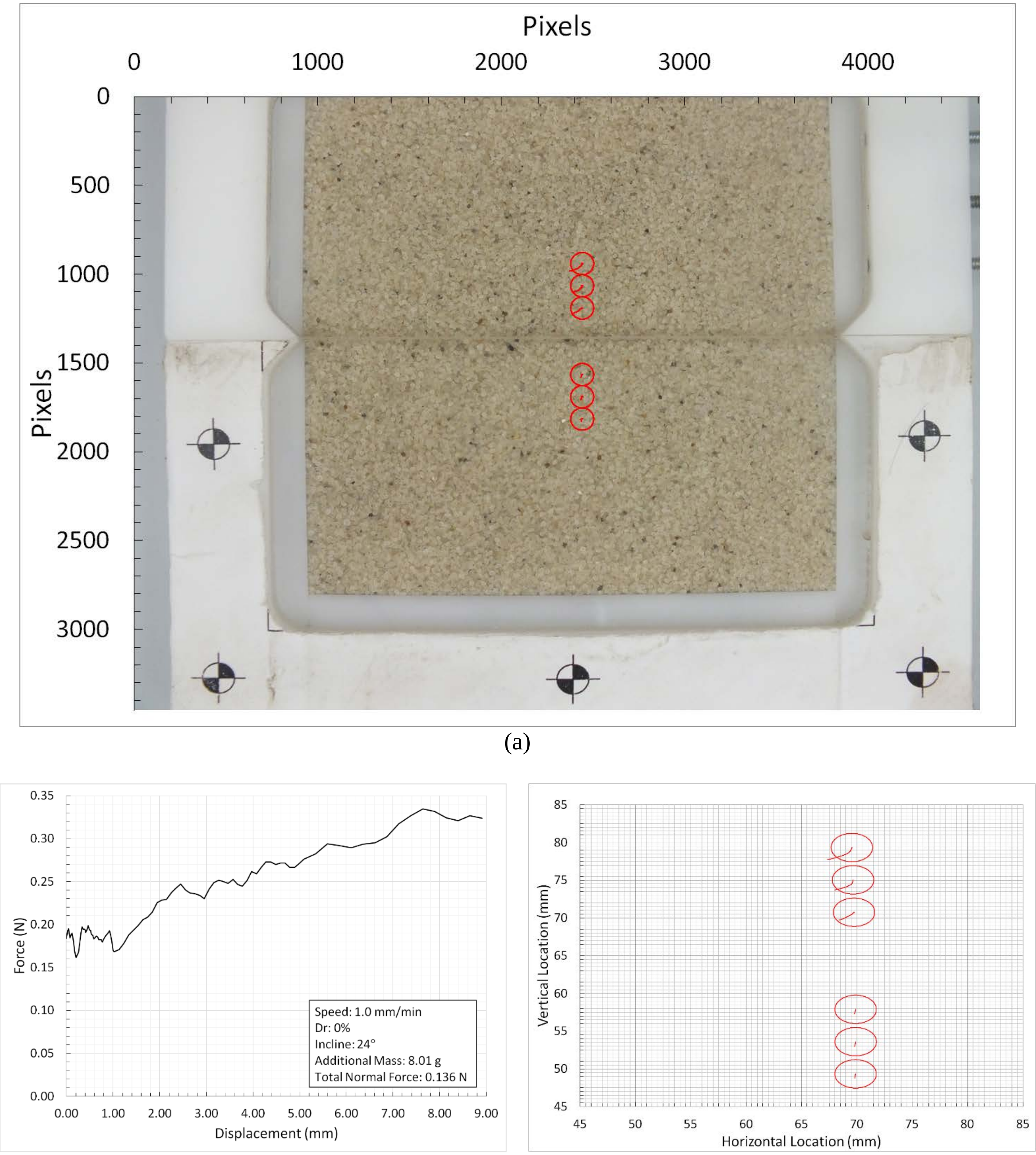

(a)

(b)

(c)

Figure: E.9 Sand results for 1.0 mm/min, loose state, 24° incline:
(a) Image space movements, (b) Shear response, (c) Real space movements

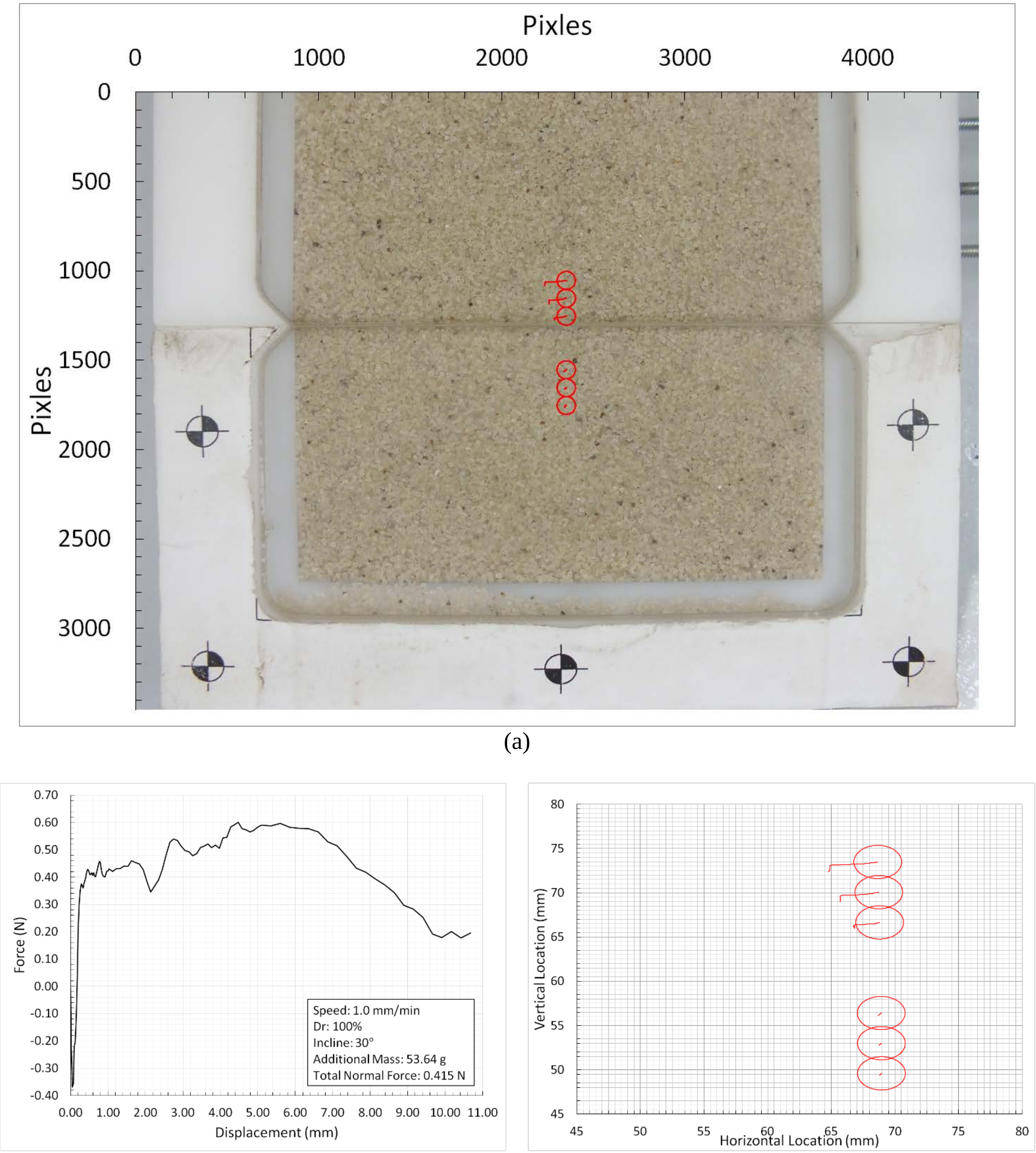

(a)

(b)

(c)

Figure: E.10 Sand results for 1.0 mm/min, dense state, 30° incline:
(a) Image space movements, (b) Shear response, (c) Real space movements

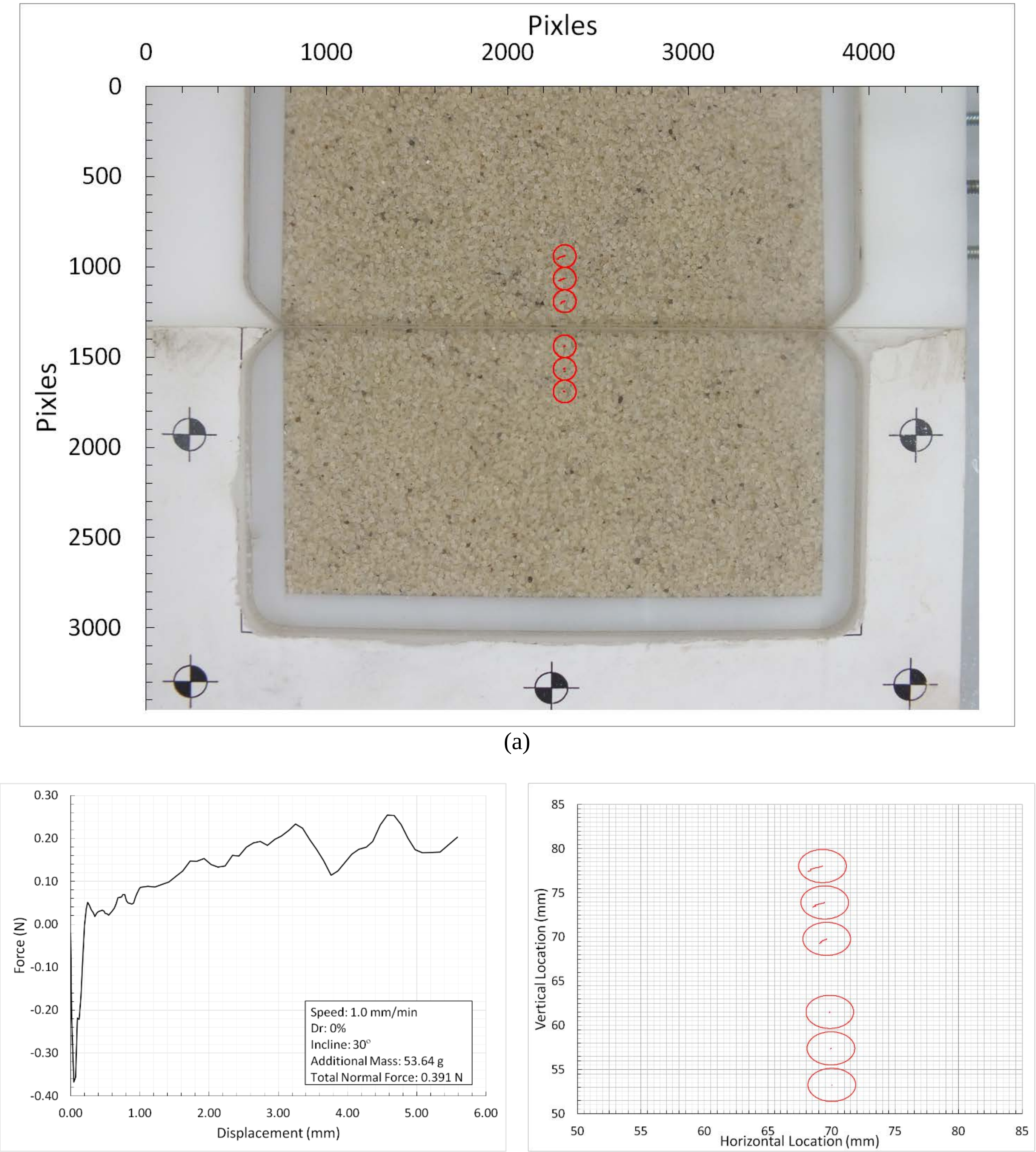

(a)

(b)

(c)

Figure: E.11 Sand results for 1.0 mm/min, loose state, 30° incline:
(a) Image space movements, (b) Shear response, (c) Real space movements

Appendix F Wet Glass Beads Direct Shear Results

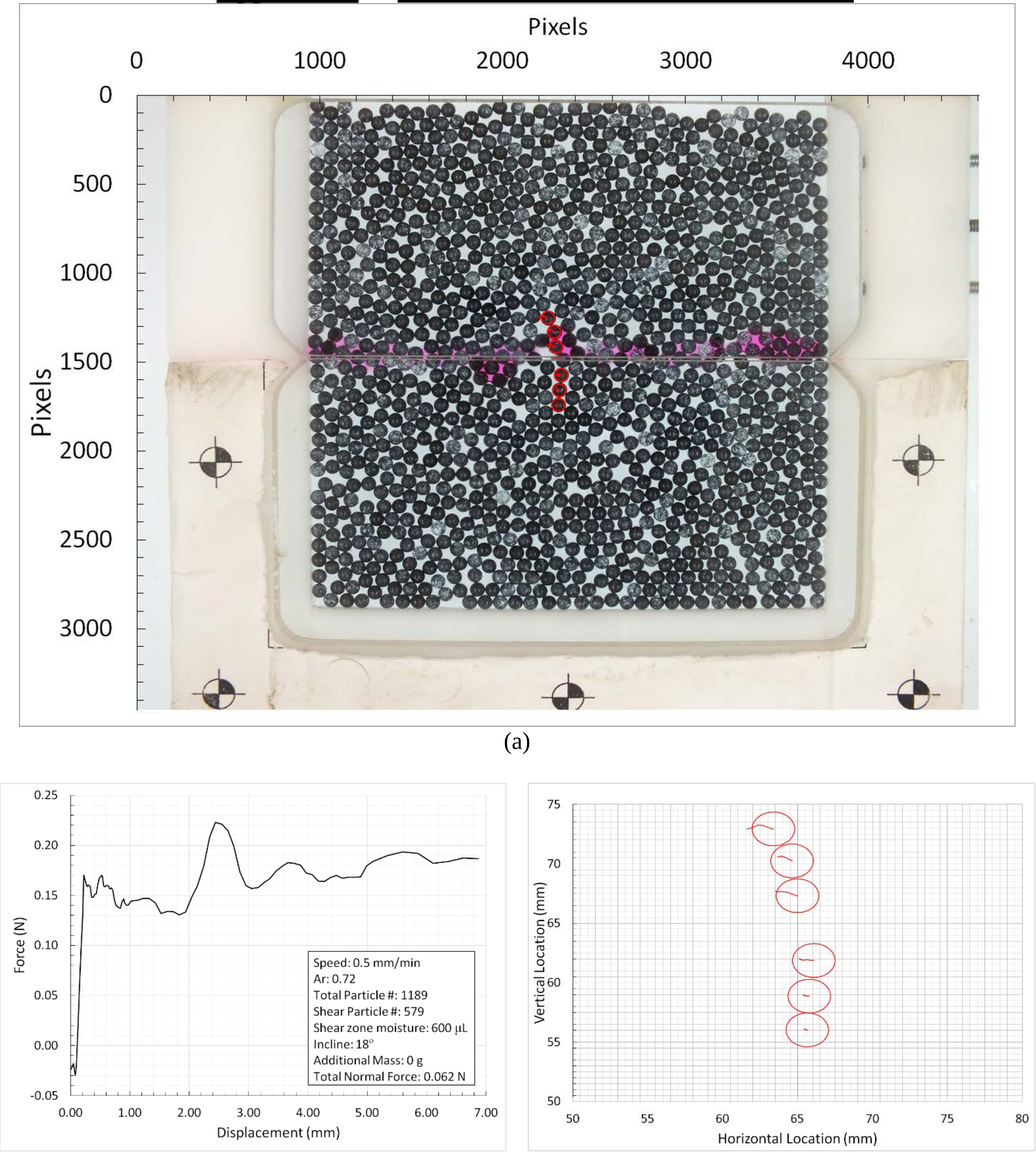

(a)

(b)

(c)

Figure: F.1 Glass beads results for 0.5 mm/min, loose state, 18° incline: (a) Image space movements, (b) Shear response, (c) Real space movements

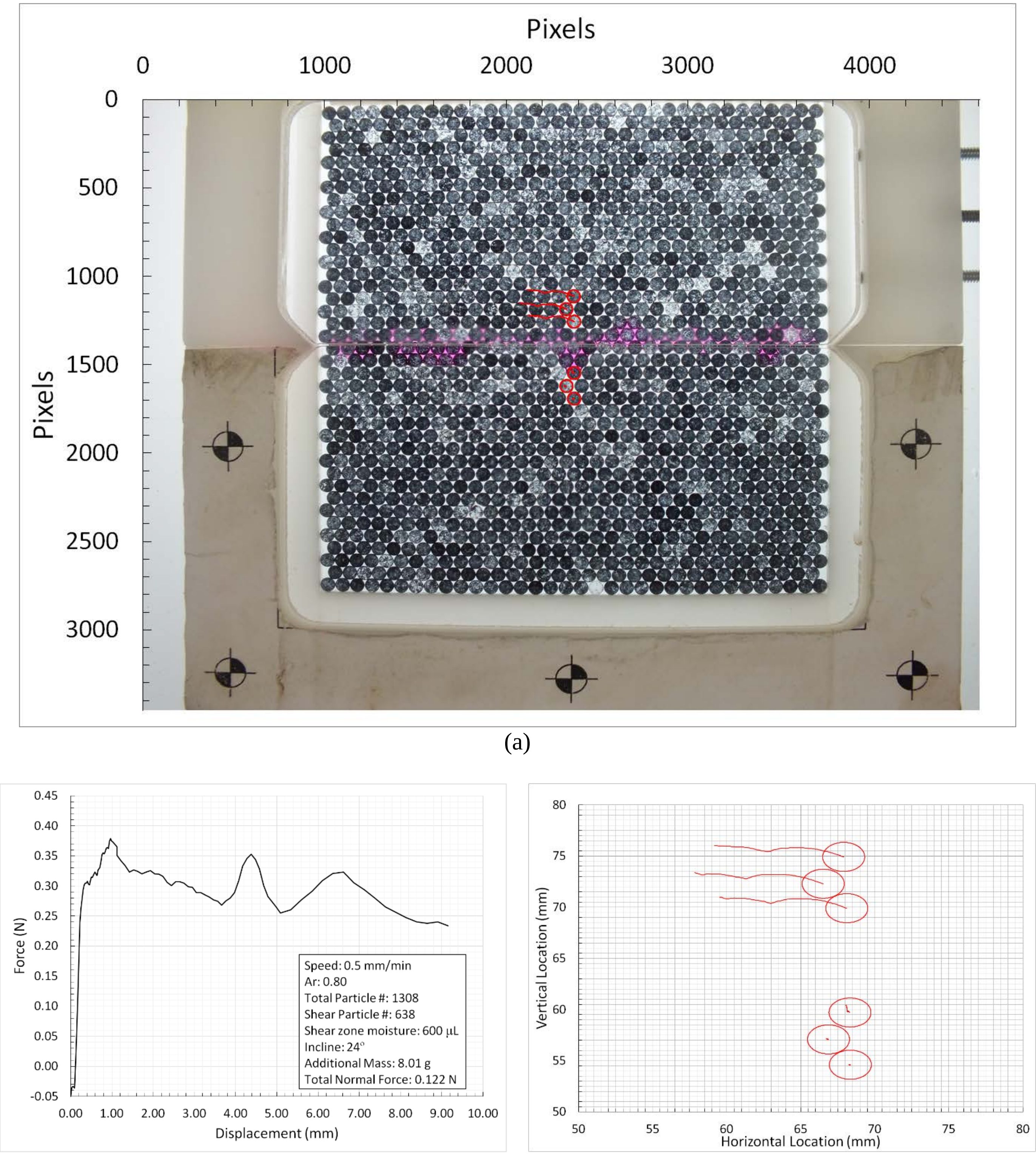

Speed: 0.5 mm/min
Ar: 0.80
Total Particle #: 1308
Shear Particle #: 638
Shear zone moisture: 600 µL
Incline: 24°
Additional Mass: 8.01 g
Total Normal Force: 0.122 N

(a)

(b)

(c)

Figure: F.2 Glass beads results for 0.5 mm/min, dense state, 24° incline:
(a) Image space movements, (b) Shear response, (c) Real space movements

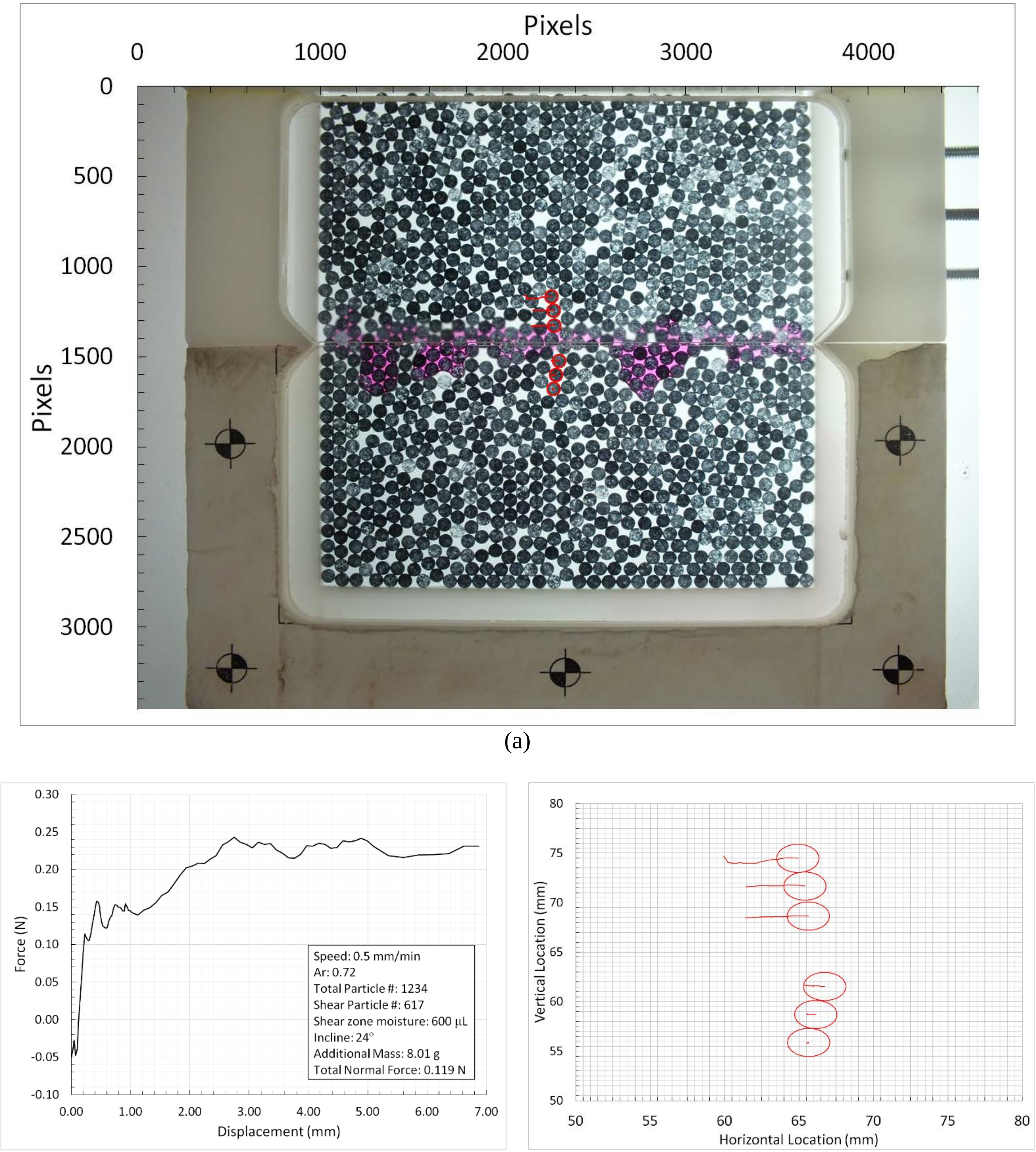

(a)

(b)

(c)

Figure: F.3 Glass beads results for 0.5 mm/min, loose state, 24° incline:
(a) Image space movements, (b) Shear response, (c) Real space movements

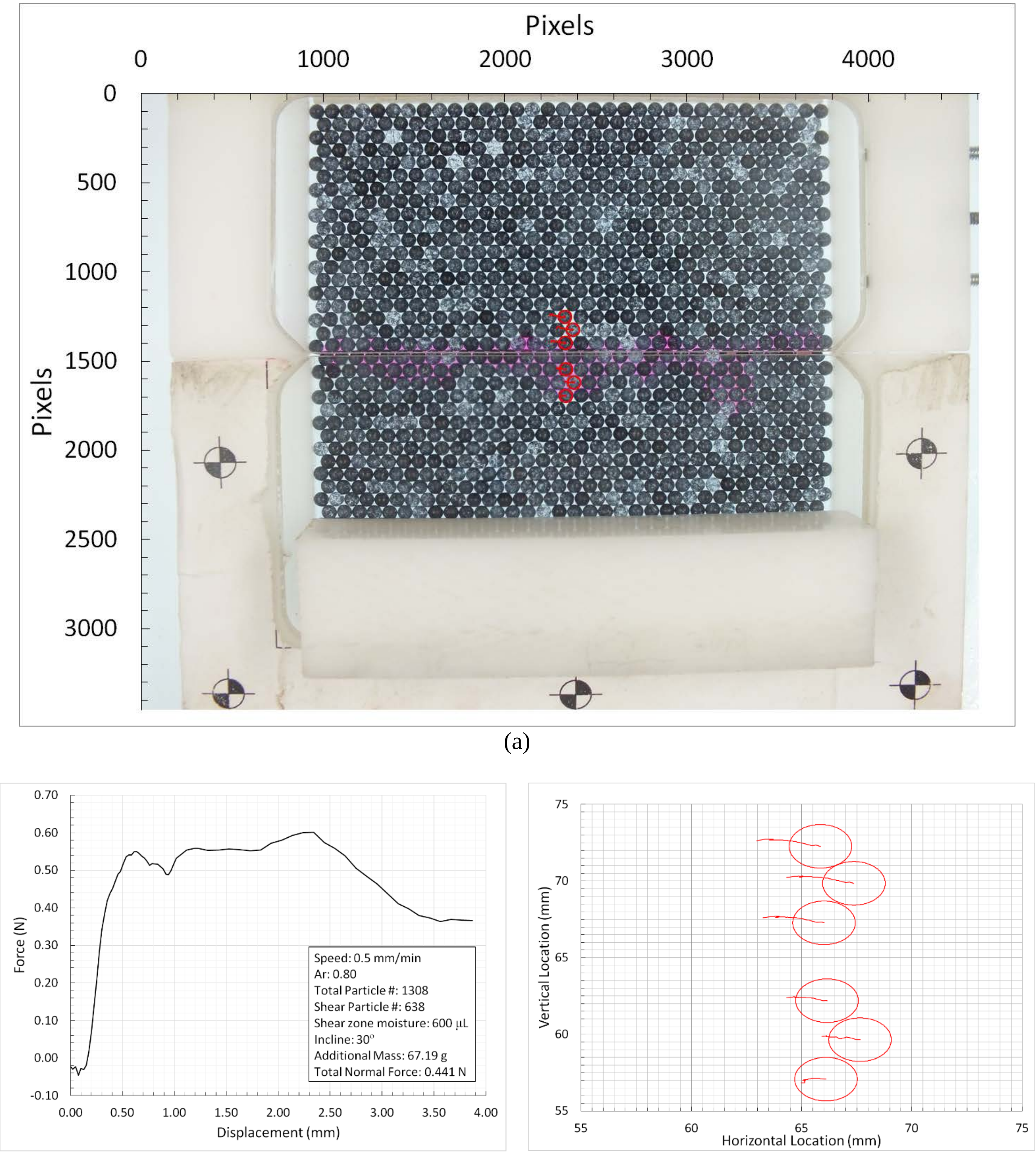

(a)

(b)

(c)

Figure: F.4 Glass beads results for 0.5 mm/min, dense state, 30° incline: (a) Image space movements, (b) Shear response, (c) Real space movements

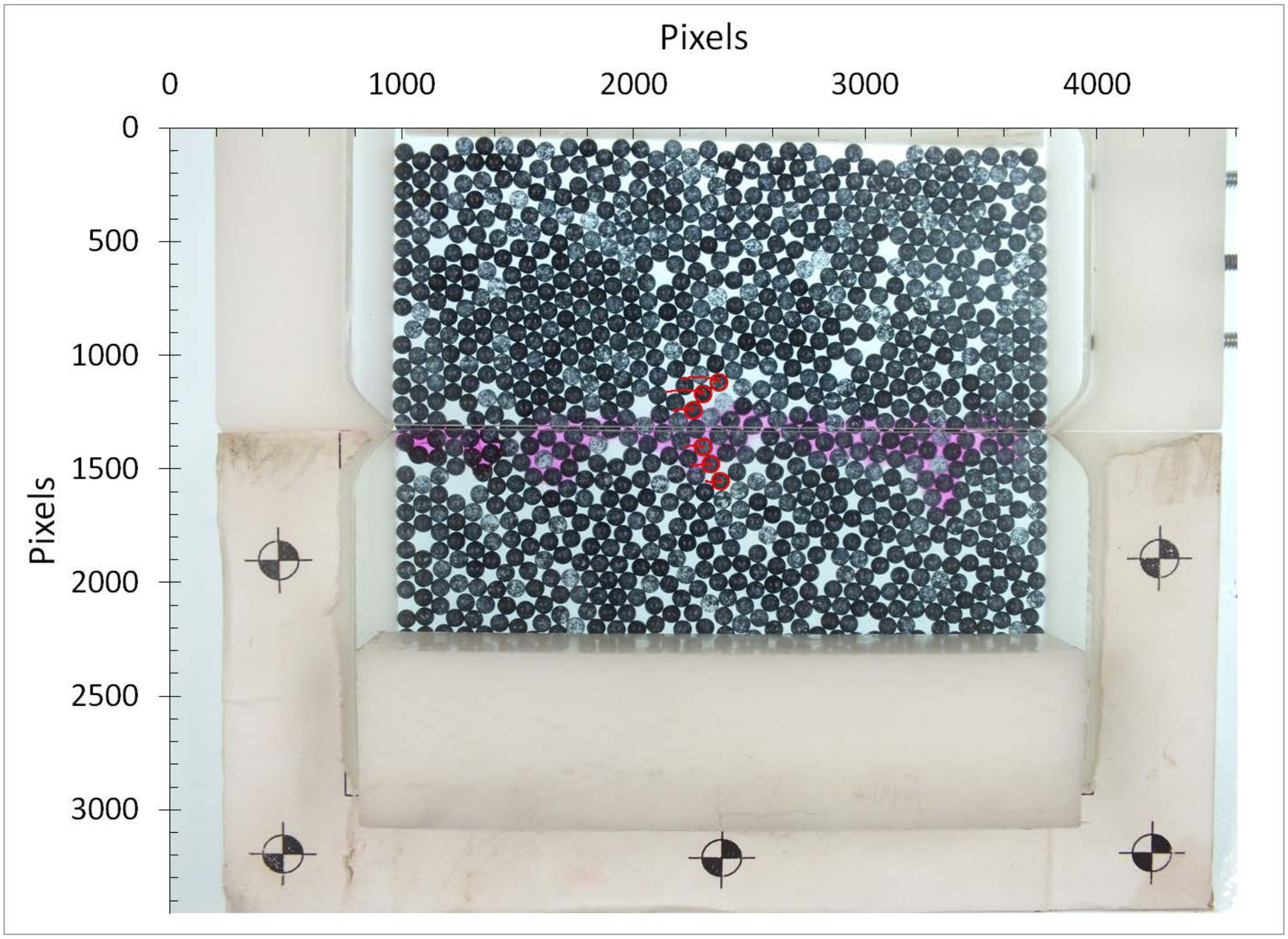

(a)

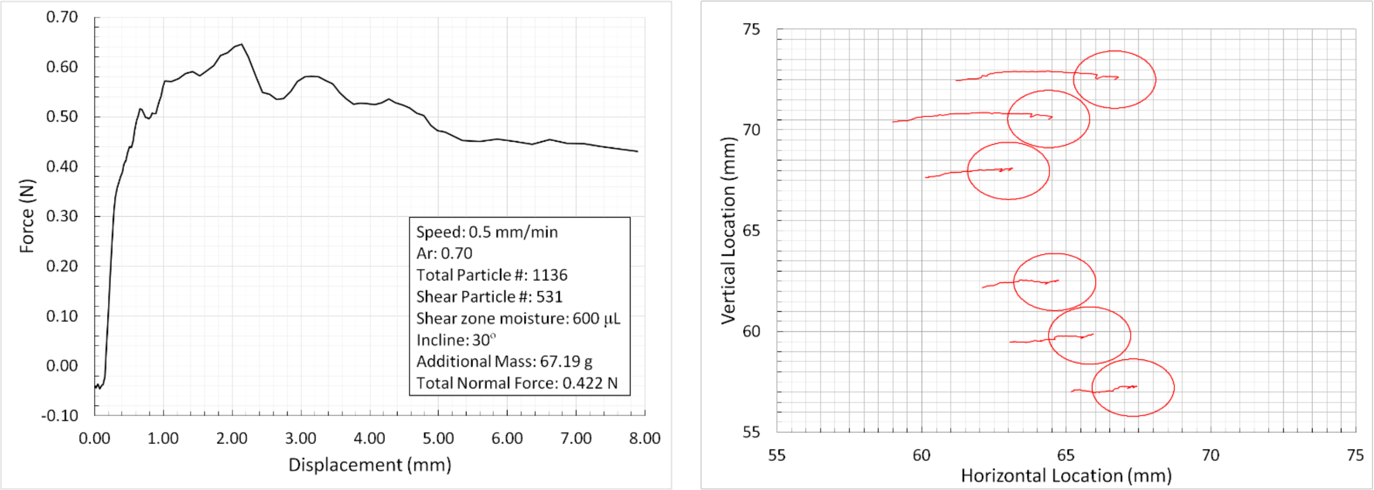

(b) (c)

Figure: F.5 Glass beads results for 0.5 mm/min, loose state, 30° incline: (a) Image space movements, (b) Shear response, (c) Real space movements

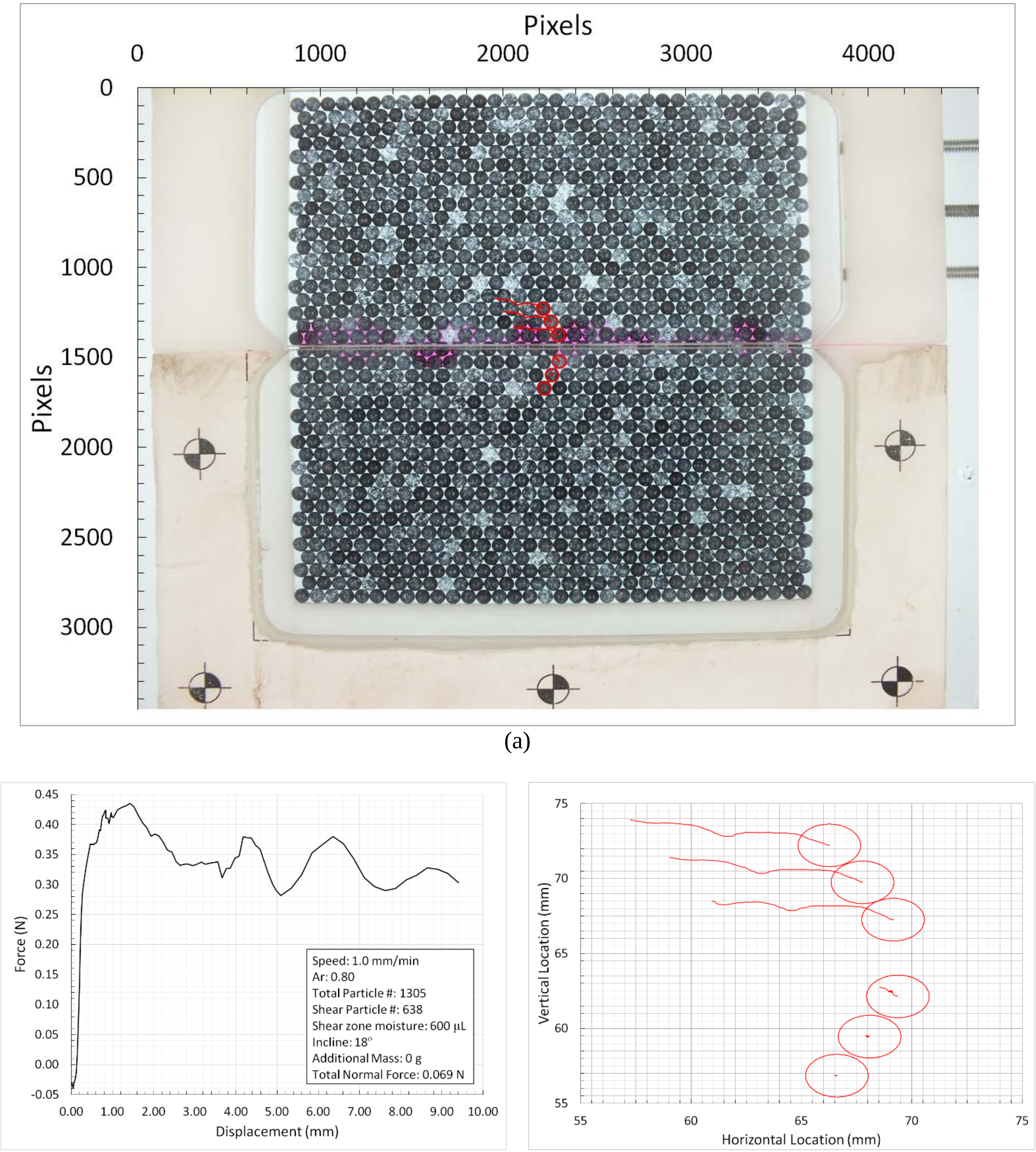

(a)

(b)

(c)

Figure: F.6 Glass beads results for 1.0 mm/min, dense state, 18° incline:
(a) Image space movements, (b) Shear response, (c) Real space movements

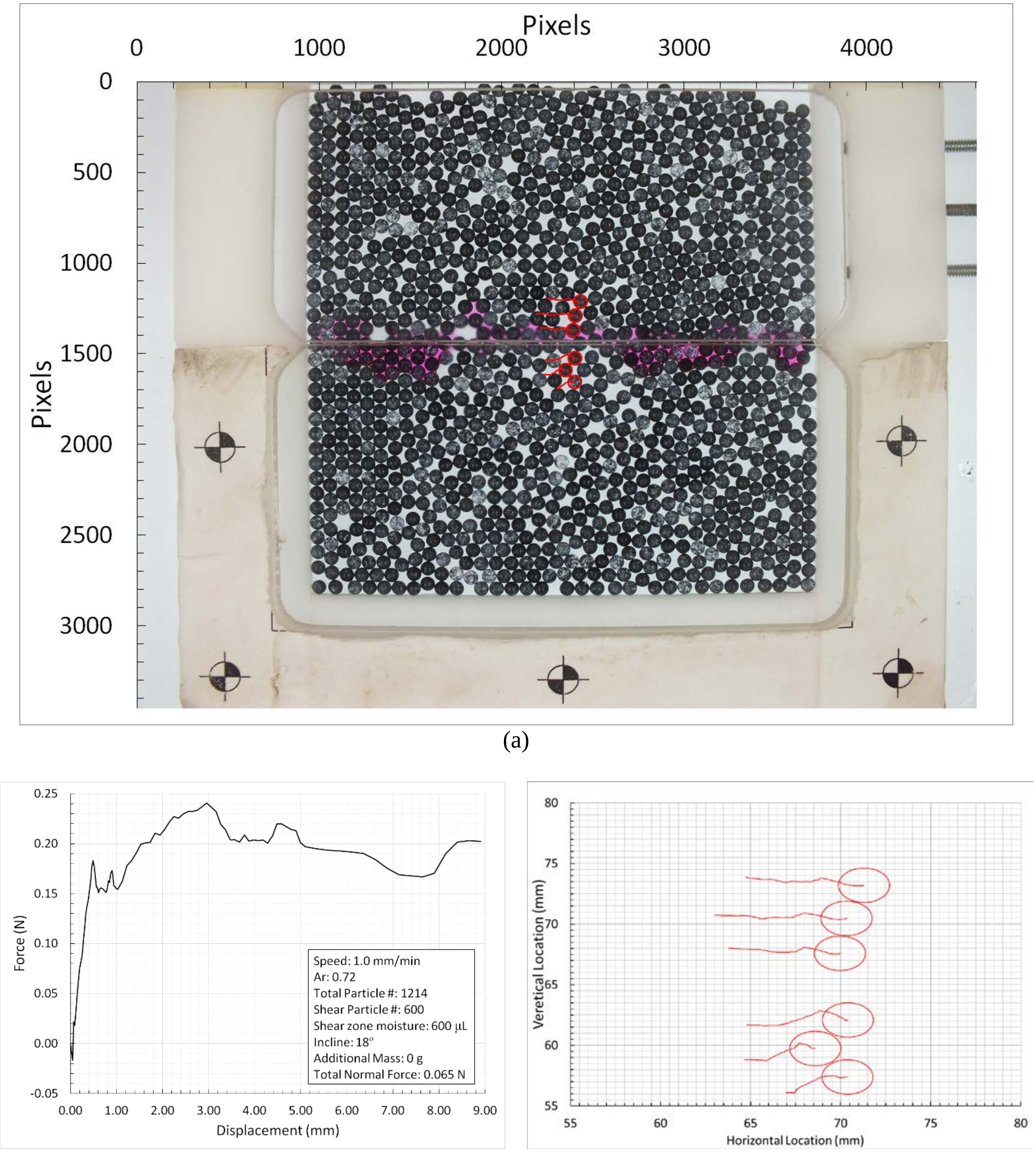

(a)

(b)

(c)

Figure: F.7 Glass beads results for 1.0 mm/min, loose state, 18° incline:
(a) Image space movements, (b) Shear response, (c) Real space movements

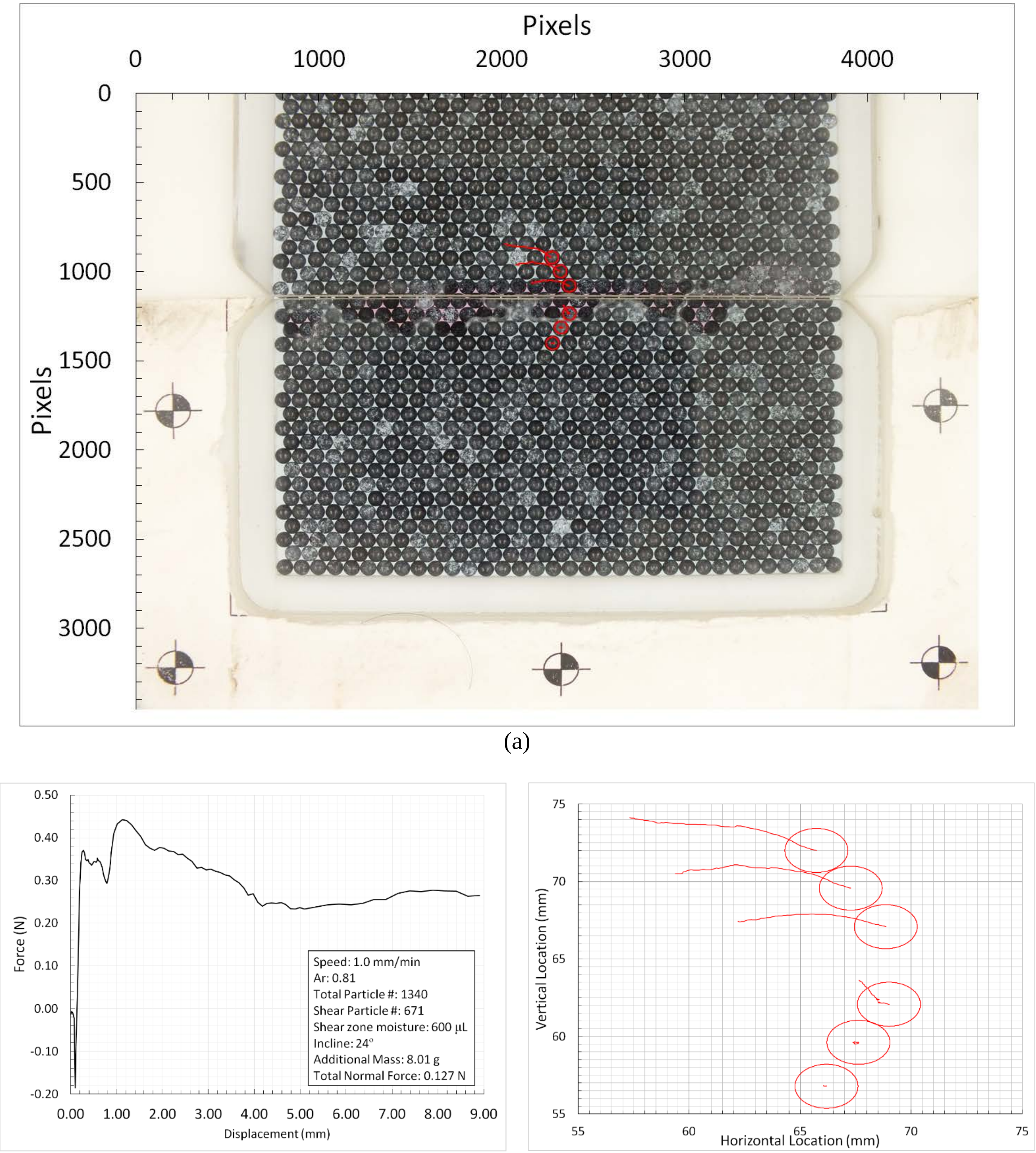

(a)

(b) (c)

Figure: F.8 Glass beads results for 1.0 mm/min, dense state, 24° incline:
(a) Image space movements, (b) Shear response, (c) Real space movements

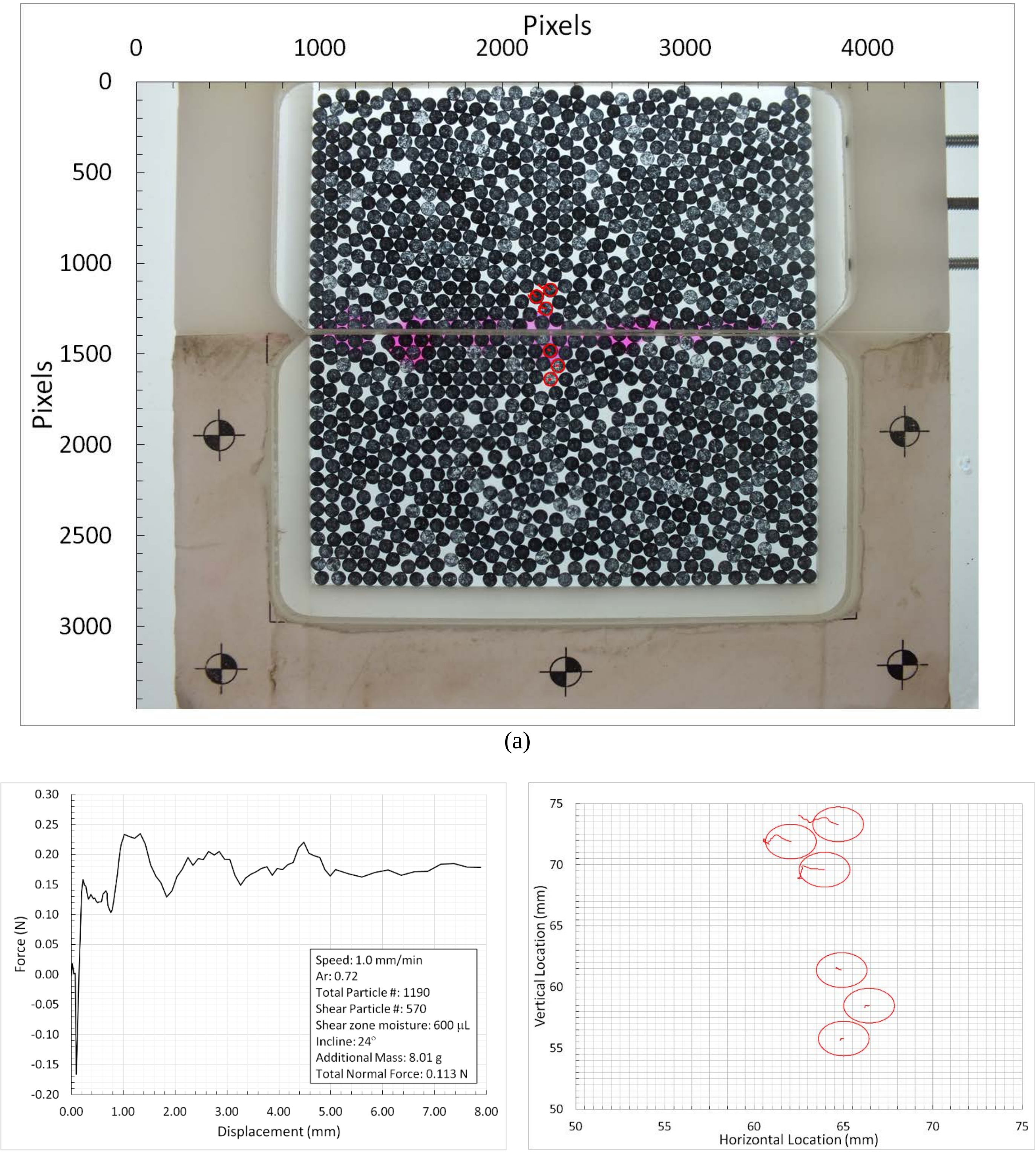

(a)

(b)

(c)

Figure: F.9 Glass beads results for 1.0 mm/min, loose state, 24° incline:
(a) Image space movements, (b) Shear response, (c) Real space movements

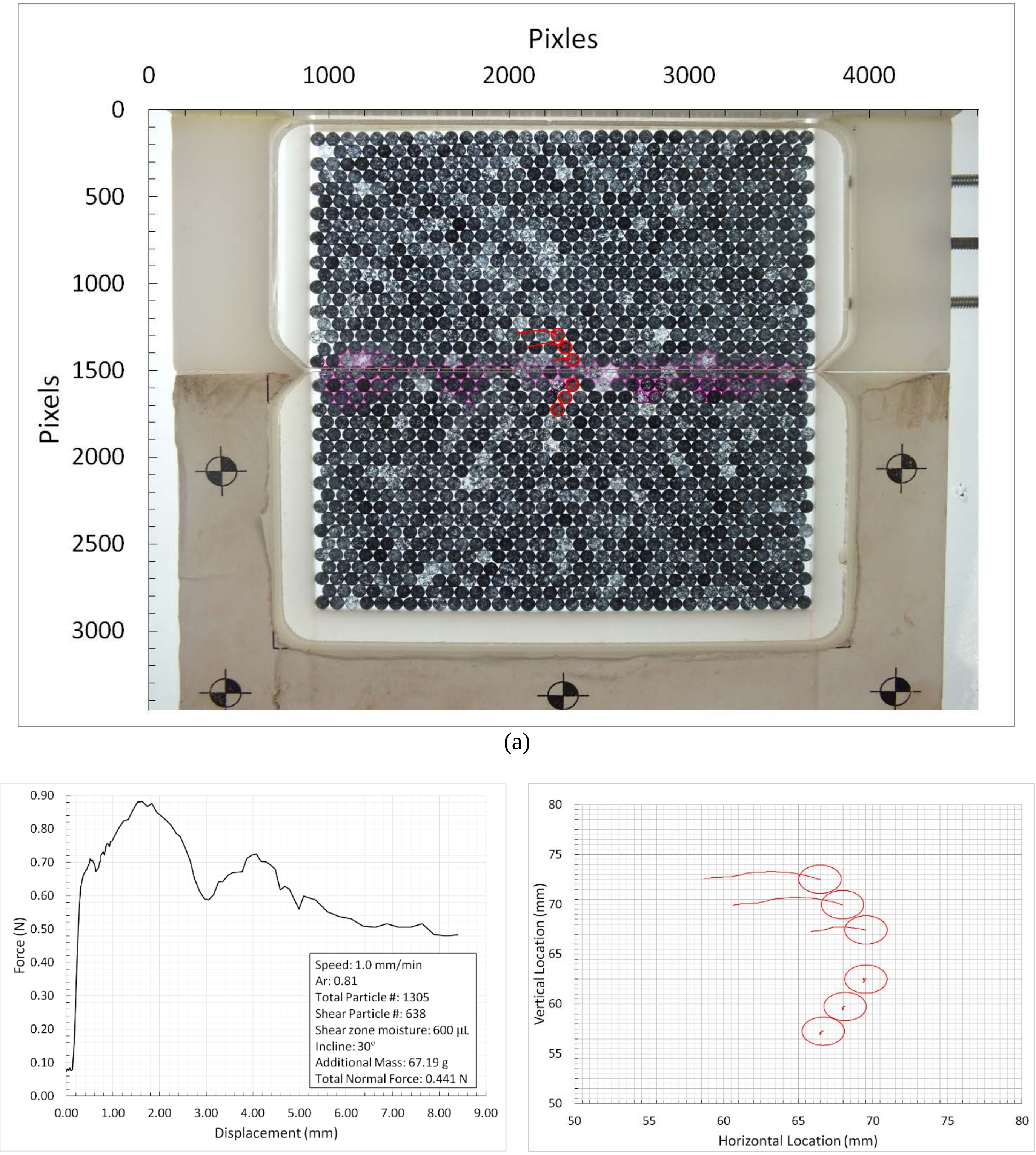

(a)

(b)

(c)

Figure: F.10 Glass beads results for 1.0 mm/min, dense state, 30° incline: (a) Image space movements, (b) Shear response, (c) Real space movements

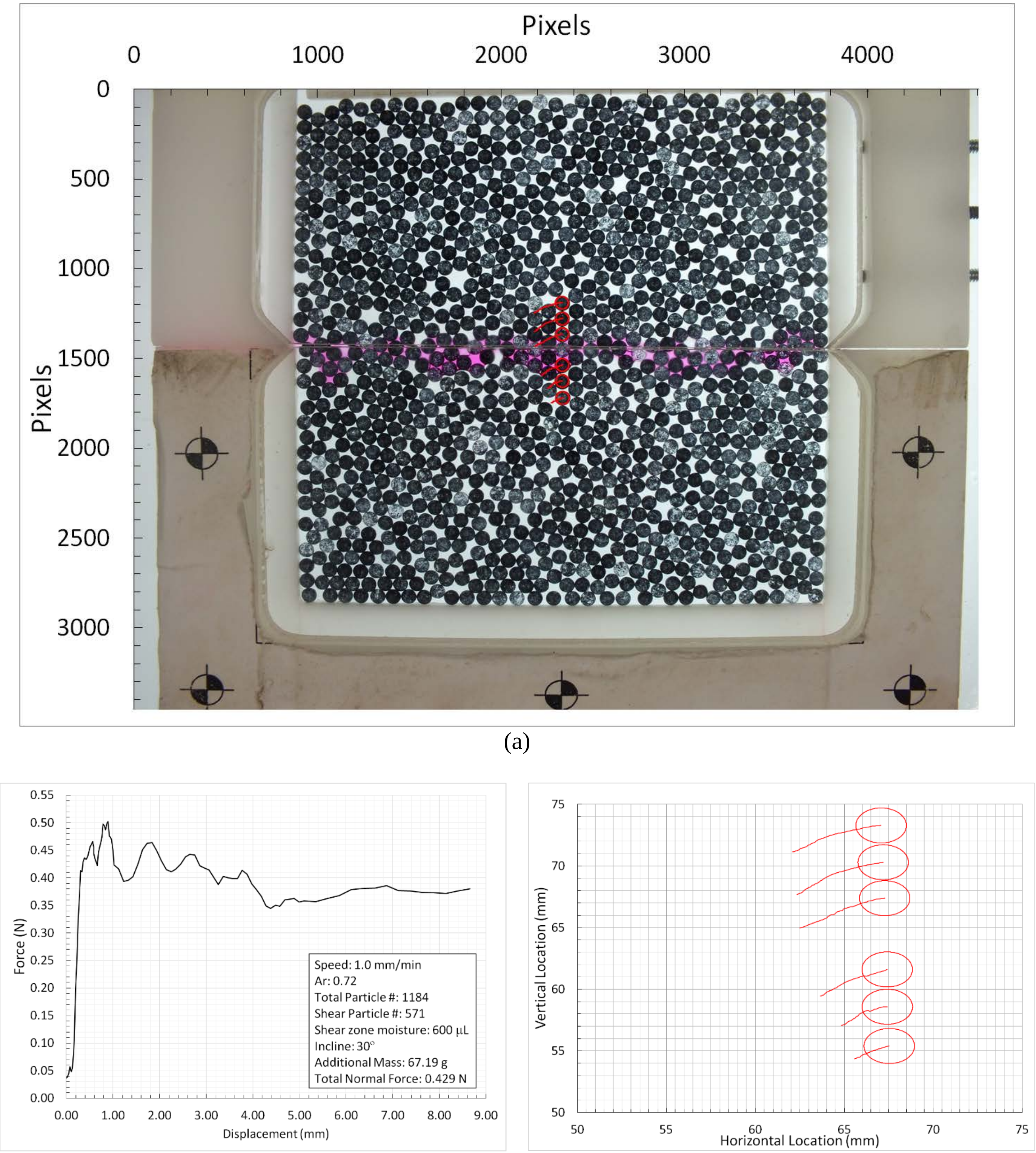

(a)

(b)

(c)

Figure: F.11 Glass beads results for 1.0 mm/min, loose state, 30° incline: (a) Image space movements, (b) Shear response, (c) Real space movements

Appendix G Wet Sand Direct Shear Results

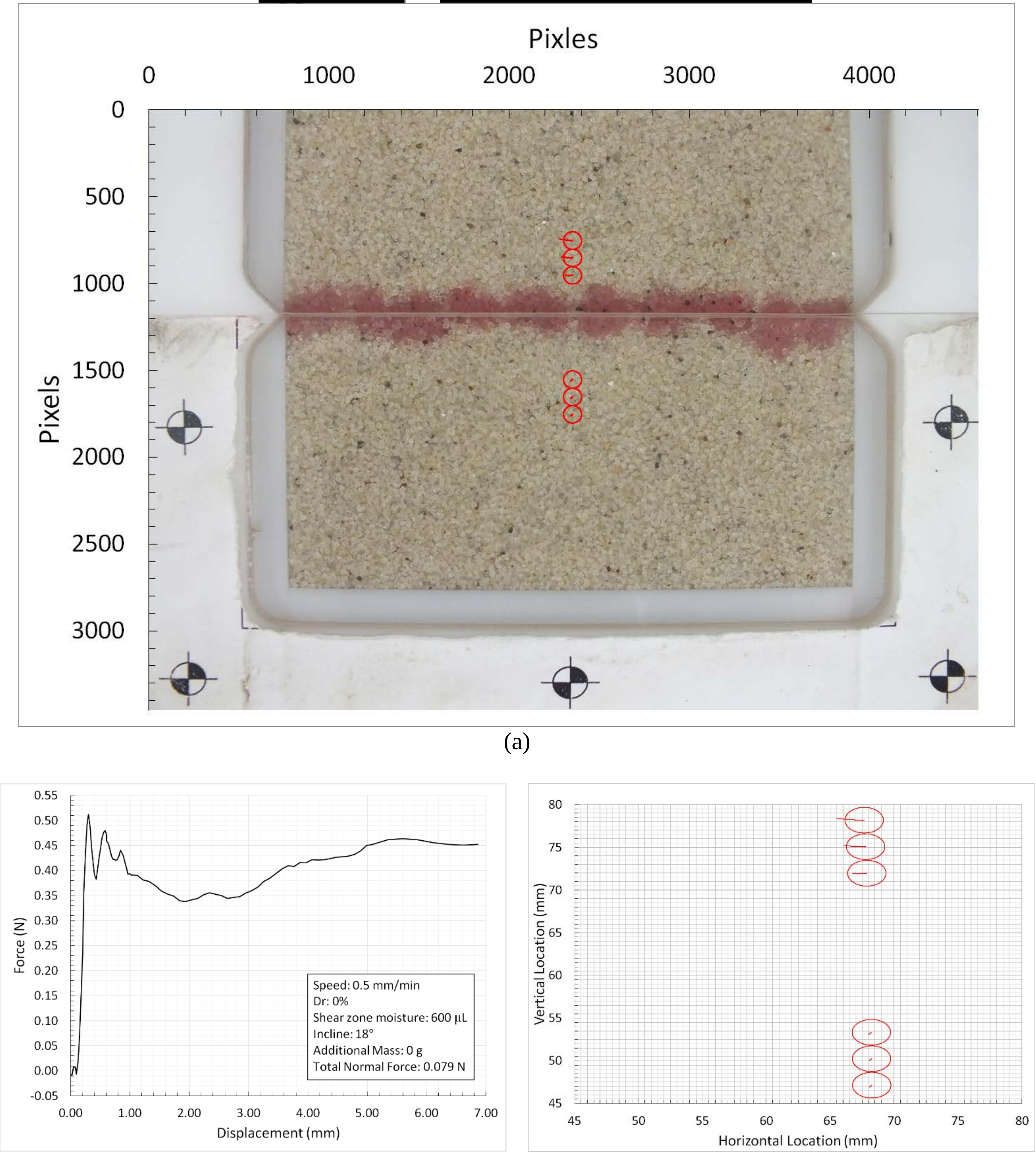

(a)

(b) (c)

Figure: G.1 Sand results for 0.5 mm/min, loose state, 18° incline:
(a) Image space movements, (b) Shear response, (c) Real space movements

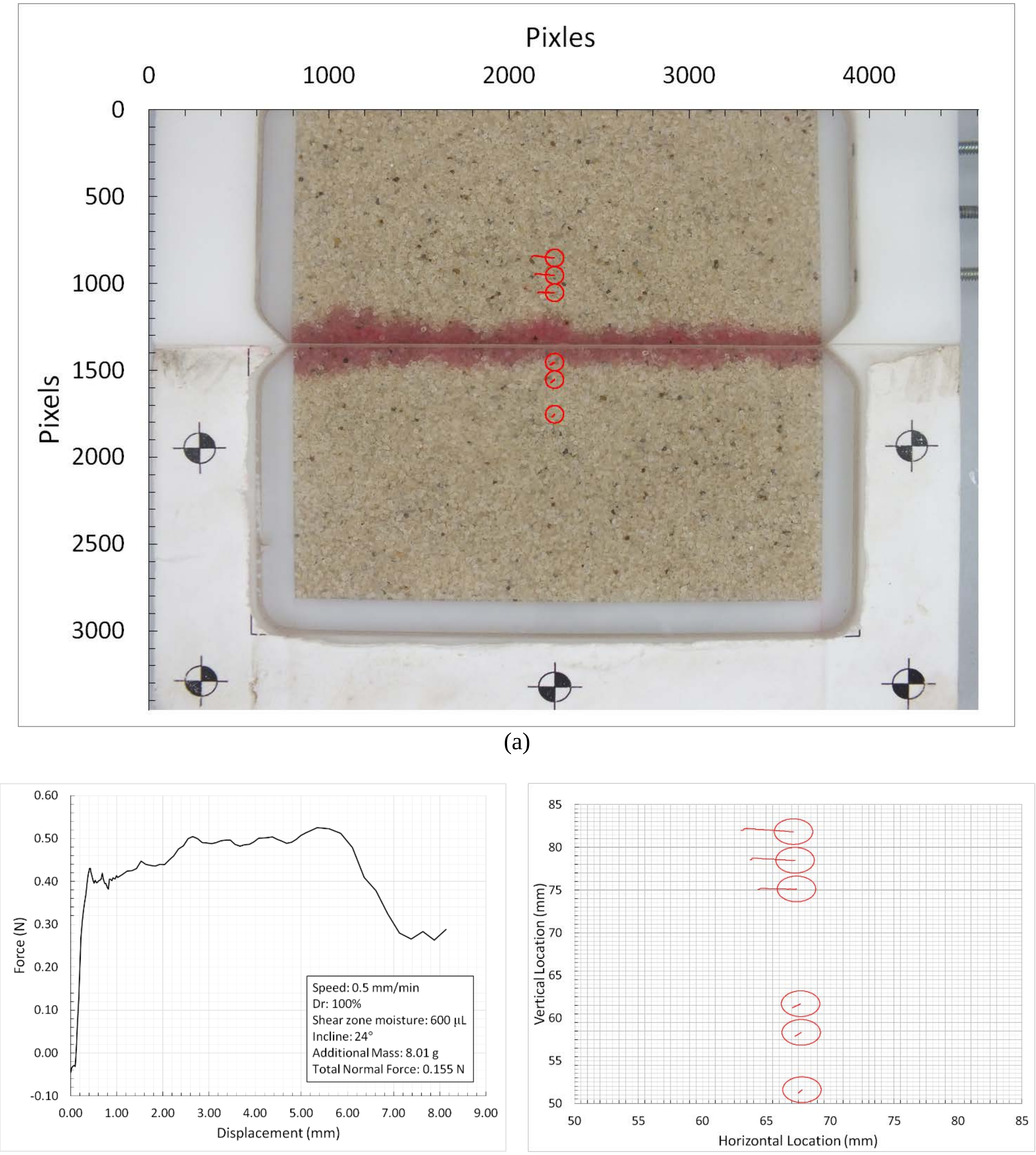

(a)

(b)

(c)

Figure: G.2 Sand results for 0.5 mm/min, dense state, 24° incline: (a) Image space movements, (b) Shear response, (c) Real space movements

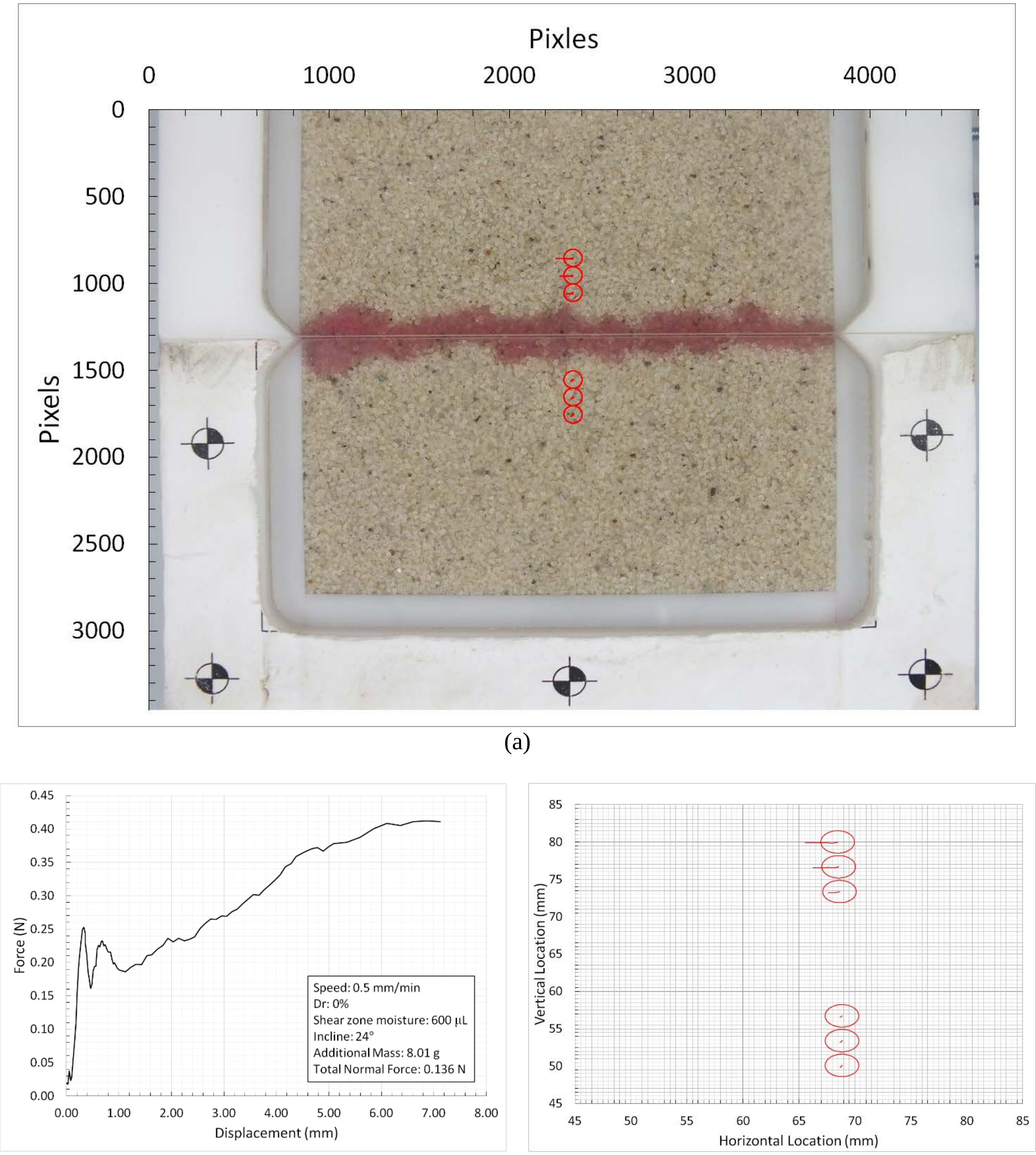

(a)

(b)

(c)

Figure: G.3 Sand results for 0.5 mm/min, loose state, 24° incline:
(a) Image space movements, (b) Shear response, (c) Real space movements

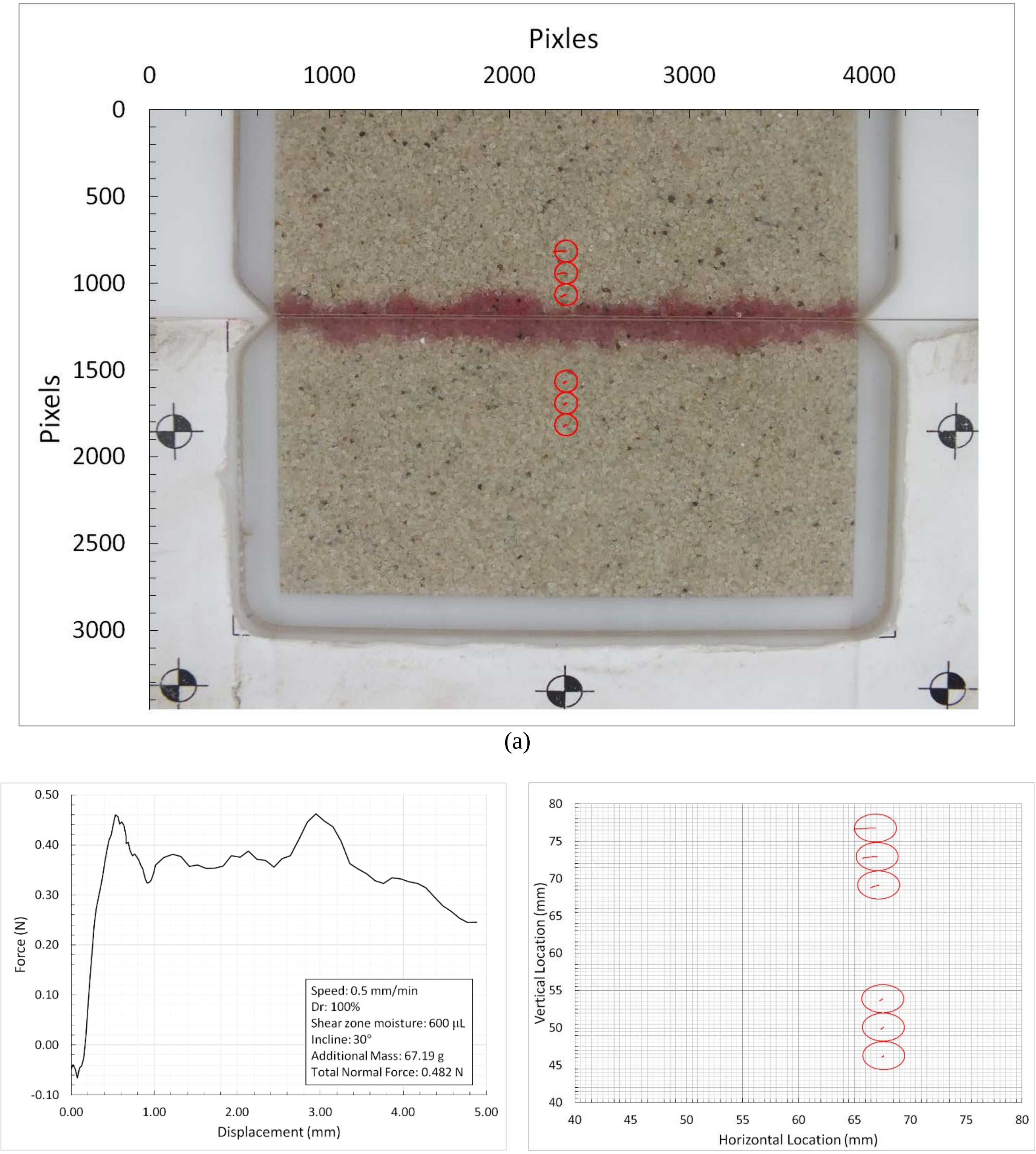

(a)

(b) (c)

Figure: G.4 Sand results for 0.5 mm/min, dense state, 30° incline:
(a) Image space movements, (b) Shear response, (c) Real space movements

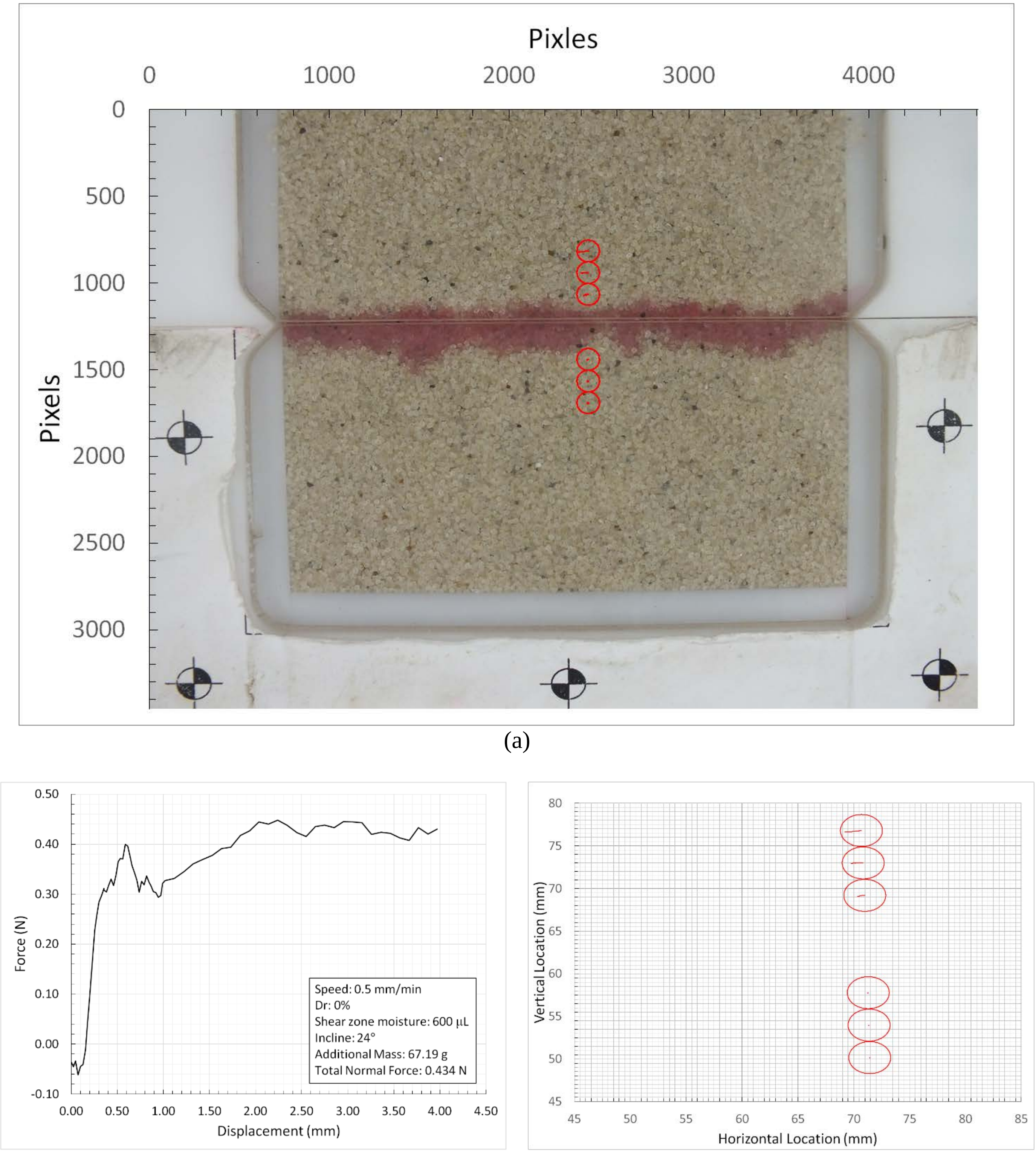

(a)

(b)

(c)

Figure: G.5 Sand results for 0.5 mm/min, loose state, 30° incline:
(a) Image space movements, (b) Shear response, (c) Real space movements

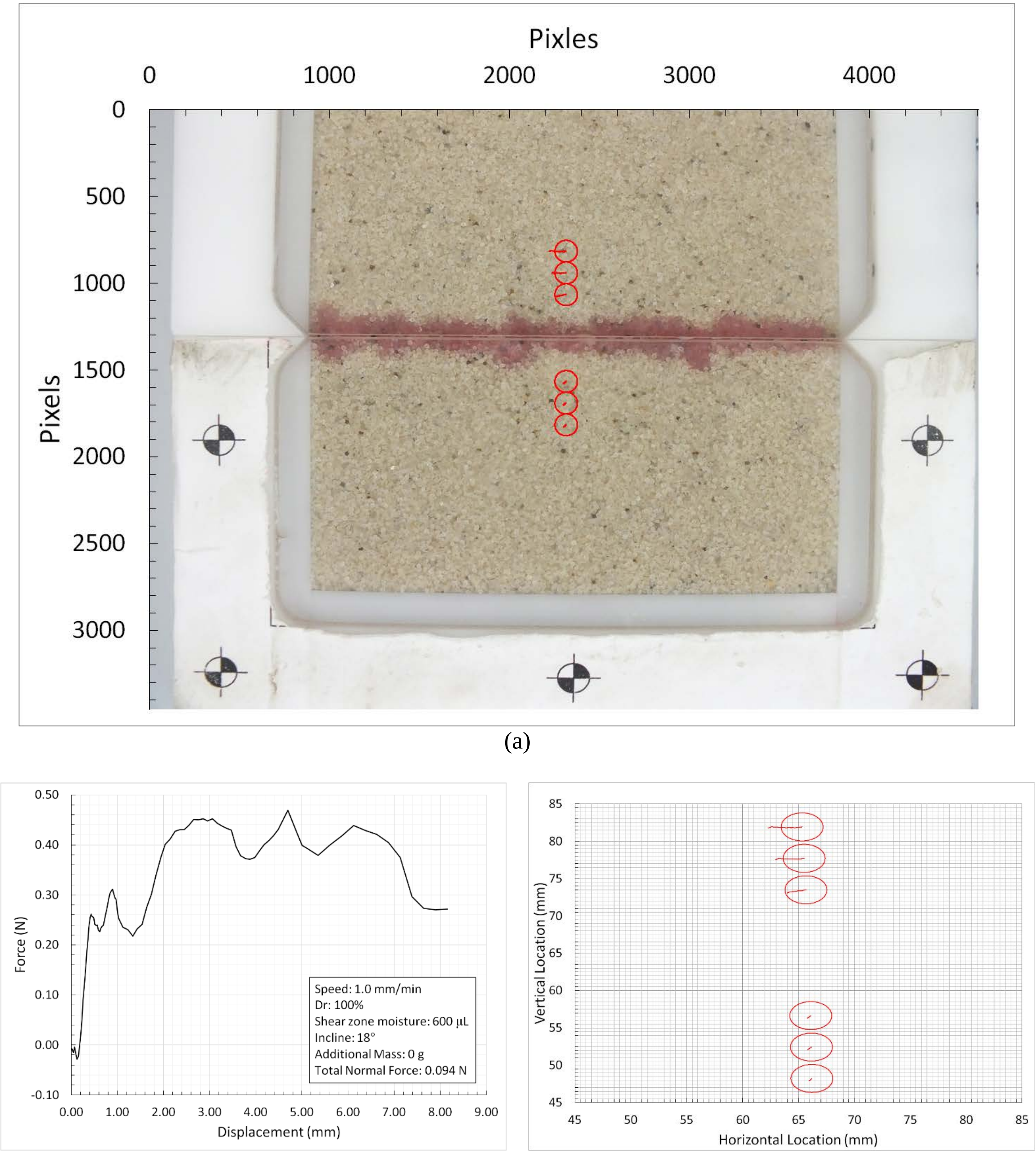

(a)

(b)

(c)

Figure: G.6 Sand results for 1.0 mm/min, dense state, 18° incline: (a) Image space movements, (b) Shear response, (c) Real space movements

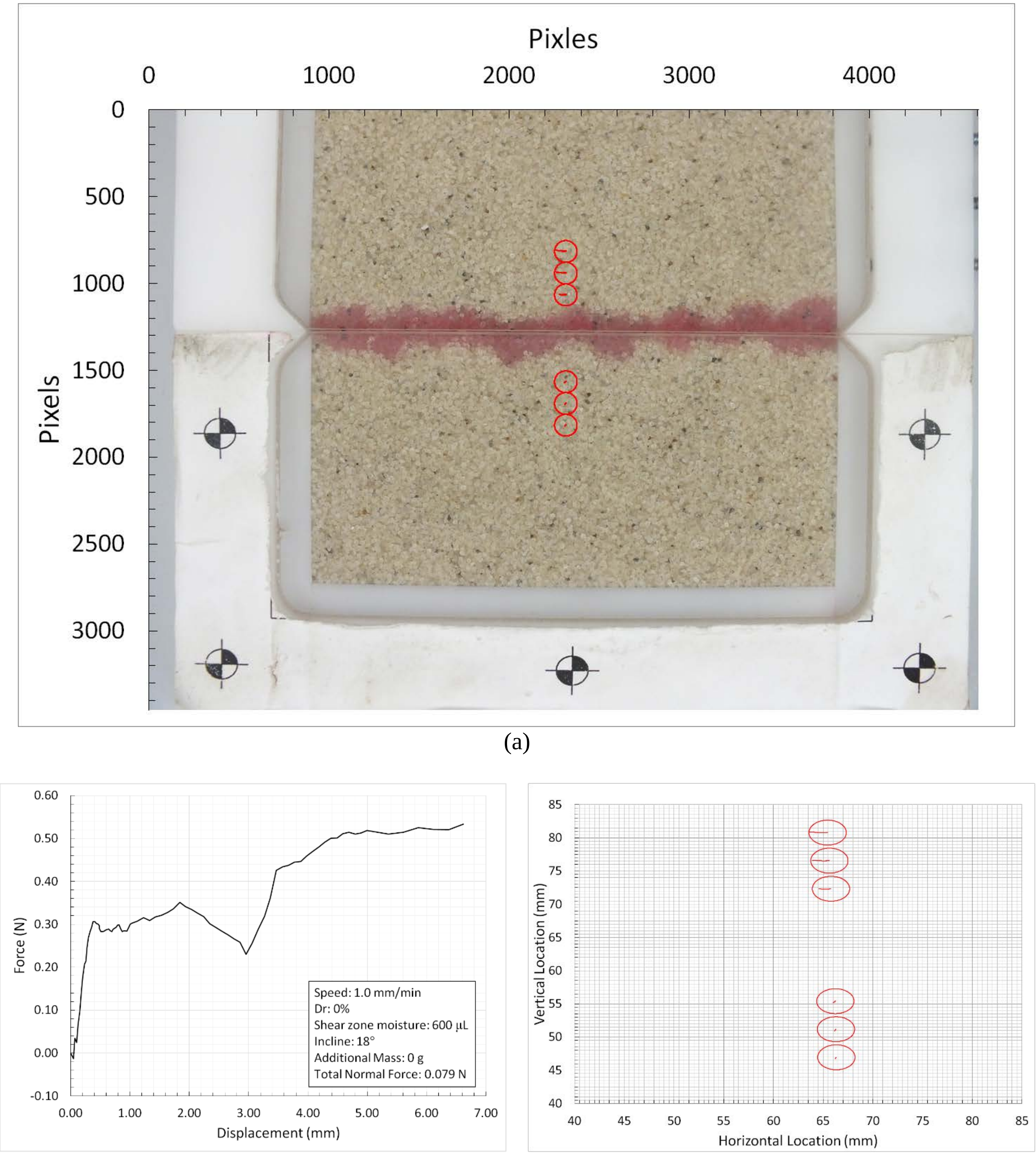

(a)

(b)

(c)

Figure: G.7 Sand results for 1.0 mm/min, loose state, 18° incline:
(a) Image space movements, (b) Shear response, (c) Real space movements

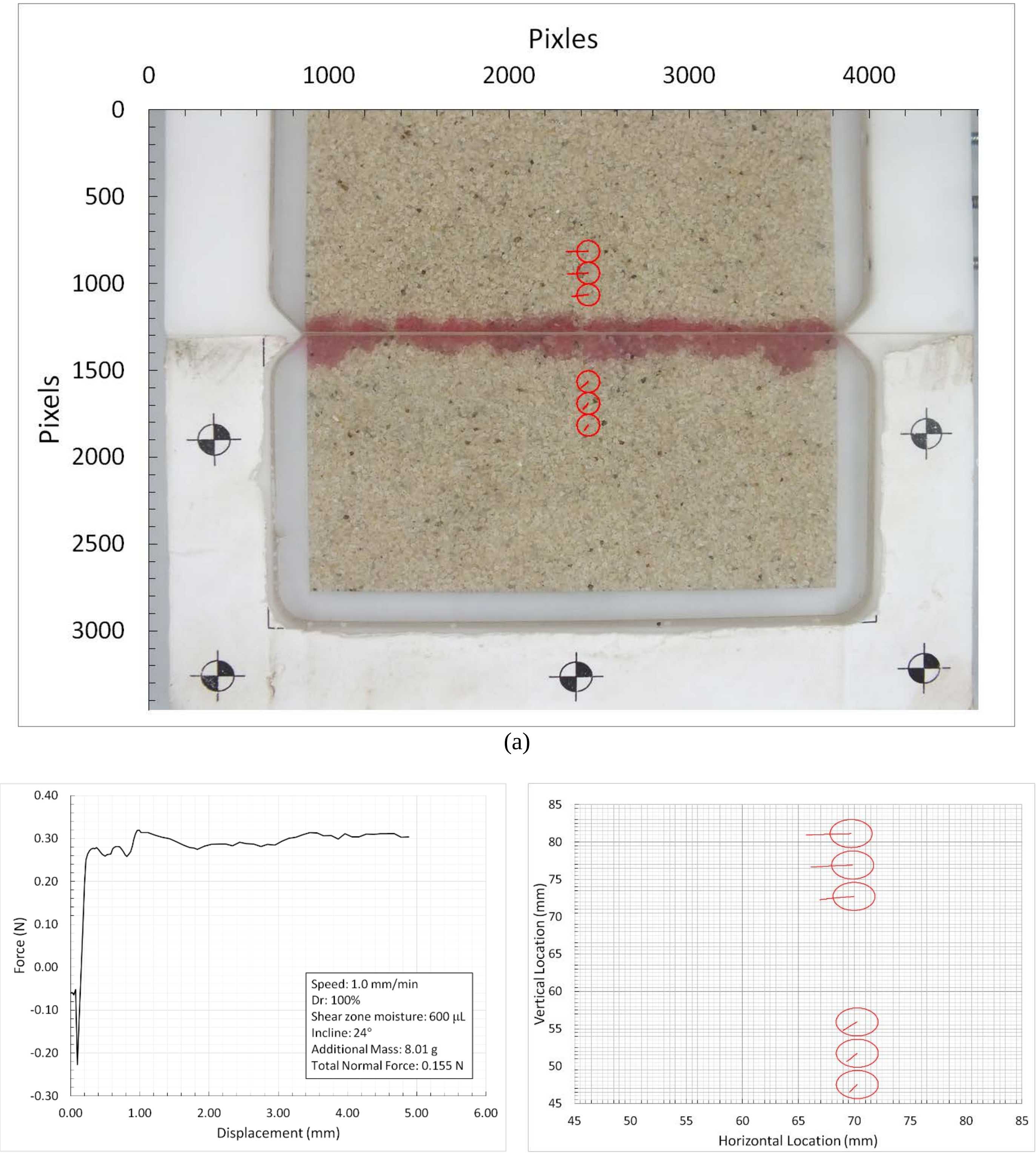

(a)

(b)

(c)

Figure: G.8 Sand results for 1.0 mm/min, dense state, 24° incline:
(a) Image space movements, (b) Shear response, (c) Real space movements

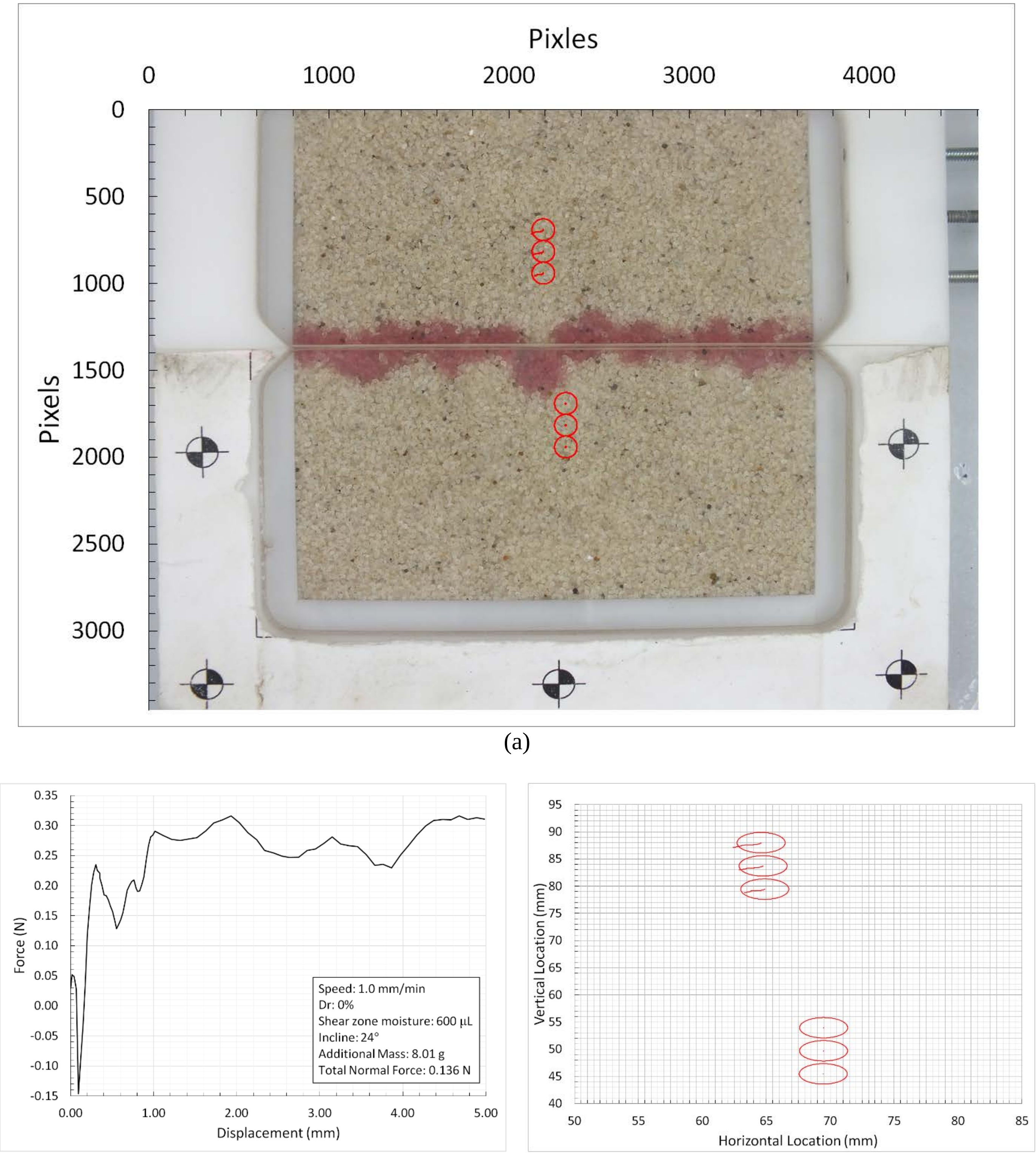

(a)

(b)

(c)

Figure: G.9 Sand results for 1.0 mm/min, loose state, 24° incline:
(a) Image space movements, (b) Shear response, (c) Real space movements

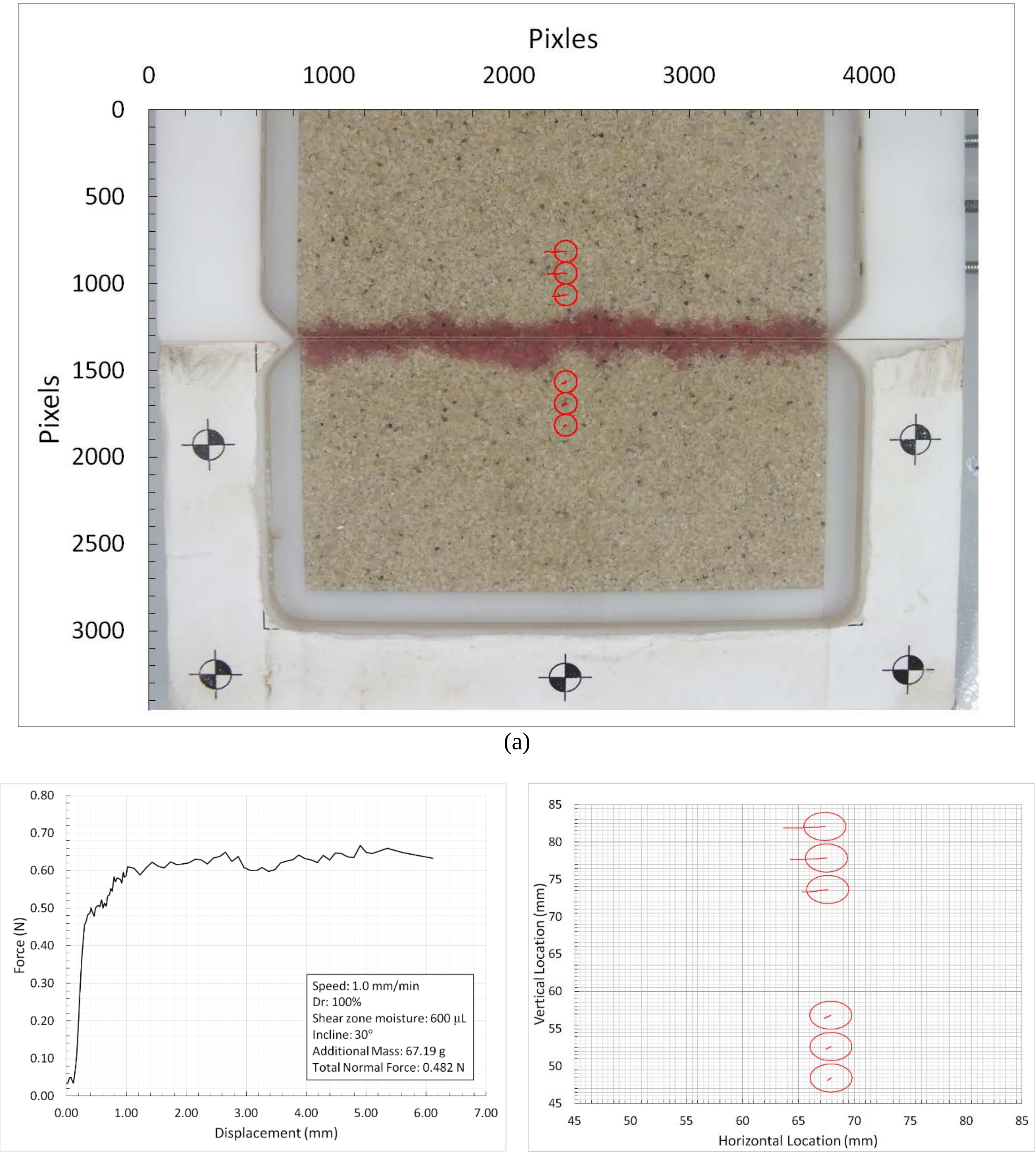

(a)

(b) (c)

Figure: G.10 Sand results for 1.0 mm/min, dense state, 30° incline:
(a) Image space movements, (b) Shear response, (c) Real space movements

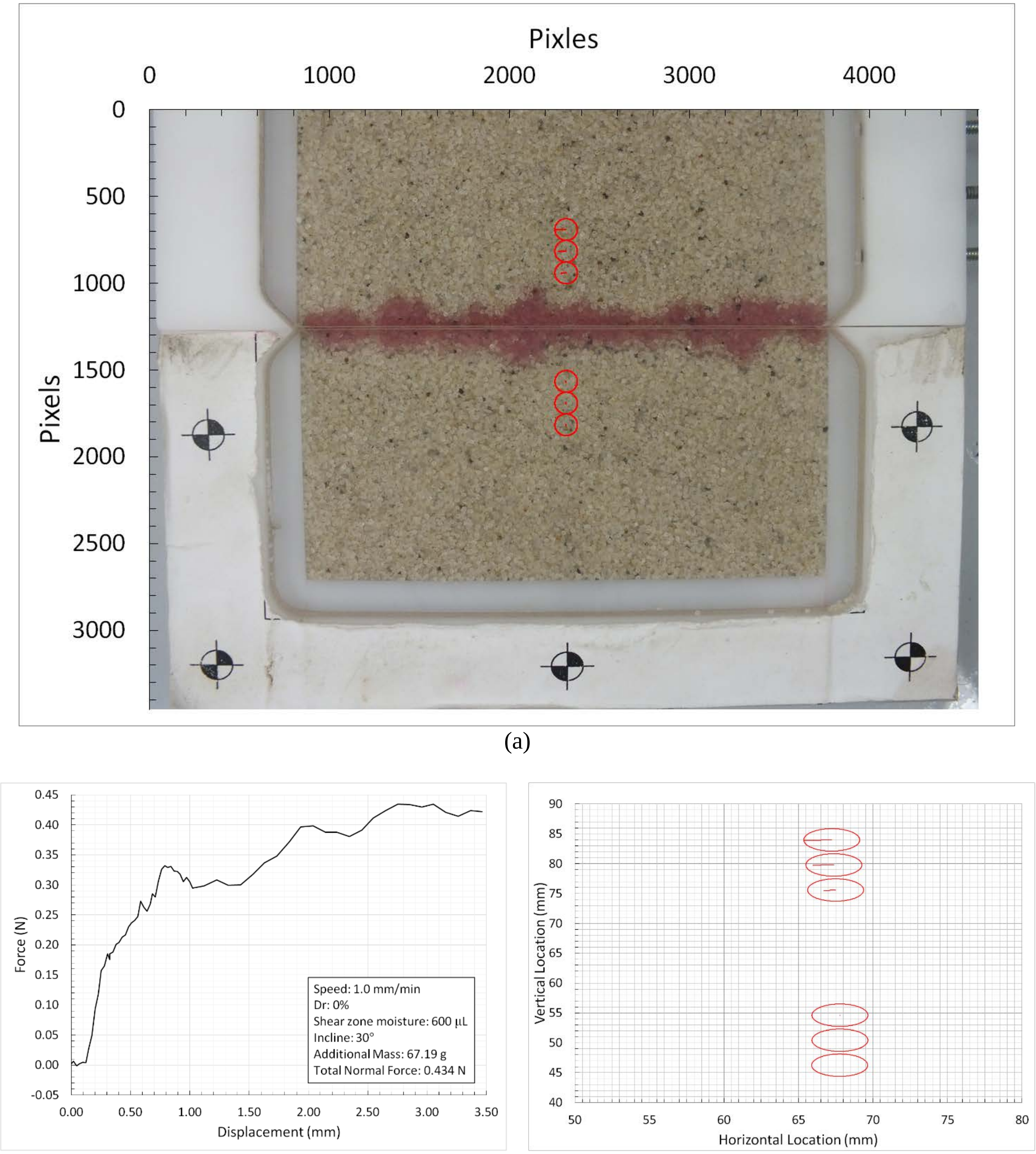

(a)

(b)

(c)

Figure: G.11 Sand results for 1.0 mm/min, loose state, 30° incline:
(a) Image space movements, (b) Shear response, (c) Real space movement